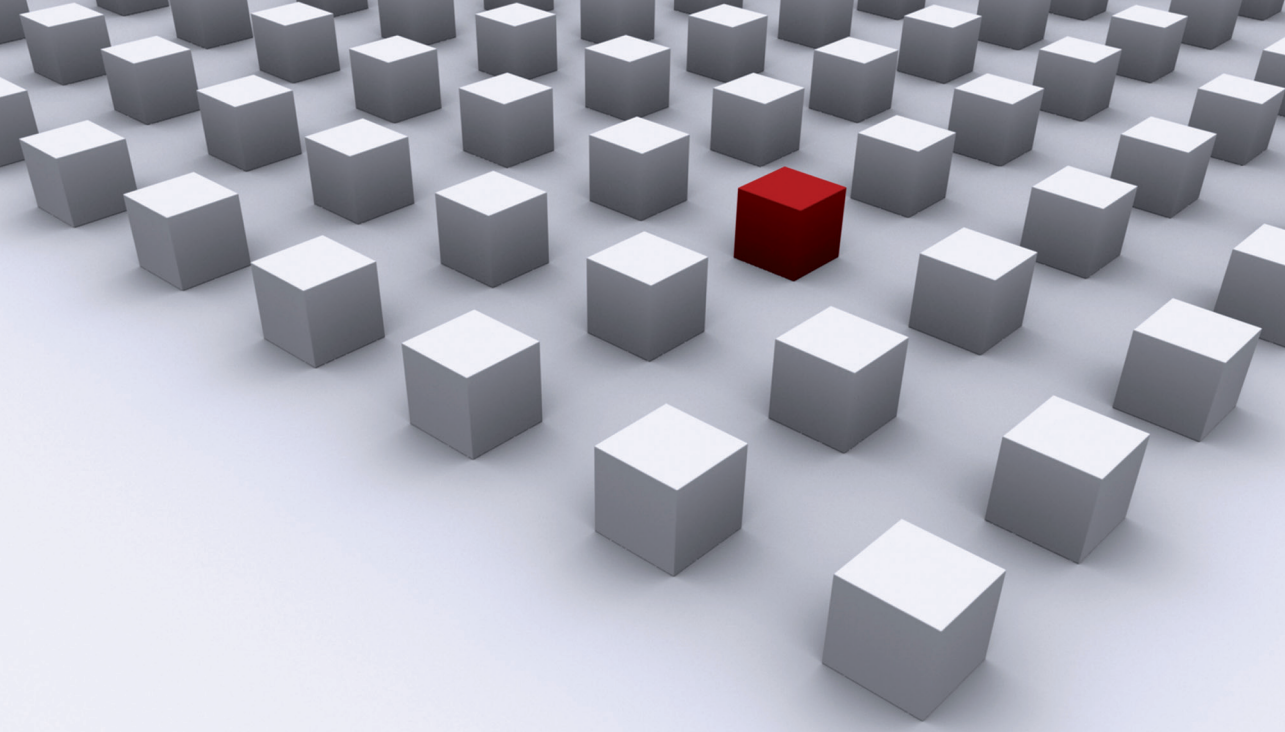

Benjamin Geiger

From few to many particles: Semiclassical approaches to interacting quantum systems

Universitätsverlag Regensburg

55 Dissertationsreihe Physik

Benjamin Geiger

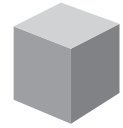

From few to many particles: Semiclassical approaches to interacting quantum systems

From few to many particles: Semiclassical approaches to interacting quantum systems

Dissertation zur Erlangung des Doktorgrades der Naturwissenschaften (Dr. rer. nat.)
der Fakultät für Physik der Universität Regensburg
vorgelegt von

Benjamin Geiger

aus Radolfzell am Bodensee
im April 2020

Die Arbeit wurde von Prof. Dr. Klaus Richter angeleitet.
Das Promotionsgesuch wurde am 11.03.2020 eingereicht.
Das Kolloquium fand am 29.05.2020 statt.

Prüfungsausschuss:	Vorsitzender:	Prof. Dr. Jascha Repp
	1. Gutachter:	Prof. Dr. Klaus Richter
	2. Gutachter:	Prof. Dr. Ferdinand Evers
	weiterer Prüfer:	Prof. Dr. Christoph Lehner

Dissertationsreihe der Fakultät für Physik der Universität Regensburg, Band 55

Herausgegeben vom Präsidium des Alumnivereins der Physikalischen Fakultät:
Klaus Richter, Andreas Schäfer, Werner Wegscheider

Benjamin Geiger

From few to many particles: Semiclassical approaches to interacting quantum systems

Universitätsverlag Regensburg

Bibliografische Informationen der Deutschen Bibliothek.
Die Deutsche Bibliothek verzeichnet diese Publikation
in der Deutschen Nationalbibliografie. Detailierte bibliografische Daten
sind im Internet über http://dnb.ddb.de abrufbar.

1. Auflage 2020

Leibnizstraße 13, 93055 Regensburg

Konzeption: Thomas Geiger
Umschlagentwurf: Franz Stadler, Designcooperative Nittenau eG
Layout: Benjamin Geiger
Druck: Docupoint, Magdeburg
ISBN: 978-3-86845-164-1

Weitere Informationen zum Verlagsprogramm erhalten Sie unter:
www.univerlag-regensburg.de

From few to many particles: Semiclassical approaches to interacting quantum systems

Dissertation
zur Erlangung des Doktorgrades
der Naturwissenschaften (Dr. rer. nat.)
der Fakultät für Physik
der Universität Regensburg

vorgelegt von

Benjamin Geiger

aus

Radolfzell am Bodensee

April 2020

Promotionsgesuch eingereicht am: 11.03.2020

Die Arbeit wurde angeleitet von: Prof. Dr. Klaus Richter

List of used acronyms:

1D – one-dimensional/one dimension
3D – three-dimensional/three dimensions
BCS – Bardeen-Cooper-Schrieffer
BEC – Bose-Einstein-condensation/condensate
BGS – Bohigas-Giannoni-Schmit
EBK – Einstein-Brillouin-Keller
LL – Lieb-Liniger
OTOC – out-of-time-ordered correlator
QCE – quantum cluster expansion
RG – renormalization group
SPA – stationary phase approximation
WKB – Wentzel-Kramers-Brillouin

Contents

Introduction

A great success of theoretical physics lies in the stepwise combination of small, specialized theories to more fundamental, unified ones, that require a smaller set of assumptions or parameters. While the discovery of each successful unification is usually driven by the insufficiency of older theories, their greatest value lies in the prediction of new phenomena. However, although the new theories often add important new aspects to the theoretical description of the physical effects that had been well explained without them, the "old" theory can remain equally valid in such situations. Even within a single theoretical framework, very different (equivalent) approaches, as well as approximate methods can be formulated, that can lead to very different (approximately) equivalent interpretations. The practical implication of this is nicely summarized in a quote by Richard Feynman, stating that "[...] every theoretical physicist who is any good knows six or seven different theoretical representations for exactly the same physics" [1]. This can, of course, not be applied to new experimental discoveries, where sometimes not a single theoretical representation is known, but it describes very well how a physical problem should be approached from as many different viewpoints as possible to capture all of its physical aspects. However, it is not the task of a single physicist to *find* all these representations, and in the study of new phenomena, it is usually a whole community that works on very similar problems, hopefully exploring them in different ways.

This thesis tries to complement some of the standard approaches that are nowadays used in few- and many-body systems with selected semiclassical methods. The latter are, although approximate (but not perturbative) in nature, a very useful tool when it comes to acquiring a physical intuition to otherwise "black box" exact techniques, and can complement the understanding gained from other (approximate) methods in otherwise inaccessible regimes. To point out some of the advantages of semiclassical methods, a brief overview of some standard methods and stepping stones in the treatment of few- and many-body systems is given in the following. It is far from being a complete summary of methods and means only to highlight some of the common characteristics and shortcomings that set the basis for the theoretical work in the main part.

From few to many

Single-particle problems, formally also comprising the relative motion in separable two-body problems, have clearly been of paramount importance in the early development of quantum mechanics. The Bohr-Sommerfeld quantization of the hydrogen atom was one of the first steps towards a full quantum theory. Once found, the latter had to be tested by applying it to the simplest and best explored kinds of systems, i.e., classically separable (single-particle) systems like the harmonic oscillator, the Coulomb problem,

and many other systems that can be treated exactly in quantum mechanics. However, these systems are very special and already at the level of the three-body problem, one usually obtains classically chaotic behavior [2]. In the same way, the quantum description of systems with more than two interacting particles does not allow for a fully analytic description in most cases[1] and approximate methods have to be found.

The simplest approximations, especially used in molecular and condensed matter physics, comprise the linear combination of atomic orbitals and tight binding approximations, often combined with Born-Oppenheimer approximations to adiabatically separate the fast electronic motion from the motion of the heavy nuclei [4–6]. A first important stepping stone in the description of atoms and molecules that included the nontrivial effects of the interactions between the electrons was the introduction of the Hartree-Fock method as a many-body variational technique [7]. By assigning a single-particle wave function to each of the electrons in an atom or molecule, it is one of the early implementations of the idea of each particle "feeling" the other particles only in terms of a mean field. It is a common feature of such mean-field approaches that the quantum correlations between the particles are neglected by finding an effective noninteracting theory that then describes the excitations in the system by quasiparticles [8]. However, especially in systems with only a few particles, the correlations between the particles are very important and the true ground state energy of the system can differ strongly from the variational ground state obtained in Hartree-Fock theory, as the latter neglects the correlation energy. To get better approximations for such systems, more elaborate algorithms are needed.

An early extension that takes superpositions of Slater determinants into account is the configuration interaction method introduced in early quantum chemistry [9]. It is, however, limited to rather small particle numbers, such that other methods have taken its place in more recent developments[2]. A widely used modern tool in electronic systems is the density functional theory (see [7] or [10] for a review) that uses the fact that, if the many-body ground state is not degenerate, its electron density uniquely determines the (external) potential. As this potential is the only non-universal part in the electronic Hamiltonian, all ground state expectation values turn out to be functionals of the electron density. Unfortunately, although the latter is guaranteed by the theorem of Hohenberg and Kohn [11], the explicit functionals are not known and already at the level of calculating the energy one has to use approximations for the unknown exchange energy functional. Moreover, the density functional theory is only capable of determining the ground state properties of the (possibly strongly correlated) system, to albeit good approximation.

A complementary approach for fermionic systems is found in the Fermi liquid theory that can be formally derived in many-body perturbation theory [8] and deals exclusively with excitations in terms of fermionic quasiparticles. In fact, most macroscopic fermionic systems, such as the electrons in metals or (fermionic) cold atom gases, are well described

[1] Excluding the special class of quantum integrable models [3] here.

[2] Nevertheless, the enormous increase in computational power in the past decades has made it possible to use (advanced) configuration interaction approaches using bases of several billions of Slater determinants [9].

within this theory, that is adiabatically connected to the case of free fermions. Usually, such mean field quasiparticle descriptions become exact in the thermodynamic limit in the low-temperature regimes, where the corrections from quantum correlations are of subleading order in the system size. An important exception are systems close to phase transitions, where the correlation length diverges, as it will be discussed in more detail in the introduction of chapter 2. In contrast to some of the other methods discussed here, perturbative approaches are very well controlled by a small parameter, but they are always limited to the vicinity of known limits. Moreover, they can only capture analytic effects, such that phase transitions cannot be described. A famous example in fermionic systems is the instability of the Fermi sea (in a Fermi Liquid or free fermionic gas) against small attractive interactions, leading to the formation of the Bardeen-Cooper-Schrieffer (BCS) ground state that is non-analytic in the coupling between the fermions [12].

In bosonic systems, the mean-field description often boils down to quasi-classical field equations. An important example is the Gross-Pitaevskii, or nonlinear Schrödinger equation [13], that is commonly used in the theory of Bose-Einstein condensation (BEC) in the presence of short-range interactions [14]. There, collective bosonic Bogoliubov excitations above the mean-field ground state can be found by a quadratic expansion of the field operators around the condensate [15]. The Bogoliubov equations that determine the excitations are then often referred to as the Bogoliubov-de Gennes equations, as they are the analogues to the respective equations in the BCS theory of superconductivity, however for bosonic operators. Although these mean-field methods are very powerful tools that can be used also in regimes that are not accessible by perturbative approaches (see, e.g., [16] for an application on both sides of a quantum phase transition), they are not devised for the study of effects that stem from finite system sizes and cannot capture the correlations among particles. Moreover, they are restricted to small excitations of the condensate and thus to extremely low temperatures when equilibrium properties are concerned.

Out of the methods devised for the calculation of thermal equilibrium expectation values, the standard method of cluster expansions will be introduced in more detail in chapter 1, also including a brief historical overview, and is therefore not further discussed here.

The most prominent approach to many-body equilibrium physics has been mentioned already in the context of Fermi liquid theory, namely the many-body perturbation theory. For finite temperatures, it uses the temperature, or imaginary-time Green's functions, equipped with diagrammatic approaches [8]. Due to the similarity to the well-known perturbation theory in (real time) quantum field theories, this approach is also referred to as thermal field theory. But it has distinct differences like the appearance of discrete Matsubara frequencies due to the periodicity (or anti-periodicity in the case of Fermions) of the fields with respect to the temperature, being enforced by the trace in the definition of the partition function [8]. The obvious drawback of the perturbative approach is its limited applicability, i.e., explicit calculations are restricted to perturbative regimes. It is, however, possible to approximately evaluate the path integrals non-perturbatively using stochastic methods. Especially in bosonic systems, state of the art path integral Monte-Carlo calculations can yield predictions for tens of parti-

cles [17], but the computational effort is enormous. Unfortunately, this is complicated in fermionic systems due to the sign problems [7], that can only be overcome in selected applications [18]. Although these computational methods are, together with exact diagonalization approaches, sometimes the only way to obtain accurate results in certain regimes, their more or less black-box processing does not provide very much insight into possible underlying mechanisms (although they might help in their discovery).

Finally, one should also mention a special class of many-body systems that allows for an exact analytical treatment, i.e., the quantum integrable systems [3]. These models are of one-dimensional nature and they have in common that they fulfill the Yang-Baxter equation at some stage. For the one-dimensional Lieb-Liniger model [19], that will be used in this thesis, it incorporates the fact that the scattering of any number of particles decomposes into commuting two-particle scattering events [20].

From many to few: the advent of ultracold atomic gases

Most of the theoretical developments sketched so far have roughly followed the experimental demands and discoveries: The early few-particle applications were devised for fermions[3], as the only experimentally relevant few-particle systems were composed of electrons in atoms and molecules or, in the description of nuclei, protons, and neutrons, all of them being of fermionic nature. Also in the many-particle solid state systems, the description of the electronic properties were of predominant relevance, but also the phonons, being bosonic quasiparticles of lattice vibrations, started playing an experimental role. Photons, as the only elementary particles of bosonic nature that are easily observable, do not couple directly to each other and cannot be confined to a system with a fixed number of particles. The same holds true for the bosonic quasiparticles appearing in mean-field theories. Although they generically have residual interactions, their number is not conserved, thus requiring a statistical description.

The situation is different in dilute cold atomic gases, where the atoms behave similar to elementary bosons and fermions, depending on their total spin, such that these systems have long been candidates for well-controlled experimental applications. Although cooling down gases to ultracold regimes, that are dominated by quantum effects, is a standard procedure in modern experiments ([22,23] and references therein), it has taken more than 70 years from the prediction to the experimental realization of a Bose-Einstein condensate in such a system [24]. But once this breakthrough was achieved, the experimental progress in the field developed extremely fast. While the early experiments were performed with macroscopic numbers of atoms, the experimental capacities of trapping and detection have drastically improved in this respect and experiments with only a few hundred atoms [25] are now possible. Even few-particle systems with single-atom resolution have been realized in recent experiments [26, 27]. Simultaneously, the advent of Feshbach resonances in cold atom gases [28, 29] has allowed to tune the two-particle scattering length in ultracold bosonic and fermionic gases to arbitrary values. Together

[3] However, before the discovery of the spin statistic theorem, Thomas [21] discovered that the Tritium nucleus could collapse if the neutrons are in a symmetric state and have vanishing mutual interaction.

with the possibility of "painting" arbitrary potentials [30] in some of these systems this has paved the way to gain full control over a wide class of artificially designed many- and few-particle systems that can model condensed matter or even high-energy systems on larger scales and open the way to new kinds of physics, e.g., Bloch oscillations without a lattice due to strong interactions [31] and Efimov physics in bosonic gases [32,33], to name two examples, accompanied with a renewed interest in correlated few-body systems [34]. By using strongly anisotropic trapping potentials, effectively one-dimensional quantum gases can be realized [35–38] with arbitrarily strong interactions due to confinement induced resonances [39], bringing some of the formerly purely theoretical low-dimensional model systems closer to experiment.

The power of semiclassical methods

It is important to stress right at the start that the meaning of the term "semiclassical" is not homogeneous among the literature. While rigorous semiclassical methods developed during the last century can be used to obtain well-controlled approximate results in *quantum* mechanics, many authors abuse the term for introducing ad hoc *classical* methodology in certain approximations. Some of these are extremely successful, and of great value especially in the teaching of quantum mechanics, as the human intuition on classical systems is usually much better trained, but the way these approximations are presented as "semiclassical arguments" have, in my opinion, created the connotation of semiclassical methods being a conglomeration of classical arguments that have turned out to work miraculously well also in quantum mechanics. This might be partially owed to the first "old quantum theory" [40] being also referred to as semiclassical by some authors. The respective "semiclassical" constructions have unarguably been very important in the development of quantum mechanics, with the Bohr model of the quantized orbits being an intermediate step between classical particle mechanics and wave mechanics. But although it seems to incorporate already the idea of the electron having a wavelength, this interpretation was not part of the original formulation and the picture of an electron following a classical orbit is incompatible with modern quantum mechanics.

One could take the radical view that the invention of the Schrödinger equation has proven the concept of particles unnecessary, as one can explain everything in terms of waves. But calculating the orbit of a satellite orbiting earth using wave mechanics might be not a good idea, and one should accept that the concept of particles, though seemingly not fundamental, is useful in many applications, especially when macroscopic objects are concerned. Modern semiclassical physics can be understood as a bridge between the two extremes, being applicable in regimes where both particle and wave concept are useful, when they are used *in combination*. Of course, this also includes certain "obvious" cases, where certain degrees of freedom can be understood fully classically, as is the case, e.g., in the famous Stern-Gerlach experiment, where the orbital motion of the silver atoms can be understood classically, although coupled to the quantized spin. The key point is, however, that the semiclassical methods have a much broader range of applicability, as

they have to be understood as rigorous approximations of quantum mechanics in cases where the Planck constant can be considered to be small but *non-zero*.

For systems with an integrable classical limit, a semiclassical quantization rule, the Einstein-Brillouin-Keller (EBK) quantization, can be derived. A detailed presentation of the method can be found in the introduction of chapter 2, where also the subtleties of taking the "classical limit" are discussed. The EBK quantization rules yield the correct quantization of the hydrogen atom and many other elementary (single-particle) models [41], while being conceptually different from the Bohr model, as they use WKB wave functions (after Wentzel, Kramers, and Brillouin) as approximate orbitals with a trivial time evolution [42], and are thereby not restricted to single-particle systems. In the many-body context, the mean-field limit can be understood as a different type of a classical limit, where the inverse particle number takes the role of an effective Planck constant. A quantization of the mean field then yields finite-size corrected quantized energies that reduce to the Bogoliubov spectrum at low excitations, but can also be used at large energies, as will also be demonstrated in chapter 2 of this thesis, and has been used in selected applications in the literature [43, 44]. The number of particles thereby enters as a parameter and thus the complexity of the problem does not increase with the particle number, as is the case, e.g., in exact methods. Moreover, the accuracy of the semiclassical results increases with the particle number, such that it can fill the gap between the regime of few particles, that might be treatable exactly, and the mean-field limit.

When it comes to nonintegrable systems, where both the classical and quantum dynamics become more complex, a simple quantization of the above form does not exist. The semiclassical analysis then shows that the classical periodic orbits, when used correctly, contain (most of) the information about the positions of the discrete energy levels. This was formally derived by Gutzwiller with his famous trace formula [2] for the fluctuations in the density of states. It has been successfully used in various systems that exhibit classical chaos [45–47], including the Helium atom [48] that has a mixed phase space structure. On the one hand, although the trace formula is an asymptotic expansion, using the shortest periodic orbits can be sufficient in many applications where the spectrum does not have to be resolved exactly. On the other hand, by analyzing the Fourier transforms of exact quantum-mechanical spectra, one can identify the dominant classical periodic orbits, which can help understanding the underlying physics [49].

One application that is also of central relevance in this thesis is the approximation of propagators in the short-time regime. To this end, one evaluates the semiclassical van Vleck-Gutzwiller propagator, that is obtained from the stationary phase analysis of the Feynman path integral [40], only for the shortest paths. This approximation corresponds to replacing the discrete quantum-mechanical spectrum by a smooth function in a controlled manner, yielding the smooth part of the density of states (DOS) as an expansion in terms of the dominant system characteristics, known as Weyl expansion [50, 51]. Its many-body version involves propagations in high-dimensional spaces, that, in the case of noninteracting indistinguishable particles, have different contributions due to the exchange permutations. As the latter decompose into cyclic single-particle propagations in the short-time approximation, this naturally leads to a certain cluster structure and

a generalized Weyl law [52]. For interacting particles, this can be combined with the quantum cluster expansion, as will be discussed in more detail in chapter 1.

In the last 20 years, one semiclassical (but almost classical) method known as the Truncated Wigner Approximation [53, 54] (TWA) has emerged as a powerful tool that is now used by a wide community, especially in the field of cold-atom gases. It is based on the Wigner phase-space representation of an initial state of the system, that is then reinterpreted as a classical phase-space distribution that evolves according to the classical equations of motion, thus ignoring interference effects in the time evolution of expectation values. This also limits its applicability to short times smaller than the so-called Ehrenfest time in chaotic systems [55]. Although widely used, the TWA does, by far, not exploit the full potential of the semiclassical methods, as the latter *can* describe interference phenomena: Recent developments have shown that one can describe the quantum time evolution far beyond the Ehrenfest time using more sophisticated semiclassical methods of interfering (complexified) classical paths [56], also providing detailed information on the quantum spectrum.

Apart from the use of the semiclassical techniques as powerful predictive tools, their great value also lies in the relative parametric simplicity and generality of these predictions. The Weyl expansion shows that the mean DOS in, e.g., a billiard can be well described using only a few parameters like the volume and the most important characteristics of the boundaries [51]. In the case of the EBK quantization, the calculation of energy levels is reduced to classical action integrals with clear parametric dependencies that are usually hard to obtain from ab initio numerical calculations. The same holds true when the shortest periodic orbits in chaotic systems are concerned, revealing system-specific parametrizations of the level fluctuations on large energy scales, e.g., through bouncing-ball orbits in billiards [49]. The systematic analysis of the generic structure of the semiclassical approximations can also reveal universal features of certain classes of systems. By using the torus structure of the integrable classical dynamics, one can show that corresponding quantum systems should, in the generic case, have poissonian quantum fluctuations [41]. Moreover, it was shown that in uniformly hyperbolic, i.e., purely chaotic systems, the spectral form factor calculated semiclassically from correlated periodic orbits (Sieber-Richter pairs [57]) agrees with the predictions of random matrix theory, thus providing the closest-to-proof justification of the Bohigas-Giannoni-Schmit (BGS) conjecture so far [58, 59].

Outline of the thesis

This thesis is divided into two main chapters.

Chapter 1 presents an application of cluster expansions combined with the semiclassical short-time approximation. After a short introduction and historical overview in section 1.1, the general formalism of quantum cluster expansions is introduced in section 1.2, with its main focus on the canonical description. Apart from the known results, it also introduces new recurrence relations and a generalized notion of clustering for the calculation of correlation functions. After a generalization to systems with multiple species it concludes with the presentation of an exact resummation for the grand canonical description valid for homogeneous systems. The next section 1.3 then reviews the semiclassical short-time approximation of propagators and its implications for the general scaling properties of the cluster expansion. By presenting some general results on certain types of cluster integrals and a rederivation of the shifting method introduced in [60] with a focus on the thermodynamic limit scaling, this section provides some of the tools that are used in the two sections that follow. The latter focus on an application of the methods introduced so far: Section 1.4 presents novel results for the non-local pair correlation function in the a one-dimensional Bose gas with repulsive interactions and demonstrates the applicability of the scaling relations derived from the short-time approximation, as well as the potential of truncated quantum cluster expansions in high-temperature regimes. Section 1.5 moves on to three-dimensional applications of the cluster expansion. For this, some general results valid for spherically symmetric interaction potentials are derived and an exemplary model potential is discussed that can be used to model general short-range interactions in low-energy regimes. Such a short-range interaction is then implemented in a repulsive Bose gas with a few particles, presenting a novel analytic result on non-local correlations in virial expansion, and discussing different approximations for the integrated smooth part of the density of states for a few particles as obtained from the cluster expansion. Finally, the cluster expansion is applied to a system of four fermions with resonant interaction. The chapter concludes with a short summary and a few remarks on further applications in section 1.6.

While the methods of chapter 1 are useful for the description the thermal equilibrium properties of quantum gases, they cannot be applied at zero temperature and in non-equilibrium situations. Chapter 2 therefore presents complementary semiclassical methods that enable a detailed semiclassical discussion of a specific type of quantum phase transitions. The introductory section 2.1 gives a brief introduction to the theory of phase transitions. It also introduces some of the concepts and methods that are required in the subsequent sections, i.e., the quantum-classical correspondence and the phase-space formulation of quantum-mechanics, as well as the important semiclassical EBK quantization and a motivation of the so-called out-of-time-ordered correlators. The

next two sections then give a detailed analysis of two approximations of the attractive Bose gas in one dimension that exhibits a quantum phase transition. Section 2.2 introduces the model and then proceeds with a momentum truncated version using three single-particle momentum modes. After a short review of the semiclassical results obtained in an earlier work [61], it supplements the semiclassical treatment of the model with the introduction of highly accurate WKB wave-functions and demonstrates, how the exact dynamics can be visualized in phase space using Husimi functions. The section then proceeds with a detailed semiclassical and numerical study of an out-of-time-ordered correlator, uncovering a mechanism of scrambling and unscrambling close to criticality, including a discussion of the rigidity of the effect with respect to a perturbation with an external potential. The next section 2.3 relaxes the truncation used in the previous section by including two more modes. After a classical analysis of a high-symmetry manifold in the (effectively) six-dimensional phase space, uncovering the mixed character of the dynamics, the requirement of an approximate method for the quantum-mechanical diagonalization is discussed. The latter is then developed as a pre-diagonalization that is motivated from a separation of scales and adiabatic (Born-Oppenheimer) approximations. The numerical scheme is then extended to a characterization of the low-lying spectrum. Finally, the scrambling properties are shown to be very similar to the integrable three-mode approximation, also showing scrambling and unscrambling due to criticality. The results of the chapter are then summarized in section 2.4 and possible further extensions are sketched.

The thesis concludes with a very brief summary of the thesis and a comment about the possible value of the results for a broader audience.

1. Quantum cluster expansions in short-time approximation

1.1. Introduction

The description of the equilibrium properties of gases and fluids with non-negligible interactions has always been an outstanding problem in the field of thermodynamics. Although all gases can be well described by the ideal gas law at high temperatures and low densities, the interactions become crucial when the temperature is lowered. A phenomenological description using the van der Waals equation of state, that includes the effects of the interactions by introducing a reduced volume and pressure in the ideal gas law [62], has been found very early, but despite its physical appeal, it is not derived from first principles. A more fundamental approach is found in the methods of quantum statistical mechanics, also including the fundamental indistinguishability of identical particles, that is not captured by the van der Waals equation. For noninteracting particles, the commonly used grand canonical approach reduces to a single particle description using the thermal bosonic and fermionic distribution functions in terms of single-particle energies, rendering the statistics of these quantum gases fundamentally different from Boltzmann gases at low temperatures. The single-particle picture can be maintained in perturbative and mean-field approaches, but strongly correlated systems require an explicit many-particle description. As the full description is not possible in general, certain approximate methods have been introduced. Classical and quantum cluster expansions have emerged in this context as a natural way to hierarchically order the interaction effects according to the number of particles that interact in a non-separable way. Although it presents only a reformulation of the problem, one finds that at high temperatures (or low densities) the few-particle clusters become dominant. This is formalized in the virial expansion of the equation of states as [63]

$$\frac{p}{nk_BT} = 1 + B(T)n + C(T)n^2 + \dots, \tag{1.1}$$

where p is the pressure, $n = N/V$ is the particle density, k_B is the Boltzmann constant, and T is the temperature. The second virial coefficient B is completely defined by the two-body interaction, C contains the tree-body corrections, and so on. In the classical statistics, one can even show that it is only the irreducible part of the k-body problem, that enters the kth coefficients, with the irreducibility defined by a factorization criterion [63]. In the quantum description, the subtleties introduced by the nontrivial commutation relations and the indistinguishability of identical particles alter the notion of irreducibility, but the relation of the kth virial coefficient to the k-body problem

remains intact[1]. The virial expansion (1.1) is useful in the description of the thermodynamic limit of gases and liquids, but is invalid, e.g., in the statistical description of a system of three particles, even if the coefficient C, and thus the solution of the three-body problem, is included. Therefore, for intermediate, and fixed particle numbers, one should use the canonical (or micro-canonical) description. Fortunately, the starting point for cluster expansions is the canonical description, and the grand canonical formalism is then only introduced for simplification. This has led most authors to concentrate on the application of cluster expansions in the thermodynamic limit, where the ensembles become equivalent.

The classical cluster expansion was first introduced by Ursell in 1927 [65], while the quantum extension has been first studied nine years later by Uhlenbeck and Beth [66] with a focus on the calculation of the second virial coefficient, expressing the latter only in terms of scattering phases, today acknowledged as the Beth-Uhlenbeck formula [67]. Kahn and Uhlenbeck have then derived the general (implicit) form of the equation of state in the grand canonical description and discussed condensation phenomena on a formal level based on the analytic structure of the cluster expansion. As numerous authors have calculated virial coefficients for several two-body potentials in the following decades (see [63] and references therein), only selected theoretical developments based on cluster expansions are highlighted in the following. In the fifties, Lee and Yang have developed a binary collision expansion that represents all the larger clusters in terms of a series expansion of two-body operators [68,69]. It was later published in a series of five articles starting with [70]. A generalization of the grand canonical cluster expansion to multiple species, with a focus on charged particles was given in [71]. Other important theoretical works addressed the the third virial coefficient [72–74] and the low-temperature behavior of higher cluster integrals and virial coefficients [75, 76]. In the nineties, a group of authors has reinvented the cluster expansion in an operator formulation [77–79] with an emphasis on condensation phenomena [80] and first implementations of self-consistent calculations in the weakly-interacting regime [81, 82].

The above summary shows that previous research concentrated primarily on the thermodynamic-limit properties of classical and quantum gases and their phase transitions. Moreover, the research concentrated on the full cluster integrals an the reduced one-body density matrix, while few-body expectation values have not been considered (except for the formal considerations on the two-body correlation found in [78]). However, with ultra-cold atom experiments being possible today not only with macroscopic particle numbers, but even down to two or a few particles, the thermodynamic-limit equivalence of ensembles certainly breaks down, and one should naturally consider the canonical formalism in few-particle cases with well-controlled particle-numbers. Therefore, the focus here is on the canonical description of few-body systems and the smooth density of states that can be extracted from it. On the other hand, general results of the cluster expansion for arbitrary correlations will be derived that are exemplarily used for the explicit calculation of nonlocal pair correlations in selected systems.

[1] However, the virial coefficients do not vanish for noninteracting particles due to their indistinguishability [64].

1.2. The quantum cluster expansion

In this section the formalism of quantum cluster expansions (QCE) is reviewed and general new results will be derived, that hold irrespectively of the details of the physical systems. After introducing the Ursell expansion and the indistinguishability of particles as the two important mechanisms for clustering, the combinatorial nature of the resulting expansions will be discussed, with a focus on the derivation of recurrence relations and the notion of irreducible clusters. Then, after generalizing the formalism to multiple species of indistinguishable particles, the special case of homogeneous systems is discussed, where further modifications can simplify the formalism.

Let us consider a (non-relativistic) autonomous system with fixed particle number N. The dynamics of the system is then fully described by the propagator

$$G^{(N)}(\boldsymbol{y},\boldsymbol{x};t) = \langle \boldsymbol{y}|\mathrm{e}^{-\frac{it}{\hbar}\hat{H}}|\boldsymbol{x}\rangle\,, \tag{1.2}$$

where $\hat{H}$ is the N-particle Hamiltonian of the system, t is the time, and $|\boldsymbol{x}\rangle = |\boldsymbol{x}_1\rangle\otimes\cdots\otimes|\boldsymbol{x}_N\rangle = |\boldsymbol{x}_1,\ldots,\boldsymbol{x}_N\rangle$ is a product of N position eigenstates. Specifically, any many-body quantum state $\Psi(\boldsymbol{x},0) = \langle\boldsymbol{x}|\Psi(0)\rangle$ prepared at time $t = 0$ will evolve such that it is given by

$$\Psi(\boldsymbol{y},t) = \int d^{ND}x\, G^{(N)}(\boldsymbol{y},\boldsymbol{x};t)\Psi(\boldsymbol{x},0) \tag{1.3}$$

at time t (D is the space dimension). On the other hand, evaluating the propagator in imaginary time

$$t = -i\hbar\beta \tag{1.4}$$

completely determines the equilibrium thermodynamic properties of the system, with $\beta = (k_B T)^{-1}$ as the inverse temperature. For example, the canonical partition function $Z^{(N)}$ is obtained from the integral

$$Z^{(N)}(\beta) = \int d^{ND}x\, G^{(N)}(\boldsymbol{x},\boldsymbol{x};-i\hbar\beta) = \int d^{ND}x\ \langle\boldsymbol{x}|\mathrm{e}^{-\beta\hat{H}}|\boldsymbol{x}\rangle = \mathrm{Tr}^{(N)}\{\mathrm{e}^{-\beta\hat{H}}\}. \tag{1.5}$$

Integrals of the above form will be referred to as (partial) traces. To ease later notation, let us define

$$K^{(N)}(\boldsymbol{y},\boldsymbol{x};\beta) = G^{(N)}(\boldsymbol{y},\boldsymbol{x};-i\hbar\beta) \tag{1.6}$$

as the *imaginary time* propagator. By definition, it inherits the properties of the propagator and thus satisfies the equations

$$\frac{\partial}{\partial\beta}K^{(N)}(\boldsymbol{y},\boldsymbol{x};\beta) = -\hat{H}_{\boldsymbol{y}}K^{(N)}(\boldsymbol{y},\boldsymbol{x};\beta), \tag{1.7}$$

$$\lim_{\beta\to 0} K^{(N)}(\boldsymbol{y},\boldsymbol{x};\beta) = \delta^{(ND)}(\boldsymbol{y}-\boldsymbol{x}), \tag{1.8}$$

where $\delta^{(ND)}$ is the ND-dimensional Dirac delta function and $\hat{H}_{\boldsymbol{y}}$ is the Hamiltonian in position representation, i.e.,

$$\langle\boldsymbol{y}|\,\hat{H}\,|\Psi\rangle = \hat{H}_{\boldsymbol{y}}\,\langle\boldsymbol{y}|\Psi\rangle \tag{1.9}$$

for any state $|\Psi\rangle$ in the Hilbert space.

The interpretation of *propagation* in imaginary time establishes a link between thermal and dynamical approaches, where understanding of the latter can then provide better intuition for thermodynamic properties and vice versa. For example, the imaginary time propagator has the same convolution property

$$\int d^{ND}z\, K^{(N)}(\boldsymbol{y},\boldsymbol{z};\beta_1)K^{(N)}(\boldsymbol{z},\boldsymbol{x};\beta_2) = K^{(N)}(\boldsymbol{y},\boldsymbol{x};\beta_1+\beta_2) \tag{1.10}$$

as the propagator, which, for the latter, is just the semigroup property of the time evolution incorporating the intuition that the state obtained by stepwise time evolution should be the same as the one obtained, when the time evolution is performed in a single step. One could, in principle, interpret the imaginary time propagation as a generalized heat kernel that solves the "heat equation" (1.7), where the Laplace operator is substituted by the many-body Hamiltonian (and a minus sign). However, to make the analogy complete one should then reinterpret β as a real time and the quantum states as classical distributions, which does not make much sense after all, even in the case of a single, free particle. So, keeping the interpretation of the inverse temperature as *imaginary* time, the word "propagation" will be used in the following, keeping in mind that the quantum statistical considerations do not depend on time.

1.2.1. Ursell operators and symmetrization

The use of the many-body propagator does not, by itself, simplify the description. Moreover, it contains far more information than is needed to calculate thermodynamic quantities, as it contains the full information about the quantum states. So, calculating the many-body propagator is equivalent to solving the Schrödinger equation of the many-body system, which is usually not possible. One can, however, bring the propagator in a form that systematically clusters particles into subsets, such that the smaller clusters can be treated individually.

Ursell operators

The imaginary-time evolution operator is decomposed into Ursell operators [77] in the following manner. Let $\hat{H}^{(n)}(i_1,\ldots,i_n)$ be the Hamiltonian of $n \leq N$ particles labeled by $i_1,\ldots,i_n \in \{1,\ldots,N\}$ and $\hat{K}^{(n)}(i_1,\ldots,i_n) = \mathrm{e}^{-\beta\hat{H}^{(n)}(i_1,\ldots,i_n)}$. Here, $\hat{H}^{(n)}(i_1,\ldots,i_n)$ has to be thought of as an operator on the N-particle Hilbert space that has a nontrivial action only on the n-particle subspace labeled by the i_k, where it is identical to the n-particle Hamiltonian, while it reduces to the identity on the $(N-n)$-particle complement space. The first three Ursell operators $\hat{U}^{(n)}$ are then implicitly defined as

$$\begin{aligned}
\hat{K}^{(1)}(1) &= \hat{U}^{(1)}(1),\\
\hat{K}^{(2)}(1,2) &= \hat{U}^{(1)}(1)\hat{U}^{(1)}(2) + \hat{U}^{(2)}(1,2),\\
\hat{K}^{(3)}(1,2,3) &= \hat{U}^{(1)}(1)\hat{U}^{(1)}(2)\hat{U}^{(1)}(3)\\
&\quad + \hat{U}^{(1)}(1)\hat{U}^{(2)}(2,3) + \hat{U}^{(1)}(2)\hat{U}^{(2)}(1,3)\\
&\quad + \hat{U}^{(1)}(3)\hat{U}^{(2)}(1,2) + \hat{U}^{(3)}(1,2,3).
\end{aligned} \tag{1.11}$$

All higher Ursell operators are defined in the same way by decomposing $\hat{K}^{(n)}$ into all possible partitions of particles. The intuitive picture behind this decomposition is that the kth Ursell operator contains only the *additional* information of the k-particle problem that is not contained in the lower Ursell operators. For example, the second Ursell operator contains only the information that exceeds the noninteracting two-particle problem. Consequently, all Ursell operators $\hat{U}^{(k)}$ for $k \geq 2$ vanish in the noninteracting case.

The Ursell decomposition above is only a reformulation of the problem and could, in principle, yield additional complications. However, the Hamiltonian of an N-particle system can always be written in the form

$$\hat{H}^{(N)} = \sum_{i=1}^{N} \hat{H}^{(1)}(i) + \sum_{i \neq j=1}^{N} \hat{V}^{(2)}(i,j) + \sum_{i \neq j \neq k=1}^{N} \hat{V}^{(3)}(i,j,k) + \dots \tag{1.12}$$

with k-body interactions $\hat{V}^{(k)}(i_1, \dots, i_k)$ $(k \leq N)$, where the one-body operators and two-body interactions usually dominate the physics. In this case, the higher Ursell operators should become subdominant in certain regimes, such that the cluster expansion can be truncated.

In many applications, the interactions can be assumed to be short-ranged. In this case, it is expected that particles that are separated far from each other will be essentially independent. This means that the matrix elements

$$\Delta K^{(n)}(\boldsymbol{y}, \boldsymbol{x}; \beta) \equiv \langle \boldsymbol{y} | \hat{U}^{(n)} | \boldsymbol{x} \rangle \tag{1.13}$$

in coordinate space vanish if the distance of any two particles in $\boldsymbol{x}$ and $\boldsymbol{y}$ is large, making the "clustering" of particles very explicit. Note that in Eq. (1.13) $|\boldsymbol{x}\rangle$ and $|\boldsymbol{y}\rangle$ have to be understood as elements of a n-particle (sub-) Hilbert space. The propagator $K^{(N)}(\boldsymbol{y}, \boldsymbol{x}; \beta)$ can then be written in terms of the matrix elements $\Delta K^{(n)}(\boldsymbol{y}, \boldsymbol{x}; \beta)$ with $n \leq N$. Let us further refer to these matrix elements as interaction contributions of order n and identify $K^{(1)}(\boldsymbol{y}, \boldsymbol{x}; \beta) = \Delta K^{(1)}(\boldsymbol{y}, \boldsymbol{x}; \beta)$ for $n = 1$. We can now write the propagator for N distinguishable particles as a sum of interaction contributions

$$K^{(N)}(\boldsymbol{y}, \boldsymbol{x}; \beta) = \sum_{\mathcal{J} \vdash \{1,\dots,N\}} \prod_{I \in \mathcal{J}} \Delta K^{(|I|)}(\boldsymbol{y}_I, \boldsymbol{x}_I; \beta), \tag{1.14}$$

where the sum in this cluster expansion runs over all possible partitions $\mathcal{J}$ of the set of N particle indices and $\boldsymbol{x}_I = (\boldsymbol{x}_{i_1}, \dots, \boldsymbol{x}_{i_{|I|}})$ is the shorthand notation for the (ordered) particle coordinates that are part of the same interaction contribution, represented by the disjoint subsets $I \in \mathcal{J}$. As noted above, this decomposition is particularly useful when higher-order interaction contributions are subdominant, i.e., the dominant parts of the propagator factorize into clusters of smaller particle numbers. It is worth noting, that neglecting, e.g., interaction contributions of order $n \geq 3$ is conceptually different from a perturbation expansion, as two-body interactions are fully accounted for by the interaction contributions of order $n = 2$, which are nonperturbative in the interaction strength. For example, while respecting the finiteness of the system, such a truncation includes the virial expansion to second order in the thermodynamic limit.

Indistinguishability

For indistinguishable particles we have to use the symmetry projected (imaginary-time) propagator,

$$K_{\pm}^{(N)}(\boldsymbol{y},\boldsymbol{x};\beta) = \frac{1}{N!}\sum_{P\in S_N}(\pm 1)^P K^{(N)}(P\boldsymbol{y},\boldsymbol{x};\beta), \tag{1.15}$$

where the sum runs over the symmetric group S_N operating on the particle indices, $+$ and $-$ stand for bosons and fermions, respectively, and $(-1)^P$ is the sign of the permutation P.

This yields an additional factorization mechanism corresponding to the decomposition of permutations into cycles [52], which is best demonstrated in the noninteracting case where

$$K_0^{(N)}(\boldsymbol{y},\boldsymbol{x};\beta) = \prod_{i=1}^{N} K^{(1)}(\boldsymbol{y}_i,\boldsymbol{x}_i;\beta). \tag{1.16}$$

Consider a permutation $P = \sigma_1\circ\sigma_2\circ\cdots\circ\sigma_p$ in its cycle decomposition, i.e., the cycles σ_k act on disjoint index sets I_k such that $\cup_{k=1}^{p} I_k = \{1,\ldots,N\}$. The corresponding contribution to the symmetry projected propagator (1.15) is

$$K_0^{(N)}(P\boldsymbol{y},\boldsymbol{x};\beta) = \prod_{k=1}^{p} K_0^{(|I_k|)}(\boldsymbol{y}_{\sigma_k(I_k)},\boldsymbol{x}_{I_k};\beta). \tag{1.17}$$

The sum over all permutations can be rewritten as the sum of all partitions of the index set yielding

$$K_{0,\pm}^{(N)}(\boldsymbol{y},\boldsymbol{x};\beta) = \frac{1}{N!}\sum_{\mathcal{J}\vdash\{1,\ldots,N\}}\prod_{I\in\mathcal{J}}(\pm 1)^{|I|-1}\sum_{\sigma(I)=I} K_0^{(|I|)}(\boldsymbol{y}_{\sigma(I)},\boldsymbol{x}_I;\beta), \tag{1.18}$$

where the last sum runs over the $(|I|-1)!$ cyclic permutations of the set I and $\boldsymbol{x}_I = (\boldsymbol{x}_{i_1},\ldots,\boldsymbol{x}_{i_{|I|}})$ is, as in Eq. (1.14), short-hand notation for the (ordered) particle coordinates with index in I and $\boldsymbol{y}_{\sigma(I)} = (\boldsymbol{y}_{\sigma(i_1)},\ldots,\boldsymbol{y}_{\sigma(i_{|I|})})$. The apparent similarity of Eqs. (1.18) and (1.14) as a sum of all partitions shows that both, Ursell expansion and symmetrization, can be treated as a cluster expansion in a similar fashion.

Combining the two mechanisms to cluster particles yields a grouping of particles into clusters that are either part of the same interaction contribution or connected by permutation cycles (or both). This becomes important when calculating traces of the propagator, as each cluster of particles can then be treated independently from the rest of the particles while its internal dynamics is tied in a non-separable way.

Example

As an illustrative example, consider a partition of $N \geq 3$ particles into one interaction contribution of order 2 [e.g., particles one and two connected by $\hat{U}^{(2)}(1,2)$] and $N-2$ interaction contributions of order one, together with the permutation $P = (1\ 3)$. This

is one of many combinations that appear if we symmetrize Eq. (1.14) according to Eq. (1.15). It factorizes into $N-3$ single-particle propagators and the term

$$\Delta K^{(2)}\big((\boldsymbol{y}_3,\boldsymbol{y}_2),(\boldsymbol{x}_1,\boldsymbol{x}_2);\beta\big)K^{(1)}(\boldsymbol{y}_1,\boldsymbol{x}_3;\beta), \tag{1.19}$$

such that the full contribution to the cluster expansion will be

$$\frac{1}{N!}\Delta K^{(2)}\big((\boldsymbol{y}_3,\boldsymbol{y}_2),(\boldsymbol{x}_1,\boldsymbol{x}_2);\beta\big)K^{(1)}(\boldsymbol{y}_1,\boldsymbol{x}_3;\beta)\prod_{i=4}^{N}K^{(1)}(\boldsymbol{y}_i,\boldsymbol{x}_i,\beta). \tag{1.20}$$

So, in this example, we have a total of $N-2$ clusters—one cluster comprising three particles given by Eq. (1.19) and $N-3$ (trivial) single-particle clusters. Even though the factors in Eq. (1.19) are, as is, independent functions, they cannot be treated independently if we trace, e.g., the particle with index $i=3$, such that the relevant criterion of factorization into independent clusters is the particle index rather than the coordinates themselves.

1.2.2. The role of (irreducible) diagrams

As has been argued in the example above, the *index* itself rather than the coordinates define the clusters, as should be clear from the fact that the cluster expansion does not rely on a specific basis representation and can also be formulated at the level of operators [77–79]. If one is interested in thermodynamic quantities or reduced density matrices one must calculate the (partial) trace the propagator, where the indices of the particles that are traced out can be interchanged, such that different assignments of particle indices can lead to the same contribution to the cluster expansion. Already for moderate particle numbers this leads to a plethora of identical contributions in Eq. (1.14) due to particle relabeling. This suggests a diagrammatic treatment of the (symmetry-projected) cluster expansion (1.14), which will be presented in the following, with an emphasize on the aspects of irreducibility.

Diagrams

Each interaction contribution of order n is represented as a diagram connecting n initial and n final coordinates. The diagrams representing the interaction contributions of the first three orders are displayed in Fig. 1.1(a). They contain a solid line for every particle with an arrow pointing from initial to final coordinates represented by labeled dots. An interaction contribution of order n thus contains n solid lines, together with $n(n-1)/2$ curly lines connecting every pair of the n particles. The number of curly lines connected to a particle thus directly indicates the order of the interaction contribution it is part of, i.e., if a solid line has m curly lines connected to it, the corresponding particle is part of an interaction contribution of the order $m+1$, and all the other particles in this interaction contribution have to be met by m curly lines, too. The name "vertex" is avoided here to clarify that, in contrast to perturbative diagrammatic approaches, there is no meaning of these points other than the assignment of a particle

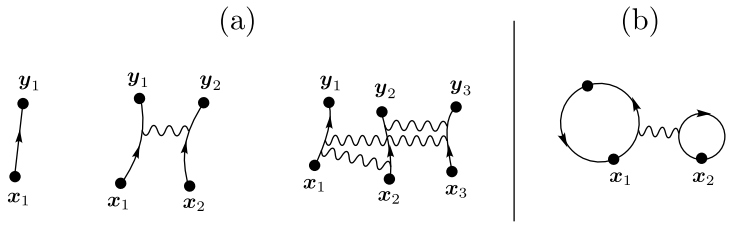

Figure 1.1: (a) Diagrams representing $\Delta K^{(n)}(\boldsymbol{y},\boldsymbol{x};\beta)$, Eq. (1.13), for $n = 1,2,3$. (b) Diagram representing the particular cluster Eq. (1.19) for $\boldsymbol{x} = \boldsymbol{y}$.

to a certain interaction contribution. Instead of using curly lines, one could give a label to each particle line indicating its affiliation to an interaction contribution. However, by graphically connecting the respective particles, one can directly determine whether a given diagram factorizes, i.e., it can be split into two diagrams without cutting any lines, or whether it is irreducible, i.e., it cannot be split up further. A full diagram represents a factorization into clusters according to Eq. (1.14) or its symmetry-projected equivalent and comprises several irreducible diagrams that represent single clusters.

The cycle structure is then either encoded in the indices of the final coordinates as compared to the initial ones or, in the case of particles that have been traced out, by the connection of the particle lines. By convention, each unlabeled bullet in a diagram stands for a coordinate that has been traced out. Such points have to connect two particle lines or, in the case of a one-cycle, a particle line with itself. Loose ends correspond to untraced particles with different initial and final coordinates, such that they always have to come in pairs. As an example, the irreducible diagram corresponding to Eq. (1.19) for $\boldsymbol{y} = \boldsymbol{x}$ and with $\boldsymbol{x}_3$ traced out is depicted in Fig. 1.1(b). In practice it is convenient to omit one-particle irreducible diagrams while stating the particle number of the (reduced) diagrams explicitly. As a diagram contains the full information on the cycle structure one is free to include the sign factors from exchange symmetry in the diagram values. Here, however, the convention is used that the value of a diagram is defined irrespective of the exchange symmetry and treat the sign factors as additional prefactors.

Let us now focus on diagrams that appear in the full trace of the cluster expansion, i.e., the canonical partition function, with the purpose of counting only distinct diagrams, then provided with multiplicities and a sign factor that encodes the particle symmetry. Consider a full diagram in the expansion that is built out of l irreducible diagrams of sizes $n_1 \geq \cdots \geq n_l$. By distributing the particle indices among the irreducible diagrams in a different way one finds equivalent full diagrams. Therefore, the multiplicity of any such diagram contains the combinatorial factor

$$\#_{\mathfrak{N}}^{N} = \frac{1}{\prod_{\nu=1}^{\infty} m_{\mathfrak{N}}(\nu)!} \frac{N!}{\prod_{i=1}^{l} n_i!} = \frac{N!}{\prod_{\nu=1}^{\infty} m_{\mathfrak{N}}(\nu)!(\nu!)^{m_{\mathfrak{N}}(\nu)}}, \tag{1.21}$$

where $m_{\mathfrak{N}}(\nu)$ is the multiplicity of the number ν in $\mathfrak{N} = \{n_1,\ldots,n_l\}$. It is the number of possible partitions of the *set* of the N particle indices into subsets of the sizes $n_1,\ldots,n_l$.

This holds irrespective of the structure of the irreducible diagrams, whereas an additional factor counts the number of ways to relabel the coordinates inside an irreducible diagram depending on its structure. The index l for the length of $\mathfrak{N}$ was only introduced to shorten notation and does not appear the second form of the combinatorial factor (1.21). If we collect all full diagrams in the cluster expansion that factorize into irreducible diagrams of the sizes $n_1, \ldots, n_l$ their sum can be written as

$$\left(\#^N_{\mathfrak{N}}\right) \prod_{i=1}^{l} S^{(0)}_{n_i,\pm}(\beta), \tag{1.22}$$

where $S^{(0)}_{n,\pm}(\beta)$ is the sum of all n-particle irreducible diagrams, including the multiplicities from internal relabeling as well as the sign factors from symmetrization. The upper index (k) with $k \in \mathbb{N}_0$ denotes the number of particles that are not traced over and will be different from zero when thermal expectation values of operators, e.g., particle densities or n-point correlation functions are concerned. Using the above definitions the partition function can be written in terms of the sums of irreducible clusters as

$$Z^{(N)}_{\pm}(\beta) = \frac{1}{N!} \sum_{\mathfrak{N} \vdash N} \#^N_{\mathfrak{N}} \prod_{n \in \mathfrak{N}} S^{(0)}_{n,\pm}(\beta). \tag{1.23}$$

Note that, in contrast to Eqs. (1.14) and (1.18), the sum runs over the partitions of the *number* N instead of the partitions of the *index set* $\{1, \ldots, N\}$. To be precise, the explicit form of Eq. (1.23) is given by

$$\begin{aligned} Z^{(N)}_{\pm}(\beta) &= \frac{1}{N!} \sum_{l=1}^{N} \sum_{\substack{n_1 \geq \cdots \geq n_l \geq 1 \\ \sum_{i=1}^{l} n_i = N}} \#^N_{\{n_1,\ldots,n_l\}} \prod_{i=1}^{l} S^{(0)}_{n_i,\pm}(\beta). \\ &= \sum_{l=1}^{N} \frac{1}{l!} \sum_{\substack{n_1,\ldots,n_l = 1 \\ \sum_{i=1}^{l} n_i = N}}^{N} \prod_{i=1}^{l} \frac{S^{(0)}_{n_i,\pm}}{n_i!} \end{aligned} \tag{1.24}$$

In this form, the cluster expansion of the canonical partition function is organized in a way that the first sum runs over the number l of irreducible clusters.

The central role of the irreducible diagrams $S^{(0)}_{n,\pm}$ as building blocks of the theory is better demonstrated when looking at the grand canonical partition function. As will be shown in section 1.2.3, it is given exactly as the exponentiated sum of irreducible diagrams, only weighted with a combinatorial factor and the fugacity z:

$$Z_G(\beta, \mu) = \exp\left(\sum_{k=0}^{\infty} \frac{z^k}{k!} S^{(0)}_k(\beta) \right), \qquad z = \mathrm{e}^{\mu\beta}. \tag{1.25}$$

Here, the index for the symmetry class $\pm$ has been omitted to highlight the simple form of the result.

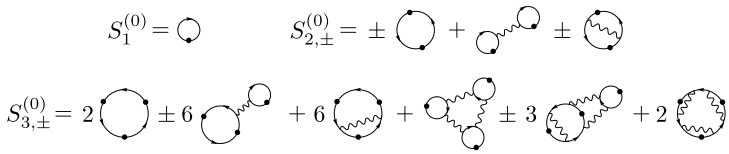

Figure 1.2: The sum of irreducible k-particle diagrams $S_k^{(0)}$ for $k = 1, 2, 3$. Most of the diagrams for $k = 3$ appear with multiplicities larger than 1. The first three diagrams in $S_{3,\pm}^{(0)}$ include only the interaction contributions up to order 2, while the rest accounts for all six possible permutations of the third-order interaction contribution. For noninteracting indistinguishable particles, only the first diagrams contribute, while for distinguishable particles only the second diagram in $S_{2,\pm}^{(0)}$ and the fourth diagram in $S_{3,\pm}^{(0)}$ contribute.

Before moving on to the implications of the combinatorial nature of the cluster expansion, let us consider, as an example, the cluster expansion for three indistinguishable particles. There are three different partitions of the particles with combinatorial factors

$$\#^3_{\{1,1,1\}} = 1, \qquad \#^3_{\{2,1\}} = 3, \qquad \#^3_{\{3\}} = 1 \tag{1.26}$$

so that the partition function is given by

$$Z_\pm^{(3)} = \frac{1}{3!}\left[\left(S_{1,\pm}^{(0)}\right)^3 + 3S_{2,\pm}^{(0)}S_{1,\pm}^{(0)} + S_{3,\pm}^{(0)}\right], \tag{1.27}$$

where the dependence on β has been omitted. The sums of the k-particle irreducible diagrams $S_{k,\pm}^{(0)}$ for $k = 1, 2, 3$ are shown in Fig. 1.2, also including the multiplicities of the individual diagrams due to internal relabeling.

We are now left with the calculation of the multiplicities due to internal relabeling and the sign factors from exchange symmetry. Let us exemplarily focus on the multiplicity of the second diagram in $S_{3,\pm}^{(0)}$. It is built from one interaction contribution of order two and one free propagation (order one). Choosing the interacting pair out of three particles already gives three possibilities corresponding to the Ursell decomposition, cf., Eq. (1.11). Then, one of the interacting particles has to be linked to the free particle by a two-cycle. This can be achieved with two distinct exchange permutations, yielding the overall multiplicity of 6. In addition, the factor ± 1 has to be introduced to account for the two-cycle. A detailed formal description of how the coefficients are determined in general can be found in [61].

1.2.3. Partial traces, recurrence relations, and expectation values

The previous subsection has introduced the basic notation and the the very general combinatorial nature of the cluster expansion for the example of the canonical partition function, i.e., the full trace of the (imaginary time) propagator. When dealing with

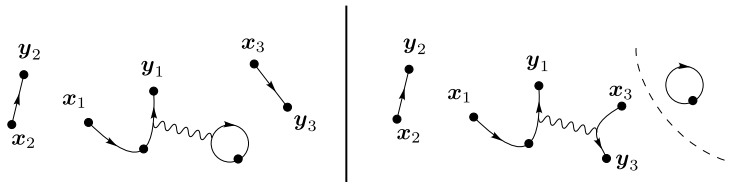

Figure 1.3: Diagrams for five particles where two particles have been traced out. Both diagrams are built from three irreducible diagrams. However, the left diagram is *coordinate* irreducible while the right one can be cut at the dashed line such that all the coordinates are in the left part of the diagram. Thus, the right diagram is coordinate *reducible*.

partial traces, the number of equivalent diagrams in the cluster sum is reduced, as only the particles that are traced out can be relabeled. This means that the combinatorial factors in Eq. (1.21) as well as the multiplicities of the irreducible diagrams with fixed coordinates have to be modified, but one can, in principle, easily write down the corresponding expressions. It is, however, much more convenient to use the combinatorial structure of the partition function to simplify the partial traces. This will be done on a purely combinatorial level, leading to the notion of *coordinate* irreducible diagrams that are the building blocks for correlation functions and expectation values. Moreover, the relations obtained for the partial traces naturally lead to recurrence relations for the partition function. At the end of the subsection, the results for the grand canonical ensemble will be derived.

Partial traces

Let us define the partial trace of the symmetry-projected N-particle propagator with $N-k$ particles traced out as

$$\rho_{\pm}^{(N,k)}(\boldsymbol{y},\boldsymbol{x};\beta) = \int d^{(N-k)D}z\, K_{\pm}^{(N)}((\boldsymbol{y},\boldsymbol{z}),(\boldsymbol{x},\boldsymbol{z});\beta), \tag{1.28}$$

where $(\boldsymbol{x},\boldsymbol{z}) = (\boldsymbol{x}_1,\ldots,\boldsymbol{x}_k,\boldsymbol{z}_{k+1},\ldots,\boldsymbol{z}_N)$ and $(\boldsymbol{y},\boldsymbol{z})$ defined analogously. The full cluster expansion that combines the Ursell decomposition (1.14) and the cycle decomposition (1.18) is the sum of all allowed (reducible) diagrams with $2k$ legs representing the coordinates $\boldsymbol{x}$ and $\boldsymbol{y}$. Every such diagram stands for a product of irreducible clusters, represented by an irreducible diagram, that either depend on some of the pairs $(\boldsymbol{x}_i,\boldsymbol{y}_i)$ or are fully traced over. Therefore, in each diagram, we can split off the part that depends on the coordinates $\boldsymbol{x}$ and $\boldsymbol{y}$ or, in other words, factorize the corresponding contribution to the cluster expansion into a part that depends on $\boldsymbol{x}$ and $\boldsymbol{y}$ and a product of fully traced irreducible clusters. In this context it is useful to introduce the notion of *coordinate irreducible* diagrams as the part of a diagram, that remains after splitting off all fully traced irreducible clusters. As an example, Fig. 1.3 shows a comparison of a

coordinate reducible and a coordinate irreducible diagram for five particles, where two particles have been traced out.

One can now proceed in the same way as in the previous subsection and define $A^{(k)}_{n,\pm}(\boldsymbol{x},\boldsymbol{y};\beta)$ as the sum of all coordinate irreducible diagrams composed of n particles. In every diagram that contributes to $A^{(k)}_{n,\pm}(\boldsymbol{y},\boldsymbol{x};\beta)$, $n-k$ particle coordinates are traced out. The respective particle indices are drawn from the $N-k$ coordinates that are traced over, such that there are

$$\binom{N-k}{n-k} = \frac{(N-k)!}{(n-k)!(N-n)!} \tag{1.29}$$

equivalent diagrams in the overall sum. The remaining $N-n$ particles will then be distributed in all possible fully traced irreducible diagrams with their sum given by $(N-n)!Z^{(N-n)}_{\pm}$, as seen in the last subsection. Thus, only by rearranging the cluster expansion, we can write the partial trace (1.28) as

$$\begin{aligned}
\rho^{(N,k)}_{\pm}(\boldsymbol{y},\boldsymbol{x};\beta) &= \frac{1}{N!}\sum_{n=k}^{N}\binom{N-k}{n-k} A^{(k)}_{n,\pm}(\boldsymbol{y},\boldsymbol{x};\beta)\cdot(N-n)!Z^{(N-n)}_{\pm}(\beta) \\
&= \frac{(N-k)!}{N!}\sum_{n=k}^{N}\frac{A^{(k)}_{n,\pm}(\boldsymbol{y},\boldsymbol{x};\beta)}{(n-k!)}Z^{(N-n)}_{\pm}(\beta) \\
&= \frac{(N-k)!}{N!}\sum_{n=k}^{N} a^{(k)}_{n,\pm}(\boldsymbol{y},\boldsymbol{x};\beta)Z^{(N-n)}_{\pm}(\beta),
\end{aligned} \tag{1.30}$$

where $Z^{(0)}_{\pm}(\beta)=1$ by convention. In Eq. (1.30) the rescaled sum of coordinate irreducible diagrams

$$a^{(k)}_{n,\pm}(\boldsymbol{y},\boldsymbol{x};\beta) = \frac{A^{(k)}_{n,\pm}(\boldsymbol{y},\boldsymbol{x};\beta)}{(n-k)!} \tag{1.31}$$

has been introduced. It is convenient to define also the rescaled sum of irreducible clusters as

$$s^{(k)}_{n,\pm}(\beta) = \frac{S^{(k)}_{n,\pm}(\beta)}{(n-k-\delta_{k0})!} \tag{1.32}$$

where δ_{kl} is the Kronecker delta and the factorial is chosen such that it cancels the internal multiplicity of the cyclic diagrams in the noninteracting case.

As the dependence on the inverse temperature β is clear from the definitions, it will be dropped in the following for better readability. Moreover, the label $\pm$ for the exchange symmetry will be omitted.

For the cases $k=1$ and $k=2$ that will be of relevance later one obtains

$$a^{(1)}_{n}(\boldsymbol{y},\boldsymbol{x}) = s^{(1)}_{n}(\boldsymbol{y},\boldsymbol{x}), \tag{1.33}$$

$$a^{(2)}_{n}(\boldsymbol{y},\boldsymbol{x}) = s^{(2)}_{n}(\boldsymbol{y},\boldsymbol{x}) + \sum_{l=1}^{n-1} s^{(1)}_{l}(\boldsymbol{y}_1,\boldsymbol{x}_1)s^{(1)}_{n-l}(\boldsymbol{y}_2,\boldsymbol{x}_2). \tag{1.34}$$

With this notation the partial trace of the propagator for $k = 1$ and $k = 2$ is conveniently written as

$$\rho^{(N,1)}(\boldsymbol{y}, \boldsymbol{x}) = \frac{1}{N} \sum_{n=1}^{N} s_n^{(1)}(\boldsymbol{y}, \boldsymbol{x}) Z^{(N-n)}, \tag{1.35}$$

$$\rho^{(N,2)}(\boldsymbol{y}, \boldsymbol{x}) = \frac{1}{N(N-1)} \left(\sum_{n=2}^{N} s_n^{(2)}(\boldsymbol{y}, \boldsymbol{x}) Z^{(N-n)} + \sum_{k=1}^{N-1} \sum_{l=1}^{N-k} s_k^{(1)}(\boldsymbol{y}_1, \boldsymbol{x}_1) s_l^{(1)}(\boldsymbol{y}_2, \boldsymbol{x}_2) Z^{(N-k-l)} \right). \tag{1.36}$$

Equations of this kind are of central relevance for the calculation of expectation values. However, they can also be used to derive recurrence relations as will be shown below.

Recurrence formulas

By tracing out the remaining particle in Eq. (1.35) one immediately finds the very useful recurrence relation for the canonical partition function

$$Z^{(N)} = \frac{1}{N} \sum_{n=1}^{N} s_n^{(0)} Z^{(N-n)} \tag{1.37}$$

that has been long known for the noninteracting case [83]. It has also been used recently as a very useful tool in quantum Monte Carlo approaches [17] where the recursive approach drastically reduces the computational effort. Tracing Eq. (1.36) one finds a different recurrence relation

$$Z^{(N)} = \frac{1}{N(N-1)} \left(\sum_{n=2}^{N} (n-1) s_n^{(0)} Z^{(N-n)} + \sum_{k=1}^{N-1} \sum_{l=1}^{N-k} s_k^{(0)} s_l^{(0)} Z^{(N-k-l)} \right). \tag{1.38}$$

More general, Eq. (1.30) yields a recursion formula for every $k \geq 1$, but the resulting expressions become, of course, more complicated with increasing k and their usefulness for practical purposes might become questionable. Nevertheless, if one wants to find new recursion formulas, one should keep in mind that the functions $s_n^{(k)}$ are related to each other by

$$\int d^D x_{k+1}\, s_n^{(k+1)}((\bar{\boldsymbol{y}}, \boldsymbol{x}_{k+1}), (\bar{\boldsymbol{x}}, \boldsymbol{x}_{k+1})) = (n-k) s_n^{(k)}(\bar{\boldsymbol{y}}, \bar{\boldsymbol{x}}) \tag{1.39}$$

for $k > 0$. Here, $\bar{\boldsymbol{x}}$ denotes the k remaining coordinates $\boldsymbol{x}_1, \ldots, \boldsymbol{x}_k$. For $k = 0$ one simply has

$$\int d^D x\, s_n^{(1)}(\boldsymbol{x}, \boldsymbol{x}) = s_n^{(0)}. \tag{1.40}$$

Expectation values

The relations for the partial traces are of use when one is interested in the thermal expectation value

$$\langle\hat{\mathcal{O}}\rangle_\beta = \frac{1}{Z_\pm^{(N)}}\,\mathrm{Tr}_\pm^{(N)}\left[\mathrm{e}^{-\beta\hat{H}}\hat{\mathcal{O}}\right] \tag{1.41}$$

of an observable $\hat{\mathcal{O}}$, where the trace is taken in the Hilbert space sector with bosonic (+) or fermionic symmetry (−). Let us start with the simple case of a one-particle observable

$$\hat{\mathcal{O}}_1 = \sum_{i=1}^{N}\hat{\mathcal{O}}_1^{(i)} = \int d^Dx\, d^Dy\, \mathcal{O}_1(\boldsymbol{x},\boldsymbol{y})\hat{\psi}^\dagger(\boldsymbol{x})\hat{\psi}(\boldsymbol{y}), \tag{1.42}$$

where $\mathcal{O}_1(\boldsymbol{x},\boldsymbol{y}) = \langle\boldsymbol{x}|\hat{\mathcal{O}}_1|\boldsymbol{y}\rangle$ and $\hat{\psi}^\dagger$ and $\hat{\psi}$ are the bosonic or fermionic field operators. The thermal expectation value of $\hat{A}$ is then given by

$$\langle\hat{\mathcal{O}}_1\rangle_\beta = \int d^Dx\, d^Dy\, \mathcal{O}_1(\boldsymbol{x},\boldsymbol{y})\langle\hat{\psi}^\dagger(\boldsymbol{x})\hat{\psi}(\boldsymbol{y})\rangle_\beta \tag{1.43}$$

in terms of the single-particle reduced density matrix or two-point correlation function

$$\langle\hat{\psi}^\dagger(\boldsymbol{x})\hat{\psi}(\boldsymbol{y})\rangle_\beta = \frac{1}{Z_\pm^{(N)}(\beta)}\,\mathrm{Tr}_\pm^{(N)}\left[\mathrm{e}^{-\beta\hat{H}}\hat{\psi}^\dagger(\boldsymbol{x})\hat{\psi}(\boldsymbol{y})\right] = \frac{N\rho_\pm^{(N,1)}(\boldsymbol{y},\boldsymbol{x};\beta)}{Z_\pm^{(N)}(\beta)}. \tag{1.44}$$

The last identity will be shown below in a more general context. Using Eq. (1.35) for $\rho_\pm^{(N,1)}$ then yields, dropping the β-dependence,

$$\langle\hat{\psi}^\dagger(\boldsymbol{x})\hat{\psi}(\boldsymbol{y})\rangle_\beta = \frac{1}{Z_\pm^{(N)}}\sum_{n=1}^{N} s_n^{(1)}(\boldsymbol{y},\boldsymbol{x})Z_\pm^{(N-n)}. \tag{1.45}$$

So, to calculate the expectation values of one-particle operators, one only needs the additional information of the irreducible clusters $s_n^{(1)}$. This can be extended to arbitrary k-particle operators. In general, the expectation value of the normal ordered product of field operators is given by

$$C_\pm^{(N,k)}(\boldsymbol{y},\boldsymbol{x}) = \langle\hat{\Psi}^\dagger(\boldsymbol{x}_1)\cdots\hat{\Psi}^\dagger(\boldsymbol{x}_k)\hat{\Psi}(\boldsymbol{y}_k)\cdots\hat{\Psi}(\boldsymbol{y}_1)\rangle_\beta \tag{1.46}$$

$$= \frac{N!}{(N-k)!}\frac{\rho_\pm^{(N,k)}((\boldsymbol{y}_1,\ldots\boldsymbol{y}_k),(\boldsymbol{x}_1,\ldots,\boldsymbol{x}_k);\beta)}{Z_\pm^{(N)}}, \tag{1.47}$$

as is shown in appendix A. Note the reversed order of the coordinates $\boldsymbol{y}_i$ in (1.46) that is important in the case of fermions. Finally, by making use of Eq. (1.30) one obtains the simple result

$$C_\pm^{(N,k)}(\boldsymbol{y},\boldsymbol{x}) = \frac{1}{Z_\pm^{(N)}}\sum_{n=k}^{N} a_{n,\pm}^{(k)}(\boldsymbol{y},\boldsymbol{x})Z_\pm^{(N-n)}. \tag{1.48}$$

The expectation value of a k-particle operator

$$\hat{\mathcal{O}}_k = \sum_{\substack{i_1,\ldots,i_k=1 \\ i_j \neq i_l}}^{N} \hat{\mathcal{O}}_k^{(i_1,\ldots,i_k)} \tag{1.49}$$

in the canonical ensemble is thus given by

$$\langle \hat{\mathcal{O}}_k \rangle_\beta = \int d^{kD}x \, d^{kD}y \, \mathcal{O}_k(\boldsymbol{x},\boldsymbol{y}) C_\pm^{(N,k)}(\boldsymbol{y},\boldsymbol{x};\beta), \tag{1.50}$$

where the dependence on β has been restored and $\mathcal{O}_k(\boldsymbol{x},\boldsymbol{y})$ is the matrix element

$$\mathcal{O}_k(\boldsymbol{x},\boldsymbol{y}) = \langle \boldsymbol{x}|\hat{\mathcal{O}}_k^{(1,\ldots,k)}|\boldsymbol{y}\rangle \,, \tag{1.51}$$

that is calculated in a k-particle subspace of the N-particle Hilbert space. Note that according to Eq. (1.48) the expectation value (1.50) is expressed only using the coordinate irreducible clusters and the canonical partition functions of subsystems.

The grand canonical ensemble

We have seen that the canonical partition function is completely determined by irreducible clusters via recursive formulas. Moreover, correlation functions and thus the expectation values they generate are completely determined by the coordinate irreducible diagrams and the irreducible clusters that enter the partition function. This again highlights the fact that, if the (coordinate) irreducible clusters are known, the calculation of the full cluster expansions is merely a combinatorial problem. The latter originates from the fact that the particle number N is fixed exactly in the canonical formalism. This condition is relaxed in the grand canonical ensemble, leading to a description that depends only on the (coordinate) irreducible diagrams while not suffering from any combinatorial difficulties.

The grand canonical partition function can be expressed through the canonical partition function as

$$Z_\pm^G(\beta,\mu) = \sum_{N=0}^{\infty} z^N Z_\pm^{(N)}(\beta), \tag{1.52}$$

where $z = \mathrm{e}^{\beta\mu}$ is the fugacity and μ is the chemical potential that controls the average number of particles in the system. The logarithmic derivative of Eq. (1.52) with respect to the fugacity is given by (omitting the index for the particle symmetry and the functional dependencies for the rest of this subsection)

$$\begin{aligned} \frac{\partial}{\partial z}\log Z^G &= \frac{1}{Z^G}\sum_{N=1}^{\infty} z^{N-1} N Z^{(N)} = \frac{1}{Z^G}\sum_{N=1}^{\infty} z^{N-1}\sum_{k=1}^{N} s_k^{(0)} Z^{(N-k)} \\ &= \frac{1}{Z^G}\left(\sum_{m=1}^{\infty} z^{m-1} s_m^{(0)}\right)\underbrace{\left(\sum_{n=0}^{\infty} z^n Z^{(n)}\right)}_{Z^G} = \sum_{m=1}^{\infty} z^{m-1} s_m^{(0)}, \end{aligned} \tag{1.53}$$

where the recurrence relation (1.37) for $Z^{(N)}$ and the Cauchy product formula have been used (assuming convergence of the series). Using $Z^G|_{z=0} = Z^{(0)} = 1$ one immediately gets

$$Z^G = \exp\left(\sum_{m=1}^{\infty} \frac{z^m}{m} s_m^{(0)}\right), \tag{1.54}$$

such that the grand potential Ω is given by the sum of irreducible clusters,

$$\Omega(\beta,\mu) = -\frac{1}{\beta}\log Z^G = -\frac{1}{\beta}\sum_{m=1}^{\infty}\frac{z^m}{m}s_m^{(0)}. \tag{1.55}$$

For the correlation functions let us first relate the expectation values in the two ensembles:

$$\begin{aligned}\langle\hat{\mathcal{O}}_k\rangle_{\beta,\mu} &= \frac{1}{Z^G}\operatorname{Tr}\left[\mathrm{e}^{-\beta(\hat{H}-\mu\hat{N})}\hat{\mathcal{O}}_k\right] = \frac{1}{Z^G}\sum_{N=0}^{\infty} z^N \operatorname{Tr}^{(N)}\left[\mathrm{e}^{-\beta\hat{H}}\hat{\mathcal{O}}_k\right] \\ &= \frac{1}{Z^G}\sum_{N=0}^{\infty} z^N Z^{(N)}\langle\hat{\mathcal{O}}_k\rangle_\beta.\end{aligned} \tag{1.56}$$

Here, the first trace is over the full Fock space. Using Eq. (1.48) one finds

$$\begin{aligned}C^{(k)}(\boldsymbol{y},\boldsymbol{x},\beta,\mu) &= \langle\hat{\Psi}^\dagger(\boldsymbol{x}_1)\cdots\hat{\Psi}^\dagger(\boldsymbol{x}_k)\hat{\Psi}(\boldsymbol{y}_k)\cdots\hat{\Psi}(\boldsymbol{y}_1)\rangle_{\beta,\mu} \\ &= \frac{1}{Z^G}\sum_{N=k}^{\infty} z^N Z^{(N)} C^{(k,N)}(\boldsymbol{y},\boldsymbol{x},\beta) \\ &= \frac{1}{Z^G}\sum_{N=k}^{\infty} z^N \sum_{l=k}^{N} a_l^{(k)}(\boldsymbol{y},\boldsymbol{x}) Z^{(N-l)} \\ &= \frac{1}{Z^G}\left(\sum_{n=k}^{\infty} z^n a_n^{(k)}(\boldsymbol{y},\boldsymbol{x})\right)\underbrace{\left(\sum_{m=0}^{\infty} z^m Z^{(m)}\right)}_{Z^G} \\ &= \sum_{n=k}^{\infty} z^n a_n^{(k)}(\boldsymbol{y},\boldsymbol{x}).\end{aligned} \tag{1.57}$$

This means that the thermal expectation values are directly determined by the coordinate irreducible diagrams. This is in analogy to the cancellation of vacuum bubbles in quantum field theories. The interpretation is, however, different, as there are no vacuum bubbles in a particle-conserving theory. It is rather the statistical average over systems with different particle numbers that leads to the simplifications in the grand canonical ensemble. Another way to view the simple expressions obtained in the grand canonical ensemble is to simply take them as the *generating functions* of the canonical partition

function and expectation values via

$$Z^{(N)} = \frac{1}{N!}\left[\frac{\partial^N}{\partial z^N} Z^G\right]_{z=0}, \tag{1.58}$$

$$\langle \hat{\mathcal{O}} \rangle_\beta = \frac{1}{N! Z^{(N)}}\left[\frac{\partial^N}{\partial z^N}\left(Z^G \langle \hat{\mathrm{O}} \rangle_{\beta,\mu}\right)\right]_{z=0}. \tag{1.59}$$

1.2.4. Generalization to multiple species

In this subsection, the generalizations of the previous results for multiple species is provided. This is of relevance not only in mixtures of fundamentally distinguishable particles but also in systems where single-particle degrees of freedom are conserved by the inter-particle interaction, thus making the particles effectively distinguishable. The most important examples comprise the cases of spin-1/2 fermions with spin-conserving interactions and composite particles with internal degrees of freedom that are robust against collisions.

The results of the previous sections are straightforwardly generalized using multi-index notation

$$\boldsymbol{n} = (n_1, \dots, n_l), \qquad \boldsymbol{n}! = \prod_{i=1}^{l} n_i!, \qquad \mathrm{e}^{\boldsymbol{n}} = (\mathrm{e}^{n_1}, \dots, \mathrm{e}^{n_l}), \tag{1.60}$$

$$\boldsymbol{z}^{\boldsymbol{n}} = \prod_{i=1}^{l} z_i^{n_i}, \qquad \partial^{\boldsymbol{n}} = \prod_{i_0}^{l} \partial_i^{n_i}, \qquad \sum_{\boldsymbol{n}=\boldsymbol{k}}^{\boldsymbol{N}} = \left(\prod_{i=1}^{l} \sum_{n_i=k_i}^{N_i}\right), \tag{1.61}$$

where l is the number of species. Let us denote the coordinates of the N_i indistinguishable particles of species i as $\boldsymbol{X}_i = (\boldsymbol{x}_1^{(i)}, \dots, \boldsymbol{x}_{N_i}^{(i)})$ and the coordinates of all particles by $\boldsymbol{X}$. Using the many-body imaginary-time propagator $K^{(\boldsymbol{N})}(\boldsymbol{Y}, \boldsymbol{X}; \beta)$ for $N_1 + \dots + N_l$ particles, the symmetry-projected propagator is generalized from (1.15) to

$$K_{\boldsymbol{\sigma}}^{(\boldsymbol{N})}(\boldsymbol{Y}, \boldsymbol{X}; \beta) = \frac{1}{\boldsymbol{N}!} \sum_{\boldsymbol{P} \in S_{\boldsymbol{N}}} \boldsymbol{\sigma}^{\boldsymbol{P}} K^{(\boldsymbol{N})}(\boldsymbol{P}\boldsymbol{Y}, \boldsymbol{X}; \beta), \tag{1.62}$$

where the sum runs over all tuples $(P^{(1)}, \dots, P^{(l)}) \in S_{\boldsymbol{N}} = S_{N_1} \times \dots \times S_{N_l}$ and the individual permutations act only on the coordinates of the respective particle species $\boldsymbol{P}\boldsymbol{Y} = (P^{(1)}\boldsymbol{Y}^{(1)}, \dots, P^{(l)}\boldsymbol{Y}^{(l)})$. The exchange symmetry in each particle species is encoded in the indices $\sigma_i = \pm 1$ for $i = 1, \dots, l$. With the same notation, the sums of (coordinate) irreducible clusters $S_{\boldsymbol{n},\boldsymbol{\sigma}}^{(\boldsymbol{k})}(\boldsymbol{Y}, \boldsymbol{X}; \beta)$ and $A_{\boldsymbol{n},\boldsymbol{\sigma}}^{(\boldsymbol{k})}(\boldsymbol{Y}, \boldsymbol{X}; \beta)$ can be introduced, with the same definitions of irreducibility as before. Here, the multi-indices $\boldsymbol{n}$ and $\boldsymbol{k}$ have to fulfill $\boldsymbol{n} \geq \boldsymbol{k}$ and $\boldsymbol{k} > 0$ in $A_{\boldsymbol{n}}^{(\boldsymbol{k})}$, making use of the partial order that can be defined by

$$\boldsymbol{s} \geq \boldsymbol{t} \Leftrightarrow s_i \geq t_i \text{ for all } i = 1, \dots, l. \tag{1.63}$$

Note that as before, abusing notation, the arguments $\boldsymbol{X}$ and $\boldsymbol{Y}$ in $S_{\boldsymbol{n},\boldsymbol{\sigma}}^{(\boldsymbol{k})}$ and $A_{\boldsymbol{n},\boldsymbol{\sigma}}^{(\boldsymbol{k})}$ are defined by the tuple $\boldsymbol{k}$ in that they contain k_j particle coordinates of the species j ($k_j = 0$

is not excluded). Then, defining the rescaled cluster sums

$$s^{(\boldsymbol{k})}_{\boldsymbol{n},\boldsymbol{\sigma}}(\boldsymbol{Y},\boldsymbol{X};\beta) = \frac{S^{(\boldsymbol{k})}_{\boldsymbol{n},\boldsymbol{\sigma}}(\boldsymbol{Y},\boldsymbol{X};\beta)}{(\boldsymbol{n}-\boldsymbol{k})!}, \tag{1.64}$$

$$a^{(\boldsymbol{k})}_{\boldsymbol{n},\boldsymbol{\sigma}}(\boldsymbol{Y},\boldsymbol{X};\beta) = \frac{A^{(\boldsymbol{k})}_{\boldsymbol{n},\boldsymbol{\sigma}}(\boldsymbol{Y},\boldsymbol{X};\beta)}{(\boldsymbol{n}-\boldsymbol{k})!}, \tag{1.65}$$

in analogy to Eqs. (1.32) and (1.31) the generalization of Eq. (1.30) to multiple species is found as

$$\rho^{\boldsymbol{N},\boldsymbol{k}}_{\boldsymbol{\sigma}}(\boldsymbol{Y},\boldsymbol{X};\beta) = \frac{(\boldsymbol{N}-\boldsymbol{k})!}{\boldsymbol{N}!}\sum_{\boldsymbol{n}=\boldsymbol{k}}^{\boldsymbol{N}} a^{(\boldsymbol{k})}_{\boldsymbol{n},\boldsymbol{\sigma}}(\boldsymbol{Y},\boldsymbol{X};\beta) Z^{(\boldsymbol{N}-\boldsymbol{n})}_{\boldsymbol{\sigma}}(\beta) \tag{1.66}$$

in terms of the canonical partition functions of the smaller systems that have the particles labeled by $\boldsymbol{n} \geq \boldsymbol{k}$ excluded. There is one important difference in the definitions (1.64) and (1.32). In the latter, the definition for $k = 0$ has a different normalization that is motivated from the cycle diagrams. In the case of multiple species, it is more convenient to avoid this special treatment of $k_i = 0$ for $i \in \{1,\ldots,l\}$. By taking $\boldsymbol{k} = \boldsymbol{e}_i$ in (1.66), where $\boldsymbol{e}_i$ is the ith unit vector, and tracing out the remaining particle one obtains an equivalent of the recursion formula (1.37) for every species $i \in \{1,\ldots,l\}$ (omitting β)

$$Z^{(\boldsymbol{N})}_{\boldsymbol{\sigma}} = \frac{1}{N_i}\sum_{\boldsymbol{n}=\boldsymbol{e}_i}^{\boldsymbol{N}} n_i s^{(0)}_{\boldsymbol{n},\boldsymbol{\sigma}} Z^{(\boldsymbol{N}-\boldsymbol{n})}_{\boldsymbol{\sigma}}, \qquad i = 1,\ldots,l. \tag{1.67}$$

Note the extra factor n_i on the right hand side that comes from the different definitions of the irreducible cluster sums.

Proceeding with the generalization of the correlators (1.47),

$$C^{(\boldsymbol{N},\boldsymbol{k})}_{\boldsymbol{\sigma}}(\boldsymbol{Y},\boldsymbol{X};\beta) = \left\langle \prod_{i=1}^{l} \hat{\Psi}^\dagger\left(\boldsymbol{x}^{(i)}_1\right)\cdots\hat{\Psi}^\dagger\left(\boldsymbol{x}^{(i)}_{k_i}\right)\hat{\Psi}\left(\boldsymbol{y}^{(i)}_{k_i}\right)\cdots\hat{\Psi}\left(\boldsymbol{y}^{(i)}_1\right)\right\rangle_\beta \tag{1.68}$$

$$= \frac{\boldsymbol{N}}{(\boldsymbol{N}-\boldsymbol{k})!}\frac{\rho^{(\boldsymbol{N},\boldsymbol{k}}_{\sigma}(\boldsymbol{Y},\boldsymbol{X};\beta)}{Z^{(\boldsymbol{N})}_{\boldsymbol{\sigma}}(\beta)}, \tag{1.69}$$

where the field operators for different species commute, one immediately finds

$$C^{(\boldsymbol{N},\boldsymbol{k})}_{\boldsymbol{\sigma}}(\boldsymbol{Y},\boldsymbol{X};\beta) = \frac{1}{Z^{(\boldsymbol{N})}_{\boldsymbol{\sigma}}(\beta)}\sum_{\boldsymbol{n}=\boldsymbol{k}}^{\boldsymbol{N}} a^{(\boldsymbol{k})}_{\boldsymbol{n},\boldsymbol{\sigma}}(\boldsymbol{Y},\boldsymbol{X};\beta) Z^{(\boldsymbol{N}-\boldsymbol{n})}_{\boldsymbol{\sigma}}(\beta). \tag{1.70}$$

Introducing the l chemical potentials $\boldsymbol{\mu} = (\mu_1,\ldots,\mu_l)$ and fugacities $\boldsymbol{z} = \mathrm{e}^{\beta\boldsymbol{\mu}}$ one then finds with the same methods as above the recursion formula for the grand canonical partition function

$$Z^G(\beta,\boldsymbol{\mu}) = \exp\left(\sum_{\boldsymbol{n}=\boldsymbol{e}_i}^{\infty} \boldsymbol{z}^{\boldsymbol{n}} s^{(0)}_{\boldsymbol{n}}(\beta)\right) Z^G(\beta,\boldsymbol{\mu})\Big|_{\mu_i\to-\infty}, \qquad i = 1,\ldots,l, \tag{1.71}$$

where the last factor is the grand partition function without species i. It is easily proven by taking logarithmic derivatives of Z^G with respect to the fugacities. The full result is the generalization of (1.54),

$$Z^G(\beta, \boldsymbol{\mu}) = \exp\left(\sum_{\boldsymbol{n}=0}^{\infty} \boldsymbol{z}^{\boldsymbol{k}} s_{\boldsymbol{n}}^{(0)}(\beta)\right). \tag{1.72}$$

Finally, the generalization of Eq. (1.57) can be given as

$$C^{(\boldsymbol{k})}(\boldsymbol{Y}, \boldsymbol{X}; \beta, \boldsymbol{\mu}) = \sum_{\boldsymbol{n}=\boldsymbol{k}}^{\infty} \boldsymbol{z}^{\boldsymbol{n}} a_{\boldsymbol{n}}^{(\boldsymbol{k})}(\boldsymbol{Y}, \boldsymbol{X}, \beta). \tag{1.73}$$

As before, they are sufficient to calculate the expectation value of any $\boldsymbol{k}$-particle observable.

1.2.5. Resummation of clusters

In this section, the important case of systems that are homogeneous in space is considered. In such systems, the total momentum is conserved, such that the many-body propagator in momentum space is diagonal in the total momentum. Moreover, tracing out one particle fixes the initial and final momentum of the respective particle to be the same, such that the total momentum of the remaining particles must be conserved. This means that the n-point correlation functions $C_{\pm}^{(N,k)}(\boldsymbol{y}, \boldsymbol{x})$, Eq. (1.48), and $C_{\pm}^{(k)}(\boldsymbol{y}, \boldsymbol{x})$, Eq. (1.57), are diagonal in the total momentum of the k particles that are not traced over. This does also apply to individual diagrams in the cluster expansion, and thus any coordinate irreducible diagram. In this section we will only focus on the reduced one-body density matrix, i.e., all but one particles are traced out. In this case one has $a_{n,\pm}^{(1)} = s_{n,\pm}^{(1)}$ and this sum of irreducible diagrams can then be written in the as

$$s_{n,\pm}^{(1)}(\boldsymbol{y}, \boldsymbol{x}) = s_{n,\pm}^{(1)}(\boldsymbol{y} - \boldsymbol{x}, 0) = \frac{1}{(2\pi)^D} \int d^D k \, \mathrm{e}^{i\boldsymbol{k}(\boldsymbol{y}-\boldsymbol{x})} \tilde{s}_{n,\pm}^{(1)}(\boldsymbol{k}), \tag{1.74}$$

with the momentum representation of the irreducible cluster sums

$$\tilde{s}_{n,\pm}^{(1)}(\boldsymbol{k}) = \int d^D z \, \mathrm{e}^{-i\boldsymbol{k}\boldsymbol{z}} s_{n,\pm}^{(1)}(\boldsymbol{z}, 0). \tag{1.75}$$

The reduced one-body density matrix in momentum representation is thus diagonal and, using Eq. (1.57), given by

$$\tilde{C}_{\pm}^{(1)}(\boldsymbol{k}) = \int d^D z \, \mathrm{e}^{-i\boldsymbol{k}\boldsymbol{z}} C_{\pm}^{(1)}(\boldsymbol{y} - \boldsymbol{x}, 0) = \sum_{n=1}^{\infty} z^n \tilde{s}_{n,\pm}^{(1)}(\boldsymbol{k}). \tag{1.76}$$

Up to this point one has not gained much from the representation in momentum space. However one should note that many irreducible diagrams now factorize. To be more specific, if a two-legged irreducible diagram in $s_{n,\pm}^{(1)}$ can be cut into two pieces such that

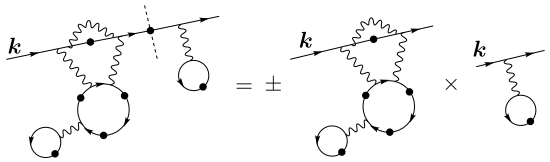

Figure 1.4: The factorization of diagrams in the reduced one-body density matrix. The diagram on the left can be cut into two pieces at the dashed line, and it has the same momentum $\boldsymbol{k}$ at this point. The value of the full diagram is then the product of the two diagrams evaluated at the same momentum $\boldsymbol{k}$. As cutting the diagram is achieved by interchanging two particle indices, one has to account for the exchange symmetry with a factor ± 1.

one ends up with two new two-legged diagrams, the full diagram is given by the product of the latter. Figure 1.4 shows an example of such a factorization. There, instead of labeling the initial and final coordinates, the momentum $\boldsymbol{k}$ is used and the sign factors from exchange symmetry have been included in the diagram values for simplicity (opposing the convention introduced in section 1.2.2), leading to the sign factor on the right hand side, as, on a formal level, any two-legged diagram that can be cut in the above manner is linked by a single exchange of particle indices. This can be seen as follows: Let $(\pm 1)^{P_a}\mathfrak{D}_a$ and $(\pm 1)^{P_b}\mathfrak{D}_b$ be the disconnected parts of the diagram and $(\pm 1)^{P_{ab}}\mathfrak{D}_{ab}$ the connected diagram, i.e., P_a, P_b, and P_{ab} are the permutations that enter the diagrams and P_a and P_b act on disjoint sets of particle indices. Let $P = (12)$ the exchange permutation of the indices 1 and 2, then

$$\begin{aligned}\mathfrak{D}_{ab}(\boldsymbol{y}_1, \boldsymbol{x}_1) &= \int d^D x_2\, \mathfrak{D}_b(\boldsymbol{y}_1, \boldsymbol{x}_2)\mathfrak{D}_a(\boldsymbol{x}_2, \boldsymbol{x}_1) \\ &= \int d^D x_2\, d^D y_2\, \delta^{(D)}(\boldsymbol{x}_2 - \boldsymbol{y}_2)\mathfrak{D}_b(\boldsymbol{y}_1, \boldsymbol{x}_2)\mathfrak{D}_a(\boldsymbol{y}_2, \boldsymbol{x}_1) \\ &= \int d^D x_2\, d^D y_2\, \delta^{(D)}(\boldsymbol{x}_2 - \boldsymbol{y}_2)\mathfrak{D}_b(\boldsymbol{y}_{P(2)}, \boldsymbol{x}_2)\mathfrak{D}_a(\boldsymbol{y}_{P(1)}, \boldsymbol{x}_1), \end{aligned} \tag{1.77}$$

such that in the connected diagram one has to account for the the additional particle exchange P as compared with the disconnected parts, giving rise to a factor $(\pm)^P = \pm 1$ for each cut. To be precise, the cycle structure of the connected diagram is given by $P_{ab} = P \circ P_a \circ P_b$ and the sign factor is given by

$$(\pm 1)^{P_{ab}} = (\pm 1)^{P \circ P_a \circ P_b} = \pm (\pm 1)^{P_a \circ P_b} = \pm (\pm 1)^{P_a} (\pm 1)^{P_b}. \tag{1.78}$$

As was explained in section 1.2.2, each irreducible diagram has a certain internal multiplicity due to possible relabeling of the particles that have been traced out. To make use of the factorization of diagrams we need to explore how the multiplicity of the full diagram is related to the multiplicities of the constituents. This can be done on a purely combinatorial level. Let us assume that we have a two-legged irreducible diagram of $n = k + l$ particles that can be cut into two such diagrams with k and l particles,

respectively, with internal multiplicities $\#_k$ and $\#_l$. The latter are due to relabeling of $k-1$ and $l-1$ traced particles, respectively, as one of the particle labels in each diagram is fixed by the legs. The multiplicity $\#_n$ of the connected n-particle diagram can then be given in terms of the multiplicities $\#_k$ and $\#_l$ by counting the ways to distribute the $n-1$ traced coordinates to the constituents. First, two of the legs are connected and are traced over in the full diagram, giving rise to $n-1$ possible assignments. Then, out of the remaining $n-2$ traced particle coordinates one has to fix $k-1$ coordinates to be part of the k-particle diagram that can then be internally relabeled in $\#_k$ ways. The remaining $l-1$ coordinates are then part of the l-particle diagram with multiplicity $\#_l$. The (bare) internal multiplicity of the full diagram is thus

$$\#_n = (n-1) \times \left[\binom{n-2}{k-1} \#_k \right] \times \#_l = (n-1)! \frac{\#_k}{(k-1)!} \frac{\#_l}{(l-1)!}, \tag{1.79}$$

or, including the scaling factor of the irreducible cluster sums in Eq. (1.32) into the internal multiplicities according to

$$\#_n^{\text{int}} = \frac{\#_n}{(n-1)!}, \tag{1.80}$$

one finds that the internal multiplicities factorize, i.e.,

$$\#_n^{\text{int}} = \#_k^{\text{int}} \times \#_l^{\text{int}}, \qquad n = k + l. \tag{1.81}$$

Thus, concluding the above considerations, the example of the diagrammatic identity in Fig. 1.4 can be either understood as an equality for a single diagram, or as an equality for the sum of all equivalent diagrams, i.e., *including* the internal multiplicities (and the sign factor). One is thus free to omit the internal multiplicities by ascribing them to the value of the diagram while still allowing for factorization. With this in mind, the one-body reduced density matrix in the grand canonical ensemble is given by

$\tilde{C}_{\pm}^{(1)}(\boldsymbol{k}) =$

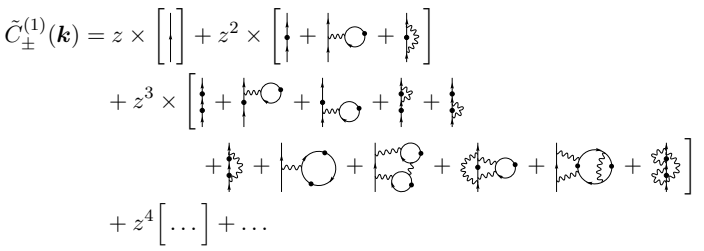

(1.82)

where the momentum $\boldsymbol{k}$ has been omitted in the diagrams. By reordering the sum ac-

cording to the number of factors in the diagrams one obtains the formal power expansion

$$\tilde{C}^{(1)}_{\pm}(\boldsymbol{k}) = z \times \Bigg[\; + z \times \Bigg(\; + \; \Bigg) + z^2 \Bigg(\; + \ldots \Bigg) + \ldots \Bigg]$$
$$\pm z^2 \times \Bigg[\; + z \times \Bigg(\; + \; \Bigg) + z^2 \Bigg(\; + \ldots \Bigg) + \ldots \Bigg]^2$$
$$+ z^3 \times \Bigg[\; + z \times \Bigg(\; + \; \Bigg) + z^2 \Bigg(\; + \ldots \Bigg) + \ldots \Bigg]^3$$
$$+ \ldots . \tag{1.83}$$

Thus, the full expansion can be reordered to a formal power series in the dressed Boltzmann factor

$$c_{\pm}(\boldsymbol{k}) = \; = \; + z \times \Bigg(\; + \; \Bigg) + z^2 \Bigg(\; + \ldots \Bigg) + \ldots \tag{1.84}$$

that contains only diagrams that cannot be cut anymore. Note, again, that the sign factors for the exchange symmetry are included in the diagrams here, opposing the convention of other sections. The one-body reduced density matrix can thus be formally written as

$$\tilde{C}^{(1)}_{\pm}(\boldsymbol{k}) = \pm \sum_{n=1}^{\infty} [\pm z c_{\pm}(\boldsymbol{k})]^n = \frac{z c_{\pm}(\boldsymbol{k})}{1 \mp z c_{\pm}(\boldsymbol{k})} = \frac{1}{[z c_{\pm}(\boldsymbol{k})]^{-1} \mp 1}. \tag{1.85}$$

This has the form of the Bose-Einstein (upper sign) or Fermi distributions (lower sign) for the occupation of the single-particle states with momentum $\boldsymbol{k}$, but with the Boltzmann factor replaced by the dressed function $c_{\pm}(\boldsymbol{k})$. In the case of vanishing interactions one has $c_{\pm}(\boldsymbol{k}) \to \mathrm{e}^{-\beta E(\boldsymbol{k})}$ with $E(\boldsymbol{k}) = \hbar^2 \boldsymbol{k}^2 / 2m$ such that the correct noninteracting result for the one-particle density matrix is obtained:

$$\tilde{C}^{(1)}_{\pm}(\boldsymbol{k}) \xrightarrow{\text{NI}} \frac{1}{\mathrm{e}^{\beta(E_{\boldsymbol{k}} - \mu)} \mp 1}. \tag{1.86}$$

Although there is no guarantee that the dressed Boltzmann factor has a positive convergence radius for finite interaction, it could give much better asymptotic approximations than other approaches. One reason for this is the fact that even for free fermions, where

$$\tilde{s}^{(1)}_{n,-}(\boldsymbol{k}) = (-1)^{n-1} \mathrm{e}^{-n\beta E_{\boldsymbol{k}}}, \tag{1.87}$$

the fugacity expansion (1.76) does not converge for $z\,\mathrm{e}^{-\beta E_{\boldsymbol{k}}} \geq 1$, i.e., $E_{\boldsymbol{k}} \leq \mu \sim E_{\mathrm{F}}$, a regime that is, however, covered by the Fermi function (1.86) being the analytic continuation of the series expression.

A natural application of Eq. (1.85) is a perturbative expansion

$$-\frac{1}{\beta} \log\left(z c_{\pm}(\boldsymbol{k})\right) = E_{\boldsymbol{k}} - \mu + b_1 \gamma + \mathcal{O}(\alpha^2) \tag{1.88}$$

in a small coupling γ to obtain a mean field description in terms of a shifted single-particle energy. A more elaborate way to proceed could be a recursive calculation of the dressed Boltzmann factor $c_\pm$ by noting that it has a self similar structure. For example, one can generate a whole class of diagrams that only contain interaction contributions of second order by truncating the series expansion of $c_\pm(\boldsymbol{k})$ after the linear term, while replacing the single dot in each diagram by the rule

$$\bullet \mapsto 1 \pm \tilde{C}_\pm^{(1)}(\boldsymbol{k}') = \left[1 \mp z c_\pm(\boldsymbol{k}')\right]^{-1} \tag{1.89}$$

before integrating over the momentum $\boldsymbol{k}'$. To be specific, one would obtain an integral equation of the form

$$c_\pm(\boldsymbol{k}) = \mathrm{e}^{-\beta E_{\boldsymbol{k}}} + z \int d^D k' \, \frac{f(\boldsymbol{k}, \boldsymbol{k}')}{1 \pm z c_\pm(\boldsymbol{k}')}, \tag{1.90}$$

with the function f being defined by the diagonal and exchange elements of the interaction contribution $\Delta K^{(2)}$ in momentum space. Extensions that generate a larger class of diagrams are also possible. Although all the ingredients are available, e.g., for short range interactions in arbitrary dimensions [84], this approach has not been taken yet and might be subject of a future project.

1.3. Short times—smooth spectra—high temperatures

The previous section has introduced the cluster expansion on a purely formal level, being valid for any kind of systems with fixed number of particles. However, despite the conceptually simple formulas that one obtains in the theory, one still has to face the fact that, in almost all situations, only the simplest diagrams can be exactly calculated. Moreover, if a finite system is considered, the values of irreducible diagrams are not independent of the external potentials or the system's boundaries. Therefore, this section is dedicated to the introduction of certain approximations that help solving some of these difficulties.

The section is structured as follows: First, using the analogy of short-time propagation and high-temperature quantum statistics, the general short-time scaling of the quantum cluster expansion is reviewed, also introducing the (smooth) density of states that defines the microcanonical ensemble. Then, the scaling is used for the analytical treatment of a certain class of diagrams that can be calculated whenever the interaction contributions of second order are known explicitly, being of use for later sections. Finally, after the implications of the high temperature scaling on the thermodynamic limit is put forward, a self-consistent method for calculating the mean energy shifts due to interaction is reviewed, with a focus on its scaling in the thermodynamic limit.

1.3.1. Short-time propagation and high-temperature scaling

This subsection gives an overview of the short-time approximation and the general dimensional scaling properties of propagators that were introduced in [52, 61, 85]. For further details, the reader is referred to the literature.

The starting point for the quantum cluster expansion was the many-body propagator. However, as was noted before, the whole theory is basis-independent and can even be formulated at the level of operators. The reason for using the (imaginary time) propagator is that it is very well understood at the level of single-particle systems, where a saddle point approximation in the Feynman path integral leads to the semiclassical Van Vleck-Gutzwiller propagator [41, 49], that comes as a sum over classical paths and admits a systematic approximation for short times. In the context of billiard systems, the short-time approximation, that takes only into account the shortest classical paths, plays a special role as it contains the information on the *smooth* part of density of states, then given by Weyl's law and the Weyl expansion [49, 50].

Now, a key step is to realize that if the temperature is large enough, the discreteness of the many-body spectrum becomes unimportant due to its high level density. This has to be contrasted to the assumption of a smooth single-particle level density, as the latter is, e.g., not capable of describing Bose-Einstein condensation in bosonic systems unless the single-particle ground state is treated separately [13]. A many-body description does not suffer from any such problems. Therefore, the discreteness of the *many-body* DOS can be neglected even for temperatures inside the quantum degenerate regime or in the presence of condensation effects as long as the number of uncondensed particles is not very small. It is then sufficient to include only the short-time information on the propagators $G^{(N)}$

to be specified in the following. For finite systems without external potentials all the propagators in the calculation are replaced by their infinite space equivalents, i.e., it is assumed that the particles do not explore the whole system in arbitrarily short times. Formally, this corresponds to only taking into account the shortest classical paths in the Van Vleck-Gutzwiller propagator. The condition for this approximation to be accurate can be estimated at the single-particle level to be

$$t \ll \frac{mV^{\frac{2}{D}}}{2\pi\hbar} \equiv t_{\mathrm{T}}, \tag{1.91}$$

where m is the mass of the particle, V is the volume of the system, and D is the dimension. The characteristic time t_{T} can be thought of as the typical traversal time through the system of a particle with momentum $\hbar V^{-1/D}$, where the latter corresponds to the minimal uncertainty in the momentum of a wave packet in the volume V. If we switch to imaginary time the condition (1.91) can be translated into

$$\lambda_T^D \ll V, \tag{1.92}$$

introducing the thermal (de Broglie) wavelength

$$\lambda_T = \sqrt{\frac{2\pi\hbar^2\beta}{m}}. \tag{1.93}$$

At this length scale the propagator of a single free particle decays in imaginary time $t = -i\hbar\beta$. This gives the intuitive picture that within the regime of validity of the short-time approximation all clusters of particles have a characteristic size that scales with λ_T that is much smaller than any length scale introduced from external confinement, such that their internal structure is essentially independent of the latter. It is worth stressing that the short-time approximation does not require that the thermal wavelength is small compared to the mean inter-particle separation, i.e., one can have

$$\frac{N\lambda_T^D}{V} > 1, \tag{1.94}$$

in contrast to the case of high-temperature expansions in the thermodynamic limit. This parameter will also be referred to as the "quantum degeneracy parameter" later, as it marks the onset of dominant quantum effects. For example, BEC sets in at $N\lambda_T^3/V = \zeta(3/2) \approx 2.61$ in three dimensions [13]. The term "quantum degenerate regime" will be used when $N\lambda_T^D/V$ is of order one or larger and will thus refer to both fermionic and bosonic gases.

As the short-time approximation specified above is obtained from taking the shortest paths in the Van Vleck-Gutzwiller propagator, it can be easily extended to include, e.g., corrections from boundaries that improve the range of applicability to even smaller temperatures and energies. The short-time approximation of the propagator thereby encodes the information on the slowly varying parts of the density of states: The bound in Eq. (1.91) plays the role of a Heisenberg time $t_{\mathrm{H}} = 2\pi\hbar/\Delta$ where Δ is the mean single-particle level spacing[2]. It can be understood as a lower bound for the time needed to

[2]Estimated around the ground state using Weyl's law for the smooth density of states.

resolve the discreteness of the spectrum. This means that the price we pay for using the short-time approximation is the loss of all information related to this discreteness. However, as the levels in noninteracting many-particle systems can be estimated to become exponentially dense in a certain window not very high in energy [86], the knowledge of the exact position of individual levels is only important very close to the ground state.

In the presence of smooth external potentials the short-time approximation can be modified such that only the internal dynamics of a cluster is mapped to infinite space, while its center of mass evolves according to the single-particle (short-time) propagator [60, 85]. This assumes that the spatial extent of a cluster is small compared to the variations of the external potential, which is justified by the short-range character of the interactions together with the short-time approximation. However, to be consistent with the latter, the external potential has to be included only as a phase factor, here evaluated in imaginary time,

$$K^{(n)}_{\text{clust}}(\boldsymbol{y},\boldsymbol{x};\beta) \approx K^{(n)}_{\text{clust}}(\boldsymbol{y},\boldsymbol{x};\beta)\Big|_{V_{\text{ext}}=0} \times \mathrm{e}^{-\beta\int_0^1 ds\,\sum_{i=1}^n V_{\text{ext}}((\boldsymbol{y}_i-\boldsymbol{x}_i)s+\boldsymbol{x}_i)} \tag{1.95}$$

that can be found from the Eikonal approximation [61]. The function $K^{(n)}_{\text{clust}}$ Eq. (1.95) represents any irreducible cluster.

The power of the short-time approximation lies in the high level of generality, leading to certain general scaling properties. Let us first focus on the full trace of a cluster as it appears, e.g., in the partition function. As the internal cluster dynamics is treated like in homogeneous systems in the short-time approximation, it is invariant with respect to a translation of all the coordinates. Without external potentials this invariant direction leads to a factor in the full trace that is proportional to the volume of the system, while in the case of slowly varying external potentials, their effect can be approximated by evaluating Eq. (1.95) at the point where all coordinates coincide, leading to a contribution

$$\int d^{(N-1)D}x\, K^{(n)}_{\text{clust}}(\boldsymbol{x},\boldsymbol{x};\beta)\Big|_{\boldsymbol{x}_1=0,V_{\text{ext}}=0} \times \int d^D x_1\, \exp\left(-\beta n V_{\text{ext}}(\boldsymbol{x}_1)\right) \tag{1.96}$$

of the respective cluster to the partition function, where the first term is calculated *independently* of the external potential[3]. Similar approximations can be applied for partial traces, where $\boldsymbol{x}_1$ should be one of the untraced coordinates or the center of mass.

Before further analyzing the short-time dynamics it is instructive to review the general dimensional scaling [61,85] of the exact non-relativistic propagators, only assuming that the form of the Hamiltonian in position representation is given in the standard form

$$\hat{H} = \sum_{i=1}^{D_{\text{tot}}} -\frac{\hbar^2}{2m_i}\triangle_i + V(\boldsymbol{x}), \tag{1.97}$$

where $V(\boldsymbol{x})$ is a function that only depends on the D_{tot} coordinates $\boldsymbol{x}$, an energy scale α, a reference mass m and Planck's constant, together with an arbitrary number of

[3] In the cluster expansion of the grand potential, i.e., for the fully traced clusters, this approximation is closely related to a local density approximation [87,88], but should be considered more general when applied to propagators and partial traces.

dimensionless parameters $\boldsymbol{\lambda}$ that encode, e.g., the mass ratios and different length scales. Explicitly, the potential has to be of the form

$$V = V(\boldsymbol{x}; \alpha, m, \hbar, \boldsymbol{\lambda}). \tag{1.98}$$

The latter assumption actually encodes the restriction that the potential should be completely determined by $\hbar$ and quantities that can either be expressed in the SI units of time, mass, and length, or can be combined to have the latter units, which is the generic situation. This means that the strongest assumption in the form of the Hamiltonian (1.97) lies in the homogeneity of degree -2 of the kinetic energy.

With the above assumptions one can show [85] that the (imaginary time) propagator can be generally written as

$$K(\boldsymbol{y}, \boldsymbol{x}; \beta, \alpha, m, \hbar, \boldsymbol{\lambda}) = \frac{1}{\lambda_T^{D_{\text{tot}}}} k\left(\frac{\boldsymbol{y}}{\lambda_T}, \frac{\boldsymbol{x}}{\lambda_T}; \beta\alpha, \boldsymbol{\lambda}\right) \tag{1.99}$$

with a dimensionless function k that depends only on dimensionless quantities.

The potential V in (1.98) is usually the sum of external and interaction potentials with their interplay encoded in the dimensionless parameters $\boldsymbol{\lambda}$. However, in the short-time approximation the internal cluster dynamics is assumed to decouple from the external potential, such that the scaling can be applied to the interactions separately. Thus, assuming an interaction potential V of the form (1.98) one can rewrite the contribution of the internal dynamics of the irreducible clusters (1.95) as

$$K^{(n)}_{\text{clust}}(\boldsymbol{y}, \boldsymbol{x}; \beta)\Big|_{V_{\text{ext}}=0} = \frac{1}{\lambda_T^{nD}} k^{(n)}_{\text{clust}}\left(\frac{\boldsymbol{y}}{\lambda_T}, \frac{\boldsymbol{x}}{\lambda_T}; \beta\alpha\right) \tag{1.100}$$

as a dimensionless function $k^{(n)}_{\text{clust}}$ that is invariant under the translation of all coordinates. Approximating the external potential by evaluating all the coordinates at the same point $\boldsymbol{z}$ then leads to

$$K^{(n)}_{\text{clust}}(\boldsymbol{y}, \boldsymbol{x}; \beta) \approx \frac{1}{\lambda_T^{nD}} k^{(n)}_{\text{clust}}\left(\frac{\boldsymbol{y}}{\lambda_T}, \frac{\boldsymbol{x}}{\lambda_T}; \beta\alpha\right) \mathrm{e}^{-n\beta V_{\text{ext}}(\boldsymbol{z})}. \tag{1.101}$$

Here, $\boldsymbol{z}$ corresponds to the invariant direction of $k^{(n)}_{\text{clust}}$ and can be understood as the center of mass position of the cluster, but in practice any of the x_i or y_i can be used. Then, however, one has to keep in mind that the coordinate $\boldsymbol{z}$ should not be traced over in any *partial* traces. By further assuming the form (1.98) also for the external potential one may write it as

$$V_{\text{ext}}(\boldsymbol{z}) = \alpha_{\text{ext}} v_{\text{ext}}\left(\sqrt{\alpha_{\text{ext}}\beta}\frac{\boldsymbol{z}}{\lambda_T}\right), \tag{1.102}$$

where α_{ext} is the energy scale and possible dimensionless parameters $\boldsymbol{\lambda}_{\text{ext}}$ have been suppressed.

Equation (1.101) implies very generally that in the short-time approximation the functions $s_n^{(k)}$ in Eq. (1.32) factorize into λ_T^{-kD} and a function of $s = \alpha\beta$ for $k > 0$. For

$k = 0$, homogeneous potentials allow for further direct analysis: If the external potential is homogeneous of degree η, i.e., $v_{\text{ext}}(\lambda x) = \lambda^\eta v_{\text{ext}}(x)$, the $\boldsymbol{z}$-integration yields

$$\frac{1}{\lambda_T^D}\int d^D z\, \mathrm{e}^{-n\beta\alpha_{\text{ext}} v_{\text{ext}}\left(\sqrt{\alpha_{\text{ext}}\beta}\frac{\boldsymbol{z}}{\lambda_T}\right)} = n^{\frac{D-d}{2}}\frac{V_{\text{eff}}}{\lambda_T^d}, \tag{1.103}$$

using the effective volume and dimension

$$V_{\text{eff}} = \left(\frac{2\pi\hbar}{m\alpha_{\text{ext}}}\right)^{\frac{D}{\eta}}\int d^D q\, \mathrm{e}^{v_{\text{ext}}(\boldsymbol{q})}, \qquad d = D\left(1+\frac{2}{\eta}\right). \tag{1.104}$$

This also includes the case without external potential by taking $\eta = \infty$. To make the factorization explicit let us define the dimensionless functions

$$\begin{aligned} b_{n,\pm}^{(k)}(\tilde{\boldsymbol{y}},\tilde{\boldsymbol{x}};s) &= \lambda_T^{kD}\, s_{n,\pm}^{(k)}(\boldsymbol{y},\boldsymbol{x},\beta,\alpha) \qquad \text{for } k>0, \\ b_{n,\pm}^{(0)}(s) &= \frac{\lambda_T^d}{V_{\text{eff}}} s_{n,\pm}^{(0)}(\beta,\alpha), \end{aligned} \tag{1.105}$$

that only depend on the rescaled coordinates $\tilde{\boldsymbol{x}} = \boldsymbol{x}/\lambda_T$ and $s = \alpha\beta$. Note that the functions $b_{n,\pm}^{(0)}$ depend on the *physical* dimension D intrinsically and the *effective* dimension d through the factor $n^{(D-d)/2}$ in (1.103), i.e., they are of the form

$$b_{n,\pm}^{(0)}(s) = n^{\frac{D-d}{2}} b_{n,\pm}^{(0)}(s)\Big|_{v_{\text{ext}}=0}. \tag{1.106}$$

1.3.2. The smooth density of states/microcanonical ensemble

As has been mentioned in the previous section, the discrete spectra of finite quantum systems are approximated by smooth functions in the short-time approximation. To be precise, the density of states (DOS) of the many-body quantum system, that is defined as

$$\rho^{(N)}(E) = \sum_{k=0}^{\infty}\delta\left(E - E_k^{(N)}\right) \tag{1.107}$$

with the discrete N-particle energies $E_k^{(N)}$, is replaced by a smooth function $\bar{\rho}^{(N)}(E)$. Moreover, due to the scaling properties of the short-time approximation, it has a very specific dependence on the energy-like interaction parameter α. By collecting all contributions that have the same number of irreducible clusters one can write the full partition function as a polynomial in the effective volume in units of the thermal wave length as [61]

$$Z_{\pm}^{(N,d)}(\beta) = \sum_{l=1}^{N}\left[z_{l,\pm}^{(N,d)} + \Delta z_{l,\pm}^{(N,d)}(\beta\alpha)\right]\left(\frac{V_{\text{eff}}}{\lambda_T^d}\right)^l, \tag{1.108}$$

where, following the notation in [61], the noninteracting clusters have been split off and the dependence on the (effective) dimension has been made explicit. The coefficients

in (1.108) can be read off from Eq. (1.24) as

$$\left[z_{l,\pm}^{(N,d)} + \Delta z_{l,\pm}^{(N,d)}(s)\right] = \frac{1}{l!} \sum_{\substack{n_1,\ldots,n_l \\ \sum_{i=1}^{l} n_i = N}} \prod_{i=1}^{l} \frac{b_{n_i,\pm}^{(0)}(s)}{n_i}, \tag{1.109}$$

where the dimensionless cluster sums defined in (1.105) have been used. For the noninteracting case, where $b_{n,\pm}^{(0)} = n^{-d/2}$, this was first reported in [89], where also recursion relations for a fast calculation are provided.

By using the general relation between the canonical partition function and the density of states via the (both-sided) Laplace transformation

$$Z(\beta) = \mathcal{L}_E[\rho(E)](\beta) = \int dE\, \mathrm{e}^{-\beta E} \rho(E), \tag{1.110}$$

one can readily show that the integrated DOS, or level counting function

$$\mathcal{N}(E) = \int_{-\infty}^{E} dE'\, \rho(E') \tag{1.111}$$

is given by [60]

$$\bar{\mathcal{N}}^{(N,d)}(E) = \sum_{l=1}^{N} \left[\frac{z_{l,\pm}^{(N,d)} \theta(E)}{\Gamma(\frac{ld}{2}+1)} + g_{l,\pm}^{(N,d)}(E/\alpha) \right] (\rho_0^{\mathrm{eff}} E)^{\frac{ld}{2}}, \tag{1.112}$$

where

$$g_{l,\pm}^{(N,d)}(\epsilon) = \epsilon^{-\frac{ld}{2}} \mathcal{L}_s^{-1} \left[\Delta z_{l,\pm}^{(N,d)}(s) s^{-\frac{ld}{2}-1} \right](\epsilon) \tag{1.113}$$

and

$$\rho_0^{\mathrm{eff}} = \frac{m V_{\mathrm{eff}}^{\frac{2}{d}}}{2\pi\hbar^2}. \tag{1.114}$$

Again, the interaction parameter α appears in a very specific way due to the assumptions of the short-time approximation, i.e., the polynomial form of the smooth density of states is not altered by the interaction, that only enters the coefficients (if E and E/α are considered as independent variables).

The smooth DOS is, of course, an important quantity by itself, as it contains a lot of information about the actual (discrete) spectrum. It has, however, also a direct application as an ingredient for the microcanonical ensemble. The microcanonical partition function $M(E)$ counts the number of states in a small energy interval Δ [62],

$$M(E) = \mathcal{N}(E+\Delta) - \mathcal{N}(E). \tag{1.115}$$

The nature of the interval Δ is thereby such that the partition function $M(E)$ should be insensitive to small variations of the energy while its value should be sufficiently small to allow one to consider the system as having a fixed energy. It thus plays the role of

smoothing the level distribution, so that, if we use the smooth counting function, one can write $M(E)$ as

$$M(E) = \bar{\rho}(E)\Delta, \tag{1.116}$$

such that it is actually *smooth* in the energy. This leads to the definition of the entropy as

$$S(E) = k_B \log \bar{\rho}(E)\Delta \tag{1.117}$$

relevant for the thermodynamic properties of the system.

1.3.3. The QCE(n)—general results

As has been seen up to this point, the short-time approximation, applied to the dynamics of individual clusters, allows one to separate the effects from external potentials and confinement from the interaction contributions, such that the irreducible diagrams have to be calculated only once and can then be used in different systems, giving rise to effective dimension and volume, or boundary corrections. In most cases, however, only a small portion of diagrams can be calculated exactly, while interaction contributions of the orders $n > 2$ require solving the n-body problem, which can only be achieved exactly for quantum integrable systems. In contrast, the two-body problem can be treated exactly in most cases, e.g., for any potential in three dimensions with rotational symmetry the problem can be reduced to solving one-dimensional Schrödinger equations, that are very well understood. It has been shown by Beth and Uhlenbeck already in 1936 that the full trace of the simplest diagram containing the interaction contribution of order two can be expressed only in terms of the scattering phases of the relative motion [67]. Different attempts have been made to generalize this formula [77, 90], but the problem of the practically unsolvable n-body problems persists.

However, the Ursell operator $U^{(2)}$ or the interaction contributions $\Delta K^{(2)}$ contain more information than the scattering phases and can be used in larger diagrams that link different particles by exchange cycles. Thus, if one treats the problems of interaction and indistinguishability separately by fully accounting for the latter while only allowing for interaction contributions of the order two, one is not restricted to small cluster sizes as, e.g., in virial expansions. The simplest way to achieve this goal is to keep only the terms in the expansion into Ursell operators (1.11) for N particles that are a product of at least $N - n$ Ursell operators. This approximation has been introduced in [61] as the QCE of order n or QCE(n), such that $n = 0$ is the noninteracting system, $n = 1$ involves (single) two-particle collisions, while the QCE(2) would include the three-particle collisions as well as two interacting pairs. In short-time approximation for *distinguishable* particles, the QCE(n) is then equivalent to a truncation of the canonical partition function and the smooth density of states as a polynomial of the effective volume V_{eff}, keeping only the terms that are $\mathcal{O}(V_{\text{eff}}^{N-n})$.

For indistinguishable particles, however, the clustering mechanism due to symmetrization (1.15) can be fully accounted for, leading to all sizes of clusters (up to the particle number N). One should thus not think of the QCE(n) in terms of a brute-force high

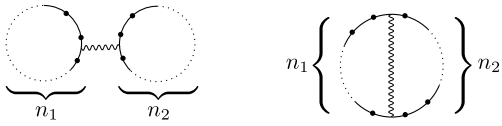

Figure 1.5: Inter-cycle (left) and intra-cycle (right) diagrams relevant for the QCE(1). In the inter-cycle diagrams, two cycle diagrams with n_1, respective n_2 particles are linked by the interaction of two of the particles. The intra-cycle diagram is a cycle diagram of $n = n_1 + n_2$ particles. The interaction between two of the particles divides the diagram into n_1, respective n_2 particles on each side of the interaction line.

temperature expansion but rather a way to systematically correct the polynomial coefficients of the smooth many-body density of states in the presence of interactions. When compared to a perturbative approach in a small coupling γ, the QCE(n) predictions will give the same[4] result for the first coefficients up to γ^n. But it also gives the *exact* result (within the scope of short-time approximation) for arbitrary interactions for the first n terms in an expansion in the parameter $\lambda_T^d/V_{\text{eff}}$ in the partition function, corresponding to the high temperature regime. Thus, the QCE(n) covers a much bigger part of the parameter space and can be thought of as interpolating between the different regimes.

The QCE(1)

The diagrams in the first order QCE contain at most one interaction contribution $\Delta K^{(2)}$, such that the irreducible diagrams are either noninteracting cycle diagrams or the interaction links two particles within a cycle (intra-cycle) or particles in two different cycles (inter-cycle) via $\Delta K^{(2)}$, as depicted in Fig. 1.5.

The calculation of the interacting diagrams can, of course, only be fully achieved if the interaction contribution $\Delta K^{(2)}$ is known. However, a great part of the calculations can be done for general interaction potentials without further specification. Let us first consider the case of interaction between different species of indistinguishable particles with masses m_1 and m_2. As the two species are distinguishable, the only irreducible diagrams within QCE(1) are then inter-cycle diagrams with n_1, respective n_2 particles of each species, see Fig. 1.5. The value of the diagram is given by

$$A^{\text{inter}}_{n_1,n_2}(\beta,\alpha) = \int d^{n_1 D}x\, d^{n_2 D}y \prod_{i=1}^{n_1-1} \Delta K^{(1)}_{m_1}(\boldsymbol{x}_{i+1},\boldsymbol{x}_i;\beta) \prod_{j=1}^{n_2-1} \Delta K^{(1)}_{m_2}(\boldsymbol{y}_{i+1},\boldsymbol{y}_i;\beta) \times \Delta K^{(2)}_{m_1,m_2}((\boldsymbol{x}_1,\boldsymbol{y}_1),(\boldsymbol{x}_{n_1},\boldsymbol{y}_{n_2});\beta,\alpha), \tag{1.118}$$

where $\Delta K^{(1)}_{m_i} = K^{(1)}_{m_i}$ is just the single-particle (imaginary time) propagator for species i with mass m_i. The explicit dependence of $A^{\text{inter}}_{n_1,n_2}$ on the masses m_i has been suppressed to ease notation. Making use of the convolution property (1.10) of $K^{(1)}_m$, all but four

[4]This can be seen, e.g., from expanding the Ursell operators as a path integral.

particles can be traced exactly, leading to

$$A^{\text{inter}}_{n_1,n_2}(\beta,\alpha) = \int d^{2D}x\, d^{2D}y\, K^{(1)}_{m_1}(\boldsymbol{x}_0,\boldsymbol{x}_1;(n_1-1)\beta) K^{(1)}_{m_2}(\boldsymbol{y}_0,\boldsymbol{y}_1;(n_2-1)\beta) \times \Delta K^{(2)}_{m_1,m_2}((\boldsymbol{x}_1,\boldsymbol{y}_1),(\boldsymbol{x}_0,\boldsymbol{y}_0);\beta,\alpha) \tag{1.119}$$

where the coordinates have been relabeled to ease notation. In short-time approximation, we can replace the propagators by their free-space equivalents (excluding external potentials for now). Then, the interaction contribution $\Delta K^{(2)}$ can be decomposed into the free motion of the center of mass and the relative motion as

$$\Delta K^{(2)}_{m_1,m_2}((\boldsymbol{x}_1,\boldsymbol{y}_1),(\boldsymbol{x}_0,\boldsymbol{y}_0);\beta,\alpha) = K^{(1)}_M(\boldsymbol{R}_1,\boldsymbol{R}_0;\beta)\, \delta K^{(1)}_\mu(\boldsymbol{r}_1,\boldsymbol{r}_0;\beta,\alpha), \tag{1.120}$$

where $\delta K^{(1)}_\mu$ is the propagator of a particle with reduced mass $\mu = m_1 m_2/(m_1+m_2)$ moving in the interaction potential, with the free propagator $K^{(1)}_\mu$ subtracted, $M = m_1 + m_2$ is the total mass of the two involved particles and

$$\boldsymbol{R}_i = \frac{m_1\boldsymbol{x}_i + m_2\boldsymbol{y}_i}{m_1+m_2}, \qquad \boldsymbol{r}_i = \boldsymbol{x}_i - \boldsymbol{y}_i \tag{1.121}$$

are center-of-mass and relative coordinates. Thus, we can write the inter-cycle diagram as

$$A^{\text{inter}}_{n_1,n_2}(\beta,\alpha) = \int d^D r_1\, d^D r_0\, \bar{K}^{(n_1,n_2)}_{m_1,m_2}(\boldsymbol{r}_1,\boldsymbol{r}_0;\beta) \times \delta K^{(1)}_\mu(\boldsymbol{r}_1,\boldsymbol{r}_0;\beta,\alpha) \tag{1.122}$$

with $\bar{K}^{(n_1,n_2)}_{m_1,m_2}$ given by

$$\bar{K}^{(n_1,n_2)}_{m_1,m_2}(\boldsymbol{r}_1,\boldsymbol{r}_0;\beta) = \int d^D R_1\, d^D R_2\, K^{(1)}_M(\boldsymbol{R}_1,\boldsymbol{R}_0;\beta) \times K^{(1)}_{m_1}(\boldsymbol{x}_0,\boldsymbol{x}_1;(n_1-1)\beta) K^{(1)}_{m_2}(\boldsymbol{y}_0,\boldsymbol{y}_1;(n_2-1)\beta), \tag{1.123}$$

with the $\boldsymbol{x}_i$ and $\boldsymbol{y}_i$ depending on the $\boldsymbol{R}_i$ and $\boldsymbol{r}_i$ for $i = 0, 1$ according to Eq. (1.121). As the free propagators in imaginary time are only normal distributions of the distance, $\bar{K}^{(n_1,n_2)}_{m_1,m_2}$ can be explicitly calculated as a Gaussian integral yielding

$$\bar{K}^{(n_1,n_2)}_{m_1,m_2}(\boldsymbol{r}_1,\boldsymbol{r}_0;\beta) = \frac{V}{[\lambda_T(m_{\text{eff}})]^D} K^{(1)}_{\bar{m}}(\boldsymbol{r}_1,\boldsymbol{r}_0;\beta), \tag{1.124}$$

where the thermal wavelength $\lambda_T = \lambda_T(m)$, Eq. (1.93), is written as a function of a mass m and

$$m_{\text{eff}} = \frac{(m_1+m_2)^2}{n_1 m_1 + n_2 m_2}, \qquad \bar{m} = \frac{m_1 m_2}{m_1+m_2}\left(\frac{m_1+m_2}{n_1 m_1 + n_2 m_2} n_1 n_2 - 1\right)^{-1}. \tag{1.125}$$

Here, everything is written in terms of the initial and final relative coordinates of the two interacting particles. One can get an even simpler formula if one uses the general scaling (1.99) of the propagator,

$$\delta K^{(1)}_\mu(\boldsymbol{r}_1,\boldsymbol{r}_0;\beta,\alpha) = \frac{1}{[\lambda_T(\mu)]^D} \delta k^{(1)}(\tilde{\boldsymbol{r}}_1,\tilde{\boldsymbol{r}}_0;\alpha\beta), \tag{1.126}$$

where $\boldsymbol{r}_i = \tilde{\boldsymbol{r}}_i \lambda_T(\mu)$, finally yielding

$$A^{\text{inter}}_{n_1,n_2}(\beta,\alpha) = \frac{V}{[\lambda_T(m_{\text{eff}})]^D}\, a^{\text{inter}}_\nu(\alpha\beta), \tag{1.127}$$

where the dimensionless function a_ν is given by

$$a^{\text{inter}}_\nu(s) = \int d^D x\, d^D y\, \nu^{-D} \mathrm{e}^{-\pi\left(\frac{\boldsymbol{x}-\boldsymbol{y}}{\nu}\right)^2} \delta k^{(1)}(\boldsymbol{x},\boldsymbol{y};s), \tag{1.128}$$

i.e., it is a normal distributed average of $\delta k^{(1)}$ over the distance characterized by the single parameter

$$\nu = \sqrt{\frac{m_1+m_2}{n_1 m_1 + n_2 m_2} n_1 n_2 - 1}. \tag{1.129}$$

Note that the case $n_1 = n_2 = 1$ is included in (1.128) as the limit $\nu \to 0$, where the normal distribution can be replaced by a Dirac delta distribution. In the case of external potentials, the species could, in principle, be subject to different external potentials, e.g., atoms in a magnetic trap will feel very different forces depending on the magnetic quantum numbers. Thus, the arguments that lead to an effective dimension and volume can only be applied, if all the external potentials have the same degree of homogeneity, then leading to the same definition of the effective dimension. The effective volume, however, is then ambiguous and can be constructed from any of the external potentials or combinations of them. The factor $n^{\frac{D-d}{2}}$ in (1.103) then is replaced by a more complicated function of the n_i that also depends on the choice of the effective volume.

For the full characterization of the diagrams, one still needs to find the internal multiplicity and the sign factors of the diagram. One has to distinguish the cases of having two different species, with the symmetry given by $\sigma_i = \pm 1$ or a single species. As there are two incompatible definitions (1.32) and (1.64) of the rescaled cluster sums depending on whether other species are involved or not, the multiplicities are given here in their unscaled form. The prefactors of the diagrams are given as

$$p^{\text{inter}}_{n_1,n_2} = \begin{cases} \sigma_1^{n_1-1}\sigma_2^{n_2-1} n_1! n_2! & \text{two species,} \\ \sigma^{n_1+n_2} \frac{(n_1+n_2)!}{1+\delta_{n_1,n_2}} & \text{one species.} \end{cases} \tag{1.130}$$

Let us now turn to the intra-cycle diagram that appears only in the case of a single species. However, as the calculation steps are very similar as in the case of the inter-cycle diagrams, it is convenient to use these results and setting $m_1 = m_2$ in the end. The intra-cycle diagram is simply obtained by interchanging $\boldsymbol{x}_1$ and $\boldsymbol{y}_1$ in $\Delta K^{(2)}$ appearing in Eq. (1.118). The only effect of this in the further calculations is that $\boldsymbol{r}_1$ has to be replaced by $-\boldsymbol{r}_1$ in the interaction part $\delta K^{(1)}_\mu$ of the propagator of the relative motion. So, the intra-cycle diagram is given by

$$A^{\text{intra}}_{n_1,n_2}(\beta,\alpha) = \frac{V}{[\lambda_T(m_{\text{eff}})]^D}\, a^{\text{intra}}_\nu(\alpha\beta) \tag{1.131}$$

with

$$a_\nu^{\text{intra}}(s) = \int d^D x\, d^D y\, \nu^{-D} \mathrm{e}^{-\pi\left(\frac{\boldsymbol{x}+\boldsymbol{y}}{\nu}\right)^2} \delta k^{(1)}(\boldsymbol{x},\boldsymbol{y};s), \tag{1.132}$$

where the minus sign has been included in the normal distribution instead of the interaction part and the effective mass m_{eff}, Eq. (1.125), and the parameter ν, Eq. (1.129), have to be evaluated at $m_1 = m_2$. The prefactor of the diagram is given as

$$p_{n_1,n_2}^{\text{intra}} = \sigma^{n_1+n_2-1} \frac{(n_1+n_2)!}{1+\delta_{n_1,n_2}}. \tag{1.133}$$

Finally, for the actual computation of the partition function one has to sum up all the diagrams with the same number of irreducible diagrams. For indistinguishable particles this can be done using the relation (c.f., [61])

$$\Delta_1 z_{l,\pm}^{(N,d)}(s) = 2^D \sum_{n=2}^{N-l+1} (\pm 1)^n n^{-\frac{d}{2}} z_{l-1,\pm}^{(N-n,d)} \sum_{n_1=1}^{n-1} \frac{a_{\nu(n_1,n-n_1)}^{\text{inter}}(s) \pm a_{\nu(n_1,n-n_1)}^{\text{intra}}(s)}{2}, \tag{1.134}$$

where the index on Δ_1 stands for the QCE(1) and $z_{0,\pm}^{(N-n,d)} = \delta_{N,n}$ has to be defined. Note that the effective dimension d has been used and the physical dimension enters only in the factor 2^D that could be absorbed into the definition of the inter- and intra-cycle diagrams. The factor $n^{-d/2}2^D$ is the product of the scaling factor $n^{(D-d)/2}$ for homogeneous external potentials, Eq. (1.106), and the term $(4/n)^{D/2}$, that stems from the proportionality factor between the mass m_{eff}, Eq. (1.125), and the particle mass m for $m_1 = m_2 = m$. Equation (1.134) is thus valid in short-time approximation for homogeneous external potentials encoded in the effective dimension d and by using the inter- and intra-cycle diagrams that are calculated in free space.

1.3.4. The thermodynamic limit and ensemble equivalence

As was discussed in section 1.2.3, the dependence on the particle number N in the cluster expansion of the canonical description is of purely combinatorial nature. This is inherited by the microcanonical description presented in section 1.3.2, leading to a nontrivial dependence of the functions $z_{l,\pm}^{(N,d)}$ and $g_{l,\pm}^{(N,d)}(\epsilon)$ on the particle number N. For small particle numbers, it is not very hard to figure out this dependence explicitly. However, the knowledge of the large-N scaling of the individual terms in the cluster expansion for the DOS gives an important insight on the relative importance of their contributions. In order to find this scaling, one best starts with the grand canonical description introduced in 1.2.3, that does not suffer from any combinatorial difficulties. However, as was mentioned before, the fugacity expansion of the grand potential (1.55) might not have a positive convergence radius in certain cases, even though it can then still serve as a generating function for the canonical description that should converge for any finite particle number.

In the following it is assumed that the grand canonical description is well defined in the sense that the grand potential is an analytic function of its arguments. This should

also be true for large volumes, i.e., phase transitions and their immediate vicinities are excluded here. With these assumptions, there is a well defined thermodynamic limit, where the different ensembles become equivalent. The latter can be rigorously shown for noninteracting systems by asymptotic analysis of the generating function relations between the ensembles. However, this can be done formally also in the case of interacting systems, revealing the scaling of the various parameters that describe the system in the thermodynamic limit, as is demonstrated in the following.

In short-time approximation, each irreducible cluster sum $s_m^{(0)}$ in the grand potential (1.55) factorizes as

$$s_m^{(0)}(\beta,\alpha) = \frac{V_{\text{eff}}}{\lambda_T^d} b_m^{(0)}(\alpha\beta), \tag{1.135}$$

according to the general scaling (1.105), such that the grand potential is given by

$$\Omega(\beta,\mu,\alpha) = -p(\beta,\mu,\alpha)V_{\text{eff}}, \tag{1.136}$$

$$p(\beta,\mu,\alpha) = \frac{1}{\beta\lambda_T^d}\sum_{m=1}^{\infty}\frac{z^m}{m} b_m^{(0)}(\alpha\beta), \tag{1.137}$$

i.e., it factorizes into the (effective) volume and the pressure p. Here, all the parameters like the effective dimension d and any dimensionless parameters $\boldsymbol{\lambda}$ that are not essential for the following have been dropped for a clearer presentation. The canonical partition function can then be obtained from the grand canonical partition function by applying Eq. (1.58), which can be rewritten as

$$Z^{(N)}(\beta,\alpha) = \frac{1}{2\pi i}\oint dz\, \frac{Z^G(\beta,\mu,\alpha)}{z^{N+1}} \tag{1.138}$$

using the Cauchy integral formula for derivatives with a contour around the origin. The level counting function $\mathcal{N}^{(N)}(E)$ is obtained via the inverse Laplace transformation that can be performed with the help of the (Bromwich) inversion integral [91]

$$\mathcal{N}^{(N)}(E,\alpha) = \frac{1}{2\pi i}\int_{\gamma-i\infty}^{\gamma+i\infty} d\beta\, \mathrm{e}^{\beta E}\frac{Z^{(N)}(\beta,\alpha)}{\beta}, \tag{1.139}$$

where γ is chosen such that it is greater than the real values of all poles of $Z^{(N)}(\beta)/\beta$, i.e., $\gamma > 0$. The divisor β in (1.139) comes from integrating the DOS to obtain the level counting function. Combining Eqs. (1.138) and (1.139) one gets

$$\begin{aligned}\mathcal{N}^{(N)}(E,\alpha) &= \frac{1}{(2\pi i)^2}\int_{\gamma-i\infty}^{\gamma+i\infty} d\beta \oint dz\, \mathrm{e}^{\beta E}\frac{Z^G(\beta,\mu,\alpha)}{\beta z^{N+1}} \\ &= \frac{1}{(2\pi i)^2}\int_{\gamma-i\infty}^{\gamma+i\infty} d\beta \oint dz\, \frac{\mathrm{e}^{\beta E-\beta\Omega(\beta,\mu,\alpha)-N\log z}}{\beta z}.\end{aligned} \tag{1.140}$$

Here, $\Omega(\beta,\mu,\alpha) = \Omega(\beta,\log(z)/\beta,\alpha)$ should be considered as a function of the fugacity z instead of the chemical potential μ. The logarithm of z is understood as the analytic

continuation along the contour around the origin, i.e., it changes by 2π for a full cycle. The exponent in (1.140) can be rewritten as

$$\begin{aligned} f(E,\beta,z,\alpha,N) &= \beta E - \beta\Omega(\beta,\mu,\alpha) - N\log z \\ &= \beta E - \frac{V_{\text{eff}}}{\lambda_T^d}\underbrace{\sum_{m=1}^{\infty}\frac{z^m}{m}b_m^{(0)}(\alpha\beta)}_{w(z,\alpha\beta)} - N\log z \\ &= N\left[\beta\frac{E}{N} - \frac{1}{N}\left(\frac{\rho_0^{\text{eff}}}{\beta}\right)^{\frac{d}{2}} w(z,\alpha\beta) - \log z\right] \\ &= N\left[\tau E_{\text{sc}} - \tau^{-\frac{d}{2}} w(z,\alpha_{\text{sc}}\tau) - \log z\right] \\ &\equiv N\tilde{f}(E_{\text{sc}},\tau,z,\alpha_{\text{sc}}), \end{aligned} \tag{1.141}$$

such that the function $\tilde{f}$ does not depend on N explicitly anymore. The scaled variables are defined as

$$E_{\text{sc}} = \frac{E}{N\varepsilon}, \qquad \alpha_{\text{sc}} = \frac{\alpha}{\varepsilon}, \qquad \tau = \beta\varepsilon, \tag{1.142}$$

making use of the intensive unit of energy

$$\varepsilon = \frac{N^{\frac{2}{d}}}{\rho_0^{\text{eff}}} = \frac{2\pi\hbar^2}{m}\left(\frac{N}{V_{\text{eff}}}\right)^{\frac{2}{d}}. \tag{1.143}$$

Note that τ can also be written as

$$\tau = \left(\frac{N\lambda_T^d}{V_{\text{eff}}}\right)^{\frac{2}{d}}, \tag{1.144}$$

i.e., it is essentially the ratio between thermal wavelength and mean inter-particle separation. With the rescaled variables one can rewrite Eq. (1.140) as

$$\mathcal{N}^{(N)}(E,\alpha) = \frac{1}{(2\pi i)^2}\int_{\gamma'-i\infty}^{\gamma'+i\infty} d\tau \oint dz\, \frac{\mathrm{e}^{N\tilde{f}(E_{\text{sc}},\tau,z,\alpha_{\text{sc}})}}{\tau z}. \tag{1.145}$$

The large-N scaling can now be obtained by applying two subsequent saddle-point approximations to Eq. (1.145), the first giving an asymptotic relation between grand canonical and canonical ensemble and the second relating the latter to the microcanonical ensemble or level counting function. The validity of the saddle point approximations is, of course, not guaranteed for all temperatures, but it should hold for large enough temperatures, where condensation effects or superfluidity do not play a dominant role[5]. Instead of performing the approximations stepwise, it is more straightforward to apply both steps simultaneously. For noninteracting fermions, this leads to the famous Bethe

[5] But even in the BEC regime the combined saddle-point approximations give the correct result [60, supplemental material].

estimate [86] for the many-body density of states[6], that is valid almost down to the ground state, where the latter emerges naturally as the point, where the approximation breaks down.

The saddle point equations can be written in the form

$$E_{\mathrm{sc}} = \frac{\partial}{\partial \tau} \tau^{-\frac{d}{2}} w(z, \alpha_{\mathrm{sc}} \tau), \tag{1.146}$$

$$\tau^{\frac{d}{2}} = -z \frac{\partial}{\partial z} w(z, \alpha_{\mathrm{sc}} \tau), \tag{1.147}$$

where the second equation is equivalent to

$$\langle \hat{N} \rangle = -\frac{\partial \Omega}{\partial \mu} = N \tag{1.148}$$

known from the equivalence of grand canonical and canonical ensemble in the thermodynamic limit. The solution(s) of Eqs. (1.146) and (1.147) are functions

$$\tau_{\mathrm{sp}} \equiv \tau_{\mathrm{sp}}(E_{\mathrm{sc}}, \alpha_{\mathrm{sc}}), \tag{1.149}$$

$$z_{\mathrm{sp}} \equiv z_{\mathrm{sp}}(E_{\mathrm{sc}}, \alpha_{\mathrm{sc}}), \tag{1.150}$$

i.e., they can only depend on the scaled variables E_{sc} and α_{sc} (and the variables that have been suppressed in the notation). The same holds true for $\tilde{f}$ and the determinant of its Hessian evaluated at the saddle,

$$\tilde{f}_{\mathrm{sp}}(E_{\mathrm{sc}}, \alpha_{\mathrm{sc}}) = \tilde{f}(E_{\mathrm{sc}}, \tau_{\mathrm{sp}}(E_{\mathrm{sc}}, \alpha_{\mathrm{sc}}), z_{\mathrm{sp}}(E_{\mathrm{sc}}, \alpha_{\mathrm{sc}}), \alpha_{\mathrm{sc}}), \tag{1.151}$$

$$h_{\mathrm{sp}}(E_{\mathrm{sc}}, \alpha_{\mathrm{sc}}) = \left| \frac{\partial^2 \tilde{f}}{\partial a_i a_j} \right|_{\mathrm{sp}}, \qquad (a_1, a_2) = (\tau, z). \tag{1.152}$$

Thus, assuming a single dominant saddle point, the level counting function $\bar{\mathcal{N}}^{(N)}$ in saddle point approximation has the form

$$\bar{\mathcal{N}}^{(N)}(E, \alpha) = \frac{\exp\left(N \tilde{f}_{\mathrm{sp}}(E_{\mathrm{sc}}, \alpha_{\mathrm{sc}})\right)}{N g(E_{\mathrm{sc}}, \alpha_{\mathrm{sc}})}, \tag{1.153}$$

where the function $g(E_{\mathrm{sc}}, \alpha_{\mathrm{sc}})$ is defined as

$$g(E_{\mathrm{sc}}, \alpha_{\mathrm{sc}}) = 2\pi \tau_{\mathrm{sp}}(E_{\mathrm{sc}}, \alpha_{\mathrm{sc}}) z_{\mathrm{sp}}(E_{\mathrm{sc}}, \alpha_{\mathrm{sc}}) \left[h_{\mathrm{sp}}(E_{\mathrm{sc}}, \alpha_{\mathrm{sc}})\right]^{\frac{1}{2}}. \tag{1.154}$$

This means that, if the scaled variables E_{sc} and α_{sc} are used in the level counting function, the remaining dependence on the particle number is very simple. Moreover, keeping the values of the scaled variables fixed such that the function $h_{\mathrm{sp}}(E_{\mathrm{sc}}, \alpha_{\mathrm{sc}})$ is a (positive) constant, one finds

$$\tilde{f}(E_{\mathrm{sc}}, \alpha_{\mathrm{sc}}) = \frac{1}{N} \log\left[g(E_{\mathrm{sc}}, \alpha_{\mathrm{sc}}) \times N \bar{\mathcal{N}}^{(N)}\right] \tag{1.155}$$

$$= \frac{1}{N} \log\left[N \bar{\mathcal{N}}^{(N)}\right] + \mathcal{O}(N^{-1}), \tag{1.156}$$

[6] It is also referred to as the stretched exponential form of the many-body DOS.

or, in other words, $\log[N\mathcal{N}^{(N)}]$ is an extensive quantity in the thermodynamic limit, provided that the scaled variables can be considered as being intensive[7]. This is closely related to the extensivity of the microcanonical entropy defined by

$$S(E,\alpha) = \log\left[\bar{\rho}^{(N)}(E,\alpha)\Delta\right] \tag{1.157}$$

with an auxiliary small energy window Δ, c.f., Eq. (1.117). It is straightforward to see that the relation between the mean DOS $\bar{\rho}^{(N)}$ and the level counting function $\mathcal{N}^{(N)}$ in saddle point approximation is given by

$$\bar{\rho}^{(N)}(E,\alpha) = \frac{\tau_{\mathrm{sp}}(E_{\mathrm{sc}},\alpha_{\mathrm{sc}})}{\varepsilon}\bar{\mathcal{N}}^{(N)}(E,\alpha), \tag{1.158}$$

such that they are related by a $\mathcal{O}(N^0)$ factor that is unimportant in the thermodynamic limit. However, the asymptotic expression in (1.156) includes the $\mathcal{O}(\log(N)/N)$ correction that has to be neglected to obtain an extensive microcanonical entropy [62].

1.3.5. The shifting method from a different viewpoint

Using only the QCE(n) diagrams up to a certain order $n \gtrsim 1$ gives good results in the high-temperature regime. However, the approximation is poor in the low-energy sector and, strictly speaking, can only be fully trusted to nth order in the coupling α, where it is assumed that $\alpha \to 0$ corresponds to the noninteracting limit for the rest of this subsection. As the N body problem can usually not be solved exactly for $N > 2$, it is desirable to use the information contained in the QCE(1) to approximate higher orders. It has proven fruitful [60] to do this on the basis of energy shifts in the density of states, instead of using the thermodynamic functions themselves. As the presentation of this shifting method in [60] is quite technical, the following presents a reformulation of the technique that tries to be clear about the individual steps of the derivation.

The general idea is to write the level counting function of the fully interacting system as a shifted version of the noninteracting result, i.e.,

$$\bar{\mathcal{N}}_{\alpha}^{(N)}(E) = \bar{\mathcal{N}}_{0}^{(N)}\left(E - \Delta^{(N)}(E,\alpha)\right) = \bar{\mathcal{N}}_{0}^{(N)}(E_0). \tag{1.159}$$

Here, the explicit dependence on the (effective) dimension d and the effective volume V_{eff} is omitted. Using Eq. (1.159), the problem can be reformulated such that all the information about interactions is encoded in the shift $\Delta^{(N)}(E,\alpha)$, and one has to find approximations for the latter. Figure 1.6 illustrates the quantities that appear in Eq. (1.159). One should note that, in contrast to mean-field approaches, it is the many-particle energy that is shifted, and not the single-particle energy.

If one is able to invert the relation between $\bar{\mathcal{N}}^{(N)}$ and the energy E, i.e., finding $E(\mathcal{N},N)$, the shift can be explicitly calculated as a function of the energy excitation index $\mathcal{N} = \bar{\mathcal{N}}_{0}^{(N)}(E_0) = \bar{\mathcal{N}}_{\alpha}^{(N)}(E)$ as

$$\Delta(\mathcal{N},\alpha,N,V_{\mathrm{eff}}) = E_{\alpha}(\mathcal{N},N,V_{\mathrm{eff}}) - E_0(\mathcal{N},N,V_{\mathrm{eff}}) \tag{1.160}$$

[7] This means that the total energy E is extensive, which should be expected from the fact that the starting point was an extensive grand potential $\Omega = -pV$.

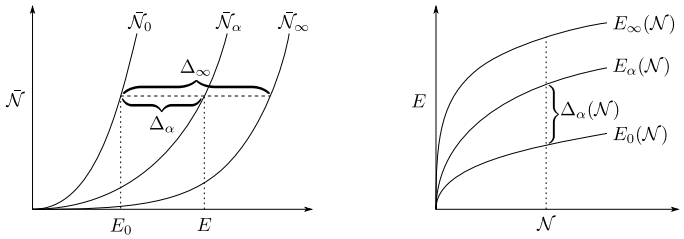

Figure 1.6: Sketch of the shifting method using $\Delta_\alpha = \Delta(\alpha)$ as a shorthand notation, omitting other arguments (see text). The value of the counting function $\bar{\mathcal{N}}_\alpha^{(N)}(E)$ can also be found from shifting the argument of the counting function without interaction, $\bar{\mathcal{N}}_0^{(N)}(E - \Delta_\alpha)$ (left). Alternatively one could think in terms of the inverted functions, all evaluated at the same "excitation index" $\mathcal{N}$ (right).

and can then be re-expressed in terms of the energies E or E_0 by using $\mathcal{N} = \bar{\mathcal{N}}_\alpha^{(N)}(E)$ or $\mathcal{N} = \bar{\mathcal{N}}_0^{(N)}(E_0)$, respectively. As the latter function is known exactly (within the scope of short-time approximation) for all energies one might hope to get better, or at least well-behaved results by approximating the shift (1.160), rather than individual coefficients in the general form of $\bar{\mathcal{N}}^{(N)}(E)$, Eq. (1.112). This is emphasized by the fact that, in the case of free fermions, the polynomial coefficients have to be balanced in a very detailed way to produce small oscillations in the smooth DOS and the level counting function for energies below the many-particle ground state, such that the result is very sensitive to errors or truncations in the coefficients [52].

Due to the general form (1.112) of $\bar{\mathcal{N}}^{(N)}(E)$ one can write the level counting function as

$$\bar{\mathcal{N}}^{(N,d)}(E, \alpha, V_{\text{eff}}) = \sum_{l=1}^{N} c_l^{(N,d)}\left(\frac{E}{\alpha}\right)(\rho_0^{\text{eff}} E)^{\frac{ld}{2}}, \tag{1.161}$$

where the dependencies on d and V_{eff} have been restored. The effective volume appears only in ρ_0^{eff}, Eq. (1.114), and the functions $c_l^{(N,d)}(\epsilon)$ depend only on the ratio $\epsilon = E/\alpha$ between the energy E and the coupling α. By treating ϵ and $\rho_0^{\text{eff}} E$ as independent variables, one can formally invert the relation (1.161) with respect to $\rho_0^{\text{eff}} E$ in the large-energy regime in terms of a series expansion. This approach can be justified by the fact that, in many situations, there exist two limits, e.g., $\alpha \to 0$ and $\alpha \to \infty$, where the coefficient functions become independent of the interaction parameter α while the polynomial form of $\bar{\mathcal{N}}^{(N)}(E)$ is preserved, such that in these limits, the inversion gives the right results, while finite couplings within the two limits will only renormalize the coefficients.

Before performing this formal inversion with respect to the volume-dependent energy scale $\rho_0^{\text{eff}} E$, it is useful to bring the level counting function into a form that makes the expected large-N scaling (1.156) explicit by using the scaled variables E_{sc} and α_{sc},

Eq. (1.142), to rewrite Eq. (1.161) as

$$y^{(N,d)}(E_{\rm sc},\epsilon) \equiv \left[\frac{\bar{\mathcal{N}}^{(N,d)}(E,\alpha)}{c_N^{(N,d)} N^{N(1+\frac{d}{2})}}\right]^{-\frac{1}{N}} = E_{\rm sc}^{-\frac{d}{2}} \left[1+\sum_{k=1}^{N-1} d_k^{(N,d)}(\epsilon)\left(E_{\rm sc}^{-\frac{d}{2}}\right)^k\right]^{-\frac{1}{N}}, \quad (1.162)$$

where the right hand side is written as a function of $E_{\rm sc}^{-d/2}$ and $\epsilon = NE_{\rm sc}/\alpha_{\rm sc}$, and

$$c_N^{(N,d)} = \frac{1}{N!\,\Gamma\left(\frac{Nd}{2}+1\right)} \quad (1.163)$$

is the leading coefficient in the cluster expansion of the smooth level counting function, Eqs. (1.112) and (1.161), that does not depend on the interaction. The new coefficients $d_k^{(N,d)}$ are given as

$$d_k^{(N,d)}(\epsilon) = \frac{c_{N-k}^{(N,d)}(\epsilon)}{c_N^{(N,d)}} N^{-k(1+\frac{d}{2})}. \quad (1.164)$$

It is easily verified (using Stirling's formula for the Gamma function) that $c_N^{(N,d)} N^{N(1+d/2)}$ scales like $N^{-1}a^N$ with an asymptotic constant a for large N (see below), such that the left hand side of Eq. (1.162) is constructed in a way that it is expected to have a nontrivial finite thermodynamic limit according to the asymptotic relation (1.156).

Now, formally inverting (1.162) shows that the scaled energy is of the form

$$E_{\rm sc} = E_{\rm sc}^{(N,d)}(y,\epsilon) = y^{-\frac{2}{d}}\left(1+\sum_{k=1}^{\infty} a_k^{(N,d)}(\epsilon)\, y^k\right), \quad (1.165)$$

where in the second step, the function has been expanded as a series in y to make the dependence on the interaction-dependent energy scale ϵ explicit. We have thus found a systematic way to calculate the energy shift Δ in terms of an expansion in the (intensive) quantity

$$y = A(N,d) \times [N\mathcal{N}]^{-\frac{1}{N}}, \quad (1.166)$$

that depends only on the excitation index $\mathcal{N}$ and the system parameters N and d in a very simple way. The explicit form of the coefficient function A is given by

$$A(N,d) = \left[\frac{\Gamma(N)\Gamma\left(\frac{Nd}{2}+1\right)}{N^{N(1+\frac{d}{2})}}\right]^{-\frac{1}{N}} \sim \left(\frac{d}{2}\right)^{-\frac{d}{2}} \mathrm{e}^{1+\frac{d}{2}} \left(2\pi^2 d\right)^{-\frac{1}{2N}}, \quad (1.167)$$

where the last relation holds for large particle numbers N. The scaled energy shift thus has the form

$$\Delta_{\rm sc}^{(N,d)}(y,\epsilon) = y^{-\frac{2}{d}} \sum_{k=1}^{\infty} \chi_k^{(N,d)}(\epsilon)\, y^k, \quad (1.168)$$

with the coefficients referred to as *partial* shifts defined by subtracting their noninteracting contribution:

$$\chi_k^{(N,d)}(\epsilon) = a_k^{(N,d)}(\epsilon) - a_k^{(N,d)}\Big|_{\alpha=0}. \quad (1.169)$$

Note that the definition of the partial shifts differs slightly from the original definitions in [60], where the first order partial shift is normalized such that it has values only between zero and one. The large-N scaling is, however, the same up to a constant factor.

The important step now is to realize that the equation (1.168) for the energy shift is actually implicit, as the shift appears also on the right hand side of the equation in the coupling dependent energy scale ϵ that only drops out in certain limits. To actually solve for the shift, the dependence on the energy through ϵ on the right hand side has to be eliminated such that the shift is represented as a function of the coupling α and y, i.e., the excitation index $\mathcal{N}$, only. Then, with the full knowledge of the functional dependence of $\mathcal{N} = \bar{\mathcal{N}}_0^{(N)}(E_0)$ on the energy of the noninteracting problem, the problem would be solved. Obviously, it is not that simple, and one simply cannot find such a solution. However, Eq. (1.168) can be used as the starting point for systematic approximations by truncating the series and then solving for the shifts self-consistently. In this context, the number of terms included in the expansion is referred to as the order of the approximation [60]. For example, the first order would only include $\chi_1^{(N,d)}(\epsilon)$, which is only given in terms of the solution of the two-particle problem.

As the partial shifts χ are naturally given in terms of the energy rather than the excitation index $\mathcal{N}$ one can avoid an inversion of the noninteracting level counting function by solving the equation for $E_0 = E - \Delta_\alpha$ (see Fig. 1.6) using $y = y(E_0)$, i.e., one has to solve the equation for the nth order shift,

$$\Delta_{\mathrm{sc}} = \left[y\left(E_{\mathrm{sc}}^{(0)}\right)\right]^{-\frac{2}{d}} \sum_{k=1}^{n} \chi_k\left(\frac{N}{\alpha_{\mathrm{sc}}}\left(E_{\mathrm{sc}}^{(0)} + \Delta_{\mathrm{sc}}\right)\right)\left[y\left(E_{\mathrm{sc}}^{(0)}\right)\right]^{k}, \tag{1.170}$$

where the index (N, d) has been omitted for better readability. This has been demonstrated to yield remarkably good results in the one-dimensional Bose gas, including the nonintegrable case of harmonic trapping [60]. There, the best agreement between the semiclassical theory and the numerical simulations has been found in the partial shifts themselves, that turned out to be remarkably rigid against the single-particle level fluctuations. The latter can have a very strong effect on the noninteracting level counting function in the low-energy regime, as a variation δ in the single-particle ground state leads to a shift of $N\delta$ in the N-particle counting function (but the effect scales as δ if the scaled energy E_{sc} is used).

The first partial shift is given in terms of the function $g_{N-1}^{(N,d)}(\epsilon)$, Eq. (1.113), as

$$\chi_1^{(N,d)}(\epsilon) = -\frac{2}{Nd}\frac{g_{N-1}^{(N,d)}(\epsilon)}{N^{1+\frac{d}{2}}c_N^{(N,d)}} = -\frac{\Gamma\left(\frac{Nd}{2}\right)N!}{N^{1+\frac{d}{2}}}\, g_{N-1}^{(N,d)}(\epsilon).$$

It can be shown to have a nontrivial scaling for large particle numbers [60], that is independent on N. This also holds true for the higher order partial shifts, but a rigorous proof to all orders is missing. There is, however, a good argument that this should hold by construction, as the starting point of the inversion, Eq. (1.162), expresses the intensive quantity $y^{(N,d)}$ by the intensive quantity E_{sc}, such that a series expansion of

the right hand side of the equation in terms of E_{sc} should yield intensive coefficients. The coefficients $a_k^{(N,d)}$ are then determined by the latter, and should thus be intensive themselves. A direct proof would thus take Eq. (1.162) as a starting point. This was, however, not possible yet in the scope of this thesis and could be part of a future project.

1.4. Application: Nonlocal correlations in the Lieb-Liniger gas

In this section, the methods introduced in sections 1.2 and 1.3 are applied to the one-dimensional Bose gas with repulsive short-range interactions, as described by the Lieb-Liniger model [19, 92], that, as it allows for an exact solution via the Bethe ansatz, can be used to systematically check the approximations. As the methods for obtaining the smooth part of the spectrum have been discussed in much detail in this model by [61], the focus is on the calculation of nonlocal pair correlations here, as defined in the following, together with a brief overview of the experimental relevance. The results of this section have already been published in [93] by the author. Although the coauthors have contributed to the final formulations used there (especially in the introductory part), the entire manuscript has been written by the author of this thesis and large parts are therefore taken over here.

1.4.1. Nonlocal correlations

The study of spatial correlations provides an intuitive and experimentally accessible window to the physical properties of interacting many-body quantum systems. The special role of low-order spatial correlation functions arises from the definitional property of multiparticle systems as having a large number of degrees of freedom. Up to the case of two or three degrees of freedom, the spatial structure of the wave function can be directly visualized and efficiently computed. When the number of degrees of freedom increases, the full description of quantum-mechanical states not only becomes highly unintuitive, but pretty soon explicit computations become a hopeless task. This is one of the reasons for the relevance of field-theoretical descriptions in terms of field operators that live in real space and provide more intuitive characterizations in terms of collective degrees of freedom such as particle density and correlation functions [8]. These theoretical descriptions have been used to successfully describe quantities accessible to measurements in noninteracting ultracold atom systems [25, 94–102].

For interacting systems state-of-the-art experiments [38, 103] have addressed so far mainly the local limit $g_2(\boldsymbol{r} \to 0)$ of the (normalized) pair correlation function[8]

$$g_2(\boldsymbol{r}) = \frac{\langle \hat{\Psi}^\dagger(0)\hat{\Psi}^\dagger(\boldsymbol{r})\hat{\Psi}(\boldsymbol{r})\hat{\Psi}(0)\rangle}{\langle \hat{\Psi}^\dagger(0)\hat{\Psi}(0)\rangle \langle \hat{\Psi}^\dagger(\boldsymbol{r})\hat{\Psi}(\boldsymbol{r})\rangle}, \tag{1.171}$$

here expressed in terms of the bosonic field operators $\hat{\Psi}$ and $\hat{\Psi}^\dagger$, while specific proposals for the measurement of truly nonlocal correlations with $\boldsymbol{r} \neq 0$ are now available [105,106].

Within the program of characterizing the spatial structure of many-body states, one-dimensional (1D) systems play a special role. One reason for this is the possibility of experimental realization [36, 37], where now controlled access to the collective behavior of a few dozens of constituents is possible [107]. Moreover, for this kind of systems, and depending on the type of interaction and other properties, the corresponding mathematical description may fall into the category of quantum integrable models and thus admits

[8] See also [104] for recent results on $g_3(0)$.

an explicit (but formal) solution in terms of a set of algebraic equations. A paradigmatic example of quantum integrability is the Lieb-Liniger model [19], a many-body Hamiltonian describing a set of N bosonic particles interacting through repulsive short-range forces, and confined to a region of finite length L. One of the remarkable consequences of quantum integrability is that the many-body eigenstates and eigenenergies of these systems are characterized by a complete set of quantum numbers labeling the rapidities of the states [19, 108]. The latter, although playing the role of quasimomenta, are, however, genuine many-body objects that do not have a direct interpretation in terms of quasiparticle excitations unless the particle number becomes infinite [92].

Although the theory of quantum integrable systems provides, in principle, results for any kind of spatial correlations to any order [109], it has two obvious drawbacks. First, the solutions of the equations relating the quantum numbers to the actual quantized quasimomenta must be found numerically, even for the case of two particles, and becomes more and more a black-box routine when the regime of a few to dozens of particles is reached. Second, in finite systems where finite temperatures enter into consideration, the usefulness of precise quantized many-body eigenstates is even more questionable, as one expects the many-body spectra to get exponentially dense [86]. These problems stem from the discrete character of the Bethe ansatz equations. Usually, one considers the thermodynamic limit to overcome them in what is known as thermodynamic Bethe ansatz [110] or by exploiting the asymptotic equivalence to grand canonical descriptions. However, besides the obvious limitation to very large particle numbers, related approaches to address nonlocal multiparticle correlations also suffer from restrictions to the extreme regimes of weak or strong coupling [111, 112] and small inter-particle separations [111].

Therefore, in this section, a different approach using cluster expansions, as introduced in the previous sections, will be used. It is thereby assumed that only short-time information, i.e., approximating the many-body dynamics by its bulk contribution with smoothed spectrum, should provide the major physical input.

This is consistent with state-of-the-art experimental measurements of nonlocal pair correlations in ultracold He_4 atomic clouds in quasi-1D geometries, as discussed in [25]. In this pioneering experiment, high-order nonlocal correlators are measured, with the two-body correlation showing a Gaussian profile as a function of the separation, a clear indication of temperatures well above deep quantum degeneracy and negligible interactions. The validity of the measurement protocol in this nearly ideal Bose gas was additionally confirmed by the compatibility of measured high-order correlations with Wick's theorem, bringing nonlocal multiparticle correlations in *interacting* quantum gases closer to experimental reach. The approach presented here works well precisely in the regime of weak degeneracy, where (thermal) boson bunching is still strongly pronounced but already starts to decay into long-range coherence present in the BEC regime [95, 100]. By providing accurate unified analytical formulas in the whole range from weak to strong interactions in the following, all their nontrivial effects on the bunching behavior will be captured in a single strike.

1.4.2. The model

The system of N bosons with zero-range repulsive interactions can be described by the well-known Lieb-Liniger (LL) model defined by the Hamiltonian [3, 19]

$$\hat{H} = \frac{\hbar^2}{2m}\left(\sum_{i=1}^{N} -\frac{\partial^2}{\partial {x_i}^2} + c\sum_{\substack{i,j=1\\ i\neq j}}^{N}\delta(x_i - x_j)\right) \tag{1.172}$$

with $c \geq 0$, $x_i \in [-L/2, L/2]$, where L is the system size, and periodic boundary conditions. The energy-like interaction parameter can be defined as $\alpha = \hbar^2 c^2/4m$ and the relevant dimensionless coupling parameter in the weakly degenerate regime is $s = \alpha\beta$. The symmetric, i.e., bosonic eigenfunctions of the Hamiltonian (1.172) can be found via a Bethe ansatz, where periodicity leads to a quantization condition in terms of N coupled transcendental equations [19].

In the limit $L \to \infty$, sometimes referred to as extended LL model, the spectrum becomes continuous. The symmetrized many-body propagator for this extended system is known exactly from integrating over all Bethe ansatz solutions [113–115]. The respective results are, however, not given in closed form but in terms of specific combinatorial rules. This can be resolved using the closed-form expressions for the wave functions introduced in [3], leading to the strikingly simple form

$$K_+^{(N)}(\boldsymbol{x}', \boldsymbol{x}; t) = \frac{1}{N!}\sum_{P\in S_N} \bar{K}^{(N)}(P\boldsymbol{x}', \boldsymbol{x}; t) \tag{1.173}$$

with

$$\bar{K}^{(N)}(\boldsymbol{x}', \boldsymbol{x}; t) = \frac{1}{(2\pi)^N}\int \mathrm{d}^N k\, \mathrm{e}^{-\frac{i\hbar t}{2m}\boldsymbol{k}^2 + i\boldsymbol{k}(\boldsymbol{x}'-\boldsymbol{x})}\prod_{j>l}\frac{k_j - k_l - ic\,\mathrm{sgn}(x_j' - x_l')}{k_j - k_l - ic\,\mathrm{sgn}(x_j - x_l)}. \tag{1.174}$$

A derivation of this result can be found in Appendix B.1. Note that, despite the similarity of Eqs. (1.173) and (1.15), the function $\bar{K}^{(N)}$ is *not* the many-body propagator $K^{(N)}$ for distinguishable particles but can be used as a substitute for bosons, as the two objects differ only by terms that cancel in the symmetric sum in (1.173). Since only symmetry-projected quantities matter eventually we are free to replace the interaction contributions $\Delta K^{(n)}$ in the Ursell decomposition (1.14) by their symmetry-projected equivalents $\Delta K_+^{(n)}$. The corresponding expressions for $n = 2, 3$ can be found in Appendix B.2. The non-symmetrized expression for $\Delta K^{(2)}$ can be calculated from the propagator for a δ potential directly, which gives exactly the same result, as it is already symmetric with respect to particle exchange (antisymmetric states are not affected by the δ potential).

1.4.3. Lieb-Liniger model for three particles—full cluster expansion

Using the results of section 1.2, specifically Eqs. (1.47), (1.36), and (1.35), one can rewrite the normalized nonlocal correlation function (1.171) as

$$g_2^{(N)}(r) = \frac{1}{\rho^2 Z^{(N)}} \left\{ \sum_{k=2}^{n} s_k^{(2)}((0,r),(0,r)) Z^{(N-k)} + \sum_{k=1}^{N-1} \sum_{l=1}^{N-k} s_k^{(1)}(0,0) s_l^{(1)}(r,r) Z^{(n-k-l)} \right\}, \tag{1.175}$$

where $\rho = N/L$ is the homogeneous particle density. Here, and in the rest of this section, the index "+" for the bosonic symmetry is omitted whenever possible to simplify the notation. By using the rescaled cluster sums $b_k^{(j)}$, Eq. (1.105), for $j = 1, 2$ and the polynomial form (1.108) of the partition functions one immediately finds that the normalized pair correlation $g_2^{(N)}(r)$ is a rational function in L/λ_T with coefficients that are dimensionless functions of the rescaled quantities r/λ_T and $s = \alpha\beta$. Moreover, due to the homogeneity of the system the diagonal part of $b_k^{(1)}(x,y)$, i.e., $b_k^{(1)}(r,r)$ does not depend on r, leading to the identification

$$b_k^{(1)}(r,r) = b_k^{(0)} \equiv b_k \tag{1.176}$$

that will be used in the following. It is also convenient to introduce the shorthand notation

$$b_k^{(2)}(r) \equiv b_k^{(2)}((0,r),(0,r)) \tag{1.177}$$

for a clearer presentation.

Let us first address the full cluster expansion of the pair correlation for $N = 3$ particles using the propagator (1.174). By expanding the general result for $g_2^{(N)}$, Eq. (1.175), with the help of Eq. (1.37) for $N = 3$ the nonlocal pair correlation function can be written as

$$g_2^{(3)}(r) = \frac{2}{3} \times \frac{1 + \left[b_2^{(2)}(r) + 2b_2 \frac{\lambda_T}{L} \right] + b_3^{(2)}(r) \frac{\lambda_T}{L}}{1 + 3b_2 \frac{\lambda_T}{L} + 2b_3 \left(\frac{\lambda_T}{L} \right)^2}. \tag{1.178}$$

The functions $b_k^{(2)}(r)$ and b_k for $k = 2, 3$ have been calculated from the interaction contributions $\Delta K_+^{(2)}$ and $\Delta K_+^{(3)}$. For $k = 2$ this yields the simple result

$$b_2^{(2)}(r) = \mathrm{e}^{-\tilde{r}^2} \left[1 - \sqrt{4\pi}\tilde{c}\, \mathrm{e}^{(\tilde{c}+|\tilde{r}|)^2} \operatorname{erfc}(\tilde{c} + |\tilde{r}|) \right], \tag{1.179}$$

$$b_2 = \frac{1}{\sqrt{2}} \left[2\mathrm{e}^{\tilde{c}^2} \operatorname{erfc}(\tilde{c}) - 1 \right], \tag{1.180}$$

where $\tilde{r} = \sqrt{2\pi} r/\lambda_T$ is the distance in terms of the thermal wavelength and

$$\tilde{c} = \lambda_T c/\sqrt{8\pi} = \operatorname{sgn}(c)\sqrt{\alpha\beta} = \operatorname{sgn}(c)\sqrt{s} \tag{1.181}$$

is the dimensionless (thermal) interaction strength. The results for the two-clusters, Eqs. (1.179) and (1.180) are valid also for the attractive case $\tilde{c} < 0$, which is the reason for

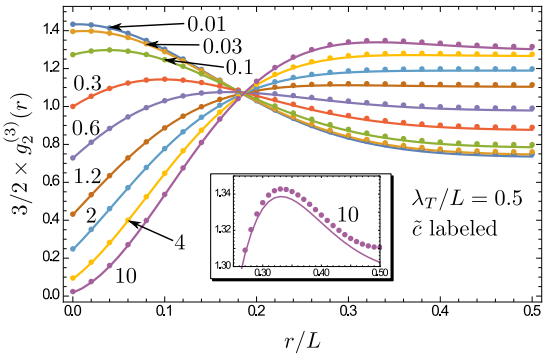

Figure 1.7: Comparison of $g_2^{(3)}(r)$, Eq. (1.178), (solid lines) with numerical calculations (dots) for $\lambda_T/L = 0.5$ and various values of the thermal interaction strength $\tilde{c}$, Eq. (1.181) (labeled). The inset shows the maximum arising for $\tilde{c} = 10$, an indicator of quasi-crystalline order.

not using the variable s introduced earlier. The corresponding expressions for $k = 3$ are more complicated and can be found in Appendix B.2, Eqs. (B.17)–(B.21), and Eq. (B.24). The integrated function b_2 in Eq. (1.180) is closely related to the virial coefficient found in [116] for the spin-balanced Gaudin-Yang model. The correct normalization

$$\int \mathrm{d}r\, g_2^{(3)}(r) = \frac{2}{3} L \tag{1.182}$$

is obtained from Eq. (1.105) only if the integration domain $(-L/2, L/2)$ can be replaced by $\mathbb{R}$ in all nontrivial integrals in the spirit of the short-time approximation, i.e., if $b_{2,3}^{(2)}(r) \approx 0$ for $|r| \geq L/2$. In the case at hand this gives the natural bound $\lambda_T \lesssim L/2$ for the short-time approximation to be valid, as both $b_{2,3}^{(2)}$ have a typical extent of λ_T. This means that one can make predictions for very low temperatures as long as the semiclassical result for $g_2^{(N)}(r)$ saturates well before $r = L/2$.

For comparison with numerical results the exact correlation functions have been calculated using the Bethe ansatz solutions similar to [109]. The details can be found in Appendix B.3. It is straightforward to show that the system size L can be eliminated completely from g_2 in both results using the scale transformation $x_i \mapsto x_i/L$, $k_i \mapsto k_i L$, $c \mapsto cL$, $\beta \mapsto \beta/L^2$, where the k_i are the quasimomenta that appear in the Bethe solutions. Thus, r and λ_T are expressed in units of L in all plots and λ_T is used as the temperature parameter rather than T or β. Figure 1.7 shows $3/2 \times g_2^{(3)}(r)$ for various values of $\tilde{c}$, Eq. (1.181), and for $\lambda_T/L = 0.5$. The absolute and relative error in the semiclassical results are smaller than 10^{-2} for all values of $\tilde{c}$ at this temperature. For higher temperatures the results are more accurate, e.g., for $\lambda_T/L = 0.3$ (not shown) both the absolute and relative error of the semiclassical result are of the order 10^{-6} for all values of $\tilde{c}$. Considering the fact that for $\lambda_T/L = 0.5$ the numerical calculations converge up

to an error of 0.1% already for a summation cutoff after only 15–30 states (depending on the interaction strength), the accuracy of the semiclassical prediction based on a continuous spectrum is impressive.

Interestingly, a feature that usually becomes visible only for very low temperatures, the non-monotonicity of $g_2^{(N)}$ in the fermionization regime of large $\tilde{c}$ [112, 117], can already be seen in Fig. 1.7. There, the maximum value of $g_2^{(3)}(r)$ at $r/L \approx 1/3$ for $\tilde{c} = 10$ is highlighted in the inset and can be interpreted as a precursor of a quasi-crystalline order in the two-particle correlations. For larger values of $\lambda_T > 0.5L$ the approximation fails as expected.

1.4.4. Exploiting the universal scaling of the short-time approximation

The general scaling properties of the short-time approximation presented in section 1.3 are not only useful to identify relevant parameters of the theory but can actually be used as a predictive tool. Let us assume that the expressions for b_n and $b_n^{(2)}(r)$ are known up to a certain cluster size $n = l - 1$. If one can find, in whatsoever way, e.g., by direct measurement [102], find an expression for the nonlocal pair correlation function $g_2^{(l)}(r)$ for fixed values of $\tilde{c}$ and (small enough) λ_T it contains all the information needed to calculate b_l and $b_l^{(2)}(r)$. The scaling behavior of the latter can then be used to calculate $g_2^{(l)}(r)$ at all temperatures in the range of validity of the short-time approximation with the same $\tilde{c}$ or to find better approximations for higher particle numbers (see next subsection). The interplay between the scaling of the functions $b_n^{(k)}$ and the form of $g_2^{(N)}$ as a rational function in λ_T/L renders this approach nontrivial. To actually calculate $b_l^{(2)}$ and b_l from $g_2^{(l)}$, one has to note that $b_n^{(2)}(r) \to 0$ for $r \to \infty$ and that the cluster expansion of $g_2^{(l)}$ contains b_l only in the denominator. This means that $g_2^{(l)}(r)/g_2^{(l)}(\infty)$ depends on $b_l^{(2)}(r)$ but not on b_l, while the latter can be found independently from $g_2^{(l)}(\infty)$. In practice, the diverging argument $r \to \infty$ has to be replaced by a value that lies inside the saturation regime of $g_2^{(l)}$. This explains why $g_2^{(l)}(r)$ has to be known for "small" values of λ_T. As the above considerations use only the homogeneity of the system, they are not restricted to 1D or to δ-like interaction potentials.

To demonstrate the power of the method, the numerical results from the Bethe ansatz calculations of $g_2^{(4)}(r)$ and $g_2^{(5)}(r)$ at $\lambda_T/L = 0.1$ and various values of $\tilde{c}$ have been used here to calculate the clusters $b_n^{(2)}$ and $b_n^{(0)}$ for $n = 4, 5$. The results were then used to calculate $g_2^{(5)}(r)$ at $\lambda_T/L = 0.4$. The comparison of the respective predictions with the numerical calculations is shown in the left part of Fig. 1.8. The nearly perfect agreement for all values of the interaction strength shows that the method is indeed applicable to the case at hand. Moreover, one an clearly see the first signatures of a quasi-crystalline order in the nonlocal correlations in the fermionization regime, with maxima separated by $L/5$ – a clear signature of the degenerate nature of the fermionization regime both visible in the numerical and semiclassical result.

The breakdown of the validity of this approach can be investigated by calculating the

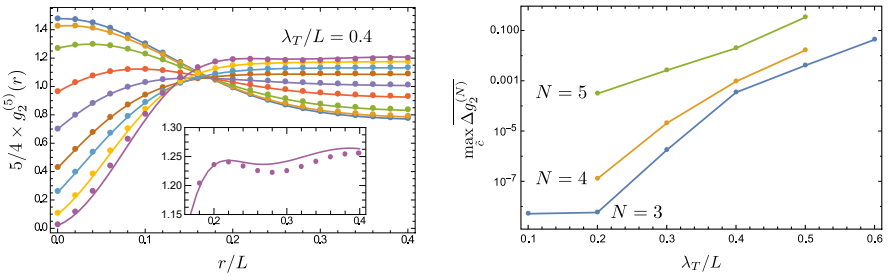

Figure 1.8: Left: The nonlocal pair correlation function for $N = 5$ particles from Bethe ansatz calculations (dots) and the semiclassical result (solid lines) for $\lambda_T/L = 0.4$ using the functions $b_n^{(2)}(r)$ and $b_n^{(0)}$ Eq. (1.105) for $n = 4, 5$ that have been recursively extracted from the numerical results for $g_2^{(4)}(r)$ and $g_2^{(5)}(r)$ at $\lambda_T/L = 0.1$. The values for $\tilde{c}$ (ranging from 0.01 to 10, from top to bottom at $r = 0$) are the same as in Fig. 1.7. The inset shows the non-monotonous behavior in the fermionization regime for $\tilde{c} = 10$ showing two maxima at approximately $r = L/5$ and $r = 2L/5$ indicating quasi-crystalline order. Right: The maximum (with respect to the interaction strength $\tilde{c}$) of the mean difference between semiclassical and numerical results (see text). While the deviation is smaller than the numerical precision for $N = 3, \lambda_T \leq 0.2L$ it increases rapidly for $\lambda_T/L \geq 0.2$.

mean absolute error in the semiclassical results for $g_2^{(N)}(r)$ using the 2-norm

$$\overline{\Delta g_2^{(N)}} = \sqrt{\frac{1}{\lambda_T} \int_0^{\lambda_T} \mathrm{d}r \left[\Delta g_2^{(N)}(r)\right]^2}, \tag{1.183}$$

where $\Delta g_2^{(N)}(r)$ is the difference between the numerical and semiclassical results. The right part of Fig. 1.8 shows the maximum of this mean error with respect to the interaction strength ranging from 0.01 to 10 for $N = 3, 4, 5$ and for various values of λ_T/L. For $N = 3$ and $\lambda_T/L \leq 0.2$ the error is smaller than the numerical precision (see Appendix B.3). The deviation for $\lambda_T = 0.1L$ is not shown for $N = 4, 5$, as this is the value used for the extraction of the functions $b_n^{(0)}, b_n^{(2)}(r)$ for $n = 4, 5$. The large offset between the graphs for the different particle numbers can be explained by the rather small numerical precision in the extracted cluster contributions, but all three curves show a roughly exponential increase in the range of $0.1 \leq \lambda_T/L \leq 0.5$, indicating a sudden breakdown of the short-time approximation.

1.4.5. Truncated cluster expansion for higher particle numbers

The full cluster expansion for $g_2^{(N)}$, Eq. (1.175), could be calculated from the propagator (1.174), in principle, for arbitrary particle numbers N. In practice one would have to (partially) trace not only $\Delta K^{(n)}$ for $1 \leq n \leq N$, which is a difficult task, but also all permutations of different products thereof. Here, only the information from interaction

contributions up to third order will be used. One way to achieve this goal is to use the QCE(2) to take into account only the desired orders. This has been proven to yield excellent results for the canonical partition function for the QCE(1) contributions [85]. The full QCE(2) has also been used in combination with the energy shifting method to second order in [60]. Here, the approximation is done at the level of cluster sizes $n \leq 3$, i.e., not taking into account the full symmetrization but having full control over the approximation through the parameter $N\lambda_T/L$ as is used in virial expansions, yielding accurate predictions for the high temperature regime.

As shown above, the full cluster expansion is a rational function in the parameter λ_T/L with coefficients that are functions of $\tilde{r}$, $\tilde{c}$, and N. With $A_n(r) = b_n^{(2)}(r) - (n-1)b_n\lambda_T/L$ one can write g_2 as

$$g_2^{(N)}(r) = \frac{N-1}{N}\left\{1 + \frac{A_2(r) + \left[\binom{N-2}{1}A_3(r) + \binom{N-2}{2}b_2A_2(r)\right]\frac{\lambda_T}{L} + \mathcal{O}(2)}{1 + \binom{N}{2}b_2\frac{\lambda_T}{L} + \mathcal{O}(2)}\right\}, \quad (1.184)$$

where $\mathcal{O}(2)$ stands for higher orders in λ_T/L. Expanding this function into a formal series in the parameter λ_T/L, while treating the functions A_n as constants to preserve normalization, results in

$$g_2^{(N)}(r) \approx \frac{N-1}{N}\left\{1 + A_2(r) + \left[(N-2)A_3(r) - (2N-3)A_2(r)b_2\right]\frac{\lambda_T}{L}\right\}. \quad (1.185)$$

The terms of order n in λ_T/L now come with coefficients that are polynomials in the particle number N of the order n, a fact that is well hidden in the rational expression for $g_2^{(N)}$. The series expansion has a positive convergence radius for any finite particle number, and the truncation is a good approximation if the ratio between the thermal wavelength and the mean inter-particle distance,

$$n_T = N\lambda_T/L, \quad (1.186)$$

is taken as a small parameter. The left part of Fig. 1.9 shows the comparison of Eq. (1.185) with numerical calculations for $N = 5$ particles and $N\lambda_T/L = 0.5$. The agreement is very good for the whole range of interaction parameters $\tilde{c}$, despite the expansion parameter being of order one. The inset shows the effect of truncating the expansion Eq. (1.185) to single two-particle clusters (first two terms in the curly bracket) and the effect of neglecting terms of subleading order in the particle number, respectively, for $\tilde{c} = 0.3$ (the latter corresponds to the thermodynamic limit that will be addressed below). Clearly, there is a major improvement by using the additional information from $b_3^{(0)}, b_3^{(2)}(r)$ and multiple clusters *only if* the crucial finite-size effect are accounted for. Also note that the fermionization limit $\tilde{c} \to \infty$ at $r = 0$ yields zero for all orders in the full expansion, which is often referred to as antibunching. This cancellation takes place between *different* $A_n(0)$, their values being fixed by equating $g_2(0) = 0$, leading to an error in the truncated expansion (1.185) for the fermionization limit that is of the order n_T^2/N.

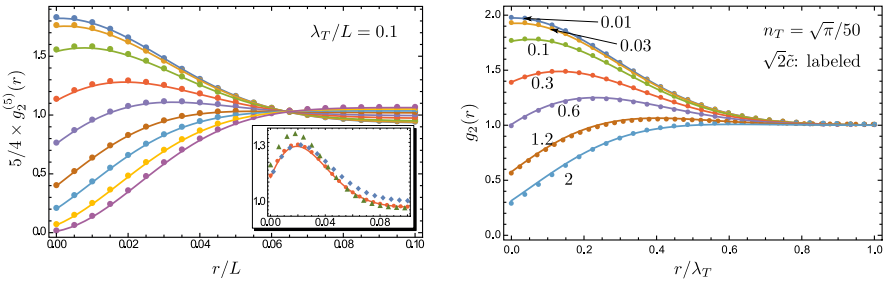

Figure 1.9: Left: Comparison of the expansion for $g_2^{(5)}$, Eq. (1.185), with numerical results (dots) for $\lambda_T/L = 0.1$ (i.e., $n_T = 0.5$) for the same range of values of $\tilde{c}$ as in Fig. 1.7. The inset shows the effect of truncating the expansion of $g_2^{(5)}$ after the single two-particle clusters [first two terms in Eq. (1.185)] (green triangles) and the effect of neglecting all coefficients that are subleading in the particle number (blue squares), i.e., Eq. (1.187), for $\tilde{c} = 0.3$. Right: Comparison of numerical results for $g_2(r)$ in the thermodynamic limit (taken from [112], error estimates not shown) with Eq. (1.187) for $n_T \approx 0.035$ and $\tilde{c}$ labeled. The numerical method in [112] cannot access the fermionization regime $\tilde{c} \gg 1$.

1.4.6. The thermodynamic limit

From the virial-like expansion Eq. (1.185) it is easy to find the thermodynamic limit by omitting all terms that are subleading in N while fixing n_T, Eq. (1.186). This gives

$$g_2(r) = 1 + b_2^{(2)}(r) + [b_3^{(2)}(r) - 2b_2 b_2^{(2)}(r)]n_T + \mathcal{O}(n_T^2). \tag{1.187}$$

Equation (1.187) can also be found within the grand canonical approach by inverting the fugacity expansion in terms of the particle number in the high-temperature limit [61]. A comparison with numerical results taken from [112] is shown in the right part of Fig. 1.9, demonstrating the validity of the result presented here in the full range of interactions. Although the first order in n_T is taken into account there, the term $b_2^{(2)}(r)$ defined by the two-body problem is dominant for the particular value of $n_T \approx 0.035$ used there. For higher values of n_T the first-order term gives non-negligible corrections. This is shown in Fig. 1.10. The left plot shows $g_2(r)$ for different values of n_T and $\tilde{c}$ given in the figure as approximate numbers. The exact values are

$$(n_T^2, \tilde{c}^2) = \left(\frac{4\pi}{10^4}, 0.18\right), \quad \left(\frac{4\pi}{10^2}, 0.1568\right), \quad \left(\frac{4\pi}{10}, 0.1125\right), \tag{1.188}$$

and are chosen to match the parameter values of the data presented in [112][9]. For $n_T^2 = 4\pi/10^4 \approx 0.035$, g_2 can be well approximated by single- and two-particle clusters. For higher values of n_T the $\mathcal{O}(n_T)$ contributions, and thus three-particle clusters, have to be included, and for $n_T^2 = 4\pi/10$, i.e., $n_T \approx 1.12$ the truncation to first order in n_T

[9]The authors of [112] use different dimensionless parameters given by $\tau = 4\pi/n_T^2$ and $\gamma = \sqrt{8\pi}\tilde{c}/n_T$.

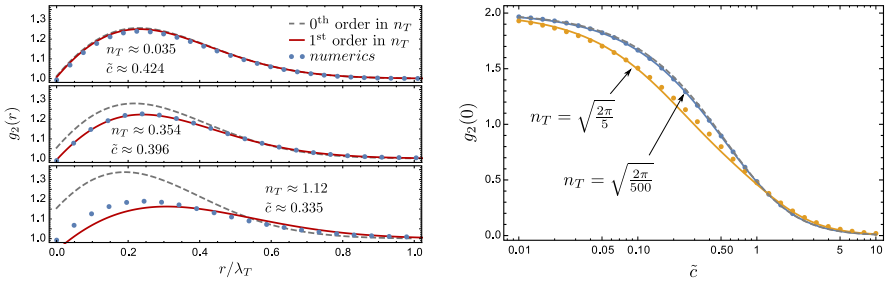

Figure 1.10: Left: Nonlocal pair correlation in the thermodynamic limit for different interaction strengths and different values of n_T such that $g_2(0) \approx 1$. In the high-temperature or low-density regime $n_T \ll 1$ only two-particle clusters contribute. For lower temperatures $\mathcal{O}(n_T)$ corrections cannot be neglected and larger clusters play a role. Right: Local correlations $g_2(0)$ with respect to the interaction parameter. Numerical data (dots) is taken from [118]. The approximation by two-particle clusters (gray dashed) is sufficient for high temperatures (low densities). By including the next order in the cluster expansion (solid line) we can see a major improvement in the regime of lower temperature.

is not sufficient anymore for a precise prediction but still gives reasonable qualitative agreement with numerical calculations. The right part of Fig. 1.10 shows the local correlations $g_2(0)$ for a wide range of the interaction parameter. A major improvement in the agreement of numerical (taken from [118]) and semiclassical results can be seen when including the first-order correction in n_T. Note that the local version $g_2(0)$ of the pair correlation can be calculated exactly by solving integral equations using the Hellmann-Feynman theorem [118] (higher local correlation functions have been found from viewing the LL model as a limiting case of the sinh-Gordon model [119]), but to the best knowledge of the author, all published analytical results for $g_2(r)$ in the weakly degenerate regime were derived in perturbation theory, i.e., they are only valid in the limits of weakly or strongly interacting bosons. The result presented here, Eq. (1.187), represents the generalization of these results for arbitrary interaction strengths in the moderate- to high-temperature regime.

1.4.7. Summary and possible further applications

This section has demonstrated that the application of the short-time approximation to the spatially dependent nonlocal pair correlation leads to essentially exact results for temperatures well above the quantum degenerate regime while still giving good results close to the latter. For the example of three particles it has been shown that the full cluster expansion in short-time approximation remains valid up to $\lambda_T \approx L/2$. In this situation, the mean inter-particle distance $L/N = 2\lambda_T/3$ is already smaller than the thermal wavelength. It was then demonstrated that the universal scaling behavior in

the short-time approximation remains valid for higher particle numbers. This was done by predicting the form of the nonlocal pair correlation function for a whole range of temperatures using the numerically extracted values of the individual clusters at a fixed temperature. Comparing the results obtained from this rescaling procedure to numerical calculations shows very good agreement down to $\lambda_T = 0.4L$, corresponding to a thermal wavelength that is *twice* the mean particle separation. This underlines the validity of the short-time approximation also in this quantum regime with $N\lambda_T/L \geq 1$.

For higher particle numbers approximations were presented that are valid well above the quantum degeneracy regime, i.e., $N\lambda_T/L \ll 1$, while still explicitly depending on the particle number and thus explicitly accounting for its finiteness. Finally, by neglecting the contributions that are subleading in the particle number, the exact results for the first two orders of the series expansion of $g_2(r)$ in the quantum degeneracy parameter $n_T = N\lambda_T/L$ were calculated, and very good agreement with the numerical results obtained by other authors was shown. While this work awaits experimental confirmation in state-of-the-art experiments with 1D trapped quantum gases in the weak degeneracy regime, it is planned to extend the analysis to momentum correlations in the 1D Bose gas that have been measured recently [120].

Possible further applications could extend the results to the case of smooth external potentials, including the latter on the level of the short-time approximation. This allows for the transfer or the results from the quantum integrable Lieb-Liniger model to these nonintegrable cases, where not only the analytical results for $b_n^{(k)}$ for $n = 1, 2, 3$, but also the numerically extracted results for $n > 3$ can be used.

Another application in one-dimensional systems, apart from the straightforward multiple-species extensions that can range from dynamical impurities, to fermionic spin-1/2 systems (i.e., the Gaudin-Yang model [108]) and mixtures of different species, could be the super-Tonks-Girardeau gas [121] that has been experimentally realized using a confinement induced resonance [122], where the interaction changes from infinitely repulsive (Tonks-Girardeau) to infinitely attractive interaction (super-Tonks-Girardeau) by continuously tuning the scattering length of the three-dimensional interaction. The idea is to use the results from the Lieb-Liniger gas also for the attractive case $\tilde{c} < 0$, however eliminating the bound states that are suppressed in the super-Tonks-Girardeau gas that gets dynamically stabilized, when approached from the Tonks-Girardeau gas regime, through the large kinetic energy in the latter. Thus, a large part of the complications introduced in the calculation of the many-body propagator through the existence of bound states is eliminated in this approach. As the smooth spectrum and nonlocal correlations of the Tonks-Girardeau gas mimic the respective properties of free spinless fermions [123], one could use a fermionic model with an effective interaction to also apply the shifting method beyond the resonance.

1.5. Application: Short-range interaction in three dimensions

In this section, the methods of cluster expansions in short-time approximation will be applied to three-dimensional (3D) systems. Although systems with lower dimensions can nowadays be prepared in experiments (as discussed in the last section), most systems are three-dimensional in nature. It is probably for this reason that Beth and Uhlenbeck applied the cluster expansion only to 3D systems when they first introduced its quantum formulation [66]. Their final result was the now-called Beth-Uhlenbeck formula for the first virial coefficient that is determined by the two-particle problem and can be expressed in terms of the scattering phases of the interaction potential. The strength of this approach is that the scattering phases are rather simple to calculate and thus a wide variety of interaction potentials can be addressed. However, spatially resolved quantities as well as information beyond the first virial coefficient are not included in these results. As mentioned earlier, there have been attempts to generalize the Beth-Uhlenbeck formula either by introducing three-body scattering phases [90] or by Ursell expansion [77], but explicit calculations beyond the perturbative regime have not been realized in this context. One reason for this could be the fact that the calculation of the single-particle propagators in three dimensions in the presence of a scattering potential cannot be given as a closed form expression except for very special potentials like the Pöschl-Teller potential [124]. Of course, approximations can be found using the general Lippmann-Schwinger equation [125], with the simplest one being the Born approximation, however leading to expressions that are perturbative in the potential strength. Here, the QCE(1) and other approximations introduced earlier in this thesis, that go beyond these approaches, will be used for short-range repulsive and attractive interactions by calculating the interaction contributions explicitly from the propagator of the scattering problem in the low energy scattering limit.

1.5.1. The QCE(1) in three dimensions

When considering short-range interactions it is usually a reasonable assumption that the interaction potential is spherically symmetric, as is usually assumed in cold-atom quantum gases with Feshbach-tunable interactions [22, 29]. The goal is to calculate the part of the (imaginary time) propagator of the relative motion $\delta K_\mu^{(1)}(\boldsymbol{r}_1, \boldsymbol{r}_0; \beta, \alpha)$ that enters the interaction contributions (1.120) and finally the reduction of the inter- and intra-cycle contributions in the QCE(1) to one-dimensional integrals. Thus, let us start with the general treatment of two particles interacting via a spherically symmetric potentials in an infinite volume. After separating off the motion of the center of mass, the Hamiltonian of the relative motion in position representation is simply given as

$$\hat{H}_{\mathrm{rel}} = -\frac{\hbar^2}{2\mu} \triangle_{\boldsymbol{r}} + V(r) \tag{1.189}$$

with $r = |\boldsymbol{r}|$ and the reduced mass μ and the spherically symmetric potential $V(r)$. The energy eigenfunctions can then be decomposed into the spherical harmonics Y_{lm} and the

solutions $u_{kl}(r)$ of the radial equation as

$$\psi_{klm}(\boldsymbol{r}) = \frac{u_{kl}(r)}{r} Y_{lm}(\theta, \phi). \tag{1.190}$$

The propagator for the relative motion can therefore be simplified using the addition theorem for spherical harmonics [91],

$$\begin{aligned} K_\mu^{(1)}(\boldsymbol{r}_1, \boldsymbol{r}_0; \beta, \alpha) &= \sum_{l=0}^{\infty} \sum_{m=-l}^{l} \frac{1}{r_1 r_0} K_{\mu,l}^{(1)}(r_1, r_0; \beta, \alpha) Y_{lm}(\theta_1, \phi_1) Y_{lm}^*(\theta_0, \phi_0) \\ &= \sum_{l=0}^{\infty} \frac{2l+1}{4\pi r_1 r_0} K_{\mu,l}^{(1)}(r_1, r_0; \beta, \alpha) P_l(\cos\gamma), \end{aligned} \tag{1.191}$$

where P_l is the lth Legendre polynomial and γ is the angle between $\boldsymbol{r}_1$ and $\boldsymbol{r}_0$. The radial component of the propagator with angular momentum quantum number l is here defined as

$$K_{\mu,l}^{(1)}(r_1, r_0; \beta, \alpha) = \int_0^\infty dk\, \mathrm{e}^{-\beta \frac{\hbar^2 k^2}{2\mu}} u_{kl}(r_1) u_{kl}^*(r_0) \tag{1.192}$$

and scales like a one-dimensional propagator (c.f., Eq. (1.99) with $D_{\mathrm{tot}} = 1$). Subtracting the noninteracting part from the propagator will only affect the radial components, such that one can write it as

$$\delta K_\mu^{(1)}(\boldsymbol{r}_1, \boldsymbol{r}_0; \beta, \alpha) = \sum_{l=0}^{\infty} \frac{2l+1}{4\pi r_1 r_0} \delta K_{\mu,l}^{(1)}(r_1, r_0; \beta, \alpha) P_l(\cos\gamma) \tag{1.193}$$

or, using the general scaling (1.99) for δK, Eq. (1.126), one obtains

$$\delta k^{(1)}(\tilde{\boldsymbol{r}}_1, \tilde{\boldsymbol{r}}_0; s) = \sum_{l=0}^{\infty} \frac{2l+1}{4\pi \tilde{r}_1 \tilde{r}_0} \delta k_l^{(1)}(\tilde{r}_1, \tilde{r}_0; s) P_l(\cos\gamma) \tag{1.194}$$

in terms of the dimensionless variables $\tilde{\boldsymbol{r}}_i = \boldsymbol{r}_i / \lambda_T(\mu)$. The dimensionless inter- and intra-cycle diagrams, Eqs. (1.128) and (1.132), are thus given as

$$a_\nu^{\mathrm{inter/intra}}(s) = \sum_{l=0}^{\infty} \int_0^\infty dx \int_0^\infty dy\, \delta k_l^{(1)}(x, y; s) f_{\nu,l}^{\mathrm{inter/intra}}(x, y) \tag{1.195}$$

with

$$\begin{aligned} f_{\nu,l}^{\mathrm{inter/intra}}(x, y) &= (2l+1) \frac{xy}{4\pi} \int d\Omega_x\, d\Omega_y\, \frac{1}{\nu^3} \mathrm{e}^{-\pi \left(\frac{x \mp y}{\nu}\right)^2} P_l(\cos\gamma) \\ &= (2l+1) \frac{4\pi xy}{\nu^3} \mathrm{e}^{-\pi \left(\frac{x^2+y^2}{\nu^2}\right)} (\mp i)^l j_l\left(2\pi i \frac{xy}{\nu^2}\right). \end{aligned} \tag{1.196}$$

Here, j_l is the lth spherical Bessel function (see [91] for the evaluation of the integral) and the upper and lower sign stand for inter- and intra-cycle diagrams, respectively. Note

that $i^l j_l(it)$ is real for real values of t. The above result shows that the values of inter- and intra-cycle diagrams are the same for the even angular momentum quantum numbers l while they have the opposite sign for odd l. Combining this result with the multiplicities (1.130) and (1.133) of the diagrams, (1.196) shows that if the interacting particles are of the same species, their contributions vanish in the case of even(odd) values of l for fermions(bosons). This is a direct consequence of the parity of the spherical harmonics in the case of two particles, where the exchange of the particles corresponds to the inversion of their relative coordinate. The calculation presented here thus shows that this property also holds in the QCE(1) as it should.

In the case of s-wave scattering, $f_{\nu,0}$ simplifies drastically, yielding

$$f_{\nu,0}^{\mathrm{inter}}(x,y) = f_{\nu,0}^{\mathrm{intra}}(x,y) = \frac{1}{\nu}\left[\mathrm{e}^{-\pi\left(\frac{x-y}{\nu}\right)^2} - \mathrm{e}^{-\pi\left(\frac{x+y}{\nu}\right)^2}\right]. \tag{1.197}$$

Remarkably, this has exactly the form of a single-particle propagator for a semi-infinite line subject to a Dirichlet boundary condition at the origin [126].

1.5.2. Low-energy approximations and s-wave scattering

One of the assumptions that has been used in the preceding sections is the short-range character of the interaction. However, this has to be specified in terms of a different length scale of the system. In equilibrium systems as are considered here, one should compare the range of the interaction to the thermal wavelength: If the latter is much larger than the extent of the interaction potential, the details of this potential cannot be resolved by the average particle, i.e., only particles with a relative kinetic energy that exceeds the average single-particle energy by far will be affected by the detailed form of the potential. In the partial wave analysis one would find that the scattering into waves with $l \geq 1$ is strongly suppressed, as the respective wave functions have to vanish at the center of the potential and are only slowly varying compared to the latter, thus being close to zero over the full range of the potential. Therefore, it is often sufficient to take only the s-wave scattering into account, especially in the low-temperature regime that is addressed in cold atom experiments [22, 29]. One has to stress that the short-time approximation does not contradict this low-temperature assumption as long as the thermal wavelength does not become comparable to the length scale given by the system size. If the latter is much larger than the range of the interaction, as is the case in almost all cold-atom experiments, there is a very big window where both short-time approximation and short-range interaction are perfectly consistent.

The low-energy scattering is then only determined by the s-wave scattering phase δ_s that should then be consistently approximated by its low-energy (i.e., large wavelength) limit, where it is determined through the scattering length a_s as the only parameter. To model this simple type of interaction that treats the potential as if it has no length, one is tempted to do this with a point-like interaction by using an interaction potential of the form

$$V_{\mathrm{int}}(\boldsymbol{r}', \boldsymbol{r}) = \text{“}g\delta^{(3)}(\boldsymbol{r}' - \boldsymbol{r})\text{”} \tag{1.198}$$

with a 3D Dirac delta distribution, similar as in 1D. However, it turns out that modeling this delta distribution, e.g., as a limiting case of a spherical step potential, its effect would vanish for any finite coupling strength g in the zero-range limit and it thus requires regularization. There are different ways to achieve this, the most popular being the Fermi or Fermi-Huang pseudo-potential [127–129] acting as (setting $\hbar^2/2m = 1$ for the moment)

$$V_{\mathrm{F}}(\boldsymbol{r})\psi(r) = 4\pi a_{\mathrm{s}}\delta^{(3)}(\boldsymbol{r})\frac{\partial}{\partial r}\left(r\psi(\boldsymbol{r})\right) \tag{1.199}$$

on the relative wave function. The effect of the derivative is to remove possible $1/r$ divergences in the wave function that are forbidden in the noninteracting case, leading to a nontrivial boundary condition

$$\psi(\boldsymbol{r}) \sim \text{const} \times \left(\frac{1}{r} - \frac{1}{a_{\mathrm{s}}}\right) \tag{1.200}$$

for $r \to 0$ (The constant is nonzero only for the rotationally symmetric s-wave functions). One has to be careful, however, when interpreting the potential (1.199). Naively, one would expect that a small attractive interaction leads to a small negative scattering length while the latter would be positive for repulsive interaction. However, the Fermi pseudo-potential allows for a bound state solution for $a_{\mathrm{s}} > 0$, with an energy that diverges for $a_{\mathrm{s}} \to 0^+$ (the plus sign indicating that $a_{\mathrm{s}} = 0$ is approached from above), while this bound state is absent for negative scattering lengths. In more recent approaches, a momentum cutoff regularization [130–132] of the contact interaction is often used, however leading to the same results. This apparently unphysical behavior has led to some confusion and inconsistency in the literature when it comes to the physical interpretation in terms of "attractive" and "repulsive" interaction.

There is, however, a perfectly meaningful interpretation of the above behavior. In experiments with tunable scattering length a_{s}, the latter is *not* a system parameter but rather a derived quantity. In cold atom experiments, the control of a_{s} is usually achieved using Feshbach resonances [29], where the scattering length has the form

$$a_{\mathrm{s}} = \frac{1}{g - g_{\mathrm{res}}} \tag{1.201}$$

in the vicinity of the resonance value g_{res} of the continuous parameter g that depends, e.g., on the magnetic field. Thus, the potential (1.199) is best interpreted as an effective description around a resonance and would be better expressed in terms of a continuous parameter g, Eq. (1.201), such that the values $a_{\mathrm{s}} \to 0^{\pm}$ correspond to the regimes $g \to \mp\infty$ far to the left and far to the right of the resonance. The noninteracting case would then correspond to the limit $g \to \infty$, while it is natural to expect that a zero energy bound state appears at the resonance $g = g_{\mathrm{res}}$ that has a negative energy for $g < g_{\mathrm{res}}$.

The soft-shell scattering potential

To clarify the above and to see how the resonance picture emerges naturally, it is instructive to use a simple model potential with finite range r_{s} to analyze the limit $r_{\mathrm{s}} \to 0$.

This will then be used to derive the s-wave part of the propagator, i.e., Eq. (1.192) with $l = 0$. Let the relative potential of two particles be given as the soft-shell potential

$$V(\boldsymbol{r}) = \frac{\hbar^2 c}{2\mu}\,\delta^{(1)}(r - r_\mathrm{s}) \tag{1.202}$$

with a finite shell radius r_s and the potential strength c. It is equivalent to imposing the (mixed) boundary condition

$$\lim_{\epsilon\to 0}\left[\frac{d}{dr}\log|u_{kl}(r)|\right]_{r_\mathrm{s}-\epsilon}^{r_\mathrm{s}+\epsilon} = c \tag{1.203}$$

at the shell, where the left hand side means the difference of evaluating the bracket outside and inside the shell and $u_{kl}(r)$ is the radial wave function defined in (1.190). Note that for the finite soft-shell potential 1.202 there is a clear definition of repulsive and attractive interaction as $c > 0$ and $c < 0$, respectively.

It is straightforward to show that the scattering phases can be expressed as

$$\tan\delta_l = \frac{\frac{c}{k}j_l(kr_\mathrm{s})}{\left(\frac{c}{k} + \frac{j_l'(kr_\mathrm{s})}{j_l(kr_\mathrm{s})}\right)n_l(kr_\mathrm{s}) - n_l'(kr_\mathrm{s})}, \tag{1.204}$$

with the spherical Bessel and Neumann functions j_l and n_l. Using the Wronskian [133]

$$n_l'(x)j_l(x) - n_l(x)j_l'(x) = \frac{1}{x^2} \tag{1.205}$$

leads to the simpler form

$$\tan\delta_l = \frac{j_l^2(kr_\mathrm{s})}{j_l(kr_\mathrm{s})n_l(kr_\mathrm{s}) - (cr_\mathrm{s}\cdot kr_\mathrm{s})^{-1}}. \tag{1.206}$$

For large wavelengths compared to the potential range r_s, i.e., $kr_\mathrm{s} \ll 1$ the known expansion for the Bessel and Neumann functions yield the low-energy scattering phases

$$\tan\delta_l = -\frac{2l+1}{[(2l+1)!!]^2}\times\frac{(kr_\mathrm{s})^{2l+1}}{1+\frac{2l+1}{cr_\mathrm{s}}} + \mathcal{O}((kr_\mathrm{s})^{2l+3}). \tag{1.207}$$

Thus, for every value of l there is a divergence at $cr_\mathrm{s} = -(2l+1)$ corresponding to a fast increase of the respective scattering phase δ_l by π that coincides with the emergence of a bound state, as shown in the following.

The equation for the bound states is obtained by matching the free solutions inside the shell to exponentially decaying solutions for $r > r_\mathrm{s}$ (i.e., the spherical Hankel functions $h^{(1)}(i\kappa r)$ with imaginary argument) yielding the quantization

$$\frac{i\,j_l^2(i\kappa r_\mathrm{s})}{n_l(i\kappa r_\mathrm{s})j_l(i\kappa r_\mathrm{s}) - (cr_\mathrm{s}\cdot i\kappa r_\mathrm{s})^{-1}} = 1, \tag{1.208}$$

where the energy is given by $E = -\frac{\hbar^2\kappa^2}{2\mu}$ if the solution exists. In the regime $\kappa r_\mathrm{s} \ll 1$ the solutions can be found as

$$\kappa r_\mathrm{s} = \left[\frac{4\Gamma\left(l+\frac{5}{2}\right)}{\Gamma\left(l-\frac{1}{2}\right)}\left(\frac{1}{cr_\mathrm{s}} - \frac{1}{2l+1}\right)\right]^{\frac{1}{2}}, \qquad l > 0, \tag{1.209}$$

$$\kappa r_\mathrm{s} = \frac{1+cr_\mathrm{s}}{cr_\mathrm{s}}, \qquad l = 0, \tag{1.210}$$

where the condition for the existence is in all cases $cr_\mathrm{s} \leq -(2l+1)$, i.e., they appear (with zero energy) exactly at the divergences of $\tan\delta_l$, Eq. (1.207).

The above shows that there are many resonances already in this simple model. However, as can be seen from Eq. (1.207), the s-wave scattering is dominant away from the resonances. One can directly read off the scattering length as

$$a_\mathrm{s} = -\left[\lim_{k\to 0} k\cot\delta_0\right]^{-1} = \frac{cr_\mathrm{s}}{cr_\mathrm{s}+1} r_\mathrm{s}. \tag{1.211}$$

The zero-range Fermi pseudo-potential now turns out to have exactly the same scattering and bound states as the shell potential in the limit $r_\mathrm{s} \to 0$, keeping the parameter $\bar{c} = c + 1/r_\mathrm{s}$ fixed to stay in the vicinity of the s-wave resonance. The reason for this is the different position of the resonances of scattering phases for $l > 0$ thus yielding the trivial limit $\delta_l \to 0$ in the zero-range limit as for the Fermi pseudo-potential. However, in this limit, the parameter regime of *repulsive* interactions $c > 0$ is pushed to $\bar{c} = \infty$ and can therefore not be accessed anymore.

To conclude the above, the pseudo-potential (1.199) and equivalent regularized zero-range potentials should only be used in the vicinity of a s-wave resonance. There, it does not make sense to interpret a positive scattering length $a_\mathrm{s} > 0$ as an indicator for repulsive interaction. As the resonance is accompanied by the formation of a bound state, one should rather understand the potential as attractive for *all* values of the scattering length. In other words, a repulsive zero-range potential has no effect (if internal degrees of freedom of the particles are left unaccounted for).

However, we are now in the position to say something also for the more general case, as we do not have to take the zero-range limit as long as we stay in the low-energy regime $kr_\mathrm{s} \ll 1$ to justify the description of interactions only in terms of the scattering length (1.211) (and the bound state for $cr_\mathrm{s} < -1$).

The low-temperature imaginary-time propagator for a soft-shell potential

As was discussed earlier, we can make use of the short-time approximation of propagators evaluated in imaginary time while still being in a regime where the thermal wavelength is much larger than the range of interactions, therefore having to include only the low-energy effects of the interaction. One can thus calculate an approximation of the s-wave part of the imaginary-time propagator (1.192) for the soft-shell potential (1.202) by replacing the radial wave functions u_{k0} by their low-energy approximations using

$$\tan\delta_0 = ka_\mathrm{s} \tag{1.212}$$

for all k and noting that error gets suppressed at low temperatures, when $\lambda_T \gg r_\mathrm{s}$. Specifically, for $kr_\mathrm{s} \gtrsim 1$ we have

$$\beta E_{k,\mathrm{rel}} = \frac{\hbar^2 k^2 \beta}{2\mu} = \frac{\lambda_T^2(\mu) k^2}{4\pi} \gtrsim \frac{\lambda_T^2(\mu)}{4\pi r_\mathrm{s}^2} \gg 1, \tag{1.213}$$

such that the respective contributions in the imaginary-time propagator are strongly suppressed due to their weighting with $\exp(-\beta E_{k,\mathrm{rel}})$.

To calculate the s-wave part of the propagator, Eq. (1.192) with $l = 0$, the relative motion is enclosed in a finite, but large volume, e.g., a large sphere with radius $R \gg r_\mathrm{s}$, that quantizes the values of k and fixes the normalization and is sent to $R \to \infty$ afterwards. Here, only the results are presented, and the reader is referred to Appendix C for the detailed derivations. Also, it is assumed that the initial and final coordinates lie outside the potential shell. In this case, the correction to the s-wave part of the propagator can be written as

$$\delta K_{\mu,0}^{(1)}(r_1, r_0; \beta, \alpha) = \frac{1}{\lambda_T(\mu)} \, \delta k_0^{(1)}(\tilde{r}_1 + \tilde{r}_0, 0; \tilde{s}), \tag{1.214}$$

$$\delta k_0^{(1)}(\tilde{z}, 0; \tilde{s}) = 2\mathrm{e}^{-\pi \tilde{z}^2} \left[1 \pm \pi \tilde{s} \mathrm{e}^{\pi(\tilde{z}+\tilde{s})^2} \operatorname{erfc}\left(\mp \sqrt{\pi}(\tilde{z} + \tilde{s}) \right) \right] \tag{1.215}$$

with the complementary error function erfc and the scaled variables

$$\tilde{z} = \tilde{r}_1 + \tilde{r}_0 = \frac{r_1 + r_0}{\lambda_T(\mu)}, \qquad \tilde{s} = -\frac{\lambda_T(\mu)}{2\pi a_\mathrm{s}}. \tag{1.216}$$

The upper and lower sign in (1.215) correspond to the repulsive ($c > 0$) and attractive ($c < 0$) case, respectively. Note that the variable $\tilde{s}$ is of the form $\sqrt{\alpha\beta}$ rather than $\alpha\beta$ used before, with α being an energy-like parameter. The reason for this choice is the fact that the sign of $\tilde{s}$ then encodes the sign of the scattering length a_s.

The result for the attractive case exactly reproduces the interaction part of the (real-time) propagators found either using the (unique) self-adjoint extension of the Hamiltonian for a point interaction [134, 135] as well as for the Fermi pseudo-potential [84] and the momentum-cutoff regularization of a delta-potential [132], showing the equivalence of the respective approaches.

It is instructive to see how the repulsive result differs from the attractive one. This can be seen by rewriting the complementary error function in (1.215) for the repulsive case as

$$-\operatorname{erfc}\left(-\sqrt{\pi}(\tilde{z} - \tilde{s})\right) = \operatorname{erfc}\left(\sqrt{\pi}(\tilde{z} - \tilde{s})\right) - 2, \tag{1.217}$$

such that the result differs from the attractive case with $\tilde{s} > 0$ by

$$-4\pi\tilde{s}\mathrm{e}^{-\pi\tilde{z}^2 + \pi(\tilde{z}-\tilde{s})^2} = -\Psi_b(\tilde{z}, \tilde{s}). \tag{1.218}$$

It is easily verified that this exactly cancels the bound state contribution present in the attractive regime beyond the resonance, such that the low-temperature imaginary-time propagator for the repulsive soft-shell potential can be obtained from the known results

by dropping the bound state contribution, as long as the two coordinates lie outside the potential sphere.

If one or more of the coordinates are within the sphere, there are additional contributions (see Appendix C) that vanish in the limit of a point potential. One can easily argue that, within QCE(1), the condition $r_\mathrm{s} \ll \lambda_T$ implies that the latter contributions are negligible as the propagator is smeared with normal distributions according to Eqs. (1.197) and (1.195), with a width ν large compared to the potential range $r_\mathrm{s}/\lambda_T \ll 1$ for any cluster size. Also in the special case $\nu = 0$, that yields the trace of $\delta k_0^{(1)}$, the contribution from within the potential is negligible.

This means that we can use the s-wave interaction correction (1.215) for the propagator together with the scattering length a_s in terms of the potential strength c and the finite range r_s, Eq. (1.211). By neglecting the contributions from $l > 0$ in Eq. (1.194) this yields the approximate interaction part of the propagator

$$\delta k^{(1)}(\tilde{\boldsymbol{r}}_1, \tilde{\boldsymbol{r}}_0; s) \approx \frac{1}{4\pi \tilde{r}_1 \tilde{r}_0} \delta k_0^{(1)}(\tilde{r}_1, \tilde{r}_0; \tilde{s}) \tag{1.219}$$

that will be used in the following.

One should, however, make a few comments when it comes to repulsive interactions in the simple model used here. The scattering length of the shell potential used in the derivation is bounded by r_s for the case $c > 0$, with r_s being the scattering length of the hard-sphere potential obtained for $c \to \infty$. Therefore, if one wants to stick with the simple model, one has to keep the potential range r_s finite to obtain a nontrivial result. The low-temperature limit sketched above then corresponds to the perturbative regime $|\tilde{s}^{-1}| \ll 1$ or $a_\mathrm{s} \ll \lambda_T$ according to Eqs. (1.213) and (1.216), such that the s-wave scattering approach would be rather trivial in this regime, only yielding known results (see, e.g., [68]). But we have seen that the analytic form of the propagator for $c > 0$, when expressed through the scattering length a_s or equivalently $\tilde{s}$ is *exactly* the same as for a resonance, except for the missing bound state. Therefore, one could equally well forget about the (hidden) dependence on the parameter c and simply use the propagator for the "repulsive" interaction in situations, where a resonance is approached from below ($a_\mathrm{s} > 0$) while only taking into account the scattering states that are adiabatically connected to the scattering states of a weakly repulsive interaction.

This approach is actually closer to experimental setups than the use of the model potential introduced above: A real gas of cold atoms usually hosts molecular bound states that actually render the gas metastable, leading to inelastic scattering and particle losses in experiments that are, however, strongly suppressed due to weak coupling of the respective molecular and atomic states. In cold atom gases, the internal degrees of freedom of the atoms lead to many different scattering channels, with most of them being closed at very low temperatures, but with closed-channel bound states that can lie very close to the continuum threshold energy of an open channel. If such a closed channel bound state can be energetically tuned by external parameters to approach the continuum, even a weak coupling between this state and the open-channel scattering states can induce a Feshbach resonance [29]. The situation of approaching such a resonance from "below" then just means that the molecular bound state in the closed channel is initially

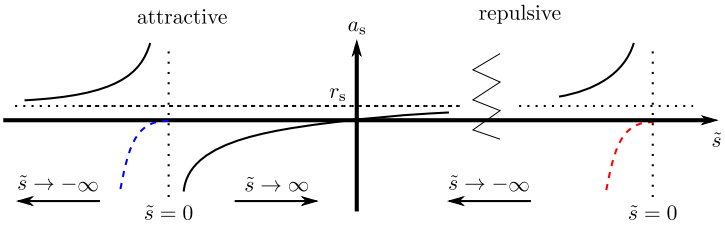

Figure 1.11: Sketch of the parametrization of the interactions used in the following. In the attractive case, the scaled interaction $\tilde{s}$, Eq. (1.216), describes the regime around a resonance with a bound state being created at $\tilde{s} = 0$ and a bound state energy $E_b \propto -\tilde{s}^2$ (sketched in dashed blue). The limit $\tilde{s} \to \infty$ corresponds to the noninteracting limit. In the repulsive case, $\tilde{s}$ is only used as a parametrization of the scattering length, that can have any dependence on a tunable parameter, and diverges when (another) resonance at $\tilde{s} = 0$ is approached adiabatically from the left. Although a bound state has to exist also at this resonance (sketched in dashed red), it is not taken into account in the calculations, assuming that it is adiabatically decoupled from the scattering states and inelastic scattering subdominant.

below the continuum threshold. The finite "background scattering length" (given by r_s in the soft-shell potential model above) plays a role in the characterization of Feshbach resonances, but a universal description is applicable in the region of diverging scattering length [29], where the resonance has exactly the shape modeled by the shell potential at its s-wave resonance, with a (hybrid) bound state that has exactly the same properties but is adiabatically connected to a closed-channel molecular state. Even though a Feshbach resonance is subject to enhanced particle losses and molecule formation at this universal regime [29], one should expect that the scattering states dominate the physics when the resonance is approached from below, as the molecular state is dynamically inaccessible well below the resonance. In contrast, the bound state should not be ignored, when tuning across the resonance from above, as the molecular state then connects to the continuum[10].

The above adiabatic exclusion of the bound state is assumed in the following, when "repulsive" interaction is considered, i.e., it is assumed that one can adiabatically tune the system from the noninteracting case to the vicinity of a resonance, where the scattering states are obtained adiabatically from the noninteracting states and the bound state can be ignored. This situation is exactly described by the soft-shell propagator for the "repulsive" interaction. Note that the parameters c and r_s of the soft-shell potential then lose their meaning for $a_s > r_s$ and are therefore not further used. Figure 1.11 summarizes the notion of "attractive" and "repulsive" interaction that is assumed here, and illustrates the parametrization through the parameter $\tilde{s} \propto a_s^{-1}$, that changes from ∞ to $-\infty$ when switching from attractive to repulsive.

[10]This can actually be used for adiabatic atom-molecule conversion in ultracold atomic gases [29]

1.5.3. The short-range interacting Bose gas

In this section, some of the methods of the previous sections are applied to a Bose gas with dominant s-wave scattering.

Nonlocal correlations

As a "low-hanging fruit", one can consider the nonlocal correlation function in the thermodynamic limit to leading order in its virial expansion (1.187). The universal density-independent part that dominates the high-temperature regime is given by

$$g_2(\boldsymbol{r}) = 1 + b_2^{(2)}(\boldsymbol{r}) \tag{1.220}$$

also in the case of three dimensions, where the first term corresponds to the "classical" correlation being constant. The function $b_2^{(2)}(\boldsymbol{r})$ only depends on the distance r of the particles and is easily calculated from (1.215) as

$$b_2^{(2)}(\boldsymbol{r}) = \mathrm{e}^{-4\pi\tilde{r}^2} + \frac{1}{\pi\tilde{r}^2}\mathrm{e}^{-4\pi\tilde{r}^2}\left[1 \pm \pi\tilde{s}\mathrm{e}^{4\pi(\tilde{r}+\tilde{s}/2)^2}\,\mathrm{erfc}\left(\mp\sqrt{4\pi}(\tilde{r}+\tilde{s}/2)\right)\right]. \tag{1.221}$$

Here, as before, the upper sign stands for the repulsive case (i.e., it excludes the bound state) while the lower sign is valid for the attractive case, also across the resonance. In the noninteracting case ($\tilde{s} \to \pm\infty$ for the attractive, respective repulsive case), only the first term remains, corresponding to the cyclic permutation of two particles. It describes thermal bunching of bosons, increasing the local correlations at $r = 0$ by a factor of two. When interactions are switched on, the correlations diverge at the origin as an artifact of the point-like approximation of the potential. One thus has to take into account a finite radius r_s of the interaction potential that is used as a lower cutoff in the distance or one can use the expression for the model shell-potential propagator for $r < r_\mathrm{s}$ given in Appendix C to obtain a regular expression also for this regime. However, when considering the radial distribution

$$g_2^{(\mathrm{rad})}(r) = \int d\Omega\, r^2 g_2(\boldsymbol{r}) = 4\pi r^2 g_2(r\boldsymbol{e}_r), \tag{1.222}$$

that is proportional to the probability of finding two particles in a distance r, the divergence is removed and yields finite correlations at the origin, that can only be positive, irrespective of the type of interactions, as the pair correlation has to be positive everywhere.

For completeness, let us also consider the scaling of the pair correlation function in specific limits. For an infinitesimal scattering length, one obtains

$$g_2(\boldsymbol{r}) = 1 + \mathrm{e}^{-4\pi\tilde{r}^2}\left[1 - \frac{4a_\mathrm{s}}{r}\right] + \mathcal{O}(a_\mathrm{s}^2), \tag{1.223}$$

valid for both attractive and repulsive regime, while first expanding g_2 with respect to r reveals the short-range scaling

$$g_2(\boldsymbol{r}) \approx 2\left(1 - \frac{a_\mathrm{s}}{r}\right)^2 \tag{1.224}$$

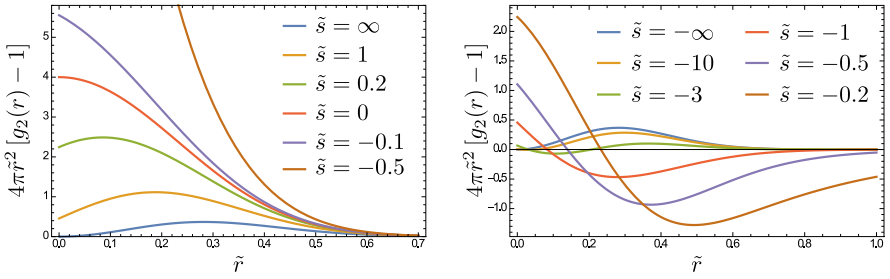

Figure 1.12: Leading order of the virial expansion of the nonlocal correlation function g_2 (with the trivial part 1 subtracted) for bosons with attractive (left) and repulsive (right) contact interactions. The probability of finding two particles at the same point ($\tilde{r}=0$) is enhanced in both cases. This is strongly enhanced in the attractive case for $\tilde{s}<0$, quickly diverging due to the bound state. The repulsive case is corrected by negative contributions for intermediate distances, effectively pushing the (everywhere positive) distribution outward.

valid for small scattering lengths $a_\mathrm{s}\ll 1$, as expected from Eq. (1.200). For $\tilde{s}=0$, i.e., for an infinite scattering length one obtains

$$g_2(\boldsymbol{r}) = 1+\mathrm{e}^{-4\pi\tilde{r}^2}\left(1+\frac{1}{\pi\tilde{r}^2}\right) \tag{1.225}$$

in both cases, with the bound state only having an influence on linear corrections in a_s^{-1}.

Figure 1.12 shows the nontrivial part of the radial distribution

$$\lambda_T(\mu)^{-2}\left[g_2^{(\mathrm{rad})}(r)-4\pi r^2\right] = 4\pi\tilde{r}^2 b_2^{(2)}(\boldsymbol{r}) \tag{1.226}$$

that only depends on the rescaled distance $\tilde{r}$ and interaction $\tilde{s}$, Eq. (1.216). The trivial metric term $4\pi r^2$ has been subtracted for better visibility. As was mentioned above, both attractive and repulsive interaction lead to an enhanced local pair correlation at $\tilde{r}=0$. However, while in the attractive case, the pair correlation increases everywhere due to the interaction, especially when $\tilde{s}<0$, the repulsive interaction leads to a reduction of the pair correlation for intermediate distances, effectively shifting the dominant radial distribution to higher values, i.e.,

$$4\pi\tilde{r}^2 \mapsto 4\pi(\tilde{r}-\epsilon)^2 \tag{1.227}$$

for $\tilde{r}\gtrsim 0.5$. The large enhancement at $\tilde{r}=0$ for large scattering lengths (small $|\tilde{s}|$) is incompatible with the intuition of a repulsive interaction, but this does not pose a problem as this picture is inadequate in the situation at hand, where $g_2(r)$ actually describes the scattering part of the nonlocal correlation function close to a resonance.

Despite the strikingly simple form of $g_2(\boldsymbol{r})$ and the straightforward derivation, the result (1.221) has not been reported to the best of the author's knowledge. The results

for the s-wave part of a gas of hard spheres can be calculated analytically without using the low-energy approximation [136, 137]. The results are equivalent for a small sphere radius compared to the thermal wavelength, i.e., in the regime where s-wave scattering is dominant.

The density of states

We are now in the position to actually calculate all the clusters that appear within the QCE(1) by using the general formulas (1.195) and (1.197) for the inter- and intra-cycle diagrams with the s-wave interaction correction (1.215). The calculations can be shortened a bit by using the fact that the interaction-independent part of (1.215) is exactly canceled in the noninteracting limit (given by $\tilde{s} \to \infty$ and $\tilde{s} \to -\infty$ in the attractive and repulsive regime, respectively) and thus is included in the coupling-dependent term. The calculation is straightforward, yielding for the repulsive case

$$a_\nu^{\text{inter/intra}}(s) = -\frac{1}{\pi}\frac{\nu}{1+\nu^2} + \frac{\nu^2}{\sqrt{\pi}\sqrt{1+\nu^2}}\sqrt{s} + \frac{\nu}{\sqrt{\pi}}\sqrt{s}\,\mathrm{e}^s\,\mathrm{erfc}\left(\sqrt{s}\right) - \frac{1+2\nu^2 s}{2}\left[\mathrm{G}_0^{(\nu)}\left((1+\nu^2)s\right) + \mathrm{e}^{(1+\nu^2)s}\,\mathrm{erfc}\left(\sqrt{(1+\nu^2)s}\right)\right]. \quad (1.228)$$

Here, to make the notation consistent, the coupling s is of the form

$$s = \pi\tilde{s}^2 \equiv \alpha\beta > 0, \qquad \alpha = \frac{\hbar^2}{\mu a_\mathrm{s}^2}, \quad (1.229)$$

and the function $\mathrm{G}_0^{(\nu)}$ is defined as

$$\mathrm{G}_0^{(\nu)}(s) = \frac{2}{\sqrt{\pi}}\mathrm{e}^s\int_0^\infty dz\,\mathrm{e}^{-\left(z+\sqrt{s}\right)^2}\,\mathrm{erf}(\nu z), \quad (1.230)$$

where the index 0 is only introduced for consistency with later definitions. For $\nu = 0$, i.e., in the case of a two-particle cluster, the expressions simplify to

$$a_0^{\text{inter/intra}}(s) = -\frac{1}{2}\mathrm{e}^s\,\mathrm{erfc}(\sqrt{s}). \quad (1.231)$$

In the attractive case, the scattering length can be either positive or negative. As the coupling s cannot have negative values, one has to introduce an additional parameter

$$\eta = -\,\mathrm{sgn}(a_\mathrm{s}) = \mathrm{sgn}(\tilde{s}) \quad (1.232)$$

to distinguish the two cases. Here, $\eta = 1$ represents the regime from the noninteracting case ($s \to \infty$) to the resonance ($s = 0$) while $\eta = -1$ covers the regime beyond the resonance, where the s-wave bound state is present. The result for the attractive case is then given by

$$a_\nu^{\text{inter/intra}}(s) = -\frac{1}{\pi}\frac{\nu}{1+\nu^2} - \eta\frac{\nu^2}{\sqrt{\pi}\sqrt{1+\nu^2}}\sqrt{s} + \eta\frac{\nu}{\sqrt{\pi}}\sqrt{s}\,\mathrm{e}^s\,\mathrm{erfc}\left(\eta\sqrt{s}\right) - \frac{1+2\nu^2 s}{2}\left[\mathrm{G}_0^{(\eta,\nu)}\left((1+\nu^2)s\right) - \mathrm{e}^{(1+\nu^2)s}\,\mathrm{erfc}\left(\eta\sqrt{(1+\nu^2)s}\right)\right]. \quad (1.233)$$

The function $\mathrm{G}_0^{(\eta,\nu)}$ is defined as

$$\mathrm{G}_0^{(\eta,\nu)}(s) = \frac{2}{\sqrt{\pi}}\mathrm{e}^s \int_0^\infty dz\, \mathrm{e}^{-\left(\eta z+\sqrt{s}\right)^2} \operatorname{erf}(\nu z). \tag{1.234}$$

Again, the result simplifies drastically for $\nu = 0$, yielding

$$a_0^{\text{inter/intra}}(s) = \frac{1}{2}\mathrm{e}^s \operatorname{erfc}(\eta\sqrt{s}) = \eta\frac{1}{2}\mathrm{e}^s \operatorname{erfc}(\sqrt{s}) + \Theta(-\eta)\mathrm{e}^s. \tag{1.235}$$

To obtain the density of states, one has to use these expressions to calculate first the partition function and then its inverse Laplace transform. This leads to the functions $g_{l,+}^{(N,d)}(\epsilon)$, Eq. (1.113), that alter the coefficients in the cluster expansion of $\bar{\mathcal{N}}^{(N,d)}(E)$. By using the expansion (1.134) of $\Delta_1 z_1^{(N,d)}$ into clusters one directly obtains

$$g_{l,+}^{(N,d)}(\epsilon) = 8\epsilon^{-\frac{ld}{2}} \sum_{n=2}^{N-l+1} n^{-\frac{d}{2}} z_{l-1,+}^{(N-n,d)} \sum_{n_1=1}^{n-1} \mathcal{L}_s^{-1}\left[s^{-\frac{ld}{2}-1} a_{\nu(n_1,n-n_2)}(s)\right](\epsilon), \tag{1.236}$$

where the labels for inter- and intra-cycle diagrams have been omitted, as the respective diagram values are the same. The inverse Laplace transforms in Eq. (1.236) can be explicitly performed for arbitrary l, but the calculations are rather technical and have therefore been moved to Appendix D.4, where also more general functions can be found that appear in the QCE(2).

The full QCE(1) can be readily applied to different particle numbers and various interactions for the cases of a homogeneous Bose gas ($d = 3$) and for harmonic trapping ($d = 6$). Figure 1.13 shows the repulsive case in a comparison of the QCE(1) results with the result from the first-order shifting method described in section 1.3.5 using the scaled variables $\alpha_{\mathrm{sc}}, E_{\mathrm{sc}}$, Eq. (1.142). As the QCE(1) result for the counting function $\bar{\mathcal{N}}^{(N,d)}$ takes negative values for small energies, the plots show the absolute values of $\bar{\mathcal{N}}^{(N,d)}$ in the respective approximations. The noninteracting limit $\alpha_{\mathrm{sc}} \to \infty$ is presented as a solid blue line in all plots. The left plot shows the case of three particles with very strong interactions, with $\alpha_{\mathrm{sc}} = 0$ corresponding to an infinite scattering length. As can be seen, both methods tend to the same results for large energies, but differ quite strongly at low energies, with the QCE(1) result even becoming negative in a whole range of energies that is well covered by the shifting method. The same behavior is seen for intermediate couplings $\alpha_{\mathrm{sc}} = 10$ in the right plot, where the counting function for $N = 8$ is shown for two different effective dimensions, with $d = 3$ corresponding to the homogeneous case and $d = 6$ describing harmonic confinement in short-time approximation. The QCE(1) result cannot be trusted up to very large excitations in both case, while the shifted counting function yields converged results for all relevant energies. In the case of $N = 8$ and $d = 6$, the energy of the result from the shifting method has been cut off at approximately $E_{\mathrm{sc}} = 0.5$, where the self-consistent solutions for the shifts start to wildly oscillate. This should, however, be attributed to numerical errors, also leading to numerically induced noise in the QCE(1) result at small energies (not shown).

When the particle number is increased, one can expect the shifts to become universal functions that only depend on the scaled energy E_{sc} and interaction α_{sc}, as well as the

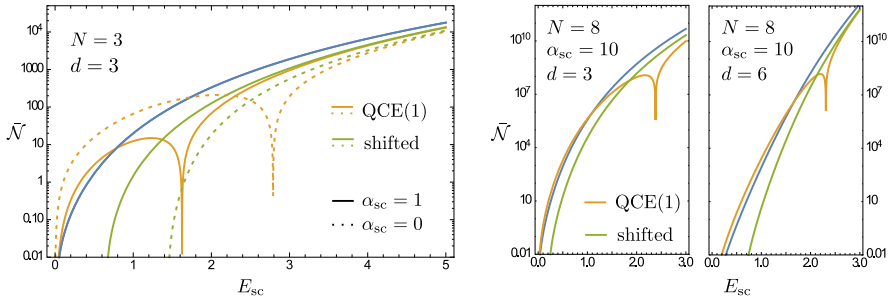

Figure 1.13: Smooth level counting function for the repulsive case calculated in the QCE(1) and with the shifting method for various particle numbers. The absolute value has been taken in the QCE(1) result to show that it has very large negative values left of the zero point that is visible in all plots as divergences due to the logarithmic scaling. The noninteracting result is shown in solid blue. Left: three particles with very strong interaction ($\alpha_{sc} = 0$ corresponds to an infinite scattering length). Right: Intermediate interactions for $N = 8$ and different effective dimensions (see labels), where $d = 6$ corresponds to harmonic trapping.

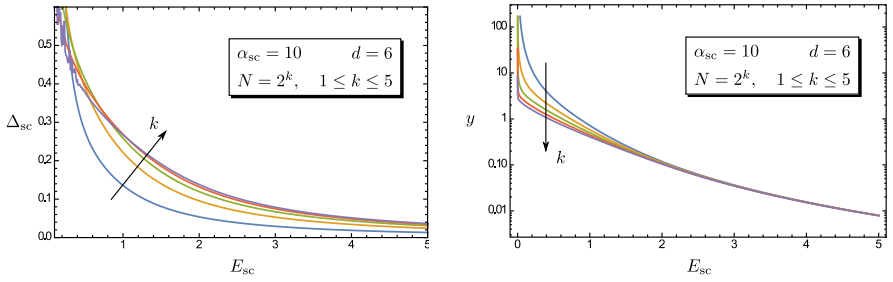

Figure 1.14: Scaling behavior of the scaled shifts Δ_{sc}, Eq. (1.170), with the particle number for the repulsive case (left) and the function $y \propto (N\bar{\mathcal{N}}^{(N)})^{-1/N}$, Eq. (1.162), for the noninteracting case (right) that are both expected to become intensive in the thermodynamic limit. Both functions quickly approach a universal limit with the interaction energy per particle given by Δ_{sc}.

effective dimension d, Eq. (1.104). This has been demonstrated for the Lieb-Liniger gas and harmonically trapped bosons in 1D in [60] and also holds true for the case at hand, as the difference in the theory is only due to the different physical dimensions. The asymptotic calculations are straightforward, but unfortunately have not been performed yet due to time constraints. To assess the applicability of the expected asymptotic universal functions, Fig. 1.14 shows the tendencies of the scaled shifts Δ_{sc}, Eq. (1.170), and the noninteracting function $y(E_{\mathrm{sc}}, \infty)$, Eq. (1.162), towards their limiting functions. The latter is used in the shifting method and should become an intensive quantity according to the asymptotic ensemble equivalence discussed in section 1.3.4, being verified here for noninteracting bosons with harmonic trapping. The calculated shifts in the left figure show numerical noise for $N = 16$ and $N = 32$ that stems from the Gamma functions and factorials that appear in the coefficients of the counting function, leading to large cancellations. This could be cured by increasing the accuracy, but the preferred approach should be the use of the asymptotic results that naturally include also the corrections of the function y for small energies through the amplitudes in Eq. (1.153) and should yield comparable results with less computational efforts.

Unfortunately, the author has not yet been able to compare the above results to full-fledged numerical calculations and/or experiments. The shifting method, in contrast to the QCE(1) is able to predict a mean energy shift of the noninteracting levels in a way that goes far beyond the perturbative regime, thus requiring the respective data for a wide range of energies and interactions to benchmark. This could be addressed using Monte-Carlo path integral approaches in the temperature regime similar to [17], but has not been done so far, and the results above have to be considered as work in progress. Also, although the results for the attractive interaction are also available here, they have not been used for bosons so far. However, the next subsection uses the attractive interaction for a small system of spin-1/2 fermions in a certain approximation.

1.5.4. The unitary Fermi gas—a few-particle perspective

A gas of spin-1/2 fermions with attractive short-range interactions in three dimensions is known to have very interesting properties. In the noninteracting case, the gas can be described by a Fermi sea with excitations above it. However, already for weak attractive interactions, this Fermi sea becomes unstable and the BCS theory of superconductivity predicts a pairing of particles with opposite spin and momentum to Cooper pairs [12], that are, however, not localized in space. For stronger attractive forces, bound states of the relative potentials allow for the formation of molecules that get localized in space, with the most favorable configuration being the pairing of two fermions with opposite spin, i.e., singlet states, as the interaction between two fermions with the same spin is suppressed due to the Pauli principle that forces the wave function to vanish at short distances. If the pairing forces are strong enough, the molecules can be described as composite bosons with a weak residual interaction, leading to Bose-Einstein condensation at low temperatures. Although the two limits seem to behave quite different at first glance, suggesting a transition between different types of physics, they are actually adiabatically connected by a crossover known as the BCS-BEC crossover [131, 138]. De-

spite both limits being well understood, the crossover regime hosts complicated physics and does not allow for a mean-field description due to strong many-body correlations. One can define a special point in the crossover that is characterized by the divergence of the two-body scattering length when a zero-energy molecular state is formed. This is referred to as the unitary point or unitary limit, as the s-wave scattering cross section

$$\sigma_0 = \frac{4\pi}{k^2}\sin^2\delta_0 \to \frac{4\pi}{k^2} \tag{1.237}$$

assumes its maximally allowed value, only restricted through the unitarity of the scattering matrix. Note that the fermions can only interact through s-wave scattering if they have different spin due to the Pauli principle. In the unitary limit (and at low enough temperatures), the physics should become independent of the length scales of the interaction potential, such that it can be modeled by a zero-range potential. For the latter, being an effective description in terms of boundary conditions of the wave function, a series of exact relations have been derived, known as Tan's relations [139–141] that introduce a quantity known as Tan's contact that describes the short-range correlations, but also appears in the spectral properties and can be calculated from an analogue of the Hellmann-Feynman theorem named as "adiabatic sweep theorem" by it's inventor,

$$\frac{\partial E}{\partial(-1/a_\mathrm{s})} = \frac{\hbar^2 V C}{4\pi m}, \qquad C = \lim_{|\boldsymbol{k}|\to\infty} k^4 n_{\boldsymbol{k},\sigma}. \tag{1.238}$$

Here, C is Tan's contact and $n_{\boldsymbol{k},\sigma}$ is the momentum distribution of the particles with spin σ. The energy E is thereby associated to any stationary state. The contact, as a measurable quantity [142], has attracted a lot of attention especially in the description of the crossover regime (see, e.g., [88, 143, 144] and references therein) as a nontrivial quantity in a highly correlated system.

It is, however, worth noting that the sweep relation for the contact shows that it is directly connected to the energy shift due to the finite inverse scattering lengths as they appear in the applications considered here. To be specific, the shifting method used for bosons directly outputs the quantity that defines the contact for a generic eigenstate. It would thus be desirable to calculate the contact using the methods introduced here. However, this has not been done to date, but a first attempt that used the large N asymptotic expressions (i.e., the stretch exponential form of the density of states) did not yield satisfactory results when approaching the unitary limit, where some results are available in the literature. Instead, this section concentrates on the calculation of the cluster expansion for four fermions as a first testing ground for the applicability of the shifting and to reproduce the physics of the whole range of interactions (of course not observing superconductivity in this few-particle system).

The QCE(1) is obviously not capable of producing two molecular states, as it contains only a single two-particle bound state. Thus, to cover also the limit of two (composite) bosons interacting via a residual interaction one has to include also the QCE(2) diagrams. However, as only the interaction contributions of second order, associated with the second Ursell operator, is known, the higher interaction contributions are left out. They are expected to be subdominant, as they have to involve at least two identical

particles, and the Pauli principle leads to a vanishing of the three-body wave functions when the three particles are close to each other, suppressing the three-body effects. The corresponding suppression has also been observed [61] in the context of the related dynamical impurity model in 1D, where already the QCE(1) yields fully satisfactory results. Of course, there is also an interaction contribution of fourth order, but it is neglected with the same argument. The diagrammatic representation of the approximate canonical partition function is thus

$4Z^{((2,2))} =$ 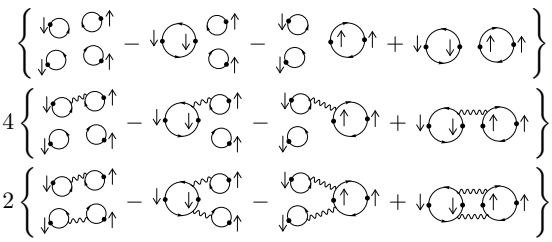

(1.239)

where the first line contains the QCE(0) (i.e., noninteracting), the second the QCE(1), and the third line contains those diagrams of the QCE(2) that only involve pairs of interacting particles. The explicit labels for the spins (arrows) are only needed to determine the allowed diagrams and can be omitted once these diagrams have been found, as they have no influence on the values of the diagrams. Note that the diagrams have the same multiplicities in each line, while their signs are different, depending on the number of exchange permutations. The diagrams of the QCE(1) have been calculated already in the last subsection, and their contribution to the partition function can be directly written down as [again omitting the intra/inter label on the functions $a_\nu(s)$]

$$\Delta_1 Z^{((2,2))} = 8\left[2^{-\frac{d}{2}} a_0(s)\left(\frac{V_{\text{eff}}}{\lambda_T^d}\right)^3 - 2\times 3^{-\frac{d}{2}} a_{\frac{1}{\sqrt{3}}}(s)\left(\frac{V_{\text{eff}}}{\lambda_T^d}\right)^2 + 4^{-\frac{d}{2}} a_1(s)\left(\frac{V_{\text{eff}}}{\lambda_T^d}\right)^1\right]. \tag{1.240}$$

The first diagram in the QCE(2) is just the product of two such diagrams and is thus also known. The last diagram can be expressed in terms of known diagrams by using the completeness relation of the full two-particle propagator, yielding the general diagrammatic relation valid for arbitrary interactions

(1.241)

Note that the irreducible four-particle QCE(1) diagrams are exactly canceled by the second term. Thus, the only missing diagrams to be calculated are the second and third diagram of the QCE(2), that both have the same value. As was the case for the QCE(1), the diagram can be reduced to single integrals and one finally obtains the expressions

for all the above QCE(2) diagrams as

$$= 64 \times 2^{-d} a_0^2(s) \left(\frac{V_{\text{eff}}}{\lambda_T^d}\right)^2, \tag{1.242}$$

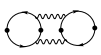

$$= 8 \frac{V_{\text{eff}}}{\lambda_T^d} 4^{-\frac{d}{2}} [a_0(2s) - 2a_1(s)], \tag{1.243}$$

$$= -32 \frac{V_{\text{eff}}}{\lambda_T^d} 4^{-\frac{d}{2}} \left\{ 4\, \mathrm{G}_0^{(\eta,\sqrt{2})}(4s) - 4\, \mathrm{H}_0^{(\eta,1,\sqrt{2})}(4s) \right\}, \tag{1.244}$$

with the function $\mathrm{G}_0^{(\eta,\nu)}$ defined in Eq. (1.234) of the last subsection and the function

$$\mathrm{H}_0^{(\eta,\lambda,\mu)}(s) = \frac{2}{\sqrt{\pi}} \mathrm{e}^s \int_0^\infty dz\, \mathrm{e}^{-\left(\eta z + \sqrt{s}\right)^2} \operatorname{erf}(\lambda z) \operatorname{erf}(\mu z). \tag{1.245}$$

By reordering according to powers of $V_{\text{eff}}/\lambda_T^d$ one obtains the coefficients $\Delta z_l^{(N,d)}$ in Eq. (1.108),

$$\Delta z_3^{(4,d)}(s) = 8 \times 2^{-\frac{d}{2}} a_0(s), \tag{1.246}$$

$$\Delta z_2^{(4,d)}(s) = 16 \left[2^{1-d} a_0^2(s) - 3^{-\frac{d}{2}} a_{\frac{1}{\sqrt{3}}}(s) \right], \tag{1.247}$$

$$\Delta z_1^{(4,d)}(s) = 4 \times 4^{-\frac{d}{2}} \left\{ a_0(2s) - 8 \left[4\, \mathrm{G}_0^{(\eta,\sqrt{2})}(4s) - 4\, \mathrm{H}_0^{(\eta,1,\sqrt{2})}(4s) \right] \right\}, \tag{1.248}$$

that then define the coefficient functions $g_l^{(4,d)}(\epsilon)$ in the level counting function (1.112) according to Eq. (1.113). The required inverse Laplace transforms can be found in Appendix D.4. Although the results above are valid also for homogeneous external potentials, the results for the inverse Laplace transform of $s^{-d/2}\, \mathrm{H}_0$ is only given as a closed form expression for odd effective dimension d. Although the case of even dimensions can be easily implemented using a semi-analytical approach with one single numerical convolution integral being required, only the case without external potentials is discussed here.

Figure 1.15 shows a comparison of the QCE(1) predictions and the prediction from including the diagrams from the QCE(2). There, the natural dimensionless coupling parameter

$$\rho_{\text{eff}} \alpha = \frac{1}{\pi} \left(\frac{V^{\frac{1}{d}}}{a_{\text{s}}} \right)^2 \tag{1.249}$$

is used, that emerges when the energy is expressed in terms of the energy unit ρ_{eff}^{-1}, Eq. (1.114). As can be seen, both approximations yield similar results for the regime with negative scattering length, i.e., $\eta = 1$, where no bound states are available. This is demonstrated in green for a rather strong coupling $\rho_{\text{eff}} \alpha = 1$. Unfortunately, the QCE(2) result suffers from oscillations for small energies, yielding unphysical negative values for $\bar{\mathcal{N}}$ there. In the presence of the bound states, i.e., for $\eta = -1$, the two results start to differ also for large excitations (orange) and when approaching the regime of large

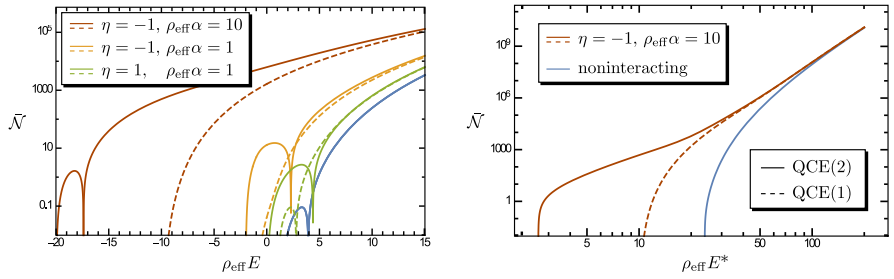

Figure 1.15: Left: Comparison of the predicted level counting functions (absolute value) from QCE(1) (dashed) and including multiple pairs from QCE(2) (solid) for various values of the coupling. For the regime with negative scattering length ($\eta = 1$), the two results are comparable for $\bar{\mathcal{N}} \gtrsim 10$, but the QCE(2) diagrams lead to noticeable oscillations at small energies. For positive scattering lengths, this problem persists at small α (large scattering length) but for larger α, the QCE(1) fails. Right: Double-logarithmic plot of the data from the left plot for $\rho_{\rm eff}\alpha = 10$, showing the different power law behavior of the QCE(2) at low energies, where only a pair of (bosonic) molecules is energetically possible.

$\rho_{\rm eff}\alpha$, the QCE(1) result cannot reproduce the shift that comes from two bound pairs. To verify the two-molecule character of the low-energy regime for this case, the right plot shows a double-logarithmic plot of the level counting function against the energy excitation $E^* = E + 2\alpha$ above the theoretical energy minimum $E = -2\alpha$ corresponding to the two bound pairs being at rest. One can clearly see a change in the power law around $E \approx 0$ (i.e., $E^* \approx 20\rho_{\rm eff}^{-1}$), where the two (bosonic) pairs can be broken up into four fermions and the largest exponent of the energy in the polynomial form of the level counting function changes from $2d/2$ to $4d/2$. There is also a regime $-\alpha < E < 0$ where one molecule and two fermions can coexist, but one has to use very strong couplings $\rho_{\rm eff}\alpha \gg 1$ to resolve it (not shown).

The result for the level counting function in the regime $-2\alpha \leq E < -\alpha$, where only the two bound states are energetically available, is actually very simple and directly reflects the bosonic character of the molecules. Defining $E^* = E + 2\alpha$ one obtains for this regime

$$\bar{\mathcal{N}}^{\rm pairs}(E^*) = \frac{(2\rho_{\rm eff}E^*)^3}{12} + \frac{(2\rho_{\rm eff}E^*)^{\frac{3}{2}}}{3\sqrt{2\pi}}\left[1 - g^{\rm pairs}\left(\frac{2\rho_{\rm eff}E^*}{\rho_{\rm eff}\alpha}\right)\right], \tag{1.250}$$

with the effective interaction of the pairs

$$g^{\rm pairs}(\epsilon^*) = 8^2\left(\frac{\epsilon^*}{4}\right)^{-\frac{3}{2}}\left[\left(1 + \frac{\epsilon^*}{4}\right)^{\frac{3}{2}} - \left(1 + \frac{3}{2}\frac{\epsilon^*}{4}\right)\right]. \tag{1.251}$$

By comparing this to the counting function for two bosons with contact interaction,

$$\bar{\mathcal{N}}^{(2)}(E) = \frac{(\rho_{\text{eff}} E)^3}{12} + \frac{(\rho_{\text{eff}} E)^{\frac{3}{2}}}{3\sqrt{2\pi}} \left[1 - g\left(\frac{E}{\alpha}\right)\right], \tag{1.252}$$

$$g(\epsilon) = 8\epsilon^{-\frac{3}{2}} \left[(1+\epsilon)^{\frac{3}{2}} - \left(1 + \frac{3}{2}\epsilon\right)\right], \tag{1.253}$$

one finds that the system does, indeed, behave like two bosons with twice the mass of the fermions, as $\rho_{\text{eff}} \propto m$ and $\rho_{\text{eff}}\alpha$ is mass-independent, but with a renormalized interaction

$$g^{\text{pairs}}(\epsilon^*) = 8g\left(\frac{\epsilon^*}{4}\right), \tag{1.254}$$

where the factor 8 cannot be removed by a redefinition of the coupling in general. However, for small scattering lengths one directly finds

$$a_{\text{s}}^{\text{pairs}} = 4a_{\text{s}} \tag{1.255}$$

for the scattering length of the pairs. Unfortunately, this overestimates the dimer-dimer scattering length for a zero-range potential $a_{dd} = 0.6a_{\text{s}}$ close to a Feshbach resonance [145] and is moreover incompatible with the mean-field prediction $a_{dd} = 2a_{\text{s}}$ [131]. The reason lies probably in the approximation of neglecting a whole class of diagrams. Still, the discrepancy is surprisingly large, and the fact that the two scattering lengths cannot be directly related due to the factor 8 in (1.254) is also puzzling when considering the otherwise identical form of the interaction. However, as the above results are to be seen as work in progress, this will not be further analyzed here.

1.6. Summary and concluding remarks

In this part of the thesis, the general tool of quantum cluster expansions has been reviewed, also generalizing the known results to include spatial information that is usually not accounted for in the applications so far. Especially with the generalization to multiple species, the full potential of the cluster expansion has been explored on an exact level, where all the combinatorial complexity has been reduced to simple recursive formulas.

After this exact analysis, the semiclassical short-time approximation has been introduced, implying a very general dimensional scaling of moderate- to high-temperature equilibrium expectation values. The short-time approximation results in a smoothed spectrum and *defines* the smooth part of the density of states, but as the approximation is done on the level of propagators, it is also applicable to arbitrary correlation functions, as has been shown in later sections. However, before doing so, the expected thermodynamic limit properties of the cluster expansion and the resulting ensemble equivalence was used to rederive a version of the "shifting method" introduced in [60], with a focus on its expected scaling in the thermodynamic limit.

As a main application, the cluster expansion for the nonlocal pair correlation function in the extended Lieb-Liniger model has been calculated analytically up to three-body clusters, and its usefulness for finite systems has been demonstrated by direct comparison with the respective numerical results. To demonstrate the general applicability of the dimensional scaling in short-time approximation as a semi-analytical tool, the four- and five-body clusters have been calculated numerically and were then used to analytically predict the behavior in different parameter regimes. All this was supplemented by full-fledged numerical calculations based on the Bethe ansatz solutions of the Lieb-Liniger model, and the validity of the short-time approximation was verified, showing that it is applicable even very close to the quantum degenerate regime. Apart from this validation of the short-time approximation, the analytical results are of interest in their own, as the analytical results obtained with the methods used here have not been reported in the literature before and compare well with available numerical results for the thermodynamic limit correlations in the respective regimes.

Although the correlations in quasi-one-dimensional systems are experimentally in reach nowadays, the rest of this part of the thesis was dedicated to the three-dimensional applications. First, the calculation for a certain class of irreducible diagrams was performed for spherically symmetric interaction potentials, reducing the effort of their calculation to the simpler one-dimensional radial description in partial wave decomposition. Then, a simple finite-range model potential was introduced to convey to the reader the naively counter-intuitive implications of zero-range limits of interaction potentials in three-dimensions. The latter naturally led to a description of resonances, with the analytic behavior around their vicinity being universal to some extent, irrespective of their physical origin, such that the results for the model potential can be used to describe also Feshbach resonances, that are commonly used in experiments.

This was done in the final subsections. In a first application, a new prediction for the virial coefficient of the normalized nonlocal pair correlation function was presented. Although explicitly given for bosons only, the result for fermions can be obtained straight-

forwardly. Then, the shifting method for the density of states was applied to a system of repulsively interacting bosons and was compared to the more complicated calculation of the quantum cluster expansion of order one. This was done for translationally invariant systems as well as for bosons that are confined by harmonic trapping. The results suggest that the shifting method is applicable in a larger energy regime, and noting that it is much easier to implement also renders it the preferred approach for this type of task. Nevertheless, the predictions still await numerical and experimental verification. Finally, the cluster expansion (equipped with the semiclassical short-time approximation) was applied to a system of four fermions across the unitary regime of infinite scattering length, showing the qualitatively correct behavior in all regimes, however also revealing certain shortcomings that stem from the introduced approximations.

Altogether, the methods presented in this chapter have proven as powerful tools that allow for the description of the equilibrium properties of quantum gases down to very low temperatures, also enabling the analysis of correlations that go beyond the standard thermodynamic descriptions. The neglect of the highly system-dependent level fluctuations in the many-body density of states has provided a unified description of regimes from very low to infinite temperatures that only depends on a few parameters and can thus be applied to whole classes of systems. However, the smoothness assumption is certainly not fulfilled at all temperatures, and the ground-state properties become dominant in the zero-temperature limit. Although the predicted smooth many-body level densities can reproduce the positions of noninteracting many-body ground states remarkably well if subleading corrections (e.g., boundary corrections) in the Weyl expansion are taken into account [52], the exact ground state properties are highly system-dependent and require a different approach. Moreover, methods of cluster expansion in short-time approximation with *imaginary* time are not devised for non-equilibrium (real-time) dynamics in quantum systems. Although the short-time approximation may be applied, it is the discrete frequency spectrum that determines the long-time dynamics, which cannot be captured in the methods of this chapter. Therefore the next chapter takes a complementary semiclassical approach that is capable of both describing individual quantum states down to the ground state in nonperturbative regimes as well as making nontrivial predictions for the quantum time evolution.

2. A semiclassical treatment of quantum critical phenomena

2.1. Introduction and concepts

One of the most interesting and important phenomena in the equilibrium physics of macroscopic bodies is, apart from the existence of an emergent description of the state in terms of only a few parameters, the possibility of a system behaving very differently depending on macroscopic parameters, although the microscopic model and its ingredients are the same in all so-called phases. Transitions between phases range from everyday life examples like the melting of ice to water and vaporization of the latter, over magnetic transitions in metals, to highly nontrivial effects like the emergence of superconductivity at very low temperatures. Although the existence of the different phases is clearly evident from experience, the theoretical description of the phenomenon has proven a difficult task. One reason for this is the emergence of nontrivial long-range correlations between particles when approaching the transition, such that their mutual interaction has to be fully accounted for (as opposed to the situation away from the transitions, where effective descriptions are often sufficient). Another difficulty lies in the fact that for finite systems the thermodynamic potentials, being derived from the statistical ensembles, are analytic functions of the system parameters, while phase transitions and critical phenomena are characterized by a non-analytic behavior that emerges in the thermodynamic limit. This non-analyticity defines the order of the transition as the lowest order derivative of the thermodynamic potential that is not continuous (Ehrenfest classification [146]).

2.1.1. Theoretical description of phase transitions

After a first phenomenological description of the liquid-gas transition was found by van der Waals in his famous equation of state (requiring the ad hoc Maxwell construction) [62], more elaborate mean-field techniques were developed. Landau's heuristic theory for phase transitions [147], based on general assumptions on the possible analytic form of the thermodynamic potential, allows for a systematic analysis around critical points in the parameter space, also introducing the general scaling of thermodynamic susceptibilities close to these points, leading to the concept of critical exponents that further characterize the transition by introducing algebraic scaling relations of susceptibilities χ of the form

$$\chi \sim (T - T_c)^{\nu}, \tag{2.1}$$

where T_c defines the (finite) critical temperature. A more fundamental analysis of these exponents that directly connects to microscopic models is obtained in the framework of

the renormalization group (RG) analysis [148, 149], incorporating the intuitive picture of macroscopic descriptions emerging from coarse-grained microscopic models. The RG analysis also establishes a notion of universality of the critical exponents, as they can be considered as properties of the RG rather than being associated to a specific system.

As it turns out, the RG analysis shows that the results from mean-field theories are valid only for dimensions above a critical dimension d^*, while thermal and/or quantum fluctuations become crucial below it [150]. However, this does not mean that fluctuations are not important above d^*, as they are actually the driving force behind the transition: A phase transition can be characterized by a certain order parameter (e.g., the magnetization) that reflects the long range correlations in the system. In the case of an actual broken symmetry, the fluctuations provide the necessary uncertainty in the microscopic degrees of freedom to restore this symmetry across the transition.

In the theories for critical phenomena mentioned above, it is usually the thermal fluctuations that are responsible for the critical behavior, leading to a finite critical temperature and a phase transition that is then said to be classical, even though the underlying physics can be of pure quantum nature, as is the case, e.g., in superconductivity. This is due to the fact that the thermal fluctuations are always dominant if the critical temperature is greater than zero [151]. At zero temperature, when thermal fluctuations are absent, the quantum fluctuations become important and can drive a *quantum* phase transition. This requires a system parameter g other than the temperature to characterize the position of the critical point, and, as the system remains in its ground state at zero temperature, the effect of the variation of this parameter has to have drastic effects on this ground state. In most cases, the formalisms of the classical phase transitions can be directly transferred to the quantum case by treating the imaginary time dimension, that represents the inverse temperature[1], analogous to a space dimension [151, 152]. Although this also leads to a characterization in terms of critical exponents, the fixed points of the RG flow (i.e., the critical points) can have very different behavior in the (imaginary) time- and spatial directions and thus have a larger set of universality classes [152]. On the other hand, the fact that the phase transition occurs at zero temperature can simplify the situation in that only the low-energy properties of the system are relevant for its characterization, such that a direct analysis of the low-lying quantum states can be performed. In particular, the fundamental energy gap Δ that separates the ground state and the first excited state can be used for a characterization of the transition, as the way the gap closes at criticality is characterized by an exponent ν

$$\Delta \sim (g - g_c)^{\nu}, \tag{2.2}$$

where g_c is the critical value of a coupling g that can be tuned by varying system parameters [152].

As a standard tool in mean field analysis, Bogoliubov theory can be applied to find low-lying excitations above a many body ground state. It can sometimes even be used as a tool to detect a transition as the point where Bogoliubov spectrum around the

[1] This formally results from the trotter decomposition of the partition function in imaginary time that is required to write the partition function in the usual form of an exponential of an action.

ground state of the system becomes imaginary [153], hence hinting at an instability of the respective "ground state". But this also means that this mean-field theory, although applicable on both sides of the transition, breaks down at the transition point and its influence on the dynamical properties of the system close to this point cannot be accounted for, as they are then dominated by the quantum fluctuations beyond the mean-field picture. This is where semiclassical methods can enter the game, as they can be used to systematically improve mean field approximations by accounting for finite size effects and correlations that are neglected in mean field approaches. To be specific, the mean-field as a large-N approximation, where N is the particle number, can be viewed as a classical $\hbar_{\text{eff}} = 1/N \to 0$ limit of a quantum system, and semiclassical methods that are well-established in the single-particle context, can be applied to find non-perturbative corrections in terms of the small parameter $\hbar_{\text{eff}}$, while treating the (real) Planck constant as a system parameter.

2.1.2. The quantum – classical correspondence

The semiclassical methods that have been introduced mainly in the context of single or few-particle systems in the past decade rely on the quantum-classical correspondence, i.e., they use the experience and intuition from classical mechanics to get a better understanding of the quantum physics. Although the starting point is often a quantum system in modern approaches, and classical dynamics can emerge unambiguously in certain approximations, one is often faced with the problem of directly associating a classical system to a quantum system (classical limit) and vice-versa (quantization). One needs to point out, however, that there is no direct correspondence of quantum and classical systems in general, as the commutativity of classical conjugate variables is replaced by non-commuting operators in quantum mechanics. This does not lead to any difficulties in the quantization of simple mechanical systems with an classical Hamiltonian function of the form

$$H(q,p) = \frac{p^2}{2m} + V(q), \tag{2.3}$$

as replacing the classical variables by quantum operators

$$q \mapsto \hat{q}, \qquad p \mapsto \hat{p}, \qquad \{q,p\} \mapsto [\hat{q},\hat{p}] = i\hbar \tag{2.4}$$

will not lead to any mixed terms that are sensitive to ordering of operators due to the commutator relation (the expression $\{q,p\}$ is the Poisson bracket). This is not true in general, however, and leads to a contradiction already at the level of the simple Hamilton function (2.3) if a canonical transformation is applied, that mixes the coordinates q and p, e.g., by defining $Q = (q-p)/\sqrt{2}, P = (q+p)/\sqrt{2}$ and then quantizing Q and P instead. The same can be done for any rotation of the original coordinates, leading to a continuum of classical models that are canonically equivalent, but with ambiguous quantization rules. Moreover, one can find general examples that rule out the possibility to define a unique quantum-classical correspondence of the kind (2.4) using the Poisson bracket and the commutator [154]. Therefore, one usually applies the convention that polynomial expressions in the variables q, p are brought into symmetric form before quantization,

which removes the ambiguity at the level of quadratic polynomials. However, one should note that this can lead to divergent terms in the quantization of field theories, that have to be eliminated (e.g., by attributing them to an infinite vacuum energy that drops out in the calculations).

Although the quantization of classical systems was historically the first task to accomplish when quantum mechanics was developed, it is the quantum description that should be viewed as the (more) fundamental one, and one should rather ask the question, whether one can define a corresponding classical model. In many cases, this can be done unambiguously by noting that all contributions due to reordering of operators should be considered as quantum corrections that depend on Planck's constant $\hbar$ and should thus be neglected in a classical description. This is, of course, not true for, e.g., spin systems, where $\hbar$ sets the energy scale and thus cannot be neglected, emphasizing the fundamentality of their quantum description.

However, simply replacing operators by classical variables and dropping the "quantum" terms that contain $\hbar$ oversimplifies the problem, as it completely ignores the dynamical aspects of both theories and suggest that one can obtain classical mechanics simply as a perturbative expansion in the small parameter $\hbar$. Instead, the unitary time evolution in quantum mechanics turns out to be non-analytic in $\hbar$, as can directly be seen in the case of a time-independent system, where the time evolution operator assumes the form

$$\hat{U}(t,t_0) = \mathrm{e}^{-\frac{\mathrm{i}}{\hbar}\hat{H}(t-t_0)}. \tag{2.5}$$

Its form suggests that one should actually think of classical mechanics as emerging from an asymptotic expansion in a *large* parameter $1/\hbar$. This idea can be made explicit by expanding the quantum-mechanical propagator into a Feynman path integral [8] [assuming a Hamiltonian of the form (2.3)]

$$\langle q_f|\hat{U}(t,t_0)|q_i\rangle = \int_{q(t_0)=q_i}^{q(t)=q_f} \mathrm{D}[q]\mathrm{e}^{\frac{\mathrm{i}}{\hbar}\int_{t_0}^{t} L(q,\dot{q},t)} \tag{2.6}$$

that can then be evaluated in a stationary phase approximation [2]. The stationary phase condition is then equivalent to Hamilton's principle of classical mechanics, if the function $L(q,\dot{q},t)$ is taken as a classical Lagrange function, showing that the classical dynamics emerges from an asymptotic, rather than a perturbative expansion. Analogous steps can be performed also if the Hamiltonian assumes a more complicated form, where the p-integration leading to the familiar form (2.6) cannot be performed explicitly [8]. Then, one obtains coupled stationary phase conditions (in the form of Hamilton's equations of motion), that again generate the classical dynamics. Although this is not carried out in detail here, one should note that the large parameter does not have to be $1/\hbar$, but could, in principle, be anything. For example, in bosonic many-body systems, where the number of particles N can be used as the relevant large parameter, one can obtain a different "classical" limit that describes the mean-field dynamics, while the reduced Planck constant $\hbar$ is merely a parameter. To make the analogy explicit, one often defines an effective Planck constant $\hbar_{\mathrm{eff}}$ in such situations, i.e., $\hbar_{\mathrm{eff}} = 1/N$ for the above mean-field limit.

2.1.3. Phase-Space Representations

Although the asymptotic expansion of the path integral can be used in many cases as an elegant derivation of a classical limit, common approaches use uncontrolled approximations when taking the continuum limit in the path integral, i.e., continuity of certain quantities is assumed, although the latter can only be guaranteed for specific functional forms of the Hamiltonian, thus leading to wrong results in general already at the level of the full path integral [155]. This can be especially problematic in coherent state path integrals that are used in the many-body context.

A more direct approach that does not require functional analysis can be obtained by using phase space representations of the quantum operators and their dynamical equations. In the context of many-particle systems, this is best done using the coherent states [156]

$$|\boldsymbol{\alpha}\rangle = \prod_i \mathrm{e}^{-\frac{|\alpha_i|^2}{2}+\alpha_i \hat{a}_i^\dagger}\,|0\rangle \tag{2.7}$$

satisfying

$$\hat{a}_i\,|\boldsymbol{\alpha}\rangle = \alpha_i\,|\boldsymbol{\alpha}\rangle\,, \tag{2.8}$$

where $\hat{a}_i^\dagger$ creates particles in mode i and $\boldsymbol{\alpha} = (\alpha_i)$ are complex numbers associated with the coherent states of each individual mode. For simplicity, let us concentrate on the case of a single mode here, as the operators for different modes commute and thus do not introduce complications.

The Wigner function associated to a density matrix $\hat{\rho}(t)$ is then defined as [156]

$$W(\alpha,\alpha^*,t) = \frac{1}{\pi^2}\int d^2z\ \mathrm{Tr}\left\{\hat{\rho}(t)\,\mathrm{e}^{z\hat{a}^\dagger - z^*\hat{a}}\right\}\mathrm{e}^{z^*\alpha - z\alpha^*}, \tag{2.9}$$

with the integration being defined as $d^2z = d\Re(z)\,d\Im(z)$. For other operators $\hat{A}(\hat{a},\hat{a}^\dagger)$, represented by the creation and annihilation operators, the Weyl transform (or Weyl symbol) is defined in the same way by replacing the density operator by $\pi\hat{A}$, i.e.,

$$A(\alpha,\alpha^*,t) = \frac{1}{\pi}\int d^2z\ \mathrm{Tr}\left\{\hat{A}(t)\,\mathrm{e}^{z\hat{a}^\dagger - z^*\hat{a}}\right\}\mathrm{e}^{z^*\alpha - z\alpha^*}, \tag{2.10}$$

where the Heisenberg picture was used and $t = 0$ corresponds to the Schrdinger form of the operator (no explicit time dependence of $\hat{A}$ for simplicity). If the operator is of polynomial form in the operators $\hat{a},\hat{a}^\dagger$, as is usually the case for many-body Hamiltonians, the resulting phase-space function can be directly obtained by symmetrically ordering all the operators and then replacing them with complex variables [154,157] according to

$$\hat{a} \mapsto \alpha, \qquad \hat{a}^\dagger \mapsto \alpha^*. \tag{2.11}$$

The expectation value of the (Schrödinger) operator $\hat{A}$ is then obtained from its corresponding (time-independent) phase space function $A(\alpha,\alpha^*)$ as a phase space average using the Wigner quasi-distribution,

$$\mathrm{Tr}\{\hat{\rho}\hat{A}\} = \int d^2z\,A(\alpha,\alpha^*)W(\alpha,\alpha^*,t). \tag{2.12}$$

One can further formalize the phase-space description by introducing the phase space equivalent of the operator product, called the Moyal star product [158]. The latter is usually represented in real variables q, p, but can also be written using complex phase space variables as

$$\star = \mathrm{e}^{\frac{1}{2}\left(\overleftarrow{\partial}_\alpha \overrightarrow{\partial}_{\alpha^*} - \overleftarrow{\partial}_{\alpha^*} \overrightarrow{\partial}_\alpha\right)}, \tag{2.13}$$

where the arrows denote that the derivative operators act to the left or to the right factor in a product. With this, the time evolution of the Wigner function is given by [157]

$$\partial_t W = \frac{1}{i\hbar}\left(H \star W - W \star H\right) \equiv \{\{H, W\}\}, \tag{2.14}$$

were the final expression defines the Moyal bracket and $H = H(\alpha, \alpha^*)$ is the Weyl symbol for the Hamiltonian. Equation (2.14) can be directly identified as the phase-space analogue of the von Neumann equation for the density matrix. By applying the Weyl transform to the Heisenberg equation of motion one directly obtains the equation of motion for arbitrary phase space functions [159]. For the time-evolved annihilation operator, one obtains[2]

$$\dot{\alpha} = \partial_t \alpha = \{\{\alpha, H\}\}. \tag{2.15}$$

This is straightforwardly generalized to the situation of having different operators $\hat{a}_i$, leading to coupled equations of motion.

To make contact to classical dynamics, one can assume that the operators $\hat{a}^{(\dagger)}$ and their phase-space analogues $\alpha^{(*)}$ are of the order $\hbar_{\mathrm{eff}}^{-1/2}$. In the context of single-particle physics, the variable α is the classical analogue of a ladder operator of a harmonic oscillator,

$$\alpha = \frac{m\omega q + ip}{\sqrt{2m\hbar\omega}}, \tag{2.16}$$

and one has $\hbar_{\mathrm{eff}} = \hbar$. On the other hand, in bosonic many-body systems, the creation and annihilation operators can be viewed as being proportional to the square-root of the occupation of the state that they are applied to, leading to an effective Planck constant $\hbar_{\mathrm{eff}} \sim 1/N$ by rescaling the operators and their phase space analogues with the particle number and treating $\hbar$ as a parameter. In both cases, the Moyal bracket with the Weyl symbol H of the Hamiltonian can be written as

$$\{\{f, H\}\} = \frac{\hbar_{\mathrm{eff}}}{\hbar}\{f, H\} + \mathcal{O}(\hbar_{\mathrm{eff}}^2), \tag{2.17}$$

i.e., it reduces to the Poisson bracket for $\hbar_{\mathrm{eff}} \to 0$ and the equation of motion for the Wigner function (2.14) becomes Liouville's equation with the statistical phase-space distribution replaced by the Wigner function, while Eq. (2.15) becomes the classical equation of motion for a single trajectory. Note that the Poisson bracket in Eq. (2.17) is with respect to the new (rescaled) coordinates and the factor $\hbar_{\mathrm{eff}}/\hbar$ can be eliminated by a redefinition of H.

[2] Note that $\alpha = \alpha(\alpha_0, \alpha_0^*, t)$ is the Weyl symbol of the Heisenberg operator $\hat{a}(t)$ while the Moyal bracket is then defined with respect to the time-independent variables α_0, α_0^*.

2.1.4. WKB wave functions and EBK torus quantization

An important semiclassical tool applicable in integrable classical dynamics is the EBK torus quantization [41,42,160] that is briefly summarized here for further reference.

In classical mechanics, integrable systems with a $2f$-dimensional phase space are characterized by the existence of f constants of motion F_i (including the Hamiltonian function, e.g., as $H = F_1$) that are independent in the sense that their mutual Poisson brackets vanish and that the tangent vectors of the (Hamiltonian) flows generated by each of them are linearly independent in each point. To be specific, the tangent vectors are defined as the vectors $\dot{\boldsymbol{x}}_i = (\dot{\boldsymbol{q}}_i, \dot{\boldsymbol{p}}_i)$ with

$$\dot{\boldsymbol{q}}_i = \{\boldsymbol{q}, F_i\}, \qquad \dot{\boldsymbol{p}}_i = \{\boldsymbol{p}, F_i\}, \qquad i = 1, \ldots, f. \tag{2.18}$$

The individual flows defined by these equations can then be considered as a natural local parametrization (with "times" t_i) on a f-dimensional Lagrangian manifold, that is globally defined by the intersection of all the manifolds obtained from fixing the individual constants of motion F_i. If the motion is bounded in phase space, this Lagrangian manifold has the topology of a (possibly degenerate) f-torus, and a trajectory that starts on this torus will stay on it forever.

Very roughly speaking, the torus quantization then breaks up the f-torus into f simple one-dimensional tori, that are then quantized individually by a Bohr-Sommerfeld quantization, where each simple torus is characterized by an action variable

$$I_j = \frac{1}{2\pi} \oint_{\Gamma_j} d\boldsymbol{q}\, \boldsymbol{p}(\boldsymbol{q}, F_1, \ldots, F_f), \qquad j = 1, \ldots, f. \tag{2.19}$$

Here, the contour Γ_j is any continuous deformation (along the torus) of a single loop around the jth one-torus in the decomposition of the f-torus, i.e., the jth irreducible loop. Formally one finds that the WKB wave function in configuration space can be written as

$$\psi(\boldsymbol{q}) = \langle \boldsymbol{q} | \psi \rangle = c \sum_l \left| \det \frac{\partial^2 S_l}{\partial \boldsymbol{q} \partial \boldsymbol{I}} \right|^{\frac{1}{2}} \mathrm{e}^{\frac{i}{\hbar} S_l(\boldsymbol{q}, \boldsymbol{I}) + i\alpha_l}, \tag{2.20}$$

where $S_l(\boldsymbol{q}, \boldsymbol{I})$ are the (local) actions that generate the canonical transformation from $(\boldsymbol{q}, \boldsymbol{p})$ to the action angle variables $(\boldsymbol{\varphi}, \boldsymbol{I})$, with the latter being the natural parametrization of the torus with $\dot{\boldsymbol{I}} = 0$, i.e., the f constant actions $\boldsymbol{I}$ represent a specific choice of the F_i, while the angles $\boldsymbol{\varphi}$ each parametrize an irreducible loop. The reason for having different actions comes from the fact that the parametrization of the torus in terms of $\boldsymbol{q}$ can only be given as $\boldsymbol{p}_l(\boldsymbol{q}, \boldsymbol{I})$ with multiple local parametrizations, or layers l that are connected at caustics, where the WKB wave function description breaks down, as one then has

$$\left| \det \frac{\partial^2 S_l}{\partial \boldsymbol{q} \partial \boldsymbol{I}} \right| = \left| \det \frac{\partial \boldsymbol{p}_l}{\partial \boldsymbol{q}} \right| \to \infty. \tag{2.21}$$

In the simple case of a one-dimensional system, these caustics are just the classical turning points. The additional phases α_l in Eq. (2.20) have to be introduced to account

for the correct phase relations between different layers[3]. These phase relations can be found by either switching to a different local description or by finding the quantum mechanical solutions in a local approximation around the caustics. This is a very difficult task in general, requiring a full classification of caustics, and goes beyond the scope of this thesis.

The requirement that the WKB wave function is uniquely defined quantizes the action variables to

$$I_j(n_j) = \left(n_j + \frac{\nu_j}{4}\right)\hbar, \qquad n_j = 0, 1, \ldots, \tag{2.22}$$

leading to a set of f quantum numbers such that all the constants of motion get quantized as $F_i(\boldsymbol{n}) = F_i(\boldsymbol{I}(\boldsymbol{n}))$, including the energy. Fortunately, the Maslov index ν_j in Eq. (2.22), that implements the phases α_l, can be calculated by counting the oriented number of simple folds (caustics of codimension 1) along the irreducible loops that, in generic situations, can be deformed in such a way that they avoid caustics with higher codimension. The orientation of the fold is thereby given by the change of sign of $\det \frac{\partial \boldsymbol{q}}{\partial \boldsymbol{p}}$ along the integration path, such that the folds that can be removed by a deformation of the torus cancel in the overall count.

The EBK quantization rule (2.22) has been successfully applied to various mechanical systems, yielding the *exact* spectrum in many cases [41], while the application of EBK quantization to many-particle systems as a quantization of the mean field has started only recently [43,44,161] (with some of the authors also including tunneling corrections). However, most applications used effective descriptions and a simplified version of EBK, i.e., the Bohr-Sommerfeld quantization in effective one-dimensional phase spaces. But it turns out that in the model of interest here discussed later, special care has to be taken when it comes to this effective description, and the knowledge of the topology of the phase space on both sides of the phase transition that it describes is crucial for a correct description.

2.1.5. The out-of-time-ordered correlator

The theory of chaotic dynamics is well established in classical mechanics, with the concepts of phase-space mixing and ergodicity playing a crucial role [42]. However, in quantum systems, the situation is more complicated and different aspects of *quantum* chaos have been found. The most straightforward approach to quantum chaos, that is restricted to quantum systems with a well-defined classical limit, is given by defining a quantum system as chaotic, if its classical analogue shows (classical) chaos. In these systems, the eigenfunctions of the Hamiltonian locally look like random waves [162], and the famous BGS conjecture states that all such systems should be well described by random matrix theory, leading to specific types of level statistics only characterized by the symmetries of the system [49]. The BGS conjecture can also be applied to quantum systems where a classical limit cannot be defined due to the lack of a small/large parameter. This scenario is then referred to as "many-body quantum chaos" [163].

[3] In general, the α_l could depend on the coordinates along the caustics.

Direct measures of chaos in quantum systems are not easily found. In systems with a chaotic classical analogue, one should expect that any wave function that is initially localized in phase space (in the sense of the associated phase-phase distribution) should spread quickly due to the classical instability, becoming more and more complex with time, until (self)interference effects start to play a crucial role. One might try to implement the classical philosophy of close-by trajectories diverging exponentially by calculating the time evolution of overlaps between two wave functions, that are initially close in phase space. However, the unitarity of the quantum-mechanical time evolution renders this overlap constant in time, i.e.,

$$\langle\psi_1(t)|\psi_0(t)\rangle = \langle\psi_1(0)|\hat{U}^\dagger(t)\hat{U}(t)|\psi_0(0)\rangle = \langle\psi_1(0)|\psi_0(0)\rangle\,. \tag{2.23}$$

More successful approaches are therefore based on operator expectation values and certain (out-of-time-ordered) correlators. The introduction of the out-of-time-ordered correlators presented in the following shares similarities to the presentation in [164], and the reader is referred to this publication and references therein for further reading.

To characterize the instability in a quantum system, one can ask the question, how a small perturbation of an initial state at time $t = 0$ affects the measurement of an observable $\hat{A}$ at later times. This can be answered in a simplified linear response theory[4] with an instant perturbation at $t = 0$: If the initial state is characterized by a density matrix $\hat{\rho}$, the perturbed density matrix, characterized by a parameter ϵ can be given as the unitary transformation generated by a hermitian operator $\hat{B}$,

$$\hat{\rho}_\epsilon = \mathrm{e}^{-i\epsilon\hat{B}}\,\hat{\rho}\,\mathrm{e}^{i\epsilon\hat{B}}. \tag{2.24}$$

For example, if $\hat{B}$ is the momentum operator, the perturbed density matrix gets shifted by ϵ in its real-space representation. The change in the expectation value of $\hat{A}$ after time t is then given by

$$\left\langle\hat{A}(t)\right\rangle_\epsilon - \left\langle\hat{A}(t)\right\rangle_0 = \mathrm{Tr}\left\{(\hat{\rho}_\epsilon - \hat{\rho})\hat{A}(t)\right\} = \epsilon\left\langle i\left[\hat{A}(t),\hat{B}\right]\right\rangle_0 + \mathcal{O}(\epsilon^2), \tag{2.25}$$

i.e., it is characterized by the commutator $[\hat{A}(t),\hat{B}(0)]$.

It is instructive to consider the case of the operators being two momentum operators at different times. In the phase space formulation introduced in section 2.1.3, using phase space coordinates (q_0,p_0), the expectation value of the commutator is then given by the phase space average of the Moyal bracket, Eq. (2.15),

$$\langle i\,[\hat{p}(t),\hat{p}(0)]\rangle = -\hbar\int dq_0\,dp_0\,W_\rho(q_0,p_0)\{\{p(q_0,p_0,t),p_0\}\}. \tag{2.26}$$

Here, W_ρ is the Wigner function associated to the density matrix $\hat{\rho}$ at time $t = 0$ that is assumed to be local in phase space in some sense. The short time behavior can then be expected to be well described by classical dynamics. Formally, this results again from approximating the Moyal bracket by its leading order in $\hbar$, i.e., the Poisson bracket, such

[4] See, e.g., [6] for the general formalism.

that the time evolution of $p(q_0, p_0, t)$ follows a classical trajectory and the Moyal bracket in Eq. (2.26) becomes

$$\{\{p(q_0, p_0, t), p_0\}\} \approx \{p_{\rm cl}(q_0, p_0, t), p_0\} = \frac{\partial p_{\rm cl}(q_0, p_0, t)}{\partial q_0} \sim \hbar\, c(q_0, p_0)\, \mathrm{e}^{\lambda_L t}, \tag{2.27}$$

in terms of the classical expectation for the element $\partial p(t)/\partial q_0$ of the the stability matrix for a generic classical trajectory in a chaotic region, with λ_L being the (largest) Lyapunov exponent [164–166]. The latter is, however, typically obtained only in a *long time* average of the divergence of two trajectories, as the direction q_0 does usually not coincide with the most unstable direction. This does not conflict with the short-time assumption, in principle, as the phase space average in (2.26) can replace a time average due to the (assumed) classical ergodicity. However, the very same average leads to large cancellations, as the unspecified phase space function c in Eq. (2.27), that can wildly fluctuate within the localization length of the Wigner function, leads to a trivially vanishing result in generic situations. Especially in thermal systems, response functions of the type (2.26) are known to decay rapidly as a consequence of thermalization [167].

The way out of this can be seen as an analogue construction as is used in the definition of the Lyapunov spectrum, where a positive definite matrix is constructed from the stability (or monodromy) matrix M as $\Lambda = M^T M$, with its positive time-dependent eigenvalues characterizing the (in)stability in the different phase-space directions [168, 169]. Similarly, one can replace the commutator $\hat{M} = i[\hat{p}(t), \hat{p}(0)]$ in Eq. (2.26) by the operator $\hat{M}^\dagger \hat{M}$, which yields the original form [165] of the out-of-time-ordered correlator or commutator (OTOC)

$$C_{\hat{A},\hat{B}}(t) = \left\langle \left[\hat{A}(t), \hat{B}(0)\right] \left[\hat{B}(0), \hat{A}(t)\right] \right\rangle = -\left\langle \left[\hat{A}(t), \hat{B}(0)\right]^2 \right\rangle, \tag{2.28}$$

again given for arbitrary (hermitian) operators. Its name comes from the unusual time ordering of two of the terms that one obtains when the commutator is expanded, namely

$$C_{\hat{A},\hat{B}}(t) = \left\langle \left\{ \hat{A}(t)\hat{B}(0), \hat{B}(0)\hat{A}(t) \right\} \right\rangle - 2\Re F_{\hat{A},\hat{B}}(t), \tag{2.29}$$

with the curly bracket in the first expression being the anticommutator and

$$F_{\hat{A},\hat{B}}(t) = \left\langle \hat{A}(t)\hat{B}(0)\hat{A}(t)\hat{B}(0) \right\rangle. \tag{2.30}$$

The latter is the object that most literature now calls the out-of-time-ordered correlator (e.g., [170–174] and references therein), while the definition with the commutator is often used only for the classical arguments that lead to the exponential growth. It is usually argued that the other terms that contribute to $C(t)$ do not show exponential behavior, as they can be written in terms of an overlap of quantum states, e.g., for a pure state[5] $\hat{\rho} = |\psi\rangle\langle\psi|$ one has

$$\mathrm{Tr}\left\{ \rho \hat{A}(t)\hat{B}(0)\hat{B}(0)\hat{A}(t) \right\} = \langle \Psi(t)|\Psi(t)\rangle\,, \qquad |\Psi(t)\rangle = \hat{B}(0)\hat{A}(t)\,|\psi\rangle\,. \tag{2.31}$$

[5] Thermal expectation values can be included by using the thermofield double state [175] that is of recent interest in high energy physics.

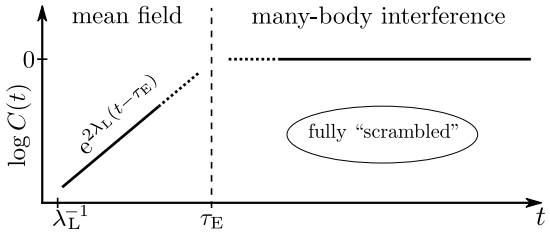

Figure 2.1: Typical behavior of an OTOC in systems that exhibit classical chaos (adapted from [177]). For early times an exponential growth with a rate of twice the Lyapunov exponent λ_L, represents the unstable classical dynamics, while (many-body) quantum interference starts playing a role at the Ehrenfest time τ_E, eventually leading to a saturation of the OTOC in a fully scrambled regime.

However, this state is not normalized if the operators $\hat{A}$ and $\hat{B}$ are not unitary which requires a slightly different definition of the OTOC [173], as $\hat{A}$ and $\hat{B}$ were assumed to be hermitian here. Although in many applications it is sufficient to work with the correlators $F(t)$, Eq. (2.30), only the definition with the commutator, Eq. (2.28) is considered here.

By construction, the OTOC is expected to grow exponentially for short times in systems that exhibit classical chaos[6]. Clearly, at very short times, the behavior can be very different (as can be seen, e.g., by using operators that commute at $t = 0$), and one has to wait for the (classical) ergodic time scale proportional to λ_L^{-1} needed for the exponential growth to become dominant. The time scale that marks the breakdown of this exponential growth is the Ehrenfest time

$$\tau_E = \frac{1}{\lambda_L} \log\Big(\frac{s_{\mathrm{cl}}}{\hbar}\Big)\,, \tag{2.32}$$

where s_{cl} is a typical action of the classical system that is independent on $\hbar$ [55, 176]. Around the Ehrenfest time, quantum interference effects become important that eventually lead to a saturation in chaotic systems [56,164,177]. Figure 2.1 shows a sketch of the typical time evolution of the OTOC, highlighting the universal regimes of exponential growth and saturation. This behavior has been demonstrated to be very well fulfilled in the quantum kicked rotor [166], being a textbook example of classical and quantum chaotic behavior, as well as in the superradiant phase of the Dicke model [178].

The Ehrenfest time (2.32) also appears in the context of scrambling in quantum systems, where it describes the time needed for a perturbation to spread over the whole (finite) available phase space [179], where the Planck constant is replaced by the inverse number of degrees of freedom (e.g., the basis size of a finite Hilbert space). Hence, the OTOC is a suitable tool to characterize the scrambling in interacting quantum systems [180,181] with clear links to thermalization [167,173,182]. The logarithmic form of

[6] Note, however, that there is a fundamental difference in the order of averaging and taking the logarithm in the definition of the Lyapunov exponent as compared with the OTOC growth rate, such that the latter does not have to coincide with $2\lambda_L$ exactly [166].

the scrambling time (as a consequence of the exponential OTOC growth) is then referred to as fast scrambling, with black holes being conjectured as being the fastest possible scramblers in nature [170].

Although the short-time behavior can be well understood classically, it is now common to define the (quantum) Lyapunov exponent λ via the exponential growth rate of the OTOC $C(t)$ or $F(t)$, which then leads to $\lambda \approx 2\lambda_L$ when compared to the classical Lyapunov exponent (if it can be defined). Surprisingly, one can show that under certain circumstances, this "quantum" Lyapunov exponent λ is bounded from above by the temperature as

$$\lambda \leq \frac{2\pi}{\hbar\beta} \tag{2.33}$$

in thermal systems [170], and the bound has been shown to be saturated by black holes, consistent with the aforementioned conjecture of black holes being the fastest scramblers. The only other system that is known to saturate this bound is the Sachdev-Ye-Kitaev model at low temperatures [171, 174, 183].

However, fast scrambling in the sense of an exponential growth of the OTOC does not necessarily require chaotic classical behavior. It has been conjectured that, if a system shows quantum critical behavior, the quantum Lyapunov exponent exhibits a maximum at this point [184]. This has been verified for the one-dimensional Bose-Hubbard model [184] and for the Dicke model [185], and the OTOC has since been established also as a tool for the detection of (excited states) quantum phase transitions [173, 186–188], with a focus on its long-time behavior. The underlying classical dynamics in these systems does not even have to be chaotic to show exponential OTOC growth, as the necessary classical instability can be generated from isolated hyperbolic fixed points in integrable systems [189–191]. Therefore, these types of models have even been used as fast-scrambling toy models describing black holes as a condensate of soft gravitons [153, 192].

One of the goals of this part of the thesis is to elucidate the differences and similarities in the scrambling properties of critical and chaotic systems. This will be done in the following sections, first using an integrable tree-mode approximation of an attractive Bose gas that is then extended to a nonintegrable case.

2.2. The attractive Lieb-Liniger gas in 3-mode approximation

In this section, a simple one-dimensional model of attractively interacting bosons is used to examine the properties of systems near quantum phase transitions in a semiclassical approach. When Lieb and Liniger introduced their model for the first time [19, 92], their analysis focused on the case of repulsive interaction. The fact that the attractive case does not allow for a well-defined thermodynamic limit with fixed density led them to the conclusion that the attractive extension of the model did not have a physical meaning. However, recent theoretical and experimental progress has shown that the attractive interaction, apart from being experimentally realizable, leads to very interesting phenomena. It has been shown that the confinement in a finite volume using periodic boundary conditions leads to a quantum phase transition at a finite coupling, where the noninteracting many-body ground state starts to form a bright soliton [16, 193, 194], leading to a broken translational symmetry.

The model can be given in first-quantized form by the Hamiltonian

$$\hat{H} = \frac{\hbar^2}{2m}\left(\sum_{k=1}^{N} -\frac{\partial^2}{\partial x_k^2} - g\sum_{i<j}\delta(x_i - x_j)\right), \tag{2.34}$$

where, $g > 0$ is the strength of the attractive coupling and periodic boundary conditions (with period L) are assumed. It is possible to find solutions of the Schrödinger equation for this Hamiltonian using the Bethe ansatz, leading to the same Bethe equations as in the repulsive case [195, 196]. However, finding the solutions of these equations turns out to be a very difficult task, as the quasimomenta that enter the Bethe ansatz have to be found in the complex plane, and even adiabatic changes in the couplings lead to bifurcations and structural changes in the sets of quasimomenta [196]. This limits the usefulness of the Bethe ansatz to small particle numbers. Only in the case of special string solutions, where the quasimomenta are distributed in subsets with the same real part, a systematic treatment for large particle numbers is possible [20]. These string solutions can only be exact solutions if the quasimomenta are purely imaginary, as is the case for the ground state that has been treated in the limit of large particle numbers N in [197, 198], where the quantum phase transition manifests itself also in a non-analyticity of the distribution of the quasimomenta. All other string solutions are only exact in either the limit of an infinite line [20] or, equivalently, in the strongly interacting limit. As an example, they have been used to find the long time limit of local correlations after quenches in large systems analytically, showing that the formation of bound pairs of particles is dominant in the strongly interacting regime [199]. However, when approaching the noninteracting regime[7], this picture breaks down, giving rise to more complicated quantum states and non-analytic behavior. This is a remnant of the quantum phase transition that occurs at an interaction value $g \sim (NL)^{-1}$, also leading to solutions of the Bethe equations that deviate strongly from the string solutions.

[7] The authors of [199] use approximations valid only in large systems where the critical interaction value approaches zero.

The appearance of a phase transition in the mean-field description is better demonstrated in a second-quantized formulation. In the following, all lengths, energies, and times are measured in units of

$$R = \frac{L}{2\pi}, \qquad E_{\mathrm{ref}} = \frac{(2\pi\hbar)^2}{2mL^2}, \qquad \tau_0 = \frac{\hbar}{E_{\mathrm{ref}}}, \tag{2.35}$$

respectively, i.e., the coordinates are described by an angle θ on a ring of radius R,

$$x = R\theta \tag{2.36}$$

with $0 \leq \theta < 2\pi$. The Hamiltonian (2.34) can then be written in terms of the field operators $\hat{\Psi}(\theta)$ and $\hat{\Psi}^\dagger(\theta)$ as

$$\hat{H} = \int_0^{2\pi} d\theta \left[\hat{\Psi}^\dagger(\theta)\left(-\frac{\partial^2}{\partial\theta^2}\right)\hat{\Psi}(\theta) - \frac{\pi\bar{\alpha}}{2}\hat{\Psi}^\dagger(\theta)\hat{\Psi}^\dagger(\theta)\hat{\Psi}(\theta)\hat{\Psi}(\theta)\right], \tag{2.37}$$

with the dimensionless coupling $\bar{\alpha} = gL/\pi^2$. The field operators satisfy the usual commutation relations

$$\left[\hat{\Psi}(\theta), \hat{\Psi}^\dagger(\theta')\right] = \delta(\theta - \theta') \tag{2.38}$$

for $0 \leq \theta, \theta' < 2\pi$ and are periodic with period 2π. The mean field limit of the Schrödinger equation is then given by the Gross-Pitaevskii equation,

$$i\frac{\partial\psi}{\partial t} = \left[-\frac{\partial^2}{\partial\theta^2} + \pi\bar{\alpha}N|\psi|^2\right]\psi, \tag{2.39}$$

where $\psi(\theta)$ is the N-particle condensate wave function, normalized to one [16]. It turns out that the stationary solution with minimal energy is then the constant wave function for

$$\alpha \equiv N\bar{\alpha} < 1. \tag{2.40}$$

At $\alpha = 1$ the Bogoliubov excitation spectrum around this solution collapses indicating a different solution becoming energetically favorable. This new mean field ground state is a bright soliton [16, 200] centered at a point on the ring, i.e., it has broken translational symmetry, leading to a (zero-energy) Goldstone mode generated by the translation along the ring [194].

To conclude, the mean field approach, equipped with the Bogoliubov theory, provides a good understanding of the quantum phase transition. However, it neglects correlation effects among particles and breaks down exactly at the critical point, such that it does not provide a way to systematically include finite size effects. Therefore, a different approach is taken in the following. As the mean-field solution involves only the lowest single-particle momentum state for $\alpha < 1$ it should be possible to approximate the many-body state by using only a few single-particle states with small momentum in this regime. The field operators are thus expanded in the momentum basis as

$$\hat{\Psi}(\theta) = \sum_{k=-\infty}^{\infty} \mathrm{e}^{ik\theta}\hat{a}_k \approx \sum_{k=-k_{\max}}^{k_{\max}} \mathrm{e}^{ik\theta}\hat{a}_k, \tag{2.41}$$

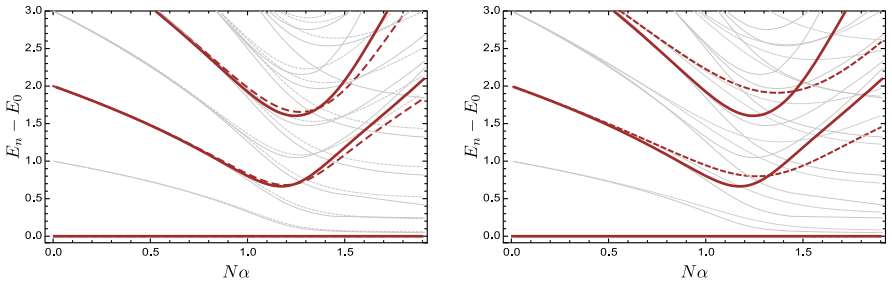

Figure 2.2: The effect of the truncation to five (left) and three (right) single-particle momentum modes on the excitation spectrum for $N = 20$ particles. The solid lines represent the data from the full Bethe ansatz solutions (taken from [196]) and the dashed lines stem from exact diagonalization of the Hamiltonian matrix. The states with zero total momentum (including the ground state) are highlighted in red.

where the momentum quantum numbers are truncated to $|k| \leq k_{\max}$, i.e., only $2k_{\max}+1$ momentum modes are used. Inserting Eq. (2.41) into the Hamiltonian (2.37) then yields the second-quantized Hamiltonian in momentum representation

$$\hat{H} = \sum_k k^2 \hat{a}_k^\dagger \hat{a}_k - \frac{\bar{\alpha}}{4} \sum_{k,l,m,n} \delta_{k+l,m+n} \hat{a}_k^\dagger \hat{a}_l^\dagger \hat{a}_m \hat{a}_n, \tag{2.42}$$

where k, l, m, n run from $-k_{\max}$ to $k_{\max}$. The interaction is clearly number and momentum conserving. The latter can be seen from the Kronecker delta in Eq. (2.42). Apart from that, the interaction couples all momentum modes equally. Formally, we have the two identities

$$\left[\hat{H}, \hat{N}\right] = 0, \qquad \left[\hat{H}, \hat{K}\right] = 0, \tag{2.43}$$

where $\hat{N}$ and $\hat{K}$ are the particle number and momentum operators,

$$\hat{N} = \sum_k \hat{a}_k^\dagger \hat{a}_k, \qquad \hat{K} = \sum_k k\, \hat{a}_k^\dagger \hat{a}_k. \tag{2.44}$$

The conservation laws (2.43) remain true also if the single-particle momentum basis is truncated. The effect of the truncation on the excitation spectrum for $N = 20$ particles is demonstrated in Fig 2.2, where $k_{\max} = 1, 2$ are compared to the full Bethe ansatz solutions. One can clearly observe that, although the quality of the approximation is lowered with the cutoff, the qualitative features of the low-lying excitations are captured already with the lowest three momentum modes.

2.2.1. 3-mode approximation

In this section, the truncation to three modes, i.e., $k_{\max} = 1$ is applied. Although the quantitative agreement with the full model is poor for $\alpha = N\bar{\alpha} \gtrsim 1$, this approximation

contains all the physics for understanding the quantum phase transition and its precursors for $\alpha > 1$ and is thus commonly used to study finite size effects in the attractive LL model [16, 153, 194, 196]. Moreover, it is also of direct experimental relevance, as it can be essentially realized in a spin-1 BEC, where the spatial degrees of freedom are frozen out and the dynamics is only in the spin degrees of freedom [201–204]. There, one can easily control the "kinetic" energy that is actually given by the quadratic Zeeman shift by varying the magnetic field, thus effectively changing the relative strength of the coupling.

From the theoretical perspective, the three-mode approximation is special, as the two constants of motion, namely the particle number $\hat{N}$ and the total momentum $\hat{K}$, allow for a complete characterization of all states in terms of the latter, while the remaining degree of freedom is effectively one-dimensional, giving rise to a regular spectrum in each sector of fixed momentum and particle number. The implications of the two constants of motion are clearer when looking at the (classical) mean field limit. There, they lead to integrable dynamics that, due to the simple analytic form of $\hat{N}$ and $\hat{K}$, can be directly represented in a two-dimensional section of phase space and one-dimensional dynamics. The detailed treatment of the classical limit and its quantization have been performed in [61] and the reader is referred there for details. Here, only the most important steps are reviewed and additional calculations are given. One important note has to be made concerning the presentation of this section: all the results from exact diagonalization of the 3-mode model that were used in [61] and [60] have been provided by the author of this manuscript. For this reason, some of the figures were created in close collaboration and reappear here without further reference.

2.2.2. Semiclassical treatment

In order to obtain the classical mean-field dynamics, the operators are translated into their Wigner symbols as phase space functions. This is done by bringing all products of operators in symmetric order, leading to additional terms due to the commutation relations, and then replacing them by classical variables,

$$\hat{a}_k \mapsto \phi_k = \frac{q_k + ip_k}{\sqrt{2}} = \sqrt{n_k}\mathrm{e}^{-i\theta_k}, \qquad \hat{a}_k^\dagger \mapsto \phi_k^* = \frac{q_k - ip_k}{\sqrt{2}} = \sqrt{n_k}\mathrm{e}^{i\theta_k}. \tag{2.45}$$

The coordinates q_k and p_k are called quadrature variables [205] and are analogous to the position and momentum of a harmonic oscillator, but have to be considered only as a pair of canonical variables as they are not a physical momentum or position of anything. The polar coordinates n_k and θ_k are related to the quadrature variables by a canonical transformation, but do not have an exact quantum analogue. This is, however, only important when the Maslov indices (c.f., section 2.1.4) are concerned, as they originate from the non-commutativity of the quantum operators. The reader is referred to [61] for more details on this issue and for the intermediate steps in the derivation of the classical Hamiltonian function. The classical analogues of the particle number $\hat{N}$ and the total momentum $\hat{K}$ are given by

$$N_{\mathrm{cl}} = \tilde{N} - \frac{3}{2}, \quad \tilde{N} = n_{-1} + n_0 + n_1, \qquad K_{\mathrm{cl}} = n_1 - n_{-1}, \tag{2.46}$$

and can be easily shown to be constants of motion of the classical system. After a point transformation to the variables $\tilde{N}$, K_{cl} and n_0 the classical energy per particle can be written in scaled variables as

$$\frac{E}{\tilde{N}} = \omega(\varphi, z) + \tilde{\alpha}\left(-\frac{1}{4} + \frac{3}{2\tilde{N}} - \frac{9}{8\tilde{N}^2}\right) - \frac{1}{\tilde{N}}, \tag{2.47}$$

where the classical dynamics is fully determined by

$$\omega(\varphi, z) = 1 - z - \frac{\tilde{\alpha}}{8}\left[(1-z)(3z+1) + 4z\sqrt{(1-z)^2 - l^2}\cos 2\varphi\right], \tag{2.48}$$

with $\tilde{\alpha} = \bar{\alpha}\tilde{N}$ and the phase space coordinates

$$z = \frac{n_0}{\tilde{N}}, \qquad \varphi = \theta_0 - \frac{1}{2}\left(\theta_1 + \theta_{-1}\right), \qquad \{\varphi, z\} = \frac{1}{\tilde{N}}. \tag{2.49}$$

In (2.48), the momentum $l = K_{\mathrm{cl}}/\tilde{N}$ enters only as a parameter, while the classical analogue to the particle number N_{cl}, Eq. (2.46), appears only as an effective quantum of action $\hbar_{\mathrm{eff}} = 1/\tilde{N}$ in the Poisson bracket defined by φ and n_0,

$$\{f, g\} = \frac{\partial f}{\partial \varphi}\frac{\partial g}{\partial n_0} - \frac{\partial f}{\partial n_0}\frac{\partial g}{\partial \varphi}, \tag{2.50}$$

while the classical equations of motion are independent of it,

$$\dot{\varphi} = \frac{\partial \omega}{\partial z}, \qquad \dot{z} = -\frac{\partial \omega}{\partial \varphi}. \tag{2.51}$$

The full EBK quantization of the three-torus then yields the quantization rules

$$\tilde{N} = N + \frac{3}{2}, \qquad N = 0, 1, \ldots, \tag{2.52}$$

$$K_{\mathrm{cl}} = K, \qquad K = 0, \pm 1, \cdots \pm N \tag{2.53}$$

for the particle number and the momentum and the numbers N and K can be identified as the eigenvalues of the respective quantum operators. With this, the relation between the different definitions $\tilde{\alpha} = \tilde{N}\bar{\alpha}$ and $\alpha = N\bar{\alpha}$ (the natural choice for numerical calculations) of the coupling can be given as

$$\tilde{\alpha} = \frac{\tilde{N}}{N}\alpha = \left(1 + \frac{3}{2N}\right)\alpha. \tag{2.54}$$

The distinction is not important in the mean field limit but should be accounted for when finite size effects are considered.

As the rest of the semiclassical analysis concentrates on the zero-momentum sector that contains the ground state, let us set $K = 0$ in the following. With this, the remaining quantization rule is simplified to

$$I(\omega) = \frac{1}{2\pi}\oint d\varphi\, [1 - z(\omega, \varphi)] = \frac{m + \frac{1}{2}}{\tilde{N}}, \qquad m = 0, 1, \ldots, \lfloor N/2 \rfloor, \tag{2.55}$$

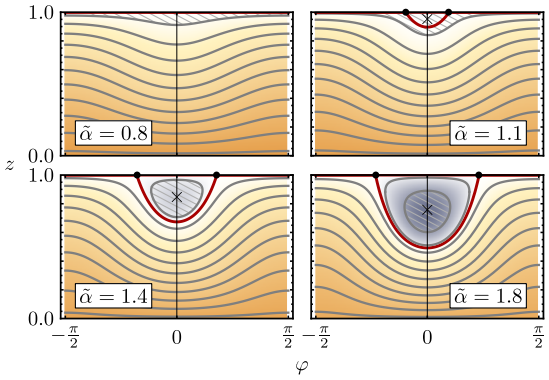

Figure 2.3: Phase space portrait of the energy $\omega(z, \varphi)$, Eq. (2.56), for different values of the coupling $\tilde{\alpha}$. The variable z denotes the relative occupation of the noninteracting ground state and φ is the conjugate angle. For $\tilde{\alpha} > 1$, a global energy minimum (cross) and a separatrix (red) connecting two hyperbolic fixed points (dots at z=1) appear. Gray lines represent the orbits (tori) that fulfill the quantization condition (2.55) for $N = 20$. Note that the quantized orbits change their character sequentially.

where $z(\varphi, \omega)$ can be obtained from inverting the simplified energy per particle for $l = 0$,

$$\omega(z, \varphi) = (1 - z) \left\{ 1 - \tilde{\alpha} \left[\frac{1 - z}{8} + z \cos^2 \varphi \right] \right\}. \tag{2.56}$$

Figure 2.3 shows the phase space plot of the energy $\omega(\varphi, z)$ with the contour lines defined by the quantized energies obtained from the condition (2.55). It involves different types of classical trajectories following lines of constant energy in phase space with periodicity $\varphi \mapsto \varphi + \pi$. For $\tilde{\alpha} < 1$ all trajectories are deformed horizontal lines (rotations). For $\tilde{\alpha} > 1$ an island centered around a new minimum energy fixed point emerges with orbits vibrating in φ, similar as for the pendulum. This goes along with the formation of a separatrix at $E = E_{\text{sep}}$ ($\omega = 0$) associated with two hyperbolic fixed points at $z = 1$ and $\cos^2 \varphi = 1/\tilde{\alpha}$, characterized by (in)stability exponents

$$\lambda_s^{(1,2)} = 2\sqrt{\tilde{\alpha} - 1} \equiv \lambda_s. \tag{2.57}$$

The energy levels that one obtains from the quantization rule (2.55) turn out to be in perfect agreement with the quantum mechanical results obtained from exact diagonalization of (2.42), as seen in Fig. 2.4 for $N = 200$ particles, where the excitation energy dependence with the coupling α is shown for the interesting regime around the critical point $\alpha = 1$. To show that also the ground state energy is correctly captured, the exact ground state has been used as a reference in both results, as can be seen in the inset, where a closeup of the region around $\alpha = 1$ is shown, revealing small errors close to the point where the quantized orbits cross the separatrix. The latter points are

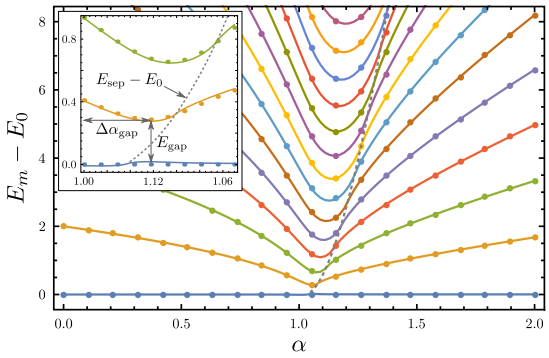

Figure 2.4: Comparison of the excitation spectrum obtained from exact diagonalization (dots) and semiclassical quantization (lines). In both cases, the exact ground state energy has been used as a reference. The dashed line shows the energy of the separatrix with respect to the ground state, indicating the points where the quantized orbits cross the separatrix.

indicated by the intersection of the respective levels with the dashed line, that shows the separatrix energy (with respect to the ground state) defined by $\omega = 0$. As it was already seen from the phase space portraits in Fig. 2.3, the quantized orbits cross the separatrix successively, and the transition for the ground state does not occur at the mean field value $\alpha = 1$ for finite particle numbers. This is again verified in Fig. 2.4, where the dashed line starts only at a coupling $\alpha \approx 1.07 > 1$. This also leads to a position of the minimal gap $E_{\rm gap}$ between the ground and first excited state that is shifted to a value $\alpha_{\rm gap} = 1 + \Delta\alpha_{\rm gap}$ that is larger than the critical interaction. As one approaches the mean field limit $N \to \infty$, the gap energy and the deviation $\Delta\alpha_{\rm gap}$ from the critical point approach zero in a power law behavior, and the respective exponents can be obtained from an asymptotic analysis of the quantization condition (2.55) [61][8]. This asymptotic gap closing is a clear evidence of a quantum phase transition that emerges in the mean field limit. However, one can clearly see that the transition of the *excited* states from one side of the separatrix to the other goes hand in hand with a bunching of levels. This suggests that the gap closing is not a feature unique to the ground an first excited state but happens also between higher neighboring states. This can be verified in the excitation spectrum, where a closer analysis of the semiclassical quantization yields a logarithmic divergence in the inverse level spacing, indicating an excited state quantum phase transition [206]. For a direct evidence of the phase transition, that also gives some insight to the physics behind it, one can calculate the derivatives of the energy level with index k with respect to the interaction and look for non-analytic behavior.

[8] The constant prefactors turn out to have the wrong value in this approach, as the relevant phase space is rescaled in this limit to stay at the gap. This was corrected by reintroducing quantum operators in a local description in [61].

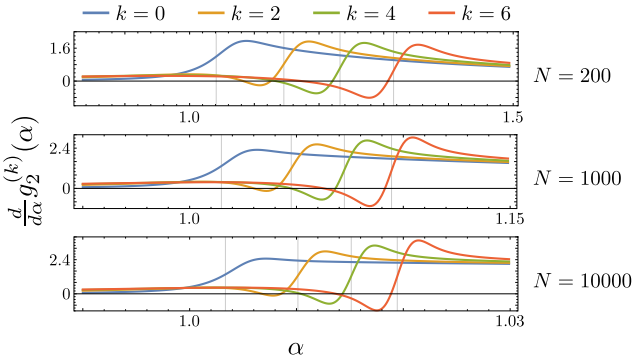

Figure 2.5: Emerging non-analytic behavior in the pair correlation function calculated in the kth interacting excited state. Note the different scales on the horizontal axis for the different particle numbers N.

Let us for a moment forget about the approximation introduced by the truncation to three modes. By means of the Hellmann-Feynman theorem applied to the Hamiltonian (2.37) and using the homogeneity of the system one obtains the relation

$$\frac{d}{d\bar{\alpha}}E_k(\bar{\alpha}) = -\frac{\pi}{2}\int_0^{2\pi} d\theta\ \langle\psi_k|\hat{\Psi}^\dagger(\theta)\hat{\Psi}^\dagger(\theta)\hat{\Psi}(\theta)\hat{\Psi}(\theta)|\psi_k\rangle = -\frac{N^2}{4}g_2^{(k)}(\bar{\alpha}), \tag{2.58}$$

where the α-dependence of the kth excitation eigenstate $|\psi_k\rangle$ has been omitted and

$$g_2^{(k)}(\bar{\alpha}) = \frac{\langle\psi_k|\hat{\Psi}^\dagger(\theta)\hat{\Psi}^\dagger(\theta)\hat{\Psi}(\theta)\hat{\Psi}(\theta)|\psi_k\rangle}{(N/2\pi)^2} \tag{2.59}$$

is the local pair correlation function normalized with the particle density, describing the probability for finding two particles at the same point. By switching to the parameter $\alpha = N\bar{\alpha}$ and abusing the notation by using the same symbols $E_k(\alpha)$ and $g_2^{(k)}(\alpha)$ for the functions expressed in terms of α one gets

$$\frac{d^2}{d\alpha^2}E_k(\alpha) = -\frac{N}{4}\frac{d}{d\alpha}g_2^{(k)}(\alpha). \tag{2.60}$$

The truncation does not change the calculation, but the field operators have to be truncated to three modes, such that they cannot resolve a single point on the ring. Still, an increase of the function $g_2^{(k)}$ can be interpreted as a sign of particles bunching together, as it is known to happen for the ground state of the full model. If one is not comfortable with the interpretation in terms of correlations, one can also view $g_2^{(k)}$ as the interaction energy per particle

$$g_2^{(k)}(\alpha) = -\frac{4}{\alpha N}\left(E_k(\alpha) - \langle\psi_k(\alpha)|\hat{H}_0|\psi_k(\alpha)\rangle\right), \tag{2.61}$$

where $\hat{H}_0$ is the noninteracting Hamiltonian of the noninteracting system. Figure 2.5 shows the numerically obtained (discrete) derivative of $g_2^{(k)}(\alpha)$ for the ground state and three different excitations and increasing particle numbers, clearly showing a sudden increase at successive "critical" interaction values, that coincide exactly with the points where the respective quantized orbits cross the separatrix. When increasing the particle number, the step gets more narrow, approaching a discontinuity in the pair correlation. This is a clear indication of a second order quantum phase transition of the ground *and* the excited states that manifests itself in the mean field limit. Moreover, this shows that the excited state quantum phase transitions have their origin in the presence of the separatrix in the mean field description. This means that, when tuning the interaction beyond the critical value $\alpha = 1$, there will always be states that correspond to quantized orbits close to or at the separatrix, thus yielding critical states for any such interaction in the mean field limit. This will play an important role later, when these states turn out to be of central relevance for the quantum dynamics in certain quench scenarios. There is one interesting result that was not mentioned explicitly up to now: Even though there is no phase transition for finite particle numbers, one can now define a precise finite-size critical coupling for every state given by the condition that the state corresponds to the quantized separatrix. There, in the classical picture, the orbit changes *discontinuously* form a vibration/libration to a rotating orbit.

Separatrix dynamics

A general semiclassical analysis, that is valid for any situation, where a classical analysis yields isolated hyperbolic fixed points in an effective two-dimensional phase space, has shown [60], that the quantization of orbits that come close to these paths yield a logarithmic divergence of the mean density of states. One can get a good intuition on why this happens by noticing that a quantization condition of the form

$$I(E) = \left(n + \frac{\nu}{4}\right) \hbar_{\text{eff}}, \tag{2.62}$$

with n labeling the excitation of the states, can be interpreted on a smooth level as the equation for the integrated density of states. Solving for the level index n and differentiating with respect to the energy yields

$$\bar{\rho}(E) = \frac{1}{\hbar_{\text{eff}}} \frac{dI(E)}{dE} = \frac{T(E)}{\hbar_{\text{eff}}}, \tag{2.63}$$

i.e., the smooth level density is determined by the time period of the quantized orbit. This (classical) time diverges logarithmically when a hyperbolic fixed point is approached and any orbit that is close enough to a separatrix will come close to at least one such fixed point. Therefore, the level density will be dominated by those points through their logarithmically diverging time contributions.

For the three-mode approximation the calculations yields

$$\bar{\rho}(E) \approx \frac{1}{2\pi\lambda} \log\left(\frac{|E - E_{\text{sep}}|}{\tilde{N}}\right) + \mathcal{O}\left(\tilde{N}^0\right) \tag{2.64}$$

with λ given by the sum of reciprocal (in)stability exponents along the way,

$$\lambda = \left(\sum_{\mathrm{FP}} \lambda_{\mathrm{FP}}^{-1} \right)^{-1} = \frac{\lambda_s}{2} = \sqrt{\tilde{\alpha} - 1}. \tag{2.65}$$

The second equality sign uses that the stability exponents λ_s, Eq. (2.57), are the same for the two hyperbolic fixed points of the three-mode model. By using the quantization rule (2.62) beyond the smooth level, one obtains a set of states around the separatrix with an asymptotically constant level spacing that scales as [61, 189]

$$\Delta E \sim \frac{2\pi\sqrt{\tilde{\alpha} - 1}}{\log \tilde{N}} \tag{2.66}$$

thus setting a unique time scale for superpositions of the respective states given by the inverse spacing

$$\tau = \frac{2\pi}{\Delta E} = \frac{1}{\lambda} \log \tilde{N} + \mathcal{O}\left(\tilde{N}^0\right). \tag{2.67}$$

It is important to note that the level spacing (2.66) is only valid for a number of states that grows sub-algebraic with the particle number (or the inverse effective Planck constant) [61]. Remarkably, the timescale (2.67) has exactly the form of the Ehrenfest time

$$\tau_{\mathrm{E}} = \frac{1}{\lambda_L} \log\left(\frac{s_{\mathrm{cl}}}{\hbar}\right) \tag{2.68}$$

defined in chaotic systems. In (2.68), λ_L is the Lyapunov exponent and s_{cl} is a typical classical action. So, the effective time scale τ can be obtained from the Ehrenfest time by substituting the Lyapunov exponent by (half of) the stability exponent and using the effective action $s_{\mathrm{cl}} = 1$ together with the effective Planck constant $\hbar_{\mathrm{eff}} = 1/\tilde{N}$. For this reason the time scale τ, Eq. (2.67), is further referred to as the *local* Ehrenfest time.

The WKB wave functions

The EBK quantization summarized above relies on the detailed knowledge of the topology of the phase space, i.e., one has to find the action-angle variables that characterize the (degenerate) three-torus where the motion takes place. This information is then crucial for the determination of the Maslov index. However, the action-angle variables do not have a quantum analogue so that the actual WKB wave functions should be defined in the original coordinates q_k (or p_k), yielding a wave function that depends on three coordinates. But this would be a very complicated task as one would have to find the full (multi-valued) action that wraps around the torus. Moreover, the natural basis of the quantum system is given by the Fock states (with three modes) that have a fixed particle number N and zero momentum, and thus can be labeled by the zero-mode occupation or occupation fraction. The latter is the quantum analogue of the variable z, so that defining the semiclassical WKB wave functions in the q_k looks like an unnecessary detour. However, the number operator $\hat{n}_0 = \hat{a}_0^\dagger \hat{a}_0$ does not have an exact conjugate "phase operator". The reason for this can be found in the periodicity of the phase together

with the lower-boundedness of $\hat{n}_0$. In the semiclassical limit, it is however legitimate to assume that any pair of conjugate classical variables *locally* corresponds to conjugate quantum operators and that in the case of the action-angle variables, where the actions are constants of motion and thus exactly fixed, the WKB wave function expressed in the angles has to look like a plane wave locally. Now, as the particle number and the total momentum (which can be negative) are closely related to two of the action variables, one can expect that using the action defined only in the two-dimensional phase space spanned by z and φ should yield good results.

The wave functions will only be given for the rotations here, but it is expected that the vibrations can be treated similarly. Let us start with the definition of the φ-representation of the Fock states with fixed momentum and particle number,

$$|m\rangle \equiv \left|\frac{N-K-m}{2}, m, \frac{N+K-m}{2}\right\rangle, \tag{2.69}$$

where the positions stand for the occupations of the $k = -1, 0, 1$ modes in this order and m has the same parity as $N \pm K$. For $K = 0$ this simplifies to the symmetric states

$$|m\rangle = \left|\frac{N-m}{2}, m, \frac{N-m}{2}\right\rangle, \qquad m = N - 2j \tag{2.70}$$

with $0 \leq j \leq \lfloor N/2 \rfloor$ being an integer. One can then define a φ representation as

$$\langle\varphi|m\rangle = \frac{1}{\sqrt{2\pi}} \mathrm{e}^{i\varphi m}, \quad 0 \leq \varphi < 2\pi \tag{2.71}$$

using the states

$$|\varphi\rangle = \sum_{\{m\}} \mathrm{e}^{-im\varphi} |m\rangle \tag{2.72}$$

that form an overcomplete basis in the sector of the three-mode Fock space with fixed particle number and momentum spanned by the states (2.70). In particular we have

$$\int_0^{2\pi} |\varphi\rangle \langle\varphi| = 1, \tag{2.73}$$

$$\langle\varphi'|\varphi\rangle = \frac{1}{2\pi} \mathrm{e}^{i(N-\lfloor N/2 \rfloor)(\varphi'-\varphi)} \frac{\sin\left[(\lfloor N/2 \rfloor + 1)(\varphi'-\varphi)\right]}{\sin(\varphi'-\varphi)}, \tag{2.74}$$

i.e., the states are not orthogonal and thus cannot be eigenstates of a hermitian operator.

The semiclassical WKB wave functions for the rotations with quantum number n can then be defined as

$$\psi_n(\varphi) \equiv \langle\varphi|\psi_n\rangle = \frac{1}{\sqrt{2\pi}} \left|\frac{\partial^2 S_n(\varphi)}{\partial\varphi \partial J}\right|^{\frac{1}{2}} \mathrm{e}^{i\tilde{N} S_n(\varphi) - if(\varphi)}, \tag{2.75}$$

where the action $S_n(\varphi)$ is given by

$$S_n(\varphi) = \int_0^{\varphi} d\varphi' z(\omega_n, \varphi') \tag{2.76}$$

and the action variable J is given by

$$J(\omega) = \frac{1}{2\pi}\int_0^{2\pi} d\varphi\, z(\omega,\varphi) = 1 - \frac{2n+1}{\tilde{N}}, \tag{2.77}$$

where the second equality is the original quantization rule applying for the rotations only [61]. It is related to the common action variable I for both types of motion, (2.55), by $J = 1 - 2I$. The function $f(\varphi)$ in (2.75) was introduced to assure the periodicity of the wave function, i.e., it compensates the Maslov index $\nu = 2$ coming from two (hidden) turning points [61] such that the function $f(\varphi)$ should fulfill

$$f(\varphi + 2\pi) = f(\varphi) + \pi. \tag{2.78}$$

In the noninteracting limit $\tilde{\alpha} \to 0$ one obtains

$$\psi_n(\varphi) = \frac{1}{\sqrt{2\pi}} \mathrm{e}^{i\left(N-2n+\frac{1}{2}\right)\varphi - if(\varphi)}. \tag{2.79}$$

By matching this to the φ-representation of the quantum mechanical states defined in (2.71) (with $m = N - 2n$) one finds

$$f(\varphi) = \frac{\varphi}{2} \tag{2.80}$$

in this limit, i.e., the additional phase is picked up continuously with a constant rate. Although this might not be exactly true for finite couplings, the effect of nonlinear contributions to $f(\varphi)$ should be subdominant. Using elementary manipulations one can finally rewrite the WKB wave function for the rotations as

$$\psi_n(\varphi) = \frac{1}{\sqrt{2\pi}} \left|\frac{\partial z}{\partial \omega}\Big/\frac{\partial J}{\partial \omega}\right|^{\frac{1}{2}} \mathrm{e}^{i\tilde{N}S_n(\varphi) - i\frac{\varphi}{2}}, \tag{2.81}$$

Where the prefactor has to be evaluated at $\omega = \omega_n$ given by the quantization rule (2.55) or (2.77).

One can get a better intuition of the prefactor by identifying the time period T_n of a full cycle of the quantized orbit and the (phase) velocity v_n along the trajectory as

$$T_n = 2\pi \left|\frac{\partial J}{\partial \omega}\right|_{\omega_n} = \int_0^{2\pi} d\varphi\, \frac{1}{v_n(\varphi)}, \qquad v_n(\varphi) = \left|\frac{\partial z}{\partial \omega}\right|_{\omega_n}^{-1}. \tag{2.82}$$

With this, the semiclassical WKB wave function is conveniently written as

$$\psi_n(\varphi) = \frac{\mathrm{e}^{i\tilde{N}S_n(\varphi) - i\frac{\varphi}{2}}}{\sqrt{T_n v_n(\varphi)}}. \tag{2.83}$$

Also, it is clear from (2.82) that the wave function is normalized to one. From Eq. (2.83) one can directly identify situations, where the WKB wave function will not be well-behaved: First, the classical velocity v_n is zero at turning points, leading to a divergence

of the wave function. Second, the velocity becomes very small if the orbit comes close to a hyperbolic fixed point, such that the probability density $|\psi_n(\varphi)|^2$ is strongly peaked around small regions around the hyperbolic fixed points, reflecting the fact that a classical "particle" would be in these regions of phase space most of the time (borrowing the intuition from the single-particle picture for a moment). As we will see later, the semiclassical description is less accurate in these situations.

To be able to directly compare the WKB wave function (2.83) with the numerical states one either has to use the φ-representation of the quantum states defined above or the wave function has to be transformed into the Fock basis. As the latter is the natural basis of the many-body quantum system, we proceed by calculating the projections $a_m^{(n)} = \langle m|\psi_n\rangle$ of the WKB wave functions as

$$a_m^{(n)} = \frac{1}{\sqrt{2\pi}} \int_0^{2\pi} \mathrm{e}^{-im\varphi} \psi_n(\varphi) = \frac{1}{\sqrt{2\pi T_n}} \int_0^{2\pi} d\varphi \, \frac{\mathrm{e}^{i\left(\tilde{N} S_n(\varphi) - \frac{\varphi}{2} - m\varphi\right)}}{\sqrt{v_n(\varphi)}}. \tag{2.84}$$

Switching to the action

$$\bar{S}_n(\varphi) = \varphi - S_n(\varphi) = \int_0^{\varphi} d\varphi' \, (1 - z(\omega_n, \varphi')) \tag{2.85}$$

that is closer related to the variable I, (2.55), and writing $m = N - 2k$ then yields

$$a_{N-2k}^{(n)} = \frac{4}{\sqrt{2\pi T_n}} \int_0^{\frac{\pi}{2}} d\varphi \, \frac{1}{\sqrt{v_n(\varphi)}} \, \cos\left(\tilde{N} \bar{S}_n(\varphi) - (2k+1)\varphi\right). \tag{2.86}$$

Here, the identity $\bar{S}_n(\varphi+\pi) = \bar{S}_n(\varphi)+2\pi I$, that follows from the π-periodicity of $z(\omega_n, \varphi)$ in φ, and leads to a π-periodicity of the exponential, as well as the antisymmetry of the exponent with respect to $\varphi = 0$ have been used.

Before comparing the semiclassical with the exact quantum-mechanical results, let us derive a simplified result obtained from evaluating the integral (2.86) in stationary phase approximation (SPA). The condition for the stationary phase is given by

$$z_s^{(k)} \equiv z(\omega_n, \varphi_s^{(n,k)}) = 1 - \frac{2k+1}{\tilde{N}} = \frac{m + \frac{1}{2}}{\tilde{N}}, \tag{2.87}$$

with $m = N - 2k$. It describes the point where the quantized orbit crosses the horizontal line at $z_s^{(k)} = (m + 1/2)/\tilde{N}$, which are exactly the quantized orbits corresponding to the noninteracting states. This is true also for overlaps of eigenstates with any two different couplings $\tilde{\alpha}_1$ and $\tilde{\alpha}_2$, and leads to a general criterion for a non-vanishing overlap between states: if the corresponding classical orbits cross, they have a finite overlap characterized by the crossing angle (in SPA), while the overlap is exponentially small otherwise.

In the case at hand we have $\tilde{\alpha}_1 = \tilde{\alpha}$ and $\tilde{\alpha}_2 = 0$ and the solution of (2.87) is given by

$$x_s^{(n,k)} \equiv \cos^2 \varphi_s^{(n,k)} = \frac{1}{z_s^{(k)}} \left[\frac{1}{\tilde{\alpha}} \left(1 - \frac{\omega_n}{1 - z_s^{(k)}} \right) - \frac{1 - z_s^{(k)}}{8} \right]. \tag{2.88}$$

The slope of $z(\omega_n, \varphi)$ at this point defines the curvature of the action $\bar{S}_n$ and is given by (omitting the n and k index)

$$\left(\frac{\partial z}{\partial \varphi}\right)_{\omega_n,\varphi_s} = -\left(\frac{\partial \omega}{\partial \varphi}\right)_{z_s,\varphi_s}\left(\frac{\partial \omega}{\partial z}\right)^{-1}_{z_s,\varphi_s}, \tag{2.89}$$

where the right hand side is easily calculated from the Hamiltonian function (2.56). However, the second term does not have to be evaluated further, as it can be identified as the velocity $v_n(\varphi_s)$ and is canceled in the SPA. Combining the above yields the eigenvector components in SPA

$$a^{(n)}_{N-2k} \approx \frac{4\cos\left(\tilde{N}\bar{S}_n\left(\varphi_s^{(n,k)}\right) - (2k+1)\varphi_s^{(n,k)} - \frac{\pi}{4}\right)}{\sqrt{T_n \times f_n^{(k)}}}, \tag{2.90}$$

where, as before, T_n is independent on k and $f_n^{(k)}$ is the analogue to $v_n(\varphi)$ given by

$$f_n^{(k)} = \left(\frac{\partial \omega}{\partial \varphi}\right)_{z_s,\varphi_s} = 2\tilde{\alpha} z_s^{(k)}\left(1 - z_s^{(k)}\right)\sqrt{x_s^{(n,k)}\left(1 - x_s^{(n,k)}\right)}, \tag{2.91}$$

with $z_s^{(k)}$ and $x_s^{(n,k)}$ given in (2.87) and (2.88), respectively.

A few remarks concerning the validity of these results should be made: First, during the calculation, one finds that using the *depletion* of the zero-mode, i.e., $1-z$ is more natural for the lower excitations, as some highly oscillating terms cancel out. This suggests that one could start off directly from the description using $\zeta = 1 - z$ as a canonical variable and defining the quantum states accordingly. For the calculation of the WKB wave functions for the vibrations, this approach is probably better suited, as the actions below and above the separatrix energy are then expected to have a smooth transition. Second, one immediately sees that approaching the noninteracting limit, where the quantized orbits approach horizontal lines (see Fig. 2.3), the integral in Eq. (2.86) should not be approximated by a stationary phase approximation. Finally, the vectors $(a_m^{(n)})$ are not necessarily normalized, as they are projected to a very specific set of plane waves: The wavenumbers $m = N - 2k$ in Eq. (2.71) are non-negative, they have a cutoff $m_{\text{cut}} = N$, and they have the same parity as the particle number N. As the WKB wave function has exactly the same behavior $\psi_n(\varphi + \pi) = (-1)^N \psi_n(\varphi)$ as the respective plane waves, the last condition is not a restriction at all, while the cutoffs can have a non-negligible effect. The stationary phase condition gives a good hint on what can happen: if the quantized orbit crosses the horizontal line at $z_s = (m + 1/2)/\tilde{N}$, the respective wavenumber m is relevant for the stationary phase analysis. If there is no such crossing, the point with stationary phase bifurcates into two saddle points in the complex plane giving rise to evanescent contributions that drop off exponentially with the distance of from a turning point in z. As long as the classical orbit stays away from the phase space boundaries $0 \leq z \leq 1$ (within a distance given by the penetration depth $\sim 1/N$ of the classically forbidden region) one can safely ignore any out-of-bound wavenumbers. Unfortunately,

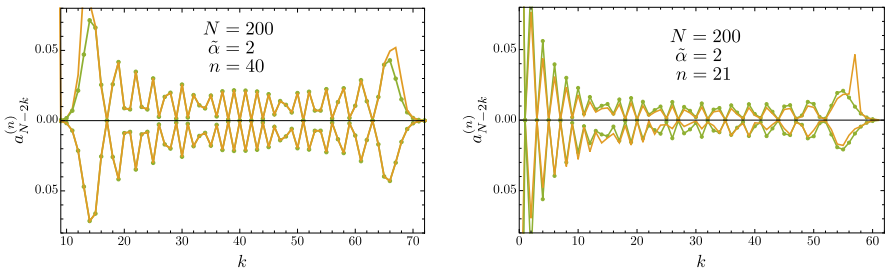

Figure 2.6: Comparison of the full semiclassical eigenvectors, Eq. (2.86), (lower panels), and the SPA result, Eq. (2.90), (upper panels), with the exact eigenvectors (green) for $N = 200$ and $\tilde{\alpha} = 2$. The curves show the squares of the (real) eigenvectors of the respective results. The solid lines connecting the discrete eigenvector components are only drawn for better visibility. Left: Excitation with $n = 40$ well above the the separatrix energy. The results from the full integration and the exact diagonalization are indistinguishable (lower panel) while the SPA approximation fails at the turning points as expected. Right: Smallest energy eigenstate above the separatrix energy ($n = 21$). The normalization of the semiclassical results deviates from the exact values, but the overall agreement is still good. Surprisingly, the SPA result is much better than the the full integration and can be renormalized such that it fits the numerical result almost everywhere (not shown), while the full integration yields larger or smaller values compared with the exact vector components depending on k.

when one approaches the separatrix energy, the quantized orbit will be very close to the line $z = 1$ for both types of motion and the results for the rotational orbits closest to the separatrix with $\omega \approx 0$ turn out to be less accurate than the ones with sufficiently large $\omega > 0$, also leading to non-normalized eigenvectors. In all other cases, the normalization of the $a_n^{(n)}$ obtained from the numerical integration of (2.86) are very close to one down to small particle numbers of the order of $N \sim 10$.

There is one further remark that should be made. It turns out that using the SPA result also in the classically forbidden regime, i.e., at one of the complex saddles, the real part of the resulting expression leads to the correct evanescent behavior, which is exploited in the figures discussed below.

Let us now turn to the actual comparison of the semiclassical and quantum-mechanical results, the latter being obtained from exact-diagonalization of $\hat{H}$, Eq. (2.42) with $k_{\max} = 1$. Figure 2.6 shows the comparisons of the semiclassical eigenvectors from the full calculation, Eq. (2.86), and the result in SPA, Eq. (2.90), with the exact eigenvectors for two different excitations. For the state with $n = 40$ well above the separatrix ($\omega_n \approx 0.125$), the full semiclassical result is indistinguishable from the exact one, with a normalization that is one to machine precision (approx. 10^{-16}). The SPA fails at the turning points where $\partial z/\partial\varphi = 0$ and can diverge for fine-tuned values of the interaction (if a turning point in z coincides with z_s for one of the values of k), while it gives

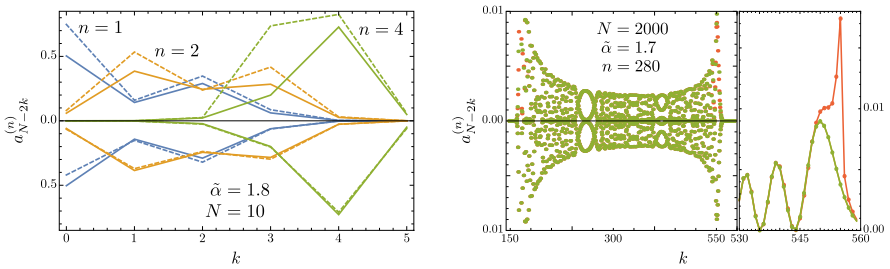

Figure 2.7: The comparison of the semiclassical and quantum mechanical eigenvectors analogous to Fig. 2.6. Left: $N = 10$, $\tilde{\alpha} = 1.8$, and $n = 1$ (blue), 2 (orange), and 4 (green). The full full integration of (2.86) still yields good results for $n > 1$ (lower panel), but the SPA is not justified anymore and gives poor approximations of the quantum states (upper panel). Right: $N = 2000$, $\tilde{\alpha} = 1.7$, and $n = 280$. Both upper and lower panel show the semiclassical results (green) *above* the exact quantum states (red). However, the full semiclassical result completely shadows the latter. Only in the SPA result, deviations can be seen at the classical turning points. This is highlighted in the right part of the figure, that shows as closeup of the turning point in z at $\varphi = 0$, see Fig. 2.3.

perfect results in the central part. For the lowest state above the separatrix energy ($n = 21, \omega_n \approx 1.27 \times 10^{-4}$) both semiclassical results yield a wrong normalization. The full integration of Eq. (2.86) gives values that are too small or too large depending on the value k and thus will not be much improved by renormalization. This is probably also connected to the fact that the semiclassical quantization is not perfect close to the separatrix, and ω_n deviates from the exact value $\omega_n \approx 1.62 \times 10^{-4}$ in the case at hand. Surprisingly, the SPA result is much more accurate and can be renormalized such that it coincides with the exact result everywhere except at few values around the turning points. This might be due to the fact that the φ representation of the WKB wave function has a divergence at the hyperbolic fixed points, i.e., for $\omega = 0$ and that this divergence strongly affects all the integrals, while the divergent term is absent in the SPA result, that is only determined by the crossing points of the quantized orbits with the horizontal lines and is thus insensitive to the hyperbolic fixed point almost everywhere.

For small particle numbers, i.e., a large effective Planck's constant, the semiclassical result and especially the SPA are expected to be poor approximations. Figure 2.7 demonstrates the effect of small and large particle numbers on the results. As it turns out, the full semiclassical result is still very good even for $N = 10$ (left part of the figure), as long as one is far enough above the separatrix energy. However, the stationary phase approximation does not give good results and cannot be justified anymore. The right part of Fig. 2.7 shows the comparison of the results for $N = 2000$. As expected, the semiclassical approximations give essentially exact results, except for the SPA diverging at the classical turning points as is typical for WKB wave functions, but can be fixed by means of uniform approximations [42].

To conclude, the semiclassical WKB wave function defined in the angle-representation for the rotating classical orbits captures essentially the full quantum state even down the few-particle case, as long as its energy is well above the separatrix energy. There, using the exact projection to the noninteracting states, one can obtain the full quantum mechanical eigenstates in the Fock basis, also capturing the transition from oscillatory to evanescent behavior at the turning points (in the condensate fraction z) of the quantized orbits. Moreover, the resulting states are correctly normalized.

Away from the classical turning points in z, the SPA works equally well for large particle numbers, however giving rise to the typical breakdown close to them.

One drawback of the WKB wave functions introduced here is that they cannot be used to extract the overlap of the states close to the separatrix energy with the low-lying noninteracting states that play an important role in quench scenarios. One way out of this dilemma could be a requantization of a local description around the hyperbolic fixed points as was used for the analysis of the fundamental gap between the ground state and the first excited state [61].

2.2.3. Phase space representation: Husimi functions

The semiclassical WKB wave functions investigated so far are analytic approximations to the actual quantum states. One can, however, directly visualize the quantum states by using one of the phase-space representations, i.e., the Wigner, Husimi Q and GlauberSudarshan P distributions [156]. Here, due to its simple computability, the Husimi function is calculated for the exact quantum states. For this one first has to calculate the coherent states in the 3-mode model. They are given in normalized form by

$$|\alpha_{-1}\alpha_0\alpha_1\rangle = \mathrm{e}^{-\frac{1}{2}(|\alpha_{-1}|^2+|\alpha_0|^2+|\alpha_1|^2)}\, \mathrm{e}^{\alpha_{-1}\hat{a}_{-1}^\dagger+\alpha_0\hat{a}_0^\dagger+\alpha_1\hat{a}_1^\dagger}\,|0\rangle\,, \tag{2.92}$$

where $|0\rangle$ is the vacuum state and the $\alpha_i = q_i + ip_i$ are complex numbers. One can easily show that the expectation values for the particle number and the momentum in a coherent state are given by

$$\langle\hat{N}\rangle = |\alpha_{-1}|^2 + |\alpha_0|^2 + |\alpha_1|^2 \equiv \bar{N}, \qquad \langle\hat{K}\rangle = |\alpha_1|^2 - |\alpha_{-1}|^2 \equiv \bar{K}. \tag{2.93}$$

Coherent states are superpositions of Fock states with different total particle number N and momentum K. The Husimi function is however given by the expectation value

$$Q_\rho(\alpha_{-1},\alpha_0,\alpha_1) = \frac{1}{\pi^3}\,\langle\alpha_{-1}\alpha_0\alpha_1|\hat{\rho}|\alpha_{-1}\alpha_0\alpha_1\rangle \tag{2.94}$$

of the density matrix of the quantum state that can (and should) be chosen to have fixed N and K. So, only the information of the projections of the coherent states to specific particle numbers and momenta is used. But these projections actually allow for a parametrization using only four independent variables, one of them being only a renormalization, such that the quantum state can be represented in a tree-dimensional subspace of the six-dimensional phase space spanned by the α_i.

Let us denote the projection of the coherent state to the sector of Fock space with N particles and momentum K by

$$|\alpha_{-1}\alpha_0\alpha_1\rangle_{N,L} = \hat{P}_{N,L}\,|\alpha_{-1}\alpha_0\alpha_1\rangle\,, \tag{2.95}$$

where $\hat{P}_{N,L}$ is the projector to the respective subspace. The full coherent state is then just the sum of the projected states.

By expanding the projected state into Fock states, changing to polar coordinates $\alpha_i = \sqrt{\bar{n}_i}\mathrm{e}^{i\vartheta_i}$, and expressing it in terms of the expectation values $\bar{N}$ and $\bar{K}$, Eq. (2.93), one finds that the fixed particle number and momentum lead to the $U(1)$ symmetries in two of the angles, i.e., two of the angles contribute only a phase, such that the projected coherent state is given by

$$|\alpha_{-1}\alpha_0\alpha_1\rangle_{N,K} = \mathrm{e}^{iN\bar{\varphi}_N + iK\bar{\varphi}_K}\,[P_{\bar{N}}(N)]^{\frac{1}{2}}\;\,|\bar{z},\bar{\varphi},\bar{l}\rangle_{N,K}\,, \tag{2.96}$$

where the new angles and scaled parameters $\bar{z}$ and $\bar{l}$ are given by

$$\bar{\varphi} = \vartheta_0 - \frac{\vartheta_1+\vartheta_{-1}}{2}, \quad \bar{\varphi}_N = \frac{\vartheta_1+\vartheta_{-1}}{2}, \quad \bar{\varphi}_K = \frac{\vartheta_1-\vartheta_{-1}}{2} \tag{2.97}$$

and

$$\bar{z} = \frac{\bar{n}_0}{\bar{N}} \in [0,1], \qquad \bar{l} = \frac{\bar{K}}{\bar{N}} \in [-(1-\bar{z}), 1-\bar{z}]. \tag{2.98}$$

This is in complete analogy to the transformations that are used to eliminate the constants of motion in the classical analysis of the 3-mode model, thus the individual steps are not repeated here. The function $P_{\bar{N}}(N)$ in Eq. (2.96) is the Poisson distribution of the number N with parameter $\bar{N}$ and reflects the probability distribution of the particle number N in the coherent state. As the phases and the normalization with the Poisson distribution do not have a physical meaning, the projected coherent state is reduced to a superposition of coherent single-particle excitations

$$|\bar{z},\bar{\varphi},\bar{l}\rangle_{N,K} = \frac{1}{2\pi\sqrt{N!}}\int_0^{2\pi} d\theta\,\mathrm{e}^{iK\theta}\left[\hat{b}_{\bar{z},\bar{\varphi},\bar{l}}(\theta)^\dagger\right]^N|0\rangle\,, \tag{2.99}$$

with the parametrized single-particle modes

$$\hat{b}_{\bar{z},\bar{\varphi},\bar{l}}(\theta) = \sqrt{\frac{1-\bar{z}-\bar{l}}{2}}\mathrm{e}^{-i\theta}\hat{a}_{-1} + \sqrt{\bar{z}}\mathrm{e}^{-i\bar{\varphi}}\hat{a}_0 + \sqrt{\frac{1-\bar{z}+\bar{l}}{2}}\mathrm{e}^{i\theta}\hat{a}_1. \tag{2.100}$$

The integration over the angle θ has only been introduced to simplify the notation and ensures the correct total momentum K of the state. The states (2.99) are not normalized to one but they fulfill the completeness relation (omitting the index N, K on the states)

$$\frac{(N+2)(N+1)}{2\pi}\int_0^1 d\bar{z}\int_0^\pi d\bar{\varphi}\int_{-(1-\bar{z})}^{1-\bar{z}} d\bar{l}\;|\bar{z},\bar{\varphi},\bar{l}\rangle\,\langle\bar{z},\bar{\varphi},\bar{l}| = \hat{P}_{N,K}, \tag{2.101}$$

i.e., they form a complete basis on the sector with particle number N and momentum K. With this, one can define the normalized Husimi Q representation of the states with fixed particle number N and fixed momentum K as

$$Q_\rho^{(N,K)}(\bar{z},\bar{\varphi},\bar{l}) = \frac{(N+2)(N+1)}{2\pi}\,\langle \bar{z},\bar{\varphi},\bar{l}|\hat{\rho}_{N,K}|\bar{z},\bar{\varphi},\bar{l}\rangle \tag{2.102}$$

for a density matrix with fixed particle number and momentum.

To obtain a two-dimensional representation one has to either trace out the phase space variable $\bar{l}$ associated with momentum or look at fixed values of $\bar{l}$. As one might expect, the phase space density in $\bar{l}$ obtained from tracing out $\bar{z}$ and $\bar{\varphi}$ then peaks at $\bar{l} = K/N$ with the peak getting more pronounced with higher N. It is thus reasonable to expect that using this value for a projection will contain most of the physics. This approach is used in the following, however with a modification. First, one defines the normalized coherent states as

$$|\bar{z},\bar{\varphi}\rangle_{\bar{l}} \equiv c(\bar{z},\bar{l})\,|\bar{z},\bar{\varphi},\bar{l}\rangle \tag{2.103}$$

with

$$|c(\bar{z},\bar{l})|^{-2} = \frac{1}{2\pi}\int_0^{2\pi} d\theta \mathrm{e}^{iK\theta}\left[\frac{1-\bar{z}-\bar{l}}{2}\mathrm{e}^{i\theta} + \bar{z} + \frac{1-\bar{z}+\bar{l}}{2}\mathrm{e}^{-i\theta}\right]^N \tag{2.104}$$

and then numerically checks, whether these states have a completeness relation. This yields, using $K > 0$ for simplicity,

$$\int_0^{1-\bar{l}} d\bar{z}\int_0^{\pi} d\bar{\varphi}\;|\bar{z},\bar{\varphi}\rangle\,\langle\bar{z},\bar{\varphi}| = \sum_{k=0}^{\lfloor\frac{N-K}{2}\rfloor} a_k(\bar{l})\,|k\rangle\,\langle k|\,, \tag{2.105}$$

where the states $|k\rangle$ are the three-mode Fock states with occupations $n_{-1} = k$, $n_1 = k + K$, and $n_0 = N - K - 2k$, that span the sector with fixed particle number and momentum. One then finds numerically that th coefficients $a_k(\bar{l})$ are almost uniform for $\bar{l} = K/N$ such that the states $|\bar{z},\bar{\varphi}\rangle_{K/N}$ form an (almost) complete set and (2.105) is approximately proportional to the projection operator $\hat{P}_{N,K}$, with the approximation getting better with higher particle numbers, as expected.

Figure 2.8 shows the Husimi functions obtained in this way for $N = 100$, $K = 0$, and $\tilde{\alpha} = 1.9$. The left figure shows four different eigenstates, starting from the ground state with index $k = 0$ being localized at the classical energy minimum. The state with $k = 3$ then resembles a vibrational orbit while the state with $k = 9$ is energetically close to the separatrix in classical phase space and shows signatures of both kinds of classical orbits. Higher excitations ($k = 15$ is shown) clearly have the signature of rotational classical orbits. The right part of Fig. 2.8 shows the time evolution of the noninteracting ground state after a quench of the interaction to $\tilde{\alpha} = 1.9$. The time is given in units of the [finite-size corrected, see Eq. (2.141)] local Ehrenfest time scale τ, Eq. (2.67). The distribution first approaches the region where one of the classical fixed points is located, then follows the lower branch of the separatrix and comes back very close to the initial distribution

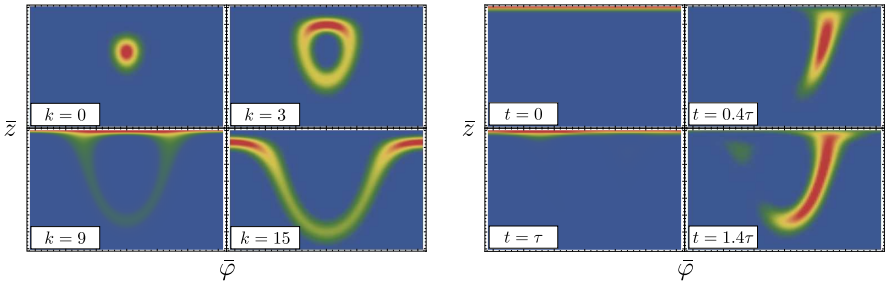

Figure 2.8: Plots of the Husimi functions for $N = 100$ and $\alpha = 1.9$. In each plot, the values of $\bar{z}$ range from 0.3 to 1 and the values of $\bar{\varphi}$ range from $-\pi/2$ to $\pi/2$. Left: the kth eigenstates for $k = 0, 3, 9, 15$. Right: Time evolution of the noninteracting ground state after a quench to the coupling $\alpha = 1.9$ for times $t = 0, 0.4\tau, \tau, 1.4\tau$, showing a revival of the initial state at $t \approx \tau$. For $t = 1.4\tau$, interference can be seen, as a part of the wave packet is split off.

at $t = \tau$. However, this revival is not perfect and one can see interference effects at later times, where a small part of the wave packet splits off (see plot for $t = 1.4\tau$). Also, the distribution is stretched stronger than one "period" before at $t = 0.4\tau$. However, one can still observe large parts of the distribution being concentrated at the boundary $z = 1$ for multiples of τ (not shown), which leads to the oscillations in the one-body entropy found in [61]. The implications of these oscillations for the out-of-time-ordered correlator are investigated in the next section.

2.2.4. The out-of-time-ordered correlator close to criticality

In this subsection, a specific quench scenario is applied and the subsequent non-equilibrium time dynamics is studied. As has been mentioned above, the semiclassical quantization around the separatrix gives rise to a very specific local level spacing given (to leading order in N) by

$$\Delta E_{\text{sep}} \approx \frac{2\pi\sqrt{\tilde{\alpha} - 1}}{\log \tilde{N}}. \tag{2.106}$$

This scaling is however only valid for a certain number of states where the classical dynamics is dominated by the vicinity of the hyperbolic fixed points. It turns out that the low-lying noninteracting states have exactly this property. Thus, if the noninteracting system is prepared at very low temperatures and the interaction is then quenched to a finite value $\tilde{\alpha} > 1$, the subsequent time dynamics will be strongly dominated by the local Ehrenfest time τ, Eq. (2.67). This has been verified in [61] for the reduced one-body density matrix, where increasing the particle number has led to a quasi-periodic time evolution of the von Neumann entropy calculated from the time evolution of the reduced density matrix. As it turns out, the conservation of the momentum renders the reduced one-body density matrix diagonal, and the only nontrivial dynamics is captured by the

time evolution of the mean condensate depletion that undergoes distinct oscillations that have also been found experimentally in the spin-1 Bose gas [204]. Here, the more intricate evolution of a certain OTOC will be studied and discussed.

The OTOC that is used here is defined by the expectation value of the squared commutator of the condensate fraction $\hat{n}_0/N$ at different times:

$$C(t) = -N^{-4} \langle \Psi | [\hat{n}_0(0), \hat{n}_0(t)]^2 | \Psi \rangle \,. \tag{2.107}$$

Here, $\hat{n}_0 = \hat{a}_0^\dagger \hat{a}_0$, and the expectation value is taken with respect to the noninteracting condensate $|\Psi\rangle = 1/\sqrt{N!}(\hat{a}_0^\dagger)^N |0\rangle$, with $|0\rangle$ being the vacuum state. The operator choice in Eq. (2.107) is the simplest nontrivial choice of operators in this model and it is worth noting that, due to the conservation of particle number $\hat{N}$ and momentum $\hat{K}$, Eq. (2.44), and $[\hat{n_0}(t), \hat{N}] = [\hat{n}_0(t), \hat{K}] = 0$, the seemingly more general definition of the OTOC

$$C_{ij}(k) = -N^{-4} \langle \Psi | [\hat{n}_i(0), \hat{n}_j(t)]^2 | \Psi \rangle \,, \qquad i,j \in \{-1,0,1\}, \tag{2.108}$$

is completely equivalent to (2.107), i.e., one has

$$C_{ij}(t) = c_{ij}\, C(t) \tag{2.109}$$

with real constants c_{ij}.

Semiclassical short-time analysis of the OTOC

The short-time mean-field (classical) dynamics of the OTOC can be obtained by noting that the operator $\hat{n}_0/N$ corresponds to the variable z and by taking only the fist non-vanishing order in N^{-1} (here identifying $N \approx \tilde{N}$) yields the phase space average of the Poisson bracket

$$C(t) \approx \frac{1}{N^2} \left\langle \{z(0), z(t)\}^2 \right\rangle_{\mathrm{PS}} = \frac{1}{N^2} \left\langle \left(\frac{\partial z(t)}{\partial \varphi(0)} \right)^2 \right\rangle_{\mathrm{PS}} , \tag{2.110}$$

where the average should be taken using the Wigner quasi-distribution function of the condensate. This is in complete analogy to the considerations in subsection 2.1.5 of the introduction of chapter 2 with $\hbar_{\mathrm{eff}} = 1/N$, which is why the steps are not reproduced here. Note that the Poisson bracket used here is defined by the phase space variables (φ, z) instead of (φ, n_0) [c.f., Eq. (2.50)]. Without calculation, one can now expect that the Wigner function of the non-interacting ground state will be exponentially localized at the upper boundary of the phase space, with a localization length that scales as $1/N$ in order to be compatible with the quantized orbit $z = 1/\tilde{N}$ that exactly reproduces the ground state in EBK torus quantization. This is also supported by the WKB wave function analysis presented earlier in this section, where the overlap of the interacting states with the noninteracting condensate was exponentially small if the corresponding quantized orbits did not meet, such that only the classical phase space close to the upper boundary can contribute to the quantum-mechanical short-time dynamics that are described by the truncated Wigner-like approach taken here.

With this line of arguing, only the classical dynamics close to the separatrix play a role for short times. There, the hyperbolic fixed points dominate the dynamics, introducing an exponential sensitivity to changes in the initial conditions with a divergence rate given by the stability exponent λ_s of the fixed points. One can thus expect $C(t)$ to behave like

$$C(t) \approx \frac{c}{N^2} \mathrm{e}^{2\lambda_s t} \tag{2.111}$$

for short times, with a constant c that is to be determined. This is indeed true, but there is one crucial point that was skipped in the arguments. The dynamics around a hyperbolic fixed point is actually decoupled such that for a trajectory starting close to the fixed point one obtains

$$z(t) = z(0)\mathrm{e}^{\pm\lambda_s t} \quad \Rightarrow \quad \frac{\partial z(t)}{\partial \varphi(0)} = 0, \tag{2.112}$$

if a local approximation is assumed. This would render those local contributions trivially zero. Therefore, a closer analysis of the classical dynamics is required that covers the whole range of relevant initial conditions.

Let us thus approximate the Hamiltonian function for small distances $\zeta = 1 - z$ from the upper boundary, while keeping the full dependence on φ:

$$\bar{\omega}(\varphi, z) = \zeta(1 - \tilde{\alpha}\cos^2\varphi). \tag{2.113}$$

This linear approximation in ζ is only valid if $(1 - \tilde{\alpha}\cos^2\varphi) \gg \zeta$. As we are interested in the case $\tilde{\alpha} > 1$, where the φ-coordinates φ_c of the hyperbolic fixed points are determined by $1 - \tilde{\alpha}\cos^2\varphi_c = 0$ this exactly *excludes* the fixed points. The philosophy of the approach here is to approximate the classical dynamics away from the fixed point by the linear approximation in ζ and switching to the local hyperbolic description when the $\varphi - \varphi_c$ becomes comparable to ζ, i.e., the fixed point is approached. This can be summarized in writing

$$\frac{\partial z(t)}{\partial \varphi(0)} = \frac{\partial z(t)}{\partial z(t_c)} \frac{\partial z(t_c)}{\partial \varphi(0)} \approx \mathrm{e}^{\lambda_s (t - t_c)} \times \left. \frac{\partial z(t_c)}{\partial \varphi(0)} \right|_{\mathrm{lin}} \tag{2.114}$$

with some intermediate time t_c where the linearization breaks down and with the second factor evaluated using the linearized Hamiltonian function $\bar{\omega}$. Here, it has been assumed that the initial angle $\varphi(0)$ is not at one of the fixed points. Then, the trajectory will approach the fixed point that is attractive in φ and thus repulsive in ζ. Therefore, only the diverging solution from (2.112) close to the fixed point is used.

Let us now solve the linearized problem with the Hamiltonian function (2.113). By using the distance $\zeta = 1 - z$ from the boundary as a variable, the equations of motion (2.51) are modified to

$$\dot{\zeta} = \frac{\partial \bar{\omega}}{\partial \varphi}, \qquad \dot{\varphi} = -\frac{\partial \bar{\omega}}{\partial \zeta} = \tilde{\alpha}\cos^2\varphi - 1 \tag{2.115}$$

subject to the initial conditions $\zeta(0) = \zeta_0$ and $\varphi(0) = \varphi_0$. As can be seen, the equation of motion for φ completely decouples from ζ. It can be solved by separation as

$$t(\varphi, \varphi_0) = \int_{\varphi_0}^{\varphi} \frac{d\varphi'}{\tilde{\alpha}\cos^2\varphi - 1}. \tag{2.116}$$

Before solving this equation, let us express $\zeta(t)$ and its derivative with respect to φ_0 by $\varphi(t)$. For the former, the energy conservation directly yields

$$\bar{\omega} = -\zeta\dot{\varphi} \quad \Rightarrow \quad \zeta(t) = \zeta(0)\frac{\dot{\varphi}(0)}{\dot{\varphi}(t)} = \zeta_0\frac{\tilde{\alpha}\cos^2\varphi_0 - 1}{\tilde{\alpha}\cos^2\varphi(t) - 1}. \tag{2.117}$$

To get the derivative of $\zeta(t)$ with respect to φ_0 one can make use of the general form of the solution of (2.116) with

$$\left(\frac{\partial\varphi}{\partial\varphi_0}\right)_t = -\left(\frac{\partial\varphi}{\partial t}\right)_{\varphi_0}\left(\frac{\partial t}{\partial\varphi_0}\right)_\varphi = -\dot{\varphi}(t)\left(-\frac{1}{\dot{\varphi}(0)}\right) = \frac{\dot{\varphi}(t)}{\dot{\varphi}(0)} = \frac{\zeta_0}{\zeta(t)} \tag{2.118}$$

which can be used to evaluate the derivative of $\zeta(t)$ with respect to φ_0, leading to

$$\left.\frac{\partial\zeta}{\partial\varphi_0}\right|_{\text{lin}} = \zeta_0\frac{\sin 2\varphi - \sin 2\varphi_0}{\cos^2\varphi - \tilde{\alpha}^{-1}}, \tag{2.119}$$

where the explicit time dependence has been suppressed for simplicity. This solution must be cut off at a certain distance δ from the fixed point located at $\varphi_c = \arccos(1/\sqrt{\tilde{\alpha}})$, where the solution of (2.116) will end up eventually. We can thus set $\varphi = \varphi_c + \delta$ and expand the the above result for small δ. To leading order, this yields

$$\left.\frac{\partial\zeta}{\partial\varphi_0}\right|_{\text{lin}} \approx \zeta_0\frac{2\cos(\varphi_0+\varphi_c)\sin(\varphi_0-\varphi_c)}{\sin(2\varphi_c)}\,\delta^{-1}. \tag{2.120}$$

The exact solution to (2.116) can be expressed as

$$\frac{\sin(\varphi+\varphi_c)}{\sin(\varphi-\varphi_c)} = \frac{\sin(\varphi_0+\varphi_c)}{\sin(\varphi_0-\varphi_c)}\mathrm{e}^{\lambda_s t}. \tag{2.121}$$

By expanding also this at $t = t_c$, where t_c defines the cutoff $\varphi(t_c) = \varphi_c + \delta$ one obtains

$$\mathrm{e}^{-\lambda_s t_c} \approx \frac{1}{\sin(2\varphi_c)}\frac{\sin(\varphi_0+\varphi_c)}{\sin(\varphi_0-\varphi_c)}\,\delta. \tag{2.122}$$

Finally, combining Eqs. (2.114), (2.120), and (2.122), one obtains the simple formula for the classical instability

$$\frac{\partial\zeta}{\partial\varphi_0} = \zeta_0\frac{\sin(2(\varphi_0+\varphi_c))}{\sin^2(2\varphi_c)}\,\mathrm{e}^{\lambda_s t}. \tag{2.123}$$

There are two details that have been put under the carpet here. First, although the result does not depend on t_c anymore, the calculation assumes that $t > t_c$ for given initial conditions, i.e., one has to wait a certain time $t_c \sim 1/\lambda_s$ given by Eq. (2.122), until an exponential growth can be expected. Second, if one uses Eqs. (2.121) and (2.120) evaluated at $t = t_c$ in (2.114) without further approximation, one finds a prefactor of the exponential that depends on the cutoff δ explicitly. This prefactor has a singular limit for $\delta \to 0$: for any finite δ, the prefactor vanishes when the initial angle φ_0 approaches the cutoff, a property that is not shared by the simple limiting expression (2.123). However,

the initial value ζ_0 can be chosen arbitrarily small, such that, although we must have $\zeta \ll \delta$, the cutoff can also become arbitrarily small. Moreover, comparing with the numerically integrated classical dynamics (not shown), one finds that the result (2.123) gives the correct prediction also for very small cutoffs (after waiting for the exponential behavior to set in). One intuitive explanation could be that the trajectory stays close to the fixed point for a longer time, such that the very small nonlinear contributions have a longer time to grow to notable size. The actual reason is, however, that the hyperbolic fixed points of the Hamiltonian $\bar{\omega}$, that is only linear in ζ, have the same stability properties as the original ones and can be transformed to the latter by a local canonical transformation.

We are now in the position to predict the short-time behavior of the OTOC. However, we need to have an estimate for the Wigner distribution for the noninteracting ground state. Let us assume that the noninteracting ground state is exponentially localized at $z = 1$ and uniform in φ, i.e., the Wigner function has the form

$$W_0(\varphi, z) = \frac{a}{\pi} \mathrm{e}^{-a(1-z)} \tag{2.124}$$

with a parameter $a \gg 1$, such that the function drops off quickly and is normalized to one (restricting φ to an interval of length π). On the other hand, the semiclassical quantization rule (2.55) is exact in the free case and gives the quantized orbit corresponding to the ground state as

$$1 - z = \frac{1}{\tilde{N}}. \tag{2.125}$$

For this to be consistent with the Wigner function above we have to fix the correct classical limit by setting

$$\int_{-\frac{\pi}{2}}^{\frac{\pi}{2}} d\varphi \int_0^1 dz\, W_0(\varphi, z)\, z = 1 - \frac{1}{\tilde{N}} \quad \Rightarrow \quad a = \tilde{N} \approx N. \tag{2.126}$$

So, as expected, the localization length given by $1/a$ scales as $1/N$. With this, one can estimate the phase space average in Eq. (2.110), assuming that the trajectories stay close to the hyperbolic fixed points for a time that is long enough that all the initial conditions can contribute to the exponential. This cannot be guaranteed for the initial conditions that start off close to the other fixed point at $-\varphi_c$, where the dynamics slows down exponentially, but these contributions have a vanishing weight in (2.123), thus justifying the average

$$\begin{aligned}
\left\langle \left(\frac{\partial z(t)}{\partial \varphi_0} \right)^2 \right\rangle_{\mathrm{PS}} &= \left\langle \left(\frac{\partial \zeta(t)}{\partial \varphi_0} \right)^2 \right\rangle_{\mathrm{PS}} \\
&= \int_{-\frac{\pi}{2}}^{\frac{\pi}{2}} d\varphi_0 \int_0^1 d\zeta_0\, W_0(\varphi_0, 1-\zeta_0) \left[\zeta_0 \frac{\sin(2(\varphi_0 + \varphi_c))}{\sin^2(2\varphi_c)} \mathrm{e}^{\lambda_s t} \right]^2 \\
&= \frac{1}{\tilde{N}^2} \frac{\mathrm{e}^{2\lambda_s t}}{\sin^4(2\varphi_c)} = \frac{1}{\tilde{N}^2} \left(\frac{\tilde{\alpha}}{\lambda_s} \right)^4 \mathrm{e}^{2\lambda_s t}.
\end{aligned} \tag{2.127}$$

The short-time behavior of the OTOC is thus estimated semiclassically as

$$C(t) \approx \left(\frac{\tilde{\alpha}}{\tilde{N}\lambda_s}\right)^4 \mathrm{e}^{2\lambda_s t}. \tag{2.128}$$

So, the OTOC for the interaction quench considered here is expected to grow exponentially for short times (with $t \gtrsim 1/\lambda_s$), and moreover, by a thorough analysis of the classical phase space, even the proportionality factor has been calculated. However, as in chaotic systems, quantum interference will become important after a certain time. In chaotic systems, this leads to a saturation regime after the Ehrenfest time. In contrast, in the integrable system at hand, and with the quench of the noninteracting condensate to the supercritical regime, one could expect that the time dynamics will be dominated by the local Ehrenfest time (2.67) defined by the local level spacing close to the separatrix energy (i.e., the excited state quantum phase transition). Moreover, as the latter is the definitional property of the Heisenberg time that sets the timescale for quantum revivals, one might expect to see strong oscillations in the OTOC rather than a saturation, even enhanced by the very regular and asymptotically *equidistant* spectrum.

It is, however, not obvious that only the states close to the excited state quantum phase transition contribute to the OTOC, and this is certainly not the case for arbitrary long times. As the classical phase-space stability analysis can be expected to become invalid quickly after the local Ehrenfest time, the long-time dynamics can only be obtained from quantum calculations.

Numerical simulation of the OTOC's dynamics

For the diagonalization of the OTOC (2.107), the states

$$|n_{-1}, n_1, n_0\rangle\,, \qquad n_j = 0, 1, \ldots \tag{2.129}$$

spanning the three-mode Fock space are used. Restricting to the sector with the particle number N and total momentum $K = 0$ one can label the states by a single quantum number as

$$|k\rangle = |k, N-2k, k\rangle\,, \qquad k = 0, 1, \ldots, \lfloor N/2 \rfloor. \tag{2.130}$$

These states are the energy eigenstates of the noninteracting system with energy $E_k = 2k$, with the condensate state now given by $|0\rangle$. The sectors with different $K \neq 0$ can be treated similarly, but they are of no relevance here, as the ground state is a zero momentum state and the operators used in the OTOC are momentum conserving.

The OTOC can then be expanded by inserting the completeness relation between the commutators as

$$\begin{aligned} C(t) &= -\frac{1}{N^4}\,\langle 0|[\hat{n}_0(t), \hat{n}_0(0)]^2|0\rangle = \frac{1}{N^4}\sum_{k=0}^{\lfloor N/2 \rfloor} |\langle k|[\hat{n}_0(t), \hat{n}_0(0)]|0\rangle|^2 \\ &= \left(\frac{2}{N}\right)^4 \sum_{k=0}^{\lfloor N/2 \rfloor} k^2\, |\langle k|\hat{n}_1(t)|0\rangle|^2\,, \end{aligned} \tag{2.131}$$

where switching to the operator $\hat{n}_1$ (that is identical to $\hat{n}_{-1}$ in the zero-momentum sector) yields a more natural description using

$$\hat{n}_1 |k\rangle \equiv \hat{n} |k\rangle = k |k\rangle . \tag{2.132}$$

It is thus clear that the central objects that characterize the OTOC are the time-dependent matrix elements

$$n_{k0}(t) = \langle k|\hat{n}(t)|0\rangle \tag{2.133}$$

with $k > 0$, as the case $k = 0$ does not contribute to the OTOC (2.131). Thus, as $n_{kl}(0) \equiv n_{kl} = k\delta_{kl}$ and therefore $n_{k0}(0) = 0$ for $k \neq 0$, the whole time dynamics of the OTOC is due to the operator $\hat{n}(t)$ losing its diagonal form. A different interpretation can be obtained by switching to the Schrödinger picture by introducing the propagator

$$K_{lm}(t) = \left\langle l \left| \mathrm{e}^{-i\hat{H}t} \right| m \right\rangle , \tag{2.134}$$

leading to forward and backward-in-time propagations,

$$n_{k0}(t) = \sum_{l,m} K^*_{lk}(t) n_{lm} K_{m0}(t) = \sum_{l} K_{kl}(-t)\, l\, K_{l0}(t). \tag{2.135}$$

Here, the asterisk denotes complex conjugation. The matrix elements $n_{k0}(t)$ can thus be understood as a forward propagation of the condensate, then perturbing the state by applying the number operator $\hat{n}$ and propagating back in time to a *different* (noninteracting) state, which is only possible due to the "perturbation".

One might think that, although the semiclassical analysis for short times required taking into account the nonlinearities in the equations of motion, quantum mechanical interference could still yield nontrivial results in a local description using a Hamiltonian

$$\hat{H}_{\mathrm{loc}} = \gamma \hat{z}^2 + \nu(\hat{z}\hat{\varphi} + \hat{\varphi}\hat{z}), \tag{2.136}$$

with real parameters γ, ν, that one would obtain from the quantization of a local description of the fixed points. Note that this Hamiltonian is a variant of the so-called xp-model that is conjectured to have a close relation to the Riemann zeros [207]. It is straightforward to show that the propagator for the Hamiltonian (2.136) is given by[9]

$$K(z', z; t) = \langle z'| \exp(-i\hat{H}_{\mathrm{loc}} t)|z\rangle = \mathrm{e}^{-i\frac{\gamma}{\nu}\sinh(\nu t) z z'} \delta\left(z' \mathrm{e}^{\frac{\nu t}{2}} - z \mathrm{e}^{-\frac{\nu t}{2}} \right). \tag{2.137}$$

In other words, any basis state $|z\rangle$ is just accelerated away from or to the fixed point without dispersion (depending on the sign of ν), i.e.,

$$|\psi(0)\rangle = |z_0\rangle \quad \Longrightarrow \quad |\psi(t)\rangle = A(t, z_0) \mathrm{e}^{\frac{\nu t}{2}} |z_0 \mathrm{e}^{\nu t}\rangle , \tag{2.138}$$

with a time dependent phase $A(t, z_0)$. Identifying $z = k/N$ in the mean-field limit one would then obtain

$$n_{k'k}(t) \propto \langle z' \mathrm{e}^{\nu t}| z \mathrm{e}^{\nu t}\rangle \propto \delta(z' - z), \tag{2.139}$$

such that the OTOC would become zero in this approximation.

[9] The derivation was performed using the Feynman path integral. As the propagators for quadratic Hamiltonians are well-understood, the proof is omitted here.

One should thus work either with the full semiclassical approximation for the propagators K_{kl} as in [177] or with the exact numerical solutions, which requires the calculation of the eigensystem of the interacting Hamiltonian for the time evolution. Here, the second approach will be taken. As the matrix elements n_{kl} are only needed for $l = 0$, they can then be very efficiently calculated by successive multiplications of matrices with a single vector, where only the matrix for the change between the noninteracting and interacting basis is not sparse (but is needed four times). For moderate particle numbers $N \lesssim 10^4$ this can be done on a normal desktop computer without approximation. If one needs to go to higher particle numbers one can do so by truncating both bases in a way that is inspired by the semiclassical analysis. For this one first uses the fact that the condensate state $|0\rangle$ only overlaps with a number of states around the separatrix that scales logarithmically with the particle number, such that the time evolution of this state requires only a few interacting states that lie close to the separatrix. In a phase space picture, the Wigner function of the time evolved state will then only be spread along the separatrix, dropping off quickly away from it. Now, the application of the number operator n could, in principle, smear out this phase-space distribution. However, the highest order effect in the effective Planck constant is a multiplication of the phase-space distribution with z, i.e., a redistribution of the weight, but not changing the shape of the Wigner function, such that it is still exponentially small away from the separatrix. One should thus expect that the overlap of the so-obtained state with interacting states away from the separatrix is small such that in the overall calculation, only the states close to the separatrix play a role.

This way of arguing might sound inconsistent for the following two reasons: First, the Wigner function does not represent the state itself but the density matrix that it defines. This is cured by the fact that we are actually only interested in the absolute values $|n_{k0}(t)|^2$, which can be written as the expectation value via

$$|n_{k0}(t)|^2 = \mathrm{Tr}\left\{\hat{\rho}_0(t)\hat{n}\hat{\rho}_k(t)\hat{n}\right\}, \tag{2.140}$$

with the density matrices $\hat{\rho}_k(t)$ of the time evolved states $\mathrm{e}^{-i\hat{H}t}|k\rangle$, such that a Wigner mapping is well defined. Second, one should be very careful using an argument based on a small Planck constant in a calculation that aims on the effects beyond the semiclassical regime. However, one can put the argument in a different way by stating that for any (fixed) time t, the quenched time evolution of the noninteracting states is calculated *exactly* (for all k), but the contributions of the interacting states far from the separatrix are projected out in a final overlap calculation, such that they could have been dropped from the beginning. Moreover, one sees that only the states $|k\rangle$ that have a non-vanishing overlap with the states close to the separatrix contribute, such that one can introduce a cutoff in k, that can be estimated semiclassically from the minimum in z of the separatrix. This cutoff is very efficient for couplings $\tilde{\alpha} \gtrsim 1$, where the separatrix is small. However, as it scales linearly with the particle number, it is less important than the cutoff in the interacting basis, that can be chosen *logarithmic* in N. The actual number of states that have to be used has to be determined by varying the cutoff. Figure 2.9 shows the relative error $r_i(t)$ in the OTOC when the number of states is truncated to $N_i = \lfloor i \log N \rfloor$ for

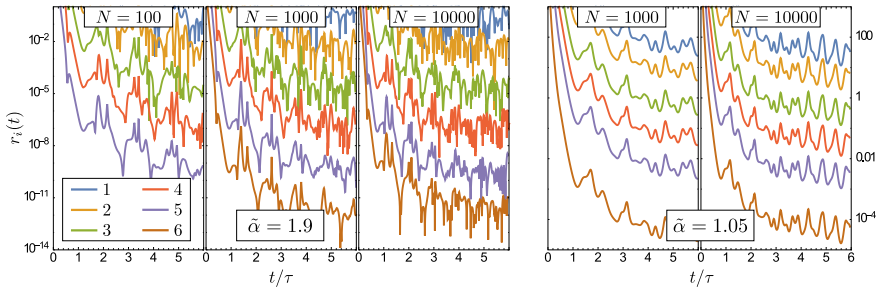

Figure 2.9: The relative error in the OTOC when using only $N_i = \lfloor i \log N \rfloor$ energy eigenstates around the separatrix energy. The left three plots show the error for $\tilde{\alpha} = 1.9$, having acceptable convergence already for $i = 1$. For $\tilde{\alpha} = 1.05$, where the separatrix is small, one needs to take more states into account.

different particle numbers and two different values of the coupling. The truncation is performed by shifting the whole spectrum with the separatrix energy by subtracting E_{sep} from the Hamiltonian and then calculating the N_i smallest eigenvalues and the corresponding states. For the calculation of the error, the full diagonalization of the Hamiltonian has also been calculated. As can be seen, the relative error decreases exponentially with i, which allows for a remarkable reduction of computational effort. This works best if $\tilde{\alpha}$ is well beyond the critical value, where $i = 1$ gives already reasonable results for later times. For $\alpha \gtrsim 1$, one should take into account a larger number of interacting states (note the different scales of the vertical axes). But in the latter case, the separatrix has only a very small extent in the classical phase space, c.f. Fig. 2.3, such that one can use a small cutoff in the states $|k\rangle$.

The OTOC can thus be calculated very efficiently in this model for quite large particle numbers, the bottleneck being the approximate diagonalization around the separatrix. Due to the simple form of the Hamiltonian as a tridiagonal matrix, it has been pushed up to $N = 10^7$. Although it would be possible to go to even larger numbers, the particle numbers $N \leq 10^6$ seem to be sufficient to uncover the nontrivial large-N scaling behavior. Figure 2.10 shows the OTOC, Eq. (2.107) for various particle numbers ranging from $N = 10$ to $N = 10^6$ and for $\tilde{\alpha} = 2$. The time is measured in units of the local Ehrenfest time scale (2.67) including finite-size corrections [61],

$$\tau = \frac{1}{\sqrt{\tilde{\alpha} - 1}} \left[\log N + 1 + \log \left(\frac{128(\tilde{\alpha} - 1)^2}{\tilde{\alpha}^2(8 - \tilde{\alpha})} \right) - \frac{\tilde{\alpha} - 1}{\tilde{\alpha}} \log(\tilde{\alpha} - 1) \right], \tag{2.141}$$

and the number of states around the separatrix has been cutoff to $\lfloor 15 \log N \rfloor$, which is expected to be much larger than required. After a fast initial growth, the OTOC reaches a maximum, but then, at around the local Ehrenfest time, it drops down several orders of magnitude. This behavior repeats in a quasiperiodic pattern, getting more and more pronounced with increasing particle number. As the first (exponential) growth of the OTOC is commonly viewed as a signature of scrambling of information, one can view

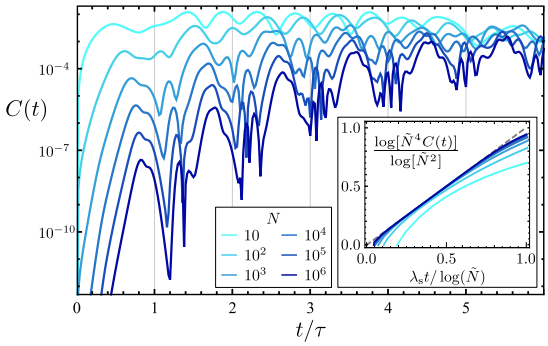

Figure 2.10: Time evolution of the OTOC $C(t)$, Eq. (2.107), for various particle numbers and $\tilde{\alpha} = 2$. $C(t)$ exhibits distinct, approximately τ-periodic oscillations, where τ, Eq. (2.141) is the local Ehrenfest time. The inset shows the initial growth of $C(t)$ approaching the semiclassical prediction, Eq. (2.128).

the quasiperiodic revivals as *unscrambling* of the information. This unscrambling can only occur if the system comes back very close to its initial configuration at (or close to) multiples of the local Ehrenfest time as it is suggested by the nearly-equidistant level spacing. One can also observe that the strength of the revivals get smaller with time, eventually approaching a quasi-saturated regime, where, as the Ehrenfest time and the Heisenberg time coincide in this model, oscillations due to the quantum nature of the system are present at any time. However, it seems that the mean saturation value is of the same order of magnitude for all particle numbers. The plot in the inset inset verifies the short-time behavior by collapsing the results for different particle numbers by assuming that the formula (2.128) holds for times smaller than half the local Ehrenfest time. Note that the semiclassical prediction for the prefactor is verified perfectly.

The unscrambling behavior seen in the OTOC is in strong contrast to the expected OTOC time evolution for a chaotic system, saturating at around the Ehrenfest time, with fluctuations that are small due to the irregular frequency spectrum. Eventually, recurrences can be enforced by the discreteness of the spectrum at around the Heisenberg time, but this time scale is typically algebraic in the (effective) Plank constant and is very large compared to the Ehrenfest time.

By directly calculating the OTOC, one uses less information than is actually generated on the fly as the individual matrix elements $n_{k0}(t)$ are summed up. Directly looking at the latter reveals a very interesting behavior. Figure 2.11 shows a logarithmic plot of the first six absolute squares $|n_{k0}(t)|^2$ for $N = 10^4$ and $\tilde{\alpha} = 3.9$. It shows that *only* $n_{10}(t)$ grows with the rate $2\lambda_s$ predicted for the OTOC and completely dominates the short-time behavior in the overall sum. However, a much more interesting finding is that one also finds exponential growth for $k > 1$, with rates that are integer multiples of $2\lambda_s$. And, as if this is not enough, even the their prefactors are consistent with a power law, such that they tend to meet in a single point. Formally, one finds that the short-time

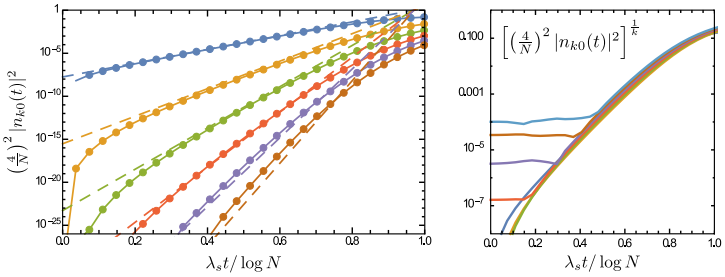

Figure 2.11: Left: Short-time behavior of the squared matrix elements $|n_{0k}(t)|^2$, Eq. (2.133), for $N = 10^4$ and $\tilde{\alpha} = 3.9$ and for $1 \leq k \leq 6$ (dots connected by solid lines) on a logarithmic scale. The dashed lines are given by $N^{-2}(\tilde{\alpha}/\lambda_s)^4 \mathrm{e}^{2k\lambda_s t}$, showing that the matrix elements $n_{0k}(t)$ grow with a rate proportional to k. Right: Collapse of the $n_{0k}(t)$ for $1 \leq k \leq 8$ using Eq. (2.143). The finite constant values at $t = 0$ for $k \geq 5$ (and beyond) are due to the numerical precision ($\sim 10^{-16}$) of the matrix elements $n_{0k}(t)$ and indicate that the respective values are effectively zero there.

behavior of the matrix elements of the number operator $\hat{n}$ is very well described by

$$\left(\frac{4}{N}\right)^2 |n_{k0}(t)|^2 = \left[\left(\frac{4}{N}\right)^2 |n_{10}(t)|^2\right]^k, \tag{2.142}$$

such that they are not independent for short times. The last equation can be rewritten in in the scaling form

$$\left[\left(\frac{4}{N}\right)^2 |n_{k0}(t)|^2\right]^{\frac{1}{k}} = \left(\frac{4}{N}\right)^2 |n_{10}(t)|^2 \sim \frac{1}{N^2}\left(\frac{\tilde{\alpha}}{\lambda_s}\right)^4 \mathrm{e}^{2\lambda_s t}, \tag{2.143}$$

such that only the left hand side of the equation depends on k. The last scaling in (2.143) originates from the dominance of the $k = 1$ term for short times $t \lesssim \log N/\lambda_s$ and the short-time prediction for the OTOC, Eq. (2.128), together with the expansion of $C(t)$ into the functions $n_{0k}(t)$. Thus, a more accurate short-time approximation of the OTOC (2.107) is given by

$$C(t) \approx \frac{1}{N^2}\sum_{k=1}^{k_{\mathrm{cut}}} k^2 \left[\frac{4}{N}|n_{01}(t)|\right]^{2k} \approx \sum_{k=1}^{k_{\mathrm{cut}}} k^2 \left[\left(\frac{\tilde{\alpha}}{\tilde{N}\lambda_s}\right)^4 \mathrm{e}^{2\lambda_s t}\right]^k, \tag{2.144}$$

where a cutoff $k_{\mathrm{cut}} \leq \lfloor N/2 \rfloor$ was introduced that controls the "order" of approximation. The second approximation is only valid for some intermediate times, where the exponential approximation is justified. So, in this respect, the semiclassical short-time result (2.128) is just the first order approximation with $k_{\mathrm{cut}} = 1$ of an expansion into powers of exponential functions.

Unfortunately, a theoretical explanation of this behavior has not been found yet. However, there are some hints that might help solving this problem. The reader might have noticed the large value of the interaction used in Fig. 2.11. One reason for this value is to demonstrate that also the semiclassical prediction for the prefactor $(\tilde{\alpha}/\lambda_s)^4 \approx 1.72$ in the equations is accurate. This could be better demonstrated at couplings close to $\tilde{\alpha} = 1$, where this prefactor diverges. However, the universal behavior breaks down (at least for $N \leq 10^4$) when approaching this point (not shown). As this is the point where the two hyperbolic fixed points in the classical phase space come close to each other, any local description would have to take into account both fixed points. Conversely, the fact that the scaling (2.143) is valid for larger couplings, where the hyperbolic fixed points are well separated, could hint at a general feature of (isolated) hyperbolic fixed points.

The form of the short-time behavior of $C(t)$ as a power series in $\mathrm{e}^{\lambda_s t}$ strongly resembles the Ansatz

$$F(t) = \langle \chi_i(t)\rho^{\frac{1}{4}}\chi_j(0)\rho^{\frac{1}{4}}\chi_i(t)\rho^{\frac{1}{4}}\chi_j(0)\rho^{\frac{1}{4}}\rangle \approx C_0 + C_1\frac{\mathrm{e}^{\lambda t}}{N} + C_2\left(\frac{\mathrm{e}^{\lambda t}}{N}\right)^2 + \dots \tag{2.145}$$

for the (regularized) thermal OTOC of Majorana operators χ_k in a (quenched) disorder average in the Sachdev-Ye-Kitaev model [174], that is motivated from a diagrammatic approach that includes summing up certain classes of diagrams [208]. A closer analysis of the applicability of the approach to the model at hand could shed light on the mechanism leading to the observed behavior of the matrix elements n_{0k}.

2.2.5. Perturbation with external potential

We have seen in the last subsection, that an interaction quench of the noninteracting condensate leads to a quasi-periodic behavior of the out-of-time-ordered correlator that can be interpreted as successive scrambling and unscrambling of the information about the initial configuration of the system. However, as the retrieval of the information on the initial state is due to the dynamics close to a separatrix, one should ask the question about the robustness of the phenomenon against integrability breaking. In the classical mean-field description one should expect that a small external perturbation of the system should manifest itself dominantly in the vicinity of the separatrix [42]. To be more specific, if a trajectory comes close to a hyperbolic fixed points, the classical forces in the equations of motion get arbitrarily small, while the dynamics slow down exponentially, such that a small perturbation can have a large effect, leading to a stochastic layer around the separatrix. On the other hand, a hidden renormalization group, that exists around the (perturbed) hyperbolic fixed points [209], suggests that the local Ehrenfest time τ, Eq. (2.67) might still play an important role, as it has exactly the analytic form of the required time renormalization.

The simplest way to get a nonintegrable extension of the 3-mode model considered here is obtained by breaking the conservation of the momentum $\hat{K}$, Eq. (2.43). This can be done by adding the perturbation

$$\gamma\hat{V} = \frac{\gamma}{2}\left[\hat{a}_0^\dagger(\hat{a}_1 + \hat{a}_{-1}) + (\hat{a}_1^\dagger + \hat{a}_{-1}^\dagger)\hat{a}_0\right] \tag{2.146}$$

to the Hamiltonian (2.42). It corresponds to an external potential of the form $\cos(\theta)$ on the ring in three-mode approximation. This perturbation has also been used to study the finite-size effects on the collapse of the wave function [194], as for finite particle numbers, the lowest energy eigenstates of the different momentum sectors have a finite gap with the unperturbed ground state, such that a finite perturbation is needed for a localization of the state. If this finite critical perturbation value $\gamma_c \sim N^{-2}$ is exceeded, a Gaussian momentum distribution is assumed, centered around the unperturbed ground state with $K = 0$. However, for the excited state quantum phase transition, the effect of such a perturbation has not been investigated in detail, and it is not clear, how the dynamics after an interaction quench as considered above are affected. One possible scenario is that the number of states that have a finite overlap with the noninteracting ground state is strongly increased by the additional degree of freedom and the extension of the quantum mechanical eigenstates along the stochastic layer in classical phase space. However, for finite perturbations, there should also be a regime, where the effect of the perturbation can be included via a perturbative expansion.

In the following, only a few results are presented that were obtained in a Bachelor project by Dominik Hahn under supervision of the author of this thesis. In the classical analysis, the perturbation leads to an additional term in the scaled Hamiltonian (2.48),

$$\Delta\omega_\gamma(\varphi, z, \varphi_l, l) = \gamma\sqrt{\frac{z}{2}}\left[\sqrt{1-z+l}\cos(\varphi-\varphi_l) + \sqrt{1-z-l}\cos(\varphi+\varphi_l)\right], \quad (2.147)$$

such that the conjugate angle φ_l to $l = K_{\mathrm{cl}}/\tilde{N}$ is not cyclic anymore and the momentum l is not conserved. To investigate the classical dynamics one can make use of Poincaré sections, i.e., by plotting only the (directed) intersections of the classical trajectories with a manifold of codimension one in phase-space (that is not parallel to the flow) [42]. There are different choices for the surface, with the most common one being the plane defined by the cyclic angles from the unperturbed model that corresponds to the broken symmetry in the perturbed model, usually guaranteeing (point-like) intersections in the unperturbed case. This would suggest that one should take the plane defined by $\varphi_l = \varphi_{l,0}$ and find all the points on a trajectory where the angle φ_l crosses this plane in the same direction. However, this choice is not very good in the case at hand, as the angle φ_l is stationary in the unperturbed case for $l = 0$, as can be seen from the equation of motion for φ_l in the unperturbed case

$$\dot{\varphi}_l = \frac{\partial\omega}{\partial l} = \frac{\tilde{\alpha}}{2}\frac{l\cos 2\varphi}{\sqrt{(1-z)^2-l^2}} \xrightarrow{l\to 0} 0. \quad (2.148)$$

For this reason, a different choice was made that is also better suited for comparison with the unperturbed case. By choosing the surface $l = 0$ for the Poincaré map the unperturbed case is degenerate, as the trajectory does not leave this plane. However, any finite perturbation γ renders the intersections point-like due to $\Delta\omega_\gamma$ and is thus suited for the analysis. Figure 2.12 shows an overlay of many Poincaré maps for different energies and for $\tilde{\alpha} = 1.9$ and $\gamma = 0.01$. The reason for showing many different energies is that the available regions in the surface of section with constant energy are small for

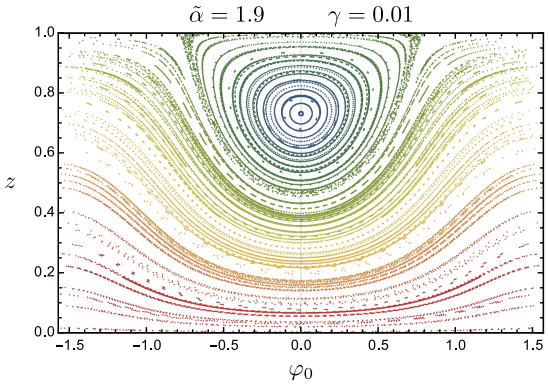

Figure 2.12: Overlay of different Poincaré surfaces of section. Different colors correspond to different energies. The initial values are $l = 0$ and random initial values in z, φ and φ_l. As the random initial conditions did not hit the chaotic region, more random initial values were used in a $\epsilon = 0.1$ window around the right fixed point, two of them being shown in the plot.

$\gamma \ll 1$ and become one-dimensional for $\gamma \to 0$, reproducing the integrable case. This is the drawback of using the unconventional surface of section $l = 0$. One can clearly see, that the perturbation is so small that most of the invariant tori are preserved. However, in the region around the separatrix of the unperturbed model, one can see a small chaotic layer, as expected. This should manifest itself in the OTOC that is very sensitive to this region.

The OTOC has been calculated for various values of the perturbation γ and for $N = 100$ and $\alpha = 1.8$. A comparison is shown in Fig. 2.13. It shows that the oscillations of the OTOC are very sensitive to the perturbation and get damped strongly for all the values of γ shown in the plot. One has to stress, however, that the oscillations seen in the nonperturbative result in Fig. 2.13 are not directly associated with the local Ehrenfest time τ, Eq. (2.67), as the number of particles is not large enough to clearly see its signatures, c.f., Fig. 2.10. Although the perturbation is varied over one order of magnitude, the mean value of the OTOC for later times seems to be rather insensitive to the strength of the perturbation for the times shown in the plot. The inset shows the short-time behavior of the ratio between the perturbed and unperturbed results for the same values of γ, indicating that the perturbation leads to faster initial scrambling, reflected in a larger growth rate. However, the latter is still dominated by the classical (in)stability exponent $\lambda_s \approx 1.9$ of the hyperbolic fixed points of the unperturbed system. This can be seen from the right part of Fig. 2.13, that shows the fitted difference $\Delta\lambda$ in the growth rate from the ansatz

$$C_\gamma(t) \approx C_0(t) \mathrm{e}^{2\Delta\lambda t} \propto \mathrm{e}^{2(\lambda_s + \Delta\lambda)t}, \tag{2.149}$$

showing that it is one order of magnitude smaller than λ_s. For the fits, a window

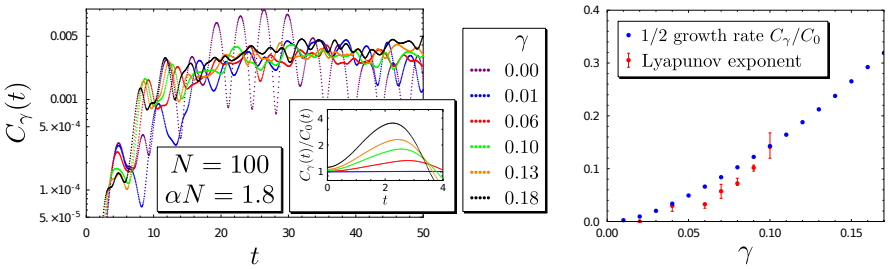

Figure 2.13: Left: Out-of-time ordered correlator in the perturbed model for $N = 100$, $\tilde{\alpha} = 1.9$ and various values of the perturbation γ (data of Dominik Hahn is used). For larger values of the perturbation, the oscillations of the OTOC are damped, but the magnitude of γ does not have a large effect on the saturation value for the times shown. The inset shows the short-time behavior of the ratio of perturbed and unperturbed OTOC, showing an additional increase due to the perturbation. Right: Comparison of the fitted growth rate with the classical Lyapunov exponent.

around the inflection points of the ratio $C_\gamma(t)/C_0(t)$ has been used. The ansatz (2.149) is motivated from the observation that, although the dynamics is not regular in the stochastic layer that emerges from the separatrix, it is still the dominant feature in the $l = 0$ surface, dividing two regular regions of phase space from each other. Classically evolving an ensemble of trajectories, characterized by a phase-space distribution, close to this region, one can expect that the distribution eventually fills a three-dimensional region of phase space only constrained by the energy conservation and bounded by the regular regions. But this can happen on very different time scales in the different directions, i.e., the divergence of two nearby trajectories due to the perturbation could be much smaller than the divergence due to the instability along the former fixed points. This should then manifest itself in a separation of scales in the OTOC, leading to two independent contributions to the initial scrambling rate.

This picture is strongly supported by the fact that the additional instability seems to coincide very well with the (maximal) classical Lyapunov exponent λ_L (see Fig. 2.13) found from a long-time average over the divergence rate of two neighboring trajectories initialized at $z = 1/\tilde{N}$ and $l = 0$ (and maximizing with respect to the initial conditions in φ, φ_l). The error bars come from a very slow convergence of the Lyapunov exponent due to the strong influence of the instability around the hyperbolic fixed points. If this apparent separation of scales persists also for larger particle numbers N, one might expect to see signatures of the unscrambling mechanism given by the local Ehrenfest time τ for $N \to \infty$, that should manifest itself in a significant decrease of the OTOC at $t \sim \tau$. Unfortunately, the necessary numerical simulations have not been performed yet and are left for future analysis.

2.3. The attractive Lieb-Liniger gas in 5-mode approximation

Up to this point, we have seen that the presence of a separatrix in the mean-field picture of the Lieb-Liniger model in three-mode approximation gives rise to an excited state quantum phase transition that leads to an emergent universal time scale for processes that dominantly involve the states in its vicinity. This time scale plays an important role in the post-quench time evolution, when the system is prepared as a noninteracting condensate state and is then quenched to finite couplings above the mean-field critical interaction. The reason for this was found in the fact that the initial state did only overlap with a few states around the classical separatrix energy, such that the dynamics is dominated by the classical hyperbolic fixed points. However, all of the analysis has been performed in the context of integrable systems, where the classical dynamics is constrained to Lagrangian surfaces, which is also reflected the quantum dynamics. Although the influence of a perturbation has been studied very briefly, adding an external potential with a finite strength actually changes the system drastically: The quantum phase transition in the attractive Lieb-Liniger gas breaks the translational symmetry. Destroying this symmetry would lead to a localization of the eigenstates already without interaction. As the (excited state) quantum phase transition is an essential ingredient for the emergence of the universal quench dynamics found in the previous sections, one should find a nonintegrable extension that is critical.

The three-mode approximation is the simplest nontrivial approach to uncover the physics of the quantum phase transition of the continuum model. As one should get better approximations by including more modes, one should also expect these refined models to show critical behavior. Therefore, this section is dedicated to the analysis of the extension of the model by increasing the momentum cutoff in the field operators, Eq. (2.41), to $k_{\max} = 2$, leading to a total of five modes that have to be included in the Hamiltonian (2.42). As the conservation of the total particle number and momentum, Eq. (2.43), is robust under the truncation, one can still restrict the quantum and (classical) mean-field analysis to fixed particle number and momentum, but the two additional degrees of freedom render the quantum and classical dynamics much more difficult. In fact, it is long known that, although the full model is quantum integrable, the cutoffs introduce signatures of chaotic behavior in the nonlinear Schrödinger equation [210], i.e., the mean field equation of the model. This also manifests itself in level repulsion in the quantum-mechanical spectrum that can eventually lead to Wigner-Dyson level statistics in some parts of the spectrum [211]. It should be clear that these numerically-induced signatures of chaotic behavior are not the subject of interest here, as they have no physical meaning. Obviously, the five-mode approximation should not be used for a quantitative analysis of the attractive Lieb-Liniger model whenever the variation of the cutoff introduces changes in the predictions. Therefore, as in the three-mode approximation, the analysis of the five-mode model performed here aims at a better understanding of quantum phase transitions in a more general context, as an example of a quantum phase transition in a model that is not completely integrable in the mean field limit.

2.3.1. Classical phase space analysis

As discussed in subsection 2.1.2 of the introduction of this chapter, the mean-field equations can be found as the classical equations of motion defined by the Hamiltonian function that is obtained by taking the classical limit of the quantum Hamiltonian. For this, one should replace the quantum operators by classical variables. However, to keep track of $\mathcal{O}(N^{-1})$ corrections one should first bring all the operator products in symmetric order. This yields the Wigner phase space representation of the operator(s) (or Wigner symbol), and the classical $N \to \infty$ limit can be studied in a controlled way. The corrections should not have an influence on the classical dynamics, as the classical equations of motion should be independent on the (effective) Planck constant, but they play an important role in the quantization of the classical system. Although this will not be done for the five-mode model, the corrections from symmetrization are included here for completeness.

Symmetrizing products of creation and annihilation operators can become a very cumbersome task when the number of operators grow. Already at the stage of a product of four bosonic operators, as needed to describe interactions, the direct calculation becomes quite lengthy and should be avoided. Fortunately, one can formulate a variant of a Wick theorem to calculate symmetrized products [212]. The statement is as follows: For n bosonic operators $\hat{A}_1, \ldots, \hat{A}_n$, the symmetrization of their product is defined as

$$\left\{\hat{A}_1 \cdots \hat{A}_n\right\}_s = \frac{1}{n!} \sum_{P \in S_n} \hat{A}_{P(1)} \cdots \hat{A}_{P(n)}, \tag{2.150}$$

where S_n is the symmetric group. Defining the contraction

$$\hat{A}_i^{\bullet} \hat{A}_j^{\bullet} = \hat{A}_i \hat{A}_j - \{\hat{A}_i \hat{A}_j\}_s = \frac{1}{2}[\hat{A}_i, \hat{A}_j], \tag{2.151}$$

where $[\cdot, \cdot]$ is the commutator, one can define the sum of k-fold contractions of a product of operators as $C_k(\hat{A}_1 \hat{A}_2 \cdots \hat{A}_n)$. For example for $k = 2$, $n = 4$ one obtains three full contractions,

$$C_2(\hat{A}_1 \hat{A}_2 \hat{A}_3 \hat{A}_4) = \hat{A}_1^{\bullet} \hat{A}_2^{\bullet} \hat{A}_3^{\bullet\bullet} \hat{A}_4^{\bullet\bullet} + \hat{A}_1^{\bullet} \hat{A}_2^{\bullet\bullet} \hat{A}_3^{\bullet} \hat{A}_4^{\bullet\bullet} + \hat{A}_1^{\bullet} \hat{A}_2^{\bullet\bullet} \hat{A}_3^{\bullet\bullet} \hat{A}_4^{\bullet}, \tag{2.152}$$

where the double bullet is only used to distinguish the two contractions. With these definitions the following theorem holds:

$$\hat{A}_1 \hat{A}_2 \cdots \hat{A}_n = \sum_{k=0}^{\lfloor n/2 \rfloor} \left\{C_k(\hat{A}_1 \hat{A}_2 \cdots \hat{A}_n)\right\}_s, \tag{2.153}$$

i.e., the product can be symmetrized in one step by summing over all possible (multiple) contractions.

Using this Wick theorem on the Hamiltonian (2.42) with the usual commutation relations yields

$$\hat{H} = \sum_k k^2 \left\{\hat{a}_k^\dagger \hat{a}_k\right\}_s - \frac{\bar{\alpha}}{4} \sum_{k,l,m,n} \delta_{k+l,m+n} \left\{\hat{a}_k^\dagger \hat{a}_l^\dagger \hat{a}_m \hat{a}_n\right\}_s + \frac{\bar{\alpha}}{2} \sum_{k,l} \left(\left\{\hat{a}_k^\dagger \hat{a}_k\right\}_s - \frac{1}{4}\right) - \sum_k \frac{k^2}{2}. \tag{2.154}$$

The second line contains the corrections due to the symmetric ordering of the operators and requires regularization if the cutoff is removed as is often the case in continuum systems. Using the cutoff $k_{\max} = 2$ and replacing the symmetrically ordered operators by products of (complex) classical variables, c.f., Eq. (2.45), one obtains the classical Hamiltonian function of the five-mode approximation as

$$H_5^{(\mathrm{cl})} = \sum_{k=-2}^{2} \left(k^2 + \frac{5\bar{\alpha}}{2}\right) \phi_k^* \phi_k - \frac{\bar{\alpha}}{4} \sum_{k,l,m,n=-2}^{2} \delta_{k+l,m+n} \phi_k^* \phi_l^* \phi_m \phi_n - \frac{25\bar{\alpha}}{8} - 5. \tag{2.155}$$

with the variables $\phi_k = \sqrt{n_k} \mathrm{e}^{-i\theta_k}$. The operators for the particle number and the momentum can be treated in the same way by symmetrizing them and then replacing the operators by complex numbers. However, as in the three-mode model, it is more convenient to define the classical constants of motion without the quantum corrections as

$$\tilde{N} = \sum_{k=-2}^{2} n_k, \qquad \tilde{K} = \sum_{k-2}^{2} k n_k. \tag{2.156}$$

One can now proceed by eliminating the constants of motion with the linear point transformation

$$\begin{pmatrix} n \\ N2 \\ K2 \\ \tilde{N} \\ \tilde{K} \end{pmatrix} = \underbrace{\begin{pmatrix} 0 & 0 & 1 & 0 & 0 \\ 1/2 & 0 & 0 & 0 & 1/2 \\ -1/2 & 0 & 0 & 0 & 1/2 \\ 1 & 1 & 1 & 1 & 1 \\ -2 & -1 & 0 & 1 & 2 \end{pmatrix}}_{A} \begin{pmatrix} n_{-2} \\ n_{-1} \\ n_0 \\ n_1 \\ n_2 \end{pmatrix}, \tag{2.157}$$

$$\boldsymbol{\theta} = A^{\mathrm{T}} \boldsymbol{\varphi}, \tag{2.158}$$

where A was chosen such that the Jacobian is one and the angles $\boldsymbol{\varphi}$ can be chosen in an interval of length 2π. Note that the transformation is canonical, i.e., the angles $\boldsymbol{\varphi}$ are the conjugate angles to the new variables. Due to the conservation of $\tilde{N}$ and $\tilde{K}$, their conjugate angles drop out from $H_5^{(\mathrm{cl})}$. The explicit inversion of the transformation (2.157) then yields

$$n_0 = n, \qquad n_{\pm 2} = N_2 \pm K_2, \qquad n_{\pm 1} = \frac{\tilde{N} - n - 2N_2}{2} \pm \frac{\tilde{K} - 4K_2}{2}. \tag{2.159}$$

Finally, one can rescale the coordinates as

$$z = \frac{n}{\tilde{N}}, \qquad z_2 = \frac{N_2}{\tilde{N}}, \qquad l_2 = \frac{K_2}{\tilde{N}}, \qquad l = \frac{\tilde{K}}{\tilde{N}}, \tag{2.160}$$

to get an $\tilde{N}$-independent description of the classical dynamics analogous to the three-mode case, with the energy per particle given by

$$\frac{H_5^{(\mathrm{cl})}}{\tilde{N}} = \omega(\varphi, z, \varphi_{z_2}, z_2, \varphi_{l_2}, l_2, l) - \frac{\tilde{\alpha}}{4} + \frac{5(\tilde{\alpha}-2)}{2\tilde{N}} - \frac{25\tilde{\alpha}}{8\tilde{N}}. \tag{2.161}$$

Here, the conjugate angles to the variable $y \in \{z_2, l_2\}$ is denoted as φ_y. The effective Hamiltonian function ω defines the classical dynamics completely. Its explicit form is given in App. E, as it is lengthy and its properties can be discussed without considering its exact form.

There are several remarks that one should make at this point. First, the coordinates z, z_2, l_2 are not completely independent, e.g., one has $|l_2| \leq z_2$ and $2z_2 + z \leq 1$. As is clear from the individual steps above, the effective Hamiltonian function reduces to the result of the three-mode model when one sets $z_2 = 0$ (and thus $l_2 = 0$). However, the dynamics effectively takes place in a six-dimensional phase space as long as $z < 1$, such that z_2 and l_2 can take nonzero values. Using the energy conservation one can reduce the dimension by one, but this is not enough to use standard techniques of visualization of the dynamics. However, we are ultimately interested in the case of zero total momentum $l = 0$. In this case, there exists an additional, discrete inversion symmetry formally given by the reversal of the single-particle momentum, i.e., by inverting the sign of the summation index in the Hamiltonian function. The Hamiltonian always has this discrete symmetry, but the total momentum is inverted under this operation. This symmetry for $l = 0$ leads to ω being symmetric with respect to the simultaneous inversion of l_2 and its conjugate angle

$$\varphi_{l_2} = \theta_2 - \theta_{-2} - 2(\theta_1 - \theta_{-1}) \tag{2.162}$$

thus making the manifold with $l_2 = 0$ and $\varphi_{l_2} = 0$ special. The derivative of ω with respect to one of these phase space coordinates then has to be *antisymmetric* under the simultaneous inversion, directly implying that their dynamics, given by

$$\dot{\varphi}_{l_2} = \frac{\partial \omega}{\partial l_2}, \qquad \dot{l}_2 = -\frac{\partial \omega}{\partial \varphi_{l_2}}, \tag{2.163}$$

becomes stationary at the manifold $l_2 = \varphi_{l_2} = 0$. Thus, the effective phase space dimension can be reduced by two for initial conditions in this high-symmetry manifold. Therefore, it is possible to analyze the dynamics in this manifold with the standard technique of Poincaré sections.

Figure 2.14 shows parts of the Poincaré maps in this high-symmetry manifold for two different energies. There, the time evolution is integrated up to $t = 500$ in the units given in Eq. (2.35). For $\omega = 0$, i.e., the energy of the separatrix of the three-mode model, a large part of the available phase space has regular dynamics, but especially

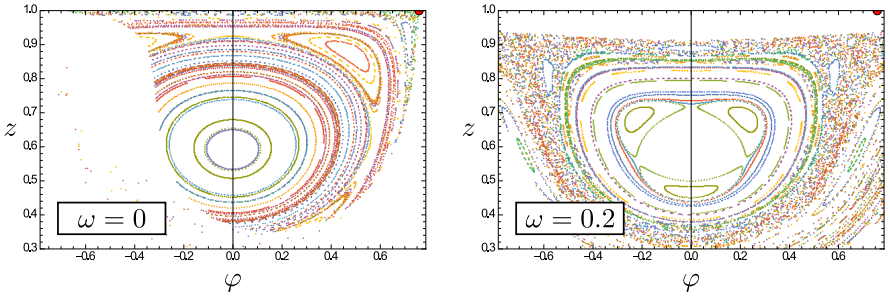

Figure 2.14: Poincaré sections in the high-symmetry manifold with $l_2 = \varphi_{l_2} = 0$ for two different energies and $\tilde{\alpha} = 1.9$. The section is taken at the points $\varphi_{z_2} = 0 \pmod{4\pi}$ with $\dot{\varphi}_{z_2} > 0$ and different colors correspond to different trajectories. For $\omega = 0$ the dynamics in the symmetry manifold has large regular structures that resemble the typical KAM scenario of broken rational tori [42], but the dynamics close to the hyperbolic fixed point of the three mode model (red dot) is chaotic. For $\omega = 0.2$ a large chaotic layer exists, verifying the non-integrability of the model. The apparently missing parts of the left plot are probably due to the detection algorithm, but this has not been checked.

when approaching the hyperbolic fixed point of the 3-mode model (red dot in the upper right corner), one finds a chaotic layer. One should note that the plots show only a small part of the Poincaré section. The motion in φ is now 2π periodic instead of π-periodic, as would be the case for $z_2 = 0$ (three-mode model). Also, one important detail has been omitted so far: Instead of fixing the angle φ_{l_2} to zero, one finds the same stationary behavior for $\varphi = 2\pi n$ with n being any integer. But for odd n this is not the same physical point, as shifting φ_{l_2} by 2π shifts the original angles $\theta_{\pm 2}$ only by π. This can also be seen in the Hamiltonian function (see App. E), where setting $\varphi_{l_2} = 0$ and $\varphi_{l_2} = 2\pi$ lead to different Hamiltonian functions. However, shifting both φ_{l_2} *and* φ_{z_2} by 2π yields the *same* physical point, c.f., Eq. (2.158), such that $\varphi_{l_2} = 0$ and $\varphi_{l_2} = 2\pi$ describe the same manifold, with φ_{z_2} ranging over an interval of 4π. Therefore, fixing $\varphi_{l_2} = 0$ or $\varphi_{l_2} = 2\pi$ in the calculation only leads to solutions that are shifted by 2π in φ_{z_2}. To demonstrate that the π-periodicity of the three-mode model is lost, Fig. 2.15 shows the full Poincaré section for $\omega = 0.2$ and $\tilde{\alpha} = 1.9$, i.e., the same values as in the right plot of Fig. 2.14.

Concluding, we have found that the classical dynamics in the special manifold that is invariant under the mirror symmetry operation, is mixed, i.e., it contains regular and chaotic regions. Therefore, one can exclude that the five-mode model is classically integrable and it is expected that the additional degree of freedom φ_{l_2} will render the rest of the phase space such that there is no further (global) constant of motion for $\tilde{\alpha} \neq 0$ and the dynamics will take place in the six-dimensional phase space in general[10]. When the coupling approaches the mean-field critical value of the interaction $\alpha = 1$,

[10]However, one can get arbitrarily close to integrability in the limit $\tilde{\alpha} \to 0$.

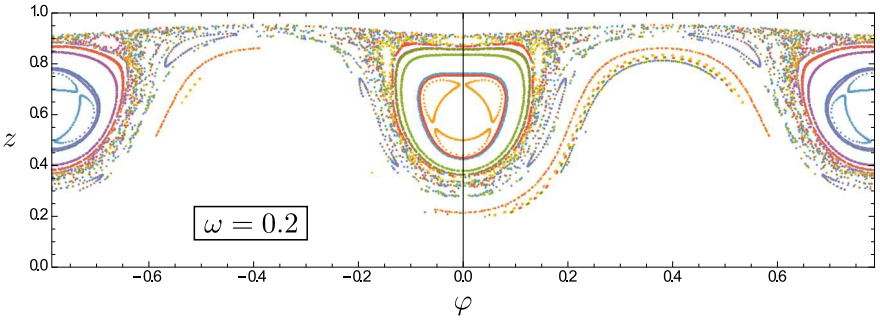

Figure 2.15: Full Poincaré section for $\tilde{\alpha} = 1.9$ and $\omega = 0.2$ in the high-symmetry manifold, demonstrating the 2π-periodicity in φ in contrast to the π-periodicity in the three-mode model.

the dynamics in the high symmetry manifold looks almost integrable, as can be seen in Fig. 2.16. The fact that the simulation shows signatures of a separatrix suggests that, if one can restrict the analysis to the high symmetry manifold, one can expect separatrix dynamics and hyperbolic instability to play an important role. However, this only applies to this special manifold, so that the initial conditions outside of it could lead to completely different results and one can expect to also find chaotic regions there.

Before coming back to the analysis of the classical phase space, let us take a look at the quantum mechanical spectral properties.

2.3.2. Quantum-mechanical treatment

As is the case with the three-mode approximation, the five-mode model is often used for the analysis of finite-size effects by performing the exact diagonalization of the Hamiltonian (for the low-lying states) [16, 196]. However, one is restricted to much smaller particle numbers, as the dimension of the relevant Hilbert space scales with the particle number as N^3 instead of N, as is the case in the three-mode approximation, where, in addition to the linear scaling, the Hamiltonian matrix can be brought into a simple tridiagonal form by ordering the basis appropriately. In the five-mode approximation, the restriction to fixed particle number and momentum leads to a Fock basis that can be labeled using three occupation numbers. Therefore, there is no (canonical) way to order the basis states that leads to a simple structure of the Hamiltonian matrix in this basis, making the problem much more complicated. Already at the stage of labeling the basis, one faces a difficult problem. One could naively calculate the basis numerically by generating a larger set of states, e.g., allowing occupations up to N in each mode and then dropping the states that do not have the correct particle number N and the desired momentum K. However, this would require N^5 intermediate states, consuming unnecessary resources. In order to control unavoidable cutoffs that one has to introduce for large particle numbers, a unique labeling of the states is desirable. The latter is

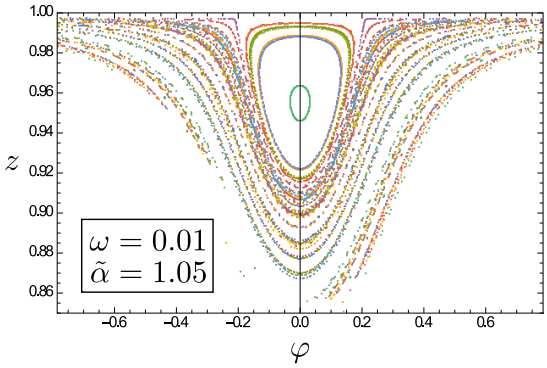

Figure 2.16: Poincaré section for $\tilde{\alpha} = 1.05$ and $\omega = 0.01$. The dynamics looks regular and one can clearly see evidence of a separatrix separating two different regions in phase space. The Trajectories are sampled more frequently when they approach one of the hyperbolic points, indicating a slowdown of the (φ, z)-dynamics.

a tedious task, but it can be performed to full generality and is given in Appendix E. One then finds that the size of the basis in the $K = 0$ sector scales roughly as $N^3/36$. Therefore, the bottleneck for the exact diagonalization is of the order of hundreds of particles. For larger particle numbers, one has to find schemes for approximations.

Figure 2.17 shows the low-lying spectrum for $K = 0$ and $N = 30$ (left) and $N = 250$ (right). One immediately sees that one obtains a much richer spectrum as compared with the three-mode model, that only produce a series similar to the lowest states seen in the right plot ($N = 250$), that can be adiabatically connected to the lowest levels of the rays starting at $\alpha = 0$. On first glance, one might think that the additional levels can cross these three-mode-type level series, which would hint at an additional symmetry. However, a closer analysis of these level "crossings" reveals a small, but finite level repulsion. This has been checked for several particle numbers and many different states, revealing avoided crossings in all cases (although some of the gaps turned out to be of the order 10^{-8} and below, however still well above machine precision). Although the gaps are very small for the low-lying spectrum, the higher excited states have a more pronounced level repulsion and one can expect the level statistics to be far from Poissonian, the latter characterizing generic integrable systems. In fact, it has been shown that even in the repulsive Lieb-Liniger gas, the level statistics agree remarkably well with the Wigner-Dyson distribution in the middle of the spectrum due to the cutoff, i.e., the levels are essentially distributed according to random matrix theory [211]. This agrees very well with the classical analysis of the mirror-symmetric manifold, where the chaotic regions grow when the energy is increased. However, in the low-energy regime, the spectrum looks rather regular.

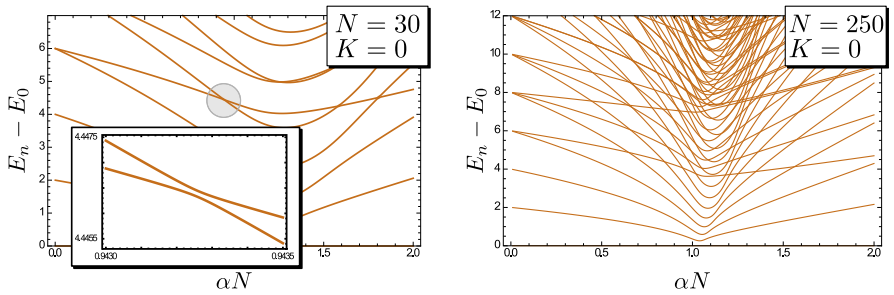

Figure 2.17: Low-lyings spectrum of the five-mode model for $K = 0$. Left: $N = 30$ particles. A new type of states exists, that was absent from in the three-mode model. The states seem to cross, hinting at a symmetry, however a closer analysis reveals avoided crossings. Right: $N = 250$ particles. The spectrum gets more complicated at higher excitations but seems to have a clear structure. Certain levels get quasi-degenerate at $\alpha > 1$.

2.3.3. Separation of scales and Born-Oppenheimer-type approximations

The fact that the classical dynamics is rather regular around the separatrix energy $\omega = 0$ even for very strong interactions, c.f., Fig. 2.14, with only a small stochastic layer that seems to emerge from the separatrix of the three-mode model, suggests that the dynamics in the coordinates (φ, z) will be strongly affected by a (coarse-grained) hyperbolic dynamics. This means that the dynamics in (φ, z) is expected to slow down due to this hyperbolicity, rendering the dynamics in the other coordinates much faster (if they do not share the same hyperbolic behavior). This motivates a Born-Oppenheimer type ansatz for separation of scales between the slow hyperbolic dynamics associated to the separatrix and the fast dynamics in the other directions.

This can be viewed in a more general context for other systems that allow for a mean-field description in terms of classical dynamics. A quantum phase transition is not expected to take place in a completely chaotic, and therefore structureless phase space. One can, at least, expect an regular "skeleton" that can separate different regions in phase space. A phase transition should then be associated with changes in these regular structures, i.e., the state has to be associated to different regions of phase space on either side of the transition in order to have different quantum mechanical properties. This could be the transition from a regular to a chaotic region, or, as is the case in the three-mode model and will be argued to hold also for the five-mode model, is the transition between two regular regions in phase space that are separated by a (weakly disturbed) separatrix. Even if a separation of scales is possible, the hardest part is to identify the fast and slow degrees of freedom. In the standard application of Born-Oppenheimer separation of scales in molecules or solids, the very different masses of electrons and nuclei, together with the standard form of the Hamiltonian as a quantized mechanical problem with the position operators appearing only in the potential, render the choices

rather obvious. Moreover, the quantum mechanical solutions of the (fast) electronic problem is only parametrized by the positions of the nuclei, but not their momentum.

However, the classical dynamics obtained in mean-field descriptions can have a very different structure, often with potentials that depend on both conjugate classical variables. Still, the situation can be special for critical systems. If one of the classical phase space variables can be used as an order parameter, it has to behave differently on both sides of the transition and, assuming that the transition is due to a separatrix, should be sensitive to the exponential slowdown due to the hyperbolic dynamics at the transition. Therefore, the idea is to use the variable z, that can be used as an order parameter in the three-mode and the full model, as well as its conjugate angle as a slow degree of freedom. This is expected to work well close to the ground state phase transition at $\tilde{\alpha} \approx \alpha = 1$. As was seen in Fig. 2.14 for $\tilde{\alpha} = 1.9$, the separatrix is replaced by a chaotic layer for strong coupling. However, for $\tilde{\alpha} = 0.05$ the dynamics is more regular, and a clear signature of a separatrix can be found close to $\omega = 0$. Another reason to choose a value close to $\tilde{\alpha} = 1$ is the numerical observation that the series of states that have a counterpart in the three-mode model develop a bunching of energy levels at an energy that lies below the other level series and are thus energetically separated, as it can already be seen in Fig. 2.17 for $N = 250$.

Up to this point, classical arguments have been used to identify a slow degree of freedom. A quantum mechanical generalized Born-Oppenheimer type approach could be applied by using the framework of adiabatic perturbation theory [213, 214]. Here, however, the insights gained from the classical picture are used to simplify the quantum calculations. The essence of the idea used here is that the characteristic energy scale introduced by the fast dynamics is larger than the ones from the slow dynamics, which is perfectly consistent with the level bunching at excited state quantum phase transitions, leading to a very small energy spacing. By assuming that the fast degrees of freedom, i.e., z_2, l_2 and the conjugate angles get quantized to a ground state energy $E_0^{(\mathrm{fast})}(\varphi, z)$ depending on the values of the slow variables z, φ, one could, in principle, derive an effective model for the slow variables for finite N (being the effective inverse Planck constant) by using the phase space representations of the states corresponding to $E_0^{(\mathrm{fast})}(\varphi, z)$. However, if one is interested in the mean field limit $N \to \infty$, the situation is simpler, as the respective states localize at the energy minimum of the fast degrees of freedom (for fixed φ, z) with the energy given by the classical minimum $E_{\mathrm{min}}^{(\mathrm{fast})}(\varphi, z)$. As this energy minimum can only be obtained numerically, a further refinement for finite particle numbers, e.g., by a semiclassical quantization of the fast degrees of freedom in a local approximation, can only be performed semi-analytically and has not been achieved yet. Still, already at the level of the effective mean-field description and using only the energy minimum $E_{\mathrm{min}}^{(\mathrm{fast})}(\varphi, z)$, one can extract nontrivial information. Figure 2.18 shows a phase space portrait of this effective description for $\tilde{\alpha} = 1.05$ obtained from replacing the phase space coordinates z_2, l_2 and their conjugate angles by the position of the energy minimum. The minimization has been obtained by noticing that $\varphi_{l_2} = l_2 = 0$ solves two of the stationary conditions for a minimum and then minimizing with respect to the coordinates φ_{z_2}, z_2 for fixed (φ, z). This leads to a unique choice of (φ_{z_2}, z_2) for

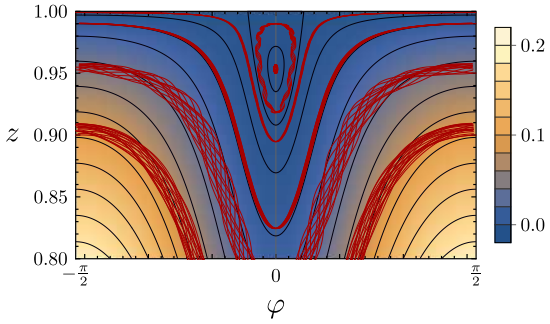

Figure 2.18: Effective mean-field phase space portrait obtained from minimizing the fast degrees of freedom (density and black contours). The red curves show the projections of the full dynamics (initialized close to the respective manifolds) to the slow degrees of freedom (φ, z).

$z < 1$ and with $0 \leq \varphi_{z_2} \leq 4\pi$. The stationary point obtained in this way has then been verified to be a local minimum using the Hessian of the Hamiltonian function ω. By sampling the phase space (with 20 points for each of the four coordinates) for all values of (φ, z) on a regular 10×10 grid, it has been verified that it is a indeed the global minimum. Using this approach, the effective phase space becomes a deformed version of the three-mode model, with the π-periodicity in φ restored and with two hyperbolic fixed points at the upper boundary that emerge for $\tilde{\alpha} > 1$. Their stability exponents have been obtained numerically to be

$$\lambda_\mathrm{s} \approx 0.42 \tag{2.164}$$

for $\alpha = 1.05$, which is very close to the three-mode result $\lambda_s = 2\sqrt{\tilde{\alpha} - 1} \approx 0.447$. Figure 2.18 also shows the projections of the full classical dynamics into the effective phase space for trajectories that were initialized close to the manifold that it describes, showing that they follow roughly the lines of constant energy, especially for small energies.

As can be easily shown using the explicit form of the classical Hamiltonian function given in App. E, the quadratic expansion around the minimum in the "fast" degrees of freedom (formally) decouples the phase space coordinates (φ_{z_2}, z_2) and (φ_{l_2}, l_2), with their frequencies being comparable and of the order of $\omega_\mathrm{fast} \gtrsim 6$ for $\tilde{\alpha} = 1.05$. One should, however, note that the maximal values of the coordinates z_2 and l_2 are coupled to each other and to z, which becomes important when $z = 1$ is approached, leading to a breakdown of the harmonic approximation, as the angular directions get flat. Nevertheless, the order of magnitude of the frequencies is encouraging as it is comparable with the gap between the ground states of the individual level series seen in Fig. 2.17.

Numerical implementation

To implement the adiabatic separation on a quantum-mechanical level, simply replacing the creation and annihilation operators corresponding to the zero mode by complex variables leads to a $U(1)$-symmetry-broken effective description for the fast degrees of freedom with an infinite-dimensional Hilbert space, rendering this approach not suitable for numerical diagonalization. Thus, a different approach has been taken here that consists of a pre-diagonalization of the projections of the Hamiltonian to subspaces of the Hilbert space $\mathcal{H}$ with a fixed mean condensate fraction $\bar{z} = \bar{n}_0/N$. In particular, a "good" basis is found using the subspaces

$$\mathcal{R}_k = \mathcal{H}_{2k-1} \oplus \mathcal{H}_{2k} \tag{2.165}$$

with $k = 1, \dots, N/2$ (and N even for simplicity), where

$$\mathcal{H}_n = \{|\psi\rangle \in \mathcal{H} : \hat{a}_0^\dagger \hat{a}_0 |\psi\rangle = n|\psi\rangle\} \tag{2.166}$$

is the subspace with fixed particle number N, total momentum $K = 0$ and zero-mode occupation n. This choice is motivated by the structure of the three-mode model, where increments of the occupations n_0 are restricted to even numbers, and it is the minimal choice that can capture the interplay between all the degrees of freedom. The latter follows from the fact that fixing the occupation n_0 *exactly*, projects out all the (off-diagonal) parts of the Hamiltonian that couple to this mode and thus misses the whole complexity of the problem. In the classical picture, this would correspond to dropping all terms that depend on the corresponding angle φ, completely decoupling the dynamics. So, combining two different occupations of the zero mode provides the minimal necessary information about the phase φ.

The dimension of the space $\mathcal{R}_k$ scales as $(N - 2k)^2$, such that the projections of the Hamiltonian to $\mathcal{R}_k$ can be effectively diagonalized for large particle numbers, yielding a k-dependent eigenbasis $\{v_\nu^{(k)} : \nu = 0, 1, \dots\}$ (ordered by energy) that spans $\mathcal{R}_k$. The space $\mathrm{span}(\{v_\nu^{(k)} : k = 0, 1 \dots\})$ may then be referred to as the ν-th band. An effective Hamiltonian is found by restricting the full Hamiltonian to the space

$$\mathcal{S}_\eta^\zeta = \bigoplus_{k=1}^{\zeta} \mathrm{span}(\{v_\nu^{(k)} : \nu \leq \eta\}), \tag{2.167}$$

where a cutoff $2\zeta \leq N$ in the condensate depletion has been introduced, as well as a cutoff η controlling the number of excitations in the fast degrees of freedom taken into account via inter-band coupling. It turns out that already for $\eta = 0$, where the effective Hamiltonian has the same structure as for the 3-mode approximation, the low-lying excitation spectrum around the critical point $\alpha = 1$ is well described. For the numerical calculations of the vectors $v_\nu^{(k)}$ two further cutoffs

$$\Sigma_2 = n_2 + n_{-2} \leq \Sigma_2^{\max}, \qquad \Delta_2 = |n_2 - n_{-2}| \leq \Delta_2^{\max} \tag{2.168}$$

were introduced, where n_2, n_{-2} are the occupations of the ± 2 single-particle momentum modes. The quantities Σ_2 and Δ_2 correspond directly to the classical variables z_2 and l_2, respectively.

For $K = 0$, the inversion symmetry of the system allows for a further reduction of the dimension by using the symmetric and antisymmetric states that cannot couple via the parity-preserving Hamiltonian. For this, before diagonalizing the $\mathcal{R}_k$-projections, a projection to the symmetric subspace that contains both the interacting and noninteracting ground state has been performed, resulting in the vectors $v_\nu^{(k)}$ being only of this symmetry class.

Characterization of the low-lying spectrum

As has been seen in Fig. 2.17, the different level series, or bands, can be identified by adiabatically relating them to the rays in the perturbative $\alpha \ll 1$ regime. Although the numerical scheme sketched above allows one to get to very large particle numbers, the computational effort is still very high, such that calculating an energy flow diagram, i.e., the dependence of the spectrum with respect to the coupling, cannot be done for large particle numbers to high precision, as all calculations have to be repeated if the coupling α changes. Moreover, the adiabatic connection can only be made by coarse graining (i.e., "by eye"), as the actual energy levels do not cross. Therefore, and for the sake of a deeper physical understanding, it is desirable find a way to distinguish states in different bands without knowing their functional dependence on the coupling α.

Unfortunately, due to the pre-diagonalization in the numerical scheme, the resulting effective Hamiltonian and its eigenfunctions contain random sign factors, as the numerically obtained vectors $v_\nu^{(k)}$ are only defined up to a phase or, restricting to real vectors, up to its sign, that is randomly picked by the Arnoldi algorithm used for diagonalization. The final eigenstates are thus useless for any further analysis, if the vectors $v_\nu^{(k)}$ are not known, but keeping the latter quickly produces very large amounts of data that contain far too much information. However, one can perform the stepwise projections to the spaces $\mathcal{S}_\eta^\zeta$ for many operators simultaneously without significantly increasing the computational effort (as long as they are sparse in the Fock basis), imprinting the random signs also in these projected operators, that can then be used to analyze the properties of the final eigenstates.

The obvious choice is to calculate, together with the effective Hamiltonian, the projected versions of the number operators. But only three of them are independent due to the number and momentum conservation, and the restriction to inversion-symmetric states reduces the number of independent number operators to two, e.g., $\hat{n}_0$ and $\hat{n}_2$. A good choice of simple operators is given by

$$\hat{n}_0, \qquad \hat{N}_2 = \frac{\hat{n}_2 + \hat{n}_{-2}}{2}, \qquad \hat{K}_2^2 = (\hat{n}_2 - \hat{n}_2)^2, \tag{2.169}$$

as these operators are parity-symmetric, such that no information is lost due to the symmetry projection. Note that these operators correspond to the variables z, z_2 and l_2^2 used in the classical analysis. For more generality, one might also want to include

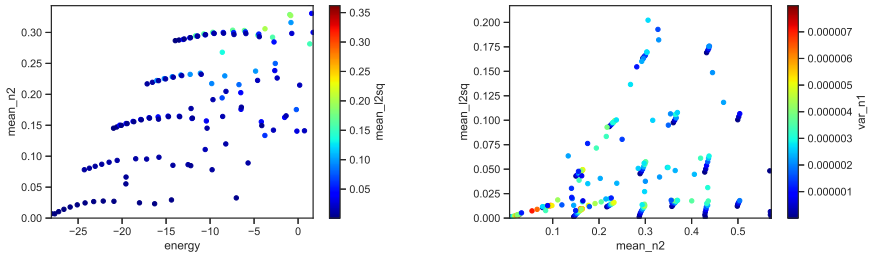

Figure 2.19: Left: Scatter plot of the energies and the the expectation values of $\hat{N}_2$ for the first 100 energy levels and for $N = 100$, $\alpha = 1.1$. The color represents the expectation values of $\hat{K}_2^2$. Right: Scatter plot of the expectation values of $\hat{N}_2$ and $\hat{K}_2^2$ for the same states with the variance of $(\hat{n}_1 + \hat{n}_{-1})^2$ as color code. The different scale of the latter is due to rescaling with the particle number and is of no importance here.

products of the operators 2.169, but this has not been done, as the above operators have turned out as a good choice to characterize the eigenstates already on the basis of the energy eigenstate expectation values

$$\begin{aligned} \mathrm{mean}_k(N_2) &= \langle\psi_k|\hat{N}_2|\psi_k\rangle\,, \\ \mathrm{var}_k(K_2) &= \langle\psi_k|\hat{K}_2^2|\psi_k\rangle\,, \\ \mathrm{var}_k(N_1) &= \langle\psi_k|(\hat{n}_1 + \hat{n}_{-1})^2|\psi_k\rangle\,, \end{aligned} \tag{2.170}$$

where k is a label of the eigenstate. The last variance in Eq. (2.170) has been calculated from the projected operators (2.169) using

$$\hat{n}_1 + \hat{n}_{-1} = \hat{N} - 2\hat{N}_2 - \hat{n}_0 \tag{2.171}$$

and is thus not exact, but this has turned out to be irrelevant in the following.

Figure 2.19 shows scatter plots of the energy and the expectation values (2.170) for the first 100 levels for $N = 100$ and $\alpha = 1.1$. The left plot clearly shows that the states have very different mean occupations in the side modes, characterized by $\mathrm{mean}_k(N_2)$, leading to distinct series in the scatter plot. However, the colors show that including the variance in the side-mode imbalance, $\mathrm{var}_k(K_2)$, can distinguish states that lie on top of each other. This is clarified in the right plot, where the aforementioned quantities are plotted against each other, revealing distinct series that were lying on top of each other in the left plot. As some of the series can overlap in the two-dimensional scatter plots, the variance $\mathrm{var}_k(N_1)$ can be used to lift this into three dimensions.

Using the cluster detection algorithm DBSCAN implemented in Python [215,216], the different series have then be labeled automatically (cutting off noisy parts). The result can be seen in Fig. 2.20, where each series of states has been given a label. Note the two outliers that have been characterized as noise. They correspond to hybrid states close

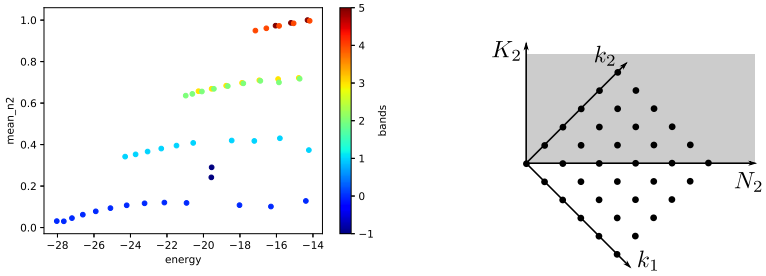

Figure 2.20: Result of automatic state labeling using the cluster detection algorithm DBSCAN. The cluster detection works better if the particle number is increased. Right: Sketch of the harmonic oscillator spectrum analogy of the level series, with the gray-shaded area representing the band structure.

to an avoided crossing. The quality of the result needed some fine-tuning for $N = 100$, but for higher particle numbers, the cluster detection is quite reliable, allowing one to directly select the states from a specific band.

One observation is that the states in the low-lying spectrum can be characterized by three "good" quantum numbers (N_2, K_2, m). The first two can be used to label the band and the excitation within each band is then labeled by m. To be specific, the quantum number $N_2 = 0, 1, 2, \ldots$ labels the series of degenerate bands seen in the left part of Fig. 2.19 according to $\mathrm{mean}_k(N_2)$, starting from the bottom. Then, for given N_2, the quantum number K_2 can be chosen as

$$L_2 = \begin{cases} 0, 2, \ldots, N_2 & N_2 \text{ even} \\ 1, 3, \ldots, N_2 & N_2 \text{ odd} \end{cases} \tag{2.172}$$

that are assigned to each of the degenerate bands with the same label N_2 according to the mean value of $[\mathrm{var}_k(K_2)]^{1/2}$ in each band. The index m then just labels the states within each band (N_2, L_2).

The above characterization of the bands with two numbers (N_2, L_2) reminds of a two-dimensional harmonic oscillator spectrum that is given by the sum of two quantum numbers $E_{\mathrm{ho}} = \hbar\omega(k_1 + k_2 + 1)$ being highly degenerate. Instead of using k_1, k_2 one can label the states by $N_2^{\mathrm{ho}} = k_1 + k_2$ and $L_2^{\mathrm{ho}} = k_1 - k_2$. The energy then depends only on N_2, as is the case in the five-mode model, while the eigenstates will depend also on L_2. The analogy is further underlined by the following two observations: First, the energy of the lowest state $[k = (N_2, L_2, m = 0)]$ of each band depends linearly on the $N_2 \sim \mathrm{mean}_{N_2,L_2,0}(N_2)$ (see left part of Fig. 2.19) as is the case for the harmonic oscillator. Second, by rescaling the vertical axis in the right part of Fig. 2.19 by plotting the square-root of $L_2 \sim \mathrm{var}_(K_2)$ will give a pattern very similar to the sketch in the right part of Fig. 2.20 that shows the pattern of quantum numbers in the two-dimensional harmonic oscillator. Finally, by not distinguishing between positive and negative values

of L_2^{ho} one ends up exactly with the observed rules for the quantum numbers N_2 and L_2 of the fast degrees of freedom in the five-mode model.

Therefore, this section concludes with the claim that the fast degrees of freedom are basically two-dimensional harmonic oscillator states. Due to the mirror symmetry that holds for $K = 0$, these states are combined to symmetric (and antisymmetric) superpositions that correspond to the superpositions of harmonic oscillator states with the same $|L_2^{\mathrm{h0}}| = |k_1 - k_2|$. It is expected that including the antisymmetric states in the analysis will fill up the gap of the apparently missing bands, then leading to an indexation of the bands similar to a two-dimensional harmonic oscillator using N_2, the absolute value $|L_2|$ and a symmetry index ± 1 that can distinguish the states with $L_2 \neq 0$ according to their mirror symmetry. The last point is supported by the observation that the energies of the antisymmetric states are almost degenerate with a set of levels of the symmetric class (not shown).

2.3.4. Rigidity of (excited states) quantum phase transition

Now, being able to push the particle numbers in the five-mode model to much higher values of the order of 10^4 particles, we are in the position to analyze the large-N asymptotic behavior and answer the question of whether an excited state quantum phase transition is expected to appear in the mean-field limit. The existence of the latter led to the distinct local Ehrenfest time scale in the three-mode model and dominated the quench dynamics of the noninteracting condensate there. The goal here is to show that the excited state phase transition exists also in the five-mode model and that it also implies the local Ehrenfest time as the dominant time scale in the aforementioned quench scenarios.

As a major result, the individual sub-spectra have a regular level spacing as expected from 1D systems, with a peak in the density of states at the energy of the separatrix of the effective phase space. This is demonstrated in Fig. 2.21, where the inverse level spacing within the lowest sub-spectrum is shown and compared to the result from the three-mode model. Moreover, the noninteracting condensate overlaps dominantly with states within this peak (gray shaded curve in Fig. 2.21), indicating that the quench dynamics of this state is dominated by only a few states around an excited state quantum phase transition with level spacings that can be expected to be asymptotically equidistant. This is because of the evident and remarkable similarity of the results from the three-mode and five-mode model, that allows to transfer the analytical results of the three-mode model to the five-mode model in this special situation of the excited state quantum phase transition. One should note, however, that there are clearly differences in the two models, that can already be seen from Fig. 2.21. First, the inverse level spacing is enhanced by approximately 10% in the five-mode model. Second, and much more important, one has more levels below the peak in the five-mode model and the ground state of the three-mode model (not shown, as $k \geq 1$ in the plot) is approximately at the energy of the $k = 9$ excited state in the five-mode model.

The dominance of a local Ehrenfest time scale similar to the three-mode model case is demonstrated in Fig. 2.22, where the quench dynamics after an interaction quench from the noninteracting condensate to a coupling of $\tilde{a} = 1.05$ is shown for different particle

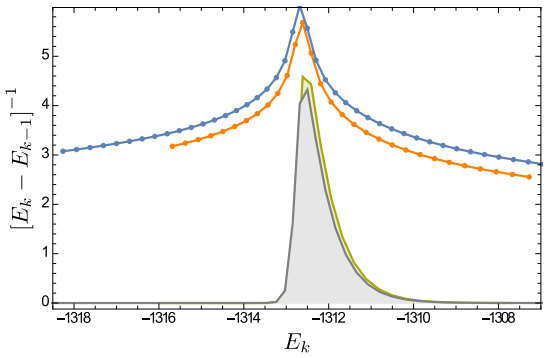

Figure 2.21: Comparison of the inverse level spacing in the three-mode model (orange) and the first level series/band in the five-mode model for $N = 5000$, $\alpha = 1.05$. The dots represent the actual energy levels, and the solid lines are for better visibility (but can be interpreted as the smooth density of states). Both models show the characteristic logarithmic peak in the density of states. The yellow/gray shaded plot shows the squared overlaps (multiplied by 20) of the eigenstates $|\psi_k\rangle$ with energy E_k of the three-/five-mode model with the noninteracting ground state.

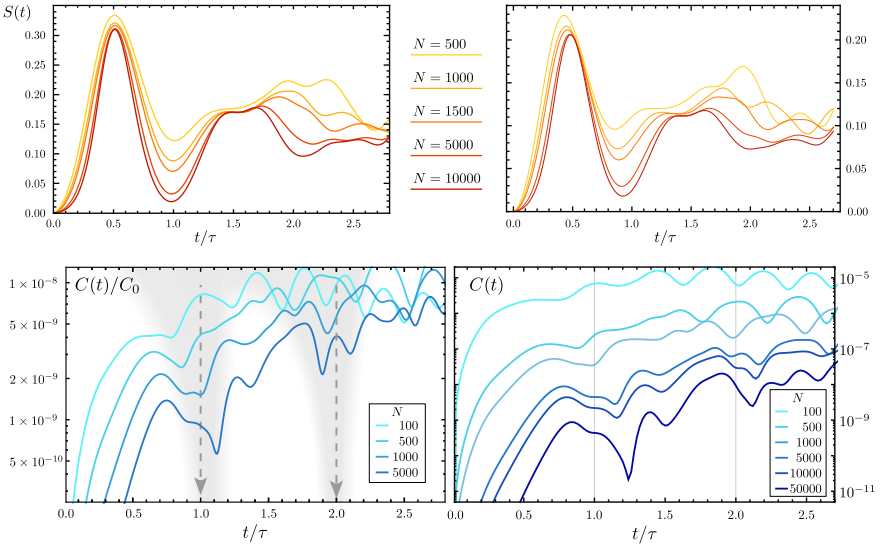

Figure 2.22: Comparison of the quench dynamics of the entropy of the reduced one-body density matrix (top) and the OTOC (2.107) (bottom) in the five-mode (left) and three-mode (right) model for $\tilde{\alpha} = 1.05$ and different particle numbers. The constant C_0 facilitates the comparison in the case of the five-mode model.

Table 2.1: Cutoffs that were used in the numerical calculations.

N	100	500	1000	1500	5000	10000
ζ	40	100	200	300	1000	2000
$\Delta_2^{\max}$	20	30	20	30	50	50
$\Sigma_2^{\max}$	40	60	40	60	100	100

numbers. The top panel shows the time evolution of the von Neumann entropy

$$S(t) = -\operatorname{Tr}\hat{\rho}(t)\log\hat{\rho}(t) \tag{2.173}$$

of the reduced one-body density matrix

$$\rho_{ij}(t) = \langle\Psi(t)|\hat{a}_i^\dagger\hat{a}_j|\Psi(t)\rangle\,, \tag{2.174}$$

where $|\Psi(t)\rangle$ is the noninteracting condensate evolved for the time t in the interacting system. One can clearly see the emergence of the first revival at the local Ehrenfest time τ, that has been estimated from the average level spacing around the separatrix, with the number of states taken into account scaling like $\log(N)$. The latter is consistent with the original derivation of the local Ehrenfest time in the three-mode model [189]. Fitting the obtained values for τ to

$$\tau = \frac{\log N}{\lambda} + c \tag{2.175}$$

for the different particle numbers, where c accounts for $\mathcal{O}(1)$ corrections, one finds $\lambda \approx 0.21$, being in excellent agreement with the stability exponent $\lambda_s = 0.42$, Eq. (2.164), found in the classical analysis of the effective phase space. Although the dynamics of the entropies look very similar, the additional modes in the five-mode approximation lead to higher absolute values. The three-mode result uses the finite-size-corrected local Ehrenfest time (2.141). The lower panel of Fig. 2.22 shows the out-of-time-ordered correlator $C(t)$, Eq. (2.107), for the five- and three-mode model, clearly showing the signatures of unscrambling in both cases with very similar time dynamics. Although the quantum revivals seem to be much weaker, the comparison with the OTOC in the three-mode model shows that this is rather due to the choice of parameters leading to a small separatrix. However, one can expect the revivals to become more pronounced for larger particle numbers even in the OTOC, as can be seen for $N = 50000$ in the three-mode case that behaves very similar to the five mode model for the particle numbers up to $N = 5000$.

For the plots in Fig. 2.22, all cutoffs have been varied to check the convergence of the results. The data presented here uses the cutoffs shown in table 2.1, where $\eta = 80$ for all the values of N. The time evolution was approximated using the first 2000 eigenstates of the effective Hamiltonian matrix for particle numbers $N \geq 500$ (for $N = 100$ all eigenstates were used). The convergence of the results with respect to this approximation has been checked, again, by varying the number of eigenstates.

At this point it is not clear whether the results obtained so far for the five-mode model can be extended to stronger couplings, where the stochastic layer around the separatrix could lead to faster scrambling and weaker revivals.

2.4. Summary and concluding remarks

In this chapter, a semiclassical approach to (quantum) phase transitions of the ground state, but also excited states has been presented. After introducing the necessary tools, the attractive one-dimensional Bose gas in three mode approximation was studied by means of the semiclassical torus quantization of its integrable classical dynamics. It has been shown that the ground and excited state quantum phase transitions have their origin in the emergence of a separatrix in the classical phase space. With this, a critical interaction can be defined – even for the finite size precursors of the phase transitions – as the point where the associated quantized classical torus changes its structure. This classically non-analytic change in topology eventually leads to a second order phase transition for quantum states in the mean-field limit that can be characterized by a sudden change in the pair correlations and the interaction energy.

For a further analysis of the system and in order to provide a tool for the direct calculation of quantum states, a simplified WKB wave-function approach was then introduced. The latter is capable of accurately describing the states well above the transition (and is expected to work well also well below), where it provides essentially exact results for the quantum states, only requiring the input of a desired excitation index. As this simplified approach breaks down exactly at the transition, a visualization of the exact quantum dynamics in phase space has been performed using the Husimi-Q representation, showing that the quantum states clearly reflect the expected quantized orbit structure away from the separatrix, while superposition of different kinds of motion takes place close to the separatrix. It has also been demonstrated that the non-equilibrium dynamics closely follows the mean-field dynamics, but with clear interference phenomena showing up at later times.

To characterize the scrambling properties of the three-mode model, the out-of-time ordered correlator of the condensate fraction at different times has been calculated, showing clear revivals after multiples of a local Ehrenfest-type time scale that can be derived from the semiclassical quantization. These revivals reflect a mechanism of unscrambling at criticality, which is absent in chaotic systems and thus presents a remarkable difference between critical behavior and chaos, despite both types of systems showing a similar short-time behavior. In a semiclassical Truncated-Wigner type calculation, a prediction of the exponential short-time behavior in the model has been derived analytically, that reproduces the quantum evolution almost perfectly, while being the first term in a quickly converging power expansion of the short-time evolution of the OTOC. While this power series has been discovered numerically, a theoretical explanation has not been obtained yet and is the subject of further research. The analysis of the three-mode model concluded with a short summary of the effects of an integrability-breaking perturbation on the short- and long-time behavior of the OTOC.

In the rest of the chapter, a mainly numerical analysis of the non-integrable extension of the previous model, obtained by taking a total of five modes into account, has been presented and compared to the results found for the three-mode model. By analyzing the classical mean-field limit of this model, it has been shown that there exists a four-dimensional high-symmetry manifold that can be analyzed with the tool of Poincaré

surfaces. One finds that the phase-space is mixed and shows large chaotic regions especially at large energies and strong coupling. In the quantum-mechanical simulations, a numerical scheme based on the idea of an adiabatic Born-Oppenheimer type approximation has been found, that is valid in the regime close to the mean-field critical coupling and allows for a full characterization of the low-lying states. With this, it was possible to calculate the OTOC and the von Neumann entropy of the reduced one-body density matrix for up to $N \sim 10^4$ particles. The results clearly show a similar behavior of scrambling and unscrambling dynamics, with the dominant time scale being of the same form as the local Ehrenfest time found in the fully integrable three-mode model. It is therefore concluded that the oscillatory time evolution of the OTOC and the corresponding unscrambling mechanism is expected to be not a feature that is unique to the model at hand, but applies to a wider class of systems that allow for a similar mean-field description, and thus a specific class of of excited state quantum phase transitions.

Conclusion

Summary

The two main chapters of this thesis have successfully implemented different semiclassical methods with their individual strengths lying in different aspects.

The first chapter has put a focus on the unified description of certain classes of interacting systems in thermal equilibrium using only a few parameters, however dropping the restriction to the thermodynamic limit that is usually assumed in this context. Before introducing semiclassical approximations, the theoretical method of quantum cluster expansions has been reviewed at a high level of detail, with a focus on the canonical description of few-particle systems that have been brought into experimental reach in recent years. Although the canonical description, when compared to grand canonical approaches, has the drawback of a combinatorial problem being introduced by the fixed particle number, the latter is essential in few-particle systems where the equivalence of ensembles is not valid. By reducing the combinatorial problem to recurrence formulas, a simple way to resolve this complexity has been provided. Thereby, a generalized framework for the calculation of arbitrary correlation functions in terms of finite expansions in nonperturbative cluster diagrams has been developed that does not suffer from any combinatorial problems and applies also to interacting systems with multiple species. These new techniques have then been combined with the semiclassical short-time approximation of (many-body) propagators that neglects the fluctuations in the many-body level density, being formally valid in situations where the thermal wavelength is much smaller than the typical extent of the system – but can be comparable to the inter-particle separation and even exceed it, thus not limiting the approximation to the high-temperature regime.

As a benchmark application that allows for an exact numerical treatment due to its quantum integrability, the one dimensional repulsive Bose gas with contact interaction has been studied in this framework. There, the nonlocal pair correlation function has been addressed for up to five particles in the few-body regime, treating the problem fully analytically for up to three particles. The theory has thereby proven to be very accurate when the full cluster expansion is taken into account, being applicable down to extremely small temperatures where the thermal wavelength becomes comparable to the system size. The general scaling of cluster expansion in the short-time approximation has also been demonstrated to be a powerful predictive tool: By extracting the values of individual clusters from the numerical data of the nonlocal correlations at a single (moderate) temperature with fixed coupling, it has been possible to accurately predict the nonlocal correlations for all temperatures (and the same coupling) within the range of validity, i.e., even down to the quantum degenerate regime for five particles. Apart

from the conceptual novelty, the fully analytical results that cover the whole range of interactions in the model are original, and even the simplest thermodynamic limit predictions were first reported by the author, being in excellent agreement with the numerical simulations performed by other authors.

In a second application, the cluster expansion for bosons and fermions in three dimensions has been addressed in nonperturbative regimes. By using only the analytical input from the solution of the two-body problem, the mean many-body energy shifts in a system of bosons has been predicted for moderate repulsive to resonant interactions with a diverging scattering length. The used method has been proven to yield very good results in the one-dimensional case with and without external confinement [60]. As the prediction is almost fully analytical it can be applied to different interactions and particle numbers, as well as smooth external potentials with ease. Therefore, only benchmark examples with up to 32 particles are presented in the thesis that await numerical verification. As a side product, the exact result for the first virial coefficient for the nonlocal correlations for resonant interactions has been obtained. The author is not aware of this result having been reported in the literature. In the case of fermions a short analysis of a spin-balanced system of four spin-1/2 fermions has been presented. The preliminary non-perturbative results show that the transition from noninteracting fermions across the unitary regime to the case of deeply bound bosonic molecules can be – at least qualitatively – described on the level of the smooth level density. The quantitative analysis requires further attention.

The focus of the second chapter has been on the semiclassical treatment of a certain class of quantum critical systems and, in particular, the study of the homogeneous one-dimensional Bose gas with attractive zero-range interaction. The latter is known to have a critical coupling beyond which the translational symmetry gets broken by the formation of a bright soliton. A similar transition occurs also in the momentum-truncated approximations to the full model, with the simplest consisting of three momentum modes. The classical mean field limit of this integrable three-mode model has been quantized earlier [61, 189] using the semiclassical torus quantization in close collaboration with the author yielding nonperturbative analytical results on the spectral properties, also predicting a distinct Ehrenfest-type time scale that dominates the non-equilibrium time dynamics of a quench across the quantum phase transition. Using this as a starting point, this thesis has then further analyzed the properties of this system and some of its extensions. A simplified but highly accurate WKB wave function approach based on the semiclassical quantization has been developed. It is capable of reproducing the essentially exact many-body quantum states in a wide energy range and for particle numbers ranging from only ten to arbitrarily many, thus essentially solving the Schrödinger equation. The main part of the chapter was dedicated to the non-equilibrium time-dynamics of a certain out-of-time-ordered correlator in a quench scenario starting from the noninteracting condensate. A thorough analysis of the short-time behavior of this correlator within a quasi-classical Truncated Wigner-like phase-space calculation has been used to analytically predict an exponential growth of this out-of-time-ordered correlator. Such a behavior is referred to as fast scrambling in the literature and is analogous to the expected behavior in chaotic systems. But due to the existence of the distinct local

Ehrenfest time that is expected to dominate the quantum time evolution as the single relevant time scale, a mechanism of *unscrambling* has been predicted and verified in a numerical simulation of this system, also validating the analytical prediction of the short-time evolution. Due to the very general underlying mechanism that can be understood semiclassically, this effect is conjectured to be present in a wide class of critical models where an excited state quantum phase transition is driven by structural changes in a mean-field classical phase space.

To provide further evidence of this conjecture, the nonintegrable extension of the the model using two more single-particle momentum modes has been studied both in its (classical) mean-field dynamics and quantum mechanically. Using a separation of scales that was inspired by the insights from the classical dynamics, a sophisticated numerical study with particle numbers well beyond the limits of brute-force diagonalization methods has shown that this nonintegrable critical model exhibits almost the same scrambling and unscrambling dynamics, hence underlining the generality of the identified unscrambling mechanism.

Thus, the second chapter, on the one hand, presented high-accuracy semiclassical results on a specific critical system in a regime that can otherwise only be treated by the exact diagonalization method. On the other hand, it demonstrated how the knowledge of the classical mean-field dynamics can help pushing numerical methods to otherwise inaccessible regimes. Similar to the first chapter, it also established a certain notion of universality in predicting a specific kind of quantum time evolution characterized by out-of-time-ordered correlators in a whole class of systems that exhibit a similar locally hyperbolic mean-field behavior.

Outlook

As one could think of numerous extensions to this work only the most promising are highlighted here. Some of them have already been outlined in more detail in the main text, while some of the results presented here are still work in progress, especially the three-dimensional applications of the cluster-expansion in short-time approximation. With the first steps done into the direction of such higher-dimensional systems, the number of possible applications has become much larger, but the additional degrees of freedom also limit the possibility of numerical validation of the approximations. A possible way to proceed is the numerical simulation of selected interaction potentials to compare some of the semiclassical predictions to the full quantum theory. This could also lead to a semi-analytical description of few-particle systems by using the numerically obtained results for the irreducible clusters to predict the thermal expectation values for whole classes of observables, parameter regimes, and even systems with different external potentials by using the general scaling properties of the semiclassical results. With this, the comparison with experimental and numerical findings reported in the literature could be performed with much less effort due to the usually relatively small number of parameters characterizing the interactions, the latter then being the only parameters that have to be adapted. This is, of course, not possible irrespective of the system parameters, but

covers a wide regime from close to quantum degeneracy up to high temperatures, thus covering a large regime that is of experimental relevance.

A more direct and less ambitious extension of the results presented in the first chapter could be the transfer of the (coordinate-dependent) clusters calculated in the Lieb-Liniger model to the nonintegrable case of an external trapping potential in the spirit of the short-time approximation. This has already been successfully implemented on the level of the density of states [60] but the implications for the nonlocal correlation functions have not been studied so far. Similarly, the influence of hard-wall boundary conditions can be studied, with the advantage that this system falls again in the category of quantum integrable systems [217], thus being a perfect benchmark system for exploring boundary-effects on the nonlocal correlations. The generalization to multiple species is less straightforward when going beyond the two-body contributions in the semiclassical theory, as these clusters have not been calculated. But as this situation is described by the integrable Gaudin-Yang model [108], the calculation of higher clusters in this model should be possible with the same methods as presented here.

One should also note that the two-particle propagators in one and three dimensions used in this work can be represented in momentum space in closed form. This can be very useful when addressing larger homogeneous systems and could be used in the exact cluster resummation of the single-particle density matrix presented in the end of the first chapter. By using the full two-particle propagators in the self-consistent approach sketched there, one might be able to obtain non-perturbative results on the momentum distribution in the one- and three-dimensional systems at hand.

In the context of the scrambling dynamics in the three-mode model, a very interesting behavior has been found: Although the semiclassical analysis in the three-mode model was able to accurately predict the short-time exponential growth of the OTOC, the numerical analysis of the model has revealed that the semiclassical result is only the first order in a power expansion of an exponential (see section 2.2.4). This behavior has been found recently also in the Sachdev-Ye-Kitaev model [174], despite the two models having a very different scrambling dynamics. The theoretical description of this behavior might therefore be of relevance in a more general context and further research is planned. In this respect, a first step could be the systematic comparison of the behavior found in the three-mode model to other simple critical models to find the necessary conditions for the effect. One candidate could be a pseudo-relativistic model introduced by the author [218] that shows similar critical behavior. This model, although being nonintegrable, allows for a separation of scales due to criticality on an analytical level, such that it might give deeper insights also on this subject.

Finally, the numerical analysis of the five-mode model has concentrated on the regime close to the mean-field value of the critical coupling of the quantum phase transition. This has been due to numerical constraints, as higher excited states are required for larger couplings and it has proven difficult to directly access a specific energy range in the spectrum without calculating all the states below. As the classical phase space looks rather regular in this regime, this has, on the one hand, restricted the analysis to a quasi-integrable case, and the question of whether excited state quantum phase transitions exist also at larger couplings has thus not been answered to satisfaction.

On the other hand, a quasi-integrable classical motion could also pave the way to an analytical quantization scheme using a characterization of periodic orbits, as has been successfully applied to the quasi-integrable configurations of the Helium atom [48].

A final conclusion

Although the most important results of this thesis have already been summarized above, it is worth to comment on the relevance of the thesis on a different level. Naturally, some of the new results presented in this thesis could be considered as important contributions to the theory of few- and many-body quantum systems in their own right. Especially some of the remarkably simple analytical results obtained here, e.g., for the non-local correlations can be considered as an important addition to the rather small number of available analytical results. However, the ingredients that led to some of the simple results have been around for decades – but it required an less conventional (semiclassical) approach to establish their direct connections. This has hopefully conveyed to the reader the general relevance of the semiclassical methods used here: They should be considered a valuable complement to other (standard) approaches by highlighting different aspects of the same physics and offering new connections between otherwise (seemingly) unrelated physical situations.

A. Proof of equation (1.47)

To derive Eq. (1.47) we perform the trace in $\langle\mathcal{O}\rangle = \mathrm{Tr}_{\pm}^{(N)}\{e^{-\beta\hat{H}}\mathcal{O}\}/Z_{\pm}^{(N)}$ in the position basis of the Hilbert space of (anti)symmetric N-particle states

$$|\boldsymbol{x}) = \frac{1}{N!}\sum_{P\in S_N}|P\boldsymbol{x}\rangle = \frac{1}{\sqrt{N!}}\hat{\Psi}^\dagger(\boldsymbol{x}_1)\ldots\hat{\Psi}^\dagger(\boldsymbol{x}_N)|0) \tag{A.1}$$

and insert a closure relation to rewrite Eq. (1.46) as

$$\begin{aligned} C_{\pm}^{(N,k)}(\boldsymbol{y},\boldsymbol{x};\beta) = \frac{1}{Z_{\pm}^{(N)}}\int d^N\boldsymbol{z}\, d^N\boldsymbol{z}'\,(\boldsymbol{z}'|\mathrm{e}^{-\beta\hat{H}}|\boldsymbol{z}) \\ \times(\boldsymbol{z}|\hat{\Psi}^\dagger(\boldsymbol{x}_1)\cdots\hat{\Psi}^\dagger(\boldsymbol{x}_k)\hat{\Psi}(\boldsymbol{y}_k)\cdots\hat{\Psi}(\boldsymbol{y}_1)|\boldsymbol{z}'). \end{aligned} \tag{A.2}$$

The first term in the integral is exactly the symmetry-projected many-body propagator $K_{\pm}^{(N)}(\boldsymbol{z}',\boldsymbol{z};\beta)$ defined in Eq. (1.15), as the symmetry projection commutes with $\hat{H}$ and is idempotent. The matrix element

$$\begin{aligned} &M(\boldsymbol{z},\boldsymbol{z}',\boldsymbol{x},\boldsymbol{y}) = (\boldsymbol{z}|\hat{\Psi}^\dagger(\boldsymbol{x}_1)\cdots\hat{\Psi}^\dagger(\boldsymbol{x}_k)\hat{\Psi}(\boldsymbol{y}_k)\cdots\hat{\Psi}(\boldsymbol{y}_1)|\boldsymbol{z}') \\ &= \frac{1}{N!}(0|\hat{\Psi}(\boldsymbol{z}_N)\cdots\hat{\Psi}(\boldsymbol{z}_1)\hat{\Psi}^\dagger(\boldsymbol{x}_1)\cdots\hat{\Psi}^\dagger(\boldsymbol{x}_k)\hat{\Psi}(\boldsymbol{y}_k)\cdots\hat{\Psi}(\boldsymbol{y}_1)\hat{\Psi}^\dagger(\boldsymbol{z}'_1)\cdots\hat{\Psi}^\dagger(\boldsymbol{z}'_N)|0) \end{aligned} \tag{A.3}$$

can be evaluated using Wick's theorem with the definition of a contraction $\hat{A}^\bullet\hat{B}^\bullet = \hat{A}\hat{B} - :\hat{A}\hat{B}:$, where $:\hat{A}\hat{B}:$ stands for normal ordering of the field operators $\hat{A},\hat{B}$. The only nonvanishing contractions are then

$$\hat{\Psi}(\boldsymbol{u})^\bullet\hat{\Psi}^\dagger(\boldsymbol{v})^\bullet = \delta^{(D)}(\boldsymbol{u}-\boldsymbol{v}), \tag{A.4}$$

and Wick's theorem states that $M(\boldsymbol{z},\boldsymbol{z}',\boldsymbol{x},\boldsymbol{y})$ is given by the sum of all full contractions of all the field operators. For a nonvanishing contribution, $\hat{\Psi}(\boldsymbol{y}_i), i=1,\ldots,k$, has to be contracted to the right while $\hat{\Psi}^\dagger(\boldsymbol{x}_j), j=1,\ldots,k$, has to be contracted to the left. The simplest full contraction is

$$\begin{aligned} &\left[\prod_{i=1}^{k}\hat{\Psi}(\boldsymbol{z}_i)^\bullet\hat{\Psi}^\dagger(\boldsymbol{x}_i)^\bullet\right]\left[\prod_{i=1}^{k}\hat{\Psi}(\boldsymbol{y}_i)^\bullet\hat{\Psi}^\dagger(\boldsymbol{z}'_i)^\bullet\right]\left[\prod_{i=k+1}^{N}\hat{\Psi}(\boldsymbol{z}_i)^\bullet\hat{\Psi}^\dagger(\boldsymbol{z}'_i)^\bullet\right] \\ &\quad = \prod_{i=1}^{k}\delta^{(D)}(\boldsymbol{z}_i-\boldsymbol{x}_i)\delta^{(D)}(\boldsymbol{y}_i-\boldsymbol{z}'_i)\prod_{i=k+1}^{N}\delta^{(D)}(\boldsymbol{z}_i-\boldsymbol{z}'_i), \end{aligned} \tag{A.5}$$

where adjacent operators are successively contracted, giving rise to the contribution

$$\frac{1}{N!Z_{\pm}^{(N)}}\int d^{N-k}\boldsymbol{z}\, K_{\pm}^{(N)}((\boldsymbol{y},\boldsymbol{z}),(\boldsymbol{x},\boldsymbol{z});\beta)=\frac{1}{N!Z_{\pm}^{(N)}}\rho_{\pm}^{(N,k)}(\boldsymbol{y},\boldsymbol{x}) \tag{A.6}$$

in Eq. (A.2). All other full contractions can be brought to the same form under the integral by

1. relabeling the integration variables $\boldsymbol{z}_i$ and $\boldsymbol{z}_i'$ such that the individual contractions have matching coordinate indexes as in (A.5) and
2. simultaneously reordering operators and coordinates in the (anti)symmetric propagator, such that the minus signs in the fermionic case cancel.

Note here that the reordering of the operators is only done on a formal level to work out the correct signs. This shows that all the $N(N-1)N!$ full contractions give exactly the same contribution (A.6) to (A.2), which proves Eq. (1.47).

B. Lieb-Liniger model

B.1. Derivation of the propagator for the extended Lieb-Liniger gas

The symmetric wave functions of the continuum limit of the LL model are known and can be written as [3, 108]

$$\chi_{\boldsymbol{k}}(\boldsymbol{x}) = \frac{1}{\sqrt{(2\pi)^N N!}} \sum_{P\in S_N} (-1)^P f(\hat{P}\boldsymbol{k}, \boldsymbol{x}) \mathrm{e}^{i(\hat{P}\boldsymbol{k})\boldsymbol{x}}. \tag{B.1}$$

Here, S_N is the symmetric group acting on the index set, $\hat{P}$ is the $N \times N$ matrix representation of the permutation P such that $(\hat{P}\boldsymbol{k})_i = k_{P(i)}$, $(-1)^P$ is the sign of the permutation P, and

$$f(\boldsymbol{k}, \boldsymbol{x}) = \prod_{j>l} \frac{k_j - k_l - ic\,\mathrm{sgn}(x_j - x_l)}{[(k_j - k_l)^2 + c^2]^{\frac{1}{2}}}. \tag{B.2}$$

They obey the Schrödinger equation

$$\hat{H}\chi_{\boldsymbol{k}}(\boldsymbol{x}) = \frac{\hbar^2 \boldsymbol{k}^2}{2m} \chi_{\boldsymbol{k}}(\boldsymbol{x}) \tag{B.3}$$

for the LL Hamiltonian defined in Eq. (1.172), but now with $x_i \in \mathbb{R}$. It has been proven in [108] that the wave functions $\chi_{\boldsymbol{k}}$ form a complete set in the domain $x_1 < \cdots < x_1$ if we choose $k_1 < \cdots < k_N$ and that they are normalized such that

$$\int_{\mathbb{R}^N} \mathrm{d}\boldsymbol{x}\, \chi_{\boldsymbol{k}'}(\boldsymbol{x}) \overline{\chi_{\boldsymbol{k}}(\boldsymbol{x})} = \prod_j \delta(k'_j - k_j), \tag{B.4}$$

where the bar denotes complex conjugation. The symmetric many-body propagator is thus given as

$$\begin{aligned} K_+^{(N)}(\boldsymbol{x}', \boldsymbol{x}; t) &= \int_D \mathrm{d}\boldsymbol{k}\, \mathrm{e}^{-\frac{i\hbar t}{2m}\boldsymbol{k}^2} \chi_{\boldsymbol{k}}(\boldsymbol{x}') \overline{\chi_{\boldsymbol{k}}(\boldsymbol{x})} \\ &= \frac{1}{N!} \int_{\mathbb{R}^N} \mathrm{d}\boldsymbol{k}\, \mathrm{e}^{-\frac{i\hbar t}{2m}\boldsymbol{k}^2} \chi_{\boldsymbol{k}}(\boldsymbol{x}') \overline{\chi_{\boldsymbol{k}}(\boldsymbol{x})}, \end{aligned} \tag{B.5}$$

where D is the domain with $k_1 < \cdots < k_N$. The second line follows from the fact that $\chi_{\boldsymbol{k}}(\boldsymbol{x})$ is an antisymmetric function with respect to exchange of any two of the k_i so that

the integrand is a symmetric function ($\boldsymbol{k}^2$ is invariant under permutations). Using the transitivity of the symmetric group it is straightforward to show that

$$\sum_{R,Q\in S_N} (-1)^{R\circ Q} f(\hat{R}\boldsymbol{k},\boldsymbol{x}')\overline{f(\hat{Q}\boldsymbol{k},\boldsymbol{x})}\mathrm{e}^{i(\hat{R}\boldsymbol{k})\boldsymbol{x}'-i(\hat{Q}\boldsymbol{k})\boldsymbol{x}} = \sum_{P,Q\in S_N} (-1)^{P} f(\hat{P}^{-1}\hat{Q}\boldsymbol{k},\boldsymbol{x}')\overline{f(\hat{Q}\boldsymbol{k},\boldsymbol{x})}\mathrm{e}^{i(\hat{Q}\boldsymbol{k})(\hat{P}\boldsymbol{x}'-\boldsymbol{x})}, \quad \text{(B.6)}$$

where the substitution $R = Q \circ P^{-1}$ was used. Note that the matrix representation of two successive permutations $R \circ S$ is $\hat{S}\hat{R}$, i.e., the order is reversed. The integrand in Eq. (B.5) thus depends only on $\hat{Q}\boldsymbol{k}$ so that the sum over the permutations Q gives just a factor of $N!$ as one can relabel the k_i in each integral. The key step now is to realize that the function f satisfies

$$f(\hat{P}\boldsymbol{k},\hat{P}\boldsymbol{x}) = (-1)^P f(\boldsymbol{k},\boldsymbol{x}) \quad \text{(B.7)}$$

for all permutations P. This will be proven at the end of the paragraph. A simple calculation then shows that

$$(-1)^P f(\hat{P}^{-1}\boldsymbol{k},\boldsymbol{x}')\overline{f(\boldsymbol{k},\boldsymbol{x})} = f(\boldsymbol{k},\hat{P}\boldsymbol{x}')\overline{f(\boldsymbol{k},\boldsymbol{x})} = \prod_{j>l} \frac{k_j - k_l - ic\,\mathrm{sgn}(x'_{P(j)} - x'_{P(l)})}{k_j - k_l - ic\,\mathrm{sgn}(x_j - x_l)} \quad \text{(B.8)}$$

Putting everything together one finds that the symmetric many-body propagator can be written as in Eq. (1.173) with the effective many-body propagator (1.174).

To complete the proof one still has to show the identity (B.7). The proof is trivial if we can show this for a permutation that interchanges only two successive numbers $m, m+1$ for $m = 1,\ldots,N-1$, as any permutation can be written as a composition of such exchange operations. The product of the denominators in the definition of f, Eq. (B.2), is invariant under permutations of the k_i. So one only has to consider the product of the numerators, that one can split [after fixing m and $P = (m \quad m+1)$] into the factor where $j = m+1, l = m$

$$k_{P(m+1)} - k_{P(m)} - ic\,\mathrm{sgn}(x_{P(m+1)} - x_{P(m)}) = -[k_{m+1} - k_m - ic\,\mathrm{sgn}(x_{m+1} - x_m)] \quad \text{(B.9)}$$

and all the other factors. One now has to prove that the product of the latter is invariant under P, as $(-1)^P = -1$ is already accounted for in the first factor (B.9). Let us define the set

$$\Omega_P = \{k_{P(j)} - k_{P(l)} - ic\,\mathrm{sgn}(x_{P(j)} - x_{P(l)}) | j > l\}, \quad \text{(B.10)}$$

where the factor that has $j = m+1, l = m$ is excluded. The proof is completed by showing that $\Omega_P = \Omega_{id}$: Let us choose an element in Ω_P. As P interchanges the sign of $j-l$ if and only if both $j = m+1$ and $l = m$, it is also an element of Ω_{id}. Together with the fact that both sets are of the same size, this shows their identity.

B.2. Second- and third-order interaction contributions

The second-order interaction contribution can easily be calculated from the propagator for a 1D δ potential $V(x) = (\hbar^2 c/m)\,\delta(x)$ [219, 220]:

$$K_\delta(x', x; t) = K_0(x', x; t) + K_c(x', x; t) \tag{B.11}$$

with

$$K_0(x', x; t) = \sqrt{\frac{m}{2\pi i\hbar t}} \mathrm{e}^{-\frac{m}{2i\hbar t}(x'-x)^2} \tag{B.12}$$

and

$$K_c(x', x; t) = -\int_0^\infty \mathrm{d}u\, \mathrm{e}^{-u} K_0\Big(|x'| + |x| + \frac{u}{c}, 0; t\Big). \tag{B.13}$$

Introducing center of mass and relative coordinates this results in

$$\Delta K^{(2)}(\boldsymbol{x}', \boldsymbol{x}; t) = K_{0,M}(R', R; t) K_{c,\mu}(r', r; t), \tag{B.14}$$

where the additional indices M and μ stand for the total and reduced mass that should be used in the expressions.

The result for the third-order interaction contribution was calculated for the fundamental domain $\mathcal{F}$ defined as the region where $x_1 < x_2 < x_3$. The result for $\boldsymbol{x}$ or $\boldsymbol{x}'$ in another domain is then obtained by projecting both coordinates into $\mathcal{F}$ (i.e., ordering them by size). Expressing relative and center-of-mass coordinates in units of the thermal wavelength $\lambda_T = \sqrt{2\pi\hbar^2\beta/m}$ through

$$(\tilde{r}_1, \tilde{r}_2, \tilde{R}) = \frac{\sqrt{2\pi}}{\lambda_T}(r_1, r_2, R) = \frac{\sqrt{2\pi}}{\lambda_T}\left(\bar{x}_2 - \bar{x}_1, \bar{x}_3 - \bar{x}_2, \frac{\bar{x}_1 + \bar{x}_2 + \bar{x}_3}{3}\right), \tag{B.15}$$

where the bar denotes the projection to $\mathcal{F}$, the simplified result in dimensionless coordinates and interaction parameter is

$$\begin{aligned}
\Delta K_+^{(3)}(\boldsymbol{x}', \boldsymbol{x}; t = -i\hbar\beta) = {} & \frac{1}{3\lambda_T^3} \exp\left[-\frac{3}{2}\left(\tilde{R}' - \tilde{R}\right)^2\right] \int_0^\infty \mathrm{d}u \int_{-u}^{u} \mathrm{d}v \\
\times \Bigg\{ & \exp\left[-u - \frac{1}{4}\left(\tilde{r}_1 - \tilde{r}_2' + \frac{v}{2\tilde{c}}\right)^2 - \frac{1}{12}\left(\tilde{r}_1 + \tilde{r}_2' + 2(\tilde{r}_1' + \tilde{r}_2) + \frac{3u}{2\tilde{c}}\right)^2\right] + [\tilde{r}_i \leftrightarrow \tilde{r}_i'] \\
& - \exp\left[-u - \frac{1}{4}\left(\tilde{r}_1 + \tilde{r}_2' + \frac{v}{2\tilde{c}}\right)^2 - \frac{1}{12}\left(\tilde{r}_1 + \tilde{r}_2' + 2(\tilde{r}_1' + \tilde{r}_2) + \frac{3u}{2\tilde{c}}\right)^2\right] + [\tilde{r}_i \leftrightarrow \tilde{r}_i'] \\
& + 3\exp\left[-u - \frac{1}{4}\left(\tilde{r}_1 + \tilde{r}_2' + \tilde{r}_1' + \tilde{r}_2 + \frac{u}{2\tilde{c}}\right)^2 - \frac{1}{12}\left((\tilde{r}_1 + \tilde{r}_2') - (\tilde{r}_1' + \tilde{r}_2) + \frac{3v}{2\tilde{c}}\right)^2\right] \Bigg\}.
\end{aligned} \tag{B.16}$$

Here, the interaction strength has been rescaled to $\tilde{c} = \lambda_T c/\sqrt{8\pi}$. The above result gets simplified if one is interested in the diagonal elements $\boldsymbol{x}' = \boldsymbol{x}$, as is the case for

$b_3^{(2)}(r)$, where one has to set $x_1 = 0$, $x_2 = r$ and integrate x_3 in Eq. (B.16) over full space. Due to the symmetry of the problem one can choose $r > 0$ and thus only has to consider three different regimes $x_3 < 0$, $0 < x_3 < r$, and $x_3 > r$. This leads to different assignments of the variables $\tilde{r}_i$ in Eq. (B.15) due to the projection onto the fundamental domain. By performing all the integrations and combining the result with the contributions from the diagrams of lower orders in the interaction contributions one obtains $b_3^{(2)}(r) = d_1(r) + d_2(r) + d_3(r)$ with

$$d_1\left(\frac{\lambda_T}{\sqrt{2\pi}}\tilde{r}\right) = \sqrt{2}\mathrm{e}^{-\frac{3}{4}\tilde{r}^2}, \tag{B.17}$$

$$d_2\left(\frac{\lambda_T}{\sqrt{2\pi}}\tilde{r}\right) = -2\sqrt{2}\mathrm{e}^{-\tilde{r}^2}\left\{\mathrm{e}^{(\frac{\tilde{r}}{2})^2}\operatorname{erfc}\left(\frac{\tilde{r}}{2}\right) + (\tilde{r}\tilde{c}-1)\mathrm{e}^{(\tilde{c}+\frac{\tilde{r}}{2})^2}\operatorname{erfc}\left(\tilde{c}+\frac{\tilde{r}}{2}\right)\right\} \tag{B.18}$$

$$- 8\sqrt{2}[F_{\tilde{c}}(\tilde{r}/2, -\tilde{r}/2) + F_{\tilde{c}}(0,\tilde{r})], \tag{B.19}$$

$$d_3\left(\frac{\lambda_T}{\sqrt{2\pi}}\tilde{r}\right) = 8\sqrt{2}\Bigg\{F_{\tilde{c}}(0,\tilde{r}) + \left[2 + 2\tilde{c}\tilde{r} + \frac{8}{3}\tilde{c}^2\right]F_{\tilde{c}}(\tilde{r}/2,\tilde{r}/2) \tag{B.20}$$

$$- \left[2\tilde{r}\tilde{c} + \frac{8}{3}\tilde{c}^2\right]F_{\tilde{c}}(\tilde{r}/2,\tilde{r}/2) + [2\tilde{r}\tilde{c}-1]G_{\tilde{c}}(\tilde{r})$$

$$+ \frac{4}{3}\tilde{c}^2\mathrm{e}^{-\tilde{r}^2}\left[\mathrm{e}^{(\frac{\tilde{r}}{2})^2}\operatorname{erf}\left(\frac{\tilde{r}}{2}\right) + \mathrm{e}^{(\tilde{c}+\tilde{r})^2}\operatorname{erfc}(\tilde{c}+\tilde{r}) - \mathrm{e}^{(\tilde{c}+\frac{\tilde{r}}{2})^2}\operatorname{erfc}\left(\tilde{c}+\frac{\tilde{r}}{2}\right)\right]\Bigg\}. \tag{B.21}$$

The functions $F_{\tilde{c}}$ and $G_{\tilde{c}}$ are defined as

$$F_{\tilde{c}}(x,y) = \tilde{c}\int_0^\infty \mathrm{d}u\,\mathrm{e}^{-4\tilde{c}u-3(u+x)^2}\operatorname{erfc}(u+y), \tag{B.22}$$

$$G_{\tilde{c}}(x) = \sqrt{3}\tilde{c}\int_0^\infty \mathrm{d}u\,\mathrm{e}^{-4\tilde{c}u-(u+x)^2}\operatorname{erf}(\sqrt{3}u). \tag{B.23}$$

The indices n of the functions d_n stand for the order of the interaction contributions that are involved, such that, e.g., d_1 is the result for free bosons. The function $b_3 = b_3^{(0)}$ is obtained from $b_3^{(2)}(r)$ by using Eq. (1.39). As many of the resulting terms from second- and third-order interaction contributions cancel after integration, only the sum of all contributions is presented here, which is given by

$$b_3 = \frac{1}{\sqrt{3}} + \frac{3}{2}\sqrt{3}\left[\mathrm{e}^{(2\tilde{c})^2}\operatorname{erfc}(2\tilde{c}) - \tilde{F}_{\frac{1}{\sqrt{3}}}(\tilde{c}) - \tilde{F}_{\sqrt{3}}(\tilde{c})\right] \tag{B.24}$$

with

$$\tilde{F}_\nu(\tilde{c}) = \frac{2}{\sqrt{\pi}}\mathrm{e}^{(1+\nu^2)\tilde{c}^2}\int_0^\infty \mathrm{d}u\,\mathrm{e}^{-(u+\sqrt{1+\nu^2}\tilde{c})^2}\operatorname{erfc}(\nu u). \tag{B.25}$$

Note that $\tilde{F}_\nu(0) = 1 - \pi/2\arctan(\nu)$, which can easily be proven by differentiating $\tilde{F}_\nu(0)$ with respect to ν, so that $\tilde{F}_\nu(0) + \tilde{F}_{\nu^{-1}}(0) = 1$ for $\nu > 0$ and thus $b_3 = 1/\sqrt{3}$ for $\tilde{c} = 0$.

B.3. Numerical calculation and error estimates

B.3.1. Numerical scheme for calculation of the pair correlation function

For the numerical calculation of the nonlocal pair correlation function the Bethe ansatz solutions [108]

$$\chi_{\boldsymbol{k}}(\boldsymbol{x}) = C(\boldsymbol{k}) \sum_{P\in S_N} (-1)^P f(\hat{P}\boldsymbol{k}, \boldsymbol{x}) \mathrm{e}^{i(\hat{P}\boldsymbol{k})\boldsymbol{x}}, \tag{B.26}$$

were used, with the function f defined in (B.2) and a (real) normalization constant $C(\boldsymbol{k})$ that depends on the quasimomenta that solve the coupled transcendental equations

$$\mathrm{e}^{ik_jL} = -\prod_{i=1}^{N} \frac{k_j - k_i + ic}{k_j - k_i - ic}, \qquad j = 1, \ldots, N. \tag{B.27}$$

Let us focus only on the case $c > 0$. In this case the logarithm of the equations (B.27) can be taken directly and the quasimomenta are determined by a set of N ordered quantum numbers that represent the branch of the logarithm that is used in the respective equation (for more details see, e.g., [3,19]). The solution is then easily found via Newton's method. The energy of the eigenstate $\chi_{\boldsymbol{k}}$ is given by

$$E(\boldsymbol{k}) = \frac{\hbar^2 \boldsymbol{k}^2}{2m}. \tag{B.28}$$

The nonlocal pair correlation function can now be written as

$$g_2^{(N)}(r) = \frac{N-1}{N} \frac{1}{Z^{(N)}} \sum_{k_1<\cdots<k_N} \mathrm{e}^{-\beta E(\boldsymbol{k})} g_{2,\boldsymbol{k}}^{(N)}(r), \tag{B.29}$$

with

$$g_{2,\boldsymbol{k}}^{(N)}(r) = L^2 \int_0^L \mathrm{d}x_3 \ldots \mathrm{d}x_N \, |\chi_{\boldsymbol{k}}(0, r, x_3, \ldots, x_N)|^2. \tag{B.30}$$

The absolute square of the wave functions involves $(N!)^2$ terms and one could now integrate them directly as was done in [109]. But one can reduce the problem to $N!$ such integrations with the help of similar manipulations as were used in Appendix B.1. This enables one to write the absolute square of the wave function as

$$|\chi_{\boldsymbol{k}}(\boldsymbol{x})|^2 = C^2(\boldsymbol{k}) \sum_{Q\in S_N} \Psi_{\hat{Q}\boldsymbol{k}}(\boldsymbol{x}), \tag{B.31}$$

where $\hat{Q}$ is the matrix representation of the permutation Q and

$$\Psi_{\boldsymbol{k}}(\boldsymbol{x}) = \sum_{P\in S_N} \Re\Big\{(-1)^P \prod_{j>l} \frac{k_{P(j)} - k_{P(l)} - ic}{k_j - k_l - ic} \, \mathrm{e}^{i(\hat{P}\boldsymbol{k}-\boldsymbol{k})\mathcal{P}_{\mathcal{F}}(\boldsymbol{x})}\Big\}. \tag{B.32}$$

Here, $\mathcal{P}_{\mathcal{F}}(\boldsymbol{x})$ is the projection of $\boldsymbol{x}$ to the fundamental domain $\mathcal{F}$ with $x_1 < \cdots < x_N$ and one can take the real part as the imaginary parts have to vanish in the overall

sums. The plane waves have to be integrated over full space in $x_3, \ldots, x_N$, which leads to different projections in the fundamental domain. Due to the translational invariance and inversion symmetry one can restrict the analysis to the cases where $0 < \cdots < x_j < r < x_{j+1} < \cdots < L$. A simple algorithm has been implemented that correctly traces out x_3 to x_N symbolically. The final expression that was used for the numerical calculation is

$$g_{2,\boldsymbol{k}}^{(N)}(r) = L \frac{\sum_{Q \in S_N} F_{\hat{Q}\boldsymbol{k}}(r)}{\sum_{Q \in S_N} G_{\hat{Q}\boldsymbol{k}}}, \tag{B.33}$$

with the functions

$$F_{\boldsymbol{k}}(r) = \sum_{P \in S_N} \Re \left\{ f_{\boldsymbol{k}}^{(P)} h_{\boldsymbol{k}}^{(P)}(r) \right\}, \tag{B.34}$$

$$G_{\boldsymbol{k}} = \sum_{P \in S_N} \Re \left\{ f_{\boldsymbol{k}}^{(P)} \int_0^L \mathrm{d}r\, h_{\boldsymbol{k}}^{(P)}(r) \right\}, \tag{B.35}$$

with the definition

$$f_{\boldsymbol{k}}^{(P)} = (-1)^P \prod_{j>l} \frac{k_{P(j)} - k_{P(l)} - ic}{k_j - k_l - ic}, \tag{B.36}$$

$$h_{\boldsymbol{k}}^{(P)}(r) = \int_0^L \mathrm{d}x_3 \ldots \mathrm{d}x_N \, \mathrm{e}^{i(\hat{P}\boldsymbol{k} - \boldsymbol{k})\mathcal{P}_{\mathcal{F}}(\boldsymbol{x})} \big|_{x_1 = 0, x_2 = r}. \tag{B.37}$$

One has to take care, as some of the sets of k_i obey certain symmetries leading to divergences in the symbolic expressions for $h_{\hat{Q}\mathbf{k}}^{(P)}$ for certain permutations Q. These cases have to be treated separately, leading to a piece-wise definition of the functions $G_{\boldsymbol{k}}$ and $F_{\boldsymbol{k}}$ with respect to $\boldsymbol{k}$. For the computation, the length L of the system can be completely eliminated by rescaling the variables according to $\boldsymbol{k} \mapsto \boldsymbol{k}L, E \mapsto EL^2, x \mapsto x/L, c \mapsto cL, \beta \mapsto \beta/L^2$. One may note that for $N = 3$ particles the integral of a plane wave can be written

$$\int_a^b \mathrm{d}x\, \mathrm{e}^{i\kappa x} = (b-a) \mathrm{e}^{i\frac{b+a}{2}\kappa} \operatorname{sinc}\left(\frac{b-a}{2} \kappa \right), \tag{B.38}$$

which is well defined for all values of κ and thus one can use this integral for $\kappa = k_{P(i)} - k_i$ for all permutations P and the respective indices i.

B.3.2. Error estimation

This appendix aims at finding an estimate for the error that occurs if the summation over quasi-momenta is truncated to a certain cutoff energy. Let us therefore write the nonlocal pair correlation function as

$$g_2^{(N)}(r) = \frac{N-1}{N} \frac{A^{(N)}(r)}{Z^{(N)}}, \tag{B.39}$$

with $A^{(N)}$ defined by Eq. (B.29), and let us denote a cutoff in the energy by a bar at the respective quantities. Both $\bar{A}^{(N)}(r)$ and $\bar{Z}^{(N)}$ are positive and monotonically increasing with the cutoff energy. Let us further write

$$\bar{A}^{(N)}(r) = [1 - \epsilon_A(r)]A^{(N)}(r), \quad \bar{Z}^{(N)} = (1 - \epsilon_Z)Z^{(N)} \tag{B.40}$$

with the positive relative errors $\epsilon_A(r)$ and ϵ_Z. The relative error of $\bar{g}_2^{(N)}(r)$ is then

$$\epsilon_g(r) = \frac{1 - \epsilon_A(r)}{1 - \epsilon_Z} - 1 = [\epsilon_Z - \epsilon_A(r)][1 + \mathcal{O}(\epsilon_Z)]. \tag{B.41}$$

Using the normalization

$$\int_0^L \mathrm{d}r\, A^{(N)}(r) = LZ^{(N)}, \tag{B.42}$$

which also holds for the truncated objects, it is easily shown that the absolute error of $\bar{g}_2^{(N)}(r)$ averages out,

$$\int_0^L \mathrm{d}r\, \epsilon_g(r) g_2^{(N)}(r) = 0. \tag{B.43}$$

Now define

$$\epsilon_g^>(r) = \begin{cases} \epsilon_g(r) & \epsilon_g(r) > 0 \\ 0 & \text{else} \end{cases} \tag{B.44}$$

$$\epsilon_g^<(r) = \epsilon_g(r) - \epsilon_g^>(r). \tag{B.45}$$

As $\epsilon_A(r)$ is positive, $\epsilon_g^>(r)$ is bound from above by $\epsilon_Z[1 + \mathcal{O}(\epsilon_Z)]$ and one has

$$\frac{1}{L}\int_0^L \mathrm{d}r\, \epsilon_g^>(r) g_2^{(N)}(r) = \frac{1}{L}\int_0^L \mathrm{d}r\, |\epsilon_g^<(r)| g_2^{(N)}(r) < \frac{N-1}{N}\,\epsilon_Z[1 + \mathcal{O}(\epsilon_Z)] \tag{B.46}$$

for the absolute error of $\epsilon_g(r) g_2^{(N)}$. Thus, even though the latter could, in principle, take large negative values down to $\epsilon_g(r) g_2^{(N)}(r) = -g_2^{(N)}(r)$ at certain points, this can only be the case in a small region that scales with the inverse of this value and with ϵ_Z, meaning that the absolute error is smaller than ϵ_Z everywhere else. However, such peaked drops in the pair correlation-function are not expected (and do not observed), as they can be regarded as unphysical.

In order to have an estimate for the relative error ϵ_Z of $Z^{(N)}$ one can use the observation that the mean density of states $\rho^{(N)}(E, c)$ in the LL model obeys $\rho^{(N)}(E, 0) \geq \rho^{(N)}(E, c) \geq \rho^{(N)}(E, \infty)$ and use the two limits for an estimate of the error in $Z^{(N)}$. As we are mainly interested in the approximation error for high temperatures, where the sum over the exact states in the partition function converges slowly, one can make use of the semiclassical approximations. The mean density of states is given by the inverse Laplace transform with respect to β of the semiclassical partition function $Z^{(N)}$,

Eq. (1.37). For the limits of free bosons and fermionization this can be written as

$$\begin{aligned} Z_{\pm}^{(N)}(\beta) &= \frac{1}{N!}\sum_{l=1}^{N}(\pm 1)^{N-l} z_l^{(N)} \left(\frac{L}{\lambda_T}\right)^l \\ &= \frac{1}{N!}\sum_{l=1}^{N}(\pm 1)^{N-l} z_l^{(N)} \left(\frac{\rho_0}{\beta}\right)^{\frac{l}{2}}, \end{aligned} \tag{B.47}$$

with $\rho_0 = mL^2/(2\pi\hbar^2)$, where the sign stands for the limits of free bosons (+) and fermionization (−), respectively. The numbers $z_l^{(N)}$ contain the sum of diagrams corresponding to the partitions of N particles into l clusters and are independent of the temperature, as $b_n = (\pm 1)^{n-1}/\sqrt{n}$ for the two limits. The mean density of states is

$$\begin{aligned} \rho_{\pm}^{(N)}(E) &= \mathcal{L}_\beta[Z_{\pm}^{(N)}(\beta)]E \\ &= \frac{1}{N!}\sum_{l=1}^{N}(\pm 1)^{N-l} z_l^{(N)} \rho_0^{\frac{l}{2}} \frac{E^{\frac{l}{2}-1}}{\Gamma(\frac{l}{2})}, \end{aligned} \tag{B.48}$$

with the gamma function $\Gamma(x)$. The relative error in the partition function is then approximated by the semiclassical error

$$\begin{aligned} \tilde{\epsilon}_{Z_\pm}(x,\beta) &= \frac{1}{Z_{\pm}^{(N)}} \int_{x/\beta}^{\infty} \mathrm{d}E\, \rho_{\pm}^{(N)}(E) \mathrm{e}^{-\beta E} \\ &= \frac{\sum_{l=1}^{N} z_l^{(N)} \left(\pm\frac{\lambda_T}{L}\right)^{N-l} Q(\frac{l}{2}, x)}{\sum_{l=1}^{N} z_l^{(N)} \left(\pm\frac{\lambda_T}{L}\right)^{N-l}}, \end{aligned} \tag{B.49}$$

where $Q(a,x)$ is the regularized incomplete gamma function

$$Q(a,x) = \frac{\Gamma(a,x)}{\Gamma(a)} = \frac{\int_x^\infty \mathrm{d}t\, t^{a-1}\mathrm{e}^{-t}}{\int_0^\infty \mathrm{d}t\, t^{a-1}\mathrm{e}^{-t}}. \tag{B.50}$$

We are interested in the regime $\lambda_T \leq 0.5L$ and, for reasonably small errors, $x \gtrsim 10$. The Numerator in Eq. (B.49) is then dominated by the $l = N$ term, and the error is largest if we minimize the denominator by using the result for the fermionization limit. This may also be seen from the fact that the ground-state energy is maximized in this limit, maximizing the ratios $\mathrm{e}^{-\beta(E_k - E_0)}$ in $Z = \mathrm{e}^{-\beta E_0}(1 + \mathrm{e}^{-\beta(E_1 - E_0)} + \dots)$. Thus, the semiclassical error estimate in the fermionization limit was used as a bound for the error at arbitrary couplings. The numerical calculations use the cutoff $x = 20$ for $N = 3, 4$, leading to $\tilde{\epsilon}_{Z_-} < 4 \times 10^{-8}$ and $\tilde{\epsilon}_{Z_-} < 8 \times 10^{-7}$, respectively (for all temperatures). The results for $N = 5$ use $x = 14$ for $\lambda_T = 0.1L$ ($\tilde{\epsilon}_{Z_-} < 6.2 \times 10^{-5}$, approximately 1.4×10^5 to 2.5×10^5 states) and $x = 22$ for $\lambda_T = 0.4L$ ($\tilde{\epsilon}_{Z_-} < 8.2 \times 10^{-7}$, approximately 250 to 1330 states), respectively, in the corresponding semiclassical approximation.

C. Propagator for shell potential

Here, the propagator for a shell potential centered at the origin is derived for a particle of mass μ. The radial wave functions u_{k0} for the shell potential

$$V(\boldsymbol{r}) = \frac{\hbar^2 c}{2\mu}\,\delta^{(1)}(r - r_\mathrm{s}) \tag{C.1}$$

centered in a sphere of radius $R > r_\mathrm{s}$ can be written as

$$u_{k0}(r) = A_k(R, r_\mathrm{s}) \times \begin{cases} \frac{\sin(k(R-r_\mathrm{s}))}{\sin(kr_\mathrm{s})}\sin(kr), & r \le r_\mathrm{s} \\ \sin(k(R-r)), & r_\mathrm{s} < r \le R \end{cases}, \tag{C.2}$$

with a normalization constant A_k that depends on the details of the potential and the quantization condition. The latter can be written in terms of the scattering phase δ_0 found in the main text as

$$\tan(kR) = -\tan(\delta_0). \tag{C.3}$$

The propagator (1.192) contains the product of the wave functions evaluated at different positions, giving rise to four different contributions that have either both coordinates on the same side or at different sides of the shell potential. It is possible to rewrite the product of the wave functions (choosing a real normalization constant) for the different contributions by using the quantization condition for all terms that involve trigonometric functions of kR. This yields

- for $r_1, r_0 > r_\mathrm{s}$:

$$\frac{u_{k0}(r_1)u_{k0}(r_0)}{A^2} = \frac{1}{2}\Re\left[\mathrm{e}^{ik(r_1-r_0)} + \mathrm{e}^{ik(r_1+r_0)} - 2\frac{\mathrm{e}^{ik(r_1+r_0)}}{1 - i\tan\delta_0}\right], \tag{C.4}$$

- for $(r_1 - r_\mathrm{s})(r_0 - r_\mathrm{s}) < 0$:

$$\frac{u_{k0}(r_1)u_{k0}(r_0)}{A^2} = \left[1 + \frac{\tan\delta_0}{\tan kr_\mathrm{s}}\right]\frac{1}{2}\Re\left[\frac{\mathrm{e}^{ik|r_1-r_0|} - \mathrm{e}^{ik(r_1+r_0)}}{1 - i\tan\delta_0}\right], \tag{C.5}$$

- for $r_1, r_0 < r_\mathrm{s}$:

$$\frac{u_{k0}(r_1)u_{k0}(r_0)}{A^2} = \frac{1}{1 + \tan^2\delta_0}\left[1 + \frac{\tan\delta_0}{\tan kr_\mathrm{s}}\right]^2\frac{1}{2}\Re\left[\mathrm{e}^{ik(r_1-r_0)} - \mathrm{e}^{ik(r_1+r_0)}\right]. \tag{C.6}$$

Here $\Re[z]$ denotes the real part of z. Note that the expressions are the same for $\delta_0 = 0$ as they should. The normalization constant is given by

$$A_k(R, r_\mathrm{s}) = \sqrt{2}\left\{\frac{\sin^2(k(R-r_\mathrm{s}))}{\sin^2(kr_\mathrm{s})} r_\mathrm{s}\left[1 - \frac{\sin(2kr_\mathrm{s})}{2kr_\mathrm{s}}\right] + (R-r_\mathrm{s})\left[1 - \frac{\sin(2k(R-r_\mathrm{s}))}{2k(R-r_\mathrm{s})}\right]\right\}^{-\frac{1}{2}}. \tag{C.7}$$

The trigonometric functions could also be rewritten independently of R using the quantization condition, yielding lengthy expressions for finite R. However, as the limit $R \to \infty$ is taken eventually (carefully respecting the boundary conditions), one can replace A_k by $\sqrt{2/R}$ in this limit independently of the details of the potential.

By approximating $\tan\delta_0 = -a_\mathrm{s}k$ and $\tan kr_\mathrm{s} = kr_\mathrm{s}$ in the limit $kr_\mathrm{s} \ll 1$ one can then follow similar steps as in [221] to replace the sum over discrete quantum numbers k by an integral using

$$\sum_k A_k^2 \times (\cdot) \to \frac{2}{\pi}\int dk\,(\cdot), \tag{C.8}$$

such that the problem reduces to the calculation of integrals of the form

$$I_l(z, \beta, a_\mathrm{s}) = \frac{1}{\pi}\int_0^\infty dk\,\Re\left[\frac{\mathrm{e}^{ikz}}{1-(-ika_\mathrm{s})^l}\right]\mathrm{e}^{-\beta\frac{\hbar^2k^2}{2\mu}}, \qquad l = 0, 1, 2. \tag{C.9}$$

Taking the real part under the integral is equivalent (up to a factor of two) to expanding the integration to the real axis. The results for the integrals are then given in terms of the propagator

$$K_\mu^{(1)}(y, x; \beta) = \sqrt{\frac{\mu}{2\pi\hbar^2\beta}}\,\mathrm{e}^{-\frac{m}{2\hbar^2\beta}(y-x)^2} \tag{C.10}$$

of a free particle of mass μ in one dimension as

$$I_0(z, \beta, a_\mathrm{s}) = K_\mu^{(1)}(z, 0; \beta), \tag{C.11}$$

$$I_1(z, \beta, a_\mathrm{s}) = \int_0^\infty du\,\mathrm{e}^{-u}K_\mu^{(1)}(z, a_\mathrm{s}u; \beta), \tag{C.12}$$

$$I_2(z, \beta, a_\mathrm{s}) = \int_0^\infty du\,\mathrm{e}^{-u}K_\mu^{(1)}\left(z, 0; \beta + \frac{2\mu u a_\mathrm{s}^2}{\hbar^2}\right). \tag{C.13}$$

The full s-wave part of the propagator in short-range approximation is then

$$K_{\mu,0}^{(1)}(r_1, r_0; \beta, a_\mathrm{s}) = \begin{cases} I_0(r_1 - r_0) + I_0(r_1 + r_0) - 2I_1(r_1 + r_0), & r_1, r_0 > r_\mathrm{s}, \\ \left(1 - \frac{a_\mathrm{s}}{r_\mathrm{s}}\right)\left[I_1(|r_1 - r_0|) - I_1(r_1 + r_0)\right], & \frac{r_1 - r_\mathrm{s}}{r_0 - r_\mathrm{s}} < 0, \\ \left(1 - \frac{a_\mathrm{s}}{r_\mathrm{s}}\right)^2\left[I_2(r_1 - r_0) - I_2(r_1 + r_0)\right], & r_1, r_0 < r_\mathrm{s}. \end{cases} \tag{C.14}$$

However, for consistency, one should approximate also, e.g., $r_0/\lambda_T \ll 1$ if $r_0 < r_\mathrm{s}$. Only in this limit, the three expressions are the same at the boundaries that connect them.

The bound state solution with energy $E = -\hbar^2\kappa^2/2m$ can be analytically given as

$$u^{(\mathrm{b})}_{\kappa,0}(r) = A_\kappa \times \begin{cases} \mathrm{e}^{-\kappa r_\mathrm{s}} \frac{\sinh \kappa r}{\sinh \kappa r_\mathrm{s}}, & r < r_\mathrm{s} \\ \mathrm{e}^{-\kappa r}, & r \geq r_\mathrm{s}, \end{cases} \tag{C.15}$$

where the normalization is dominated by the region outside the sphere for $\kappa r_\mathrm{s} \ll 1$ and can be replaced by $A_\kappa = \sqrt{2\kappa}$. Using $\kappa = 1/a_\mathrm{s}$, valid for this regime, the contribution of the bound state to the imaginary time propagator can be written as

$$\mathrm{e}^{\beta \frac{\hbar^2}{2ma_\mathrm{s}^2}} u^{(\mathrm{b})}_{\frac{1}{a_\mathrm{s}}}(r_1) u^{(\mathrm{b})}_{\frac{1}{a_\mathrm{s}}}(r_0) \tag{C.16}$$

with the wave function defined above.

Using the above it is straightforward to show that in the case $r_0, r_1 > r_\mathrm{s}$ the s-wave interaction correction to the propagator is given by

$$\delta K^{(1)}_{\mu,0}(r_1, r_0; \beta, a_\mathrm{s}) = 2\left[K^{(1)}_\mu(r_1 + r_0, 0; \beta) - \int_0^\infty du\, \mathrm{e}^{-u} K^{(1)}_\mu(r_1 + r_0, a_\mathrm{s}u; \beta)\right] \tag{C.17}$$

$$+ \Theta(-1 - cr_\mathrm{s}) \frac{2}{a_\mathrm{s}} \mathrm{e}^{\frac{\hbar^2\beta}{2ma_\mathrm{s}^2}} \mathrm{e}^{-\frac{r_1+r_0}{a_\mathrm{s}}}, \tag{C.18}$$

where the bound state exists only for $cr_\mathrm{s} < -1$. This can be further simplified to

$$\delta K^{(1)}_{\mu,0}(r_1, r_0; \beta, a_\mathrm{s}) = 2K^{(1)}_\mu(r_1 + r_0, 0; \beta) \times [1 - \tilde{s}\, g_\eta(\tilde{r}_1 + \tilde{r}_0 + \tilde{s})] \tag{C.19}$$

with $\tilde{r}_i = r_i/\lambda_T(\mu)$, $\tilde{s} = -\lambda_T(\mu)/2\pi a_\mathrm{s}$, and the function

$$g_\eta(z) = \eta\pi \mathrm{e}^{\pi z^2} \operatorname{erfc}\left(\eta\sqrt{\pi} z\right). \tag{C.20}$$

Here, $\eta = 1$ and $\eta = -1$ correspond to the attractive and repulsive case, respectively, i.e., is given by $\eta = -\operatorname{sgn}(c)$. The bound state is included here automatically in the attractive case. It is combined with the complementary error function by using the identity

$$\operatorname{erfc}(-z) = 2 - \operatorname{erfc}(z). \tag{C.21}$$

It is important to also note that, as found for the repulsive case by other authors, the scaled interaction correction $\delta k^{(1)}_0$ can be written as a spatial derivative:

$$\delta k^{(1)}_0(\tilde{z}, 0; \tilde{s}) = 2\mathrm{e}^{-\pi\tilde{z}^2}[1 - \tilde{s}\, g_\eta(\tilde{z} + \tilde{s})] = -\frac{1}{\pi}\frac{\partial}{\partial \tilde{z}} \mathrm{e}^{-\pi\tilde{z}^2} g_\eta(\tilde{z} + \tilde{s}). \tag{C.22}$$

This relation can be very helpful in integrals.

C.1. Connection to 1D delta-propagator

The imaginary time propagator for a particle of mass μ in a potential

$$V_\delta(x) = \frac{\hbar^2 c}{2\mu} \delta^{(1)}(x) \tag{C.23}$$

is found to be

$$K^{(1)}_{\delta,\mu}(x_1,x_0;\beta,c) = K^{(1)}_{\mu}(x_1,x_0;\beta) + \delta K^{(1)}_{\mu}(x_1,x_0;\beta,c), \tag{C.24}$$

with

$$\begin{aligned}\delta K^{(1)}_{\mu}(x_1,x_0;\beta,c) &= -\int_0^\infty du\, \mathrm{e}^{-u} K^{(1)}_{\mu}(|x_1|+|x_0|,-2u/c;\beta) \\ &\quad - \Theta(-c)\frac{c}{2}\mathrm{e}^{\frac{\hbar^2\beta c^2}{8\mu}}\mathrm{e}^{\frac{c}{2}(|x_1|+|x_0|)} \\ &= -K^{(1)}_{\mu}(x_1+x_0,0;\beta)\times\tilde{s}\, g_+(\tilde{x}_1+\tilde{x}_2+\tilde{s}),\end{aligned} \tag{C.25}$$

with $\tilde{s} = c\lambda_T(\mu)/4\pi$. This gives the relation between the s-wave (attractive) interaction correction in 3D and the interaction correction in 1D as

$$\delta K^{(1)}_{\mu,0}(r_1,r_0;\beta,a_\mathrm{s}) = 2\left[\delta K^{(1)}_{\mu}(r_1,r_0;\beta,-2/a_\mathrm{s}) - \delta K^{(1)}_{\mu}(r_1,r_0;\beta,\infty)\right]. \tag{C.26}$$

D. Inverse Laplace transform of special functions

This appendix derives the inverse Laplace transformations for the functions that appear in the QCE.

D.1. Function definitions

The following functions appear in the cluster expansions:

- $\mathrm{Fc}_n(s) = s^{-n}\mathrm{e}^s \operatorname{erfc}\left(\sqrt{s}\right)$,
- $\mathrm{G}_n^{(\eta,\nu)}(s) = \frac{2}{\sqrt{\pi}} s^{-n}\mathrm{e}^s \int_0^\infty dz\, \mathrm{e}^{-\left(\eta z+\sqrt{s}\right)^2} \operatorname{erf}(\nu z)$,
- $\mathrm{H}_n^{(\eta,\lambda,\mu)}(s) = \frac{2}{\sqrt{\pi}} s^{-n}\mathrm{e}^s \int_0^\infty dz\, \mathrm{e}^{-\left(\eta z+\sqrt{s}\right)^2} \operatorname{erf}(\lambda z) \operatorname{erf}(\mu z)$.

The parameter η could be any real number, but its absolute value can be absorbed into ν, λ, and μ by substitution, such that one only has to perform the calculations for $\eta = \pm 1$. The above functions cannot be further simplified. However, their inverse Laplace transform can be given in terms of elementary functions.

D.2. Laplace transform identities and recursive formula

The following identities for the two-sided (inverse) Laplace transform of a function $F(s)$ are useful

- $\mathcal{L}_s^{-1}\left[F^{(n)}(s)\right](t) = (-t)^n \mathcal{L}_s^{-1}\left[F(s)\right](t)$,
- $\mathcal{L}_s^{-1}\left[\mathrm{e}^{\alpha s}F(s)\right](t) = \mathcal{L}_s^{-1}\left[F(s)\right](t+\alpha)$,
- $\mathcal{L}_s^{-1}\left[F(\alpha s)\right](t) = \frac{1}{|\alpha|}\mathcal{L}_s^{-1}\left[F(x)\right]\left(\frac{t}{\alpha}\right)$.

Here, $F^{(n)}(s)$ denotes the nth derivative with respect to s. An useful explicit identity for the inverse Laplace transform for rational exponents of s can be given as

$$\mathcal{L}_s^{-1}\left[s^{-n}\right](t) = \frac{t^{n-1}}{\Gamma(n)}, \qquad n > 0. \tag{D.1}$$

There is another, nonstandard identity that is used in the following at several stages. Consider any function of the form

$$F_n(s) = s^{-n} F_0(s), \quad n > 0. \tag{D.2}$$

Then one easily finds the recursion

$$F_{n+1}(s) = \frac{1}{n}\left(-F_n'(s) + s^{-n} F_0'(s)\right) \equiv \frac{1}{n}\left(-F_n'(x) + F_n^\bullet(s)\right), \tag{D.3}$$

introducing the definition

$$F_n^\bullet(s) \equiv s^{-n} \frac{\partial}{\partial s}\left[s^n F_n(s)\right]. \tag{D.4}$$

The recursion relation (D.3) is solved by

$$F_n(s) = \frac{1}{\Gamma(n)} \left\{ \Gamma(\gamma) \left[\left(-\frac{d}{ds}\right)^{n-\gamma} F_\gamma(s) \right] + \sum_{l=\gamma}^{n-1} \Gamma(l) \left[\left(-\frac{d}{ds}\right)^{n-l-1} F_l^\bullet(s) \right] \right\}, \tag{D.5}$$

where the sum runs over real numbers in steps of one and

$$\gamma = n + 1 - \lceil n \rceil = \begin{cases} 1, & n \in \mathbb{N}, \\ n - \lfloor n \rfloor, & n \notin \mathbb{N}. \end{cases} \tag{D.6}$$

Here, $\lceil \cdot \rceil$ and $\lfloor \cdot \rfloor$ are the ceiling and floor functions, respectively. If the inverse Laplace transform of the functions are denoted by their lower case symbols, this is translated into

$$f_n(t) = \frac{1}{\Gamma(n)} \left\{ \Gamma(\gamma) t^{n-\gamma} f_\gamma(t) + \sum_{l=\gamma}^{n-1} \Gamma(l) t^{n-l-1} f_l^\bullet(t) \right\} \tag{D.7}$$

or, written as a sum over integer numbers,

$$f_n(t) = \frac{1}{\Gamma(n)} \left\{ \Gamma(\gamma) t^{n-\gamma} f_\gamma(t) + \sum_{k=1}^{n-\gamma} \Gamma(n-k) t^{k-1} f_{n-k}^\bullet(t) \right\}. \tag{D.8}$$

This identity is useful if the inverse Laplace transforms $f_n^\bullet(t)$ of the functions $F_n^\bullet(s)$ are known. Then the inverse Laplace transform $f_n(t)$ is expressed only in terms of known functions and the single function $f_\gamma(t)$. In the QCE only $\gamma = 1$ and $\gamma = 1/2$ are relevant, corresponding to integer and half integer values of n.

D.3. Calculation of the inverse Laplace transforms

The steps for calculation the inverse Laplace transforms are the same for all the calculations. First, for each function, one defines the related function (F_n standing for Fc_n / G_n / H_n)

$$\tilde{F}_n(\cdot) = \mathrm{e}^{-s} F_n(\cdot) \tag{D.9}$$

that comes without the factor e^s. Then, equation (D.8) is used for those functions. Finally, the result is re-expressed in terms of the inverse Laplace transforms of the original functions.

D.3.1. The function Fc_n

The function Fc_n has been treated already in [221]. However, with the definitions above one can directly give the result here and the steps are thus repeated here to show the general line of calculation. The function $\tilde{\mathrm{F}}\mathrm{c}_n$ satisfies

$$\tilde{\mathrm{F}}\mathrm{c}_l^{\bullet}(s) = s^{-l}\frac{\partial}{\partial s}\operatorname{erfc}(\sqrt{s}) = \frac{1}{\sqrt{\pi}}s^{-l-\frac{1}{2}}\mathrm{e}^{-s}. \tag{D.10}$$

The inverse Laplace transform is thus

$$\tilde{\mathrm{f}}\mathrm{c}_l^{\bullet}(t) = \mathcal{L}_s^{-1}\left[\tilde{\mathrm{F}}\mathrm{c}_l^{\bullet}(s)\right](t) = -\frac{1}{\sqrt{\pi}}\mathcal{L}_s^{-1}\left[s^{-l-\frac{1}{2}}\right](t-1) = -\frac{\Theta(t-1)}{\sqrt{\pi}}\frac{(x-1)^{l-\frac{1}{2}}}{\Gamma\left(l+\frac{1}{2}\right)} \tag{D.11}$$

and the inverse Laplace transform $\tilde{\mathrm{f}}\mathrm{c}_n(\epsilon)$ of $\tilde{\mathrm{F}}\mathrm{c}_n(s)$ is given by

$$\tilde{\mathrm{f}}\mathrm{c}_n(t) = \mathcal{L}_s^{-1}\left[\tilde{\mathrm{F}}\mathrm{c}_n(s)\right](t) \tag{D.12}$$

$$= \frac{1}{\Gamma(n)}\left\{\Gamma(\gamma)t^{n-\gamma}\,\tilde{\mathrm{f}}\mathrm{c}_\gamma(t) + \sum_{k=1}^{n-\gamma}\Gamma(n-k)t^{k-1}\,\tilde{\mathrm{f}}\mathrm{c}_{n-k}^{\bullet}(t)\right\}. \tag{D.13}$$

Finally, the inverse Laplace transform of $\mathrm{Fc}_n(s)$ is given by

$$\begin{aligned}\mathrm{fc}_n(\epsilon) &= \mathcal{L}_s^{-1}\left[\mathrm{e}^s\,\tilde{\mathrm{F}}\mathrm{c}_n(s)\right](\epsilon) = \mathcal{L}_s^{-1}\left[\tilde{\mathrm{F}}\mathrm{c}_n(s)\right](\epsilon+1)\\ &= \frac{1}{\Gamma(n)}\left\{\Gamma(\gamma)(\epsilon+1)^{n-\gamma}\,\mathrm{fc}_\gamma(\epsilon) + \sum_{k=1}^{n-\gamma}\Gamma(n-k)(\epsilon+1)^{k-1}\,\tilde{\mathrm{f}}\mathrm{c}_{n-k}^{\bullet}(\epsilon+1)\right\}\\ &= \frac{1}{\Gamma(n)}\left\{\Gamma(\gamma)(\epsilon+1)^{n-\gamma}\,\mathrm{fc}_\gamma(\epsilon) - \frac{\Theta(\epsilon)}{\sqrt{\pi}}\sum_{k=1}^{n-\gamma}\frac{\Gamma(n-k)}{\Gamma\left(n-k+\frac{1}{2}\right)}(\epsilon+1)^{k-1}\epsilon^{n-k-\frac{1}{2}}\right\}.\end{aligned} \tag{D.14}$$

For (half) integer n the function fc_γ is given by

$$\mathrm{fc}_{\frac{1}{2}}(\epsilon) = \frac{1}{\sqrt{\pi}}\frac{\Theta(\epsilon)}{\sqrt{\epsilon+1}}, \qquad \mathrm{fc}_1(\epsilon) = \frac{2}{\pi}\arctan(\sqrt{\epsilon})\Theta(\epsilon). \tag{D.15}$$

D.3.2. The function G_n

Let us first identify

$$\mathrm{G}_n^{(+1,\nu)}(s) \equiv \mathrm{G}_n^{(\nu)}(s) \tag{D.16}$$

and start with the inverse Laplace transform of this function. As the steps are identical to the steps for $\mathrm{Fc}_n(s)$, only the results are presented. The function $\mathrm{G}_n^{(\nu)}(s)$ satisfies

$$\mathrm{e}^s\left[\mathrm{e}^{-s}\,\mathrm{G}_n^{(\nu)}(s)\right]^{\bullet} = -\frac{1}{\sqrt{\pi}}\frac{\nu}{1+\nu^2}\,\mathrm{Fc}_{n+\frac{1}{2}}\left(\frac{s}{1+\nu^2}\right). \tag{D.17}$$

With this one can perform the same steps as above to find

$$\mathrm{g}_n^{(\nu)}(\epsilon) = \frac{1}{\Gamma(n)}\Bigg\{\Gamma(\gamma)(\epsilon+1)^{n-\gamma}\,\mathrm{g}_\gamma(\nu,\epsilon) - \frac{\nu}{\sqrt{\pi}}\sum_{k=1}^{n-\gamma}\Gamma(n-k)(\epsilon+1)^{k-1}\frac{\mathrm{fc}_{n-k+\frac{1}{2}}\left((1+\nu^2)\epsilon\right)}{(1+\nu^2)^{n-k}}\Bigg\}, \tag{D.18}$$

with

$$\mathrm{g}_\gamma^{(\nu)}(\epsilon) = \begin{cases} \frac{1}{\sqrt{\pi}}\frac{\Theta(\epsilon)}{\sqrt{\epsilon+1}} \times \frac{2}{\pi}\arctan\left(\nu\sqrt{\frac{\epsilon}{\epsilon+1}}\right), & \gamma = \frac{1}{2}, \\ \frac{2}{\pi}\left[\arctan(\nu) - \arctan\left(\frac{\nu}{\sqrt{1+(1+\nu^2)\epsilon}}\right)\right]\Theta(\epsilon), & \gamma = 1. \end{cases} \tag{D.19}$$

For the case $\eta = -1$ one finds

$$\mathrm{G}_n^{(-1,\nu)}(s) = \mathrm{G}_n^{(\nu)} + 2\mathrm{e}^s s^{-n}\,\mathrm{erf}\left(\sqrt{\frac{\nu^2 s}{1+\nu^2}}\right) \tag{D.20}$$

$$= \mathrm{G}_n^{(\nu)} + 2\mathrm{e}^s s^{-n} - 2\mathrm{e}^{\frac{s}{1+\nu^2}}\left(\frac{\nu^2}{1+\nu^2}\right)^n \mathrm{Fc}_n\left(\frac{\nu^2 s}{1+\nu^2}\right) \tag{D.21}$$

leading to the general result

$$\mathrm{g}_n^{(\eta,\nu)}(\epsilon) = g_n^{(\nu)}(\epsilon) + 2\Theta(-\eta)\left\{\frac{\Theta(\epsilon+1)}{\Gamma(n)}(\epsilon+1)^{n-1} - \left(\frac{\nu^2}{1+\nu^2}\right)^{n-1}\mathrm{fc}_n\left(\frac{(1+\nu^2)\epsilon+1}{\nu^2}\right)\right\}. \tag{D.22}$$

Note that the last term is not defined for $\nu = 0$, but in this case one has $g_n^{(\eta,\nu)}(\epsilon) = 0$ by definition.

D.3.3. The function H_n

The function $\mathrm{H}_n^{(\eta,\lambda,\mu)}(s)$ can be either treated directly for both η by using

$$\mathrm{e}^s\left[\mathrm{e}^{-s}\,\mathrm{H}_n^{(\eta,\lambda,\mu)}(s)\right]^\bullet = -\frac{\eta}{\sqrt{\pi}}\frac{\lambda}{(1+\lambda^2)^{n+1}}\,\mathrm{G}_{n+\frac{1}{2}}^{(\eta,\mu/\sqrt{1+\lambda^2})}\left(\frac{s}{1+\lambda^2}\right) + [\lambda \leftrightarrow \mu], \tag{D.23}$$

however, it should be computationally cheaper to represent it directly in terms of the known functions and

$$\mathrm{H}_n^{(+1,\lambda,\mu)}(s) \equiv \mathrm{H}_n^{(\lambda,\mu)}(s). \tag{D.24}$$

This yields after a few pages of calculation

$$\mathrm{H}_n^{(\eta,\lambda,\mu)}(s) = \eta\,\mathrm{H}_n^{(\lambda,\mu)}(s) + 2\theta(-\eta)\left[\mathrm{e}^s s^{-n} + D_n^{(\lambda,\mu)}(s) + D_n^{(\mu,\lambda)}(s)\right], \tag{D.25}$$

with

$$D_n^{(\lambda,\mu)}(s) = \left(\frac{\lambda^2+\mu^2}{1+\lambda^2+\mu^2}\right)^n \mathrm{e}^{\frac{s}{1+\lambda^2+\mu^2}}\, \mathrm{G}_n^{(\frac{\mu}{\lambda}\sqrt{1+\lambda^2+\mu^2})}\left(\frac{(\lambda^2+\mu^2)s}{1+\lambda^2+\mu^2}\right) - \left(\frac{\lambda^2}{1+\lambda^2}\right)^n \mathrm{e}^{\frac{s}{1+\lambda^2}}\, \mathrm{Fc}\left(\frac{\lambda^2 s}{1+\lambda^2}\right) \tag{D.26}$$

The inverse Laplace transform for $\mathrm{H}_n^{(\lambda,\mu)}(s)$ yields

$$\mathrm{h}_n^{(\lambda,\mu)}(\epsilon) = \bar{\mathrm{h}}_n^{(\lambda,\mu)}(\epsilon) + \bar{\mathrm{h}}_n^{(\mu,\lambda)}(\epsilon) \tag{D.27}$$

as the symmetric combination of

$$\bar{\mathrm{h}}_n^{(\lambda,\mu)}(\epsilon) = \frac{1}{\Gamma(n)}\Bigg\{\Gamma(\gamma)(\epsilon+1)^{n-\gamma}\,\bar{\mathrm{h}}_\gamma^{(\lambda,\mu)}(\epsilon) - \frac{\lambda}{\sqrt{\pi}}\sum_{k=1}^{n-\gamma}\Gamma(n-k)(\epsilon+1)^{k-1}\frac{\mathrm{g}_{n-k+\frac{1}{2}}^{(\mu/\sqrt{1+\lambda^2})}\left((1+\lambda^2)\epsilon\right)}{(1+\lambda^2)^{n-k}}\Bigg\}. \tag{D.28}$$

The function $\bar{\mathrm{h}}_\gamma^{(\lambda,\mu)}(\epsilon)$ has only been calculated for $\gamma = 1/2$ so far, yielding

$$\bar{\mathrm{h}}_{\frac{1}{2}}^{(\lambda,\mu)}(\epsilon) = \frac{\Theta(\epsilon)}{\sqrt{\pi}\sqrt{\epsilon+1}} \times \frac{2}{\pi}\left[\arctan\left(\frac{\mu}{\lambda}\right) - \arctan\left(\frac{\mu}{\lambda}\sqrt{\frac{1+\epsilon}{1+(1+\lambda^2+\mu^2)\epsilon}}\right)\right]. \tag{D.29}$$

Finally, the inverse Laplace transform of the function $D_n^{(\lambda,\mu)}(s)$ is given by

$$d_n^{(\lambda,\mu)}(\epsilon) = \left(\frac{\lambda^2+\mu^2}{1+\lambda^2+\mu^2}\right)^{n-1} \mathrm{g}_n^{\left(\frac{\mu}{\lambda}\sqrt{1+\lambda^2+\mu^2}\right)}\left(\frac{1+(1+\lambda^2+\mu^2)\epsilon}{\lambda^2+\mu^2}\right) - \left(\frac{\lambda^2}{1+\lambda^2}\right)^{n-1} \mathrm{fc}_n\left(\frac{1+(1+\lambda^2)\epsilon}{\lambda^2}\right). \tag{D.30}$$

Thus, putting everything together, the inverse Laplace transform of $\mathrm{H}_n^{(\eta,\lambda,\mu)}(s)$ is given by

$$\mathrm{h}_n^{(\eta,\lambda,\mu)} = \eta\left[\bar{\mathrm{h}}_n^{(\lambda,\mu)}(\epsilon) + \bar{\mathrm{h}}_n^{(\mu,\lambda)}(\epsilon)\right] + 2\Theta(-\eta)\left[\frac{\Theta(\epsilon+1)}{\Gamma(n)}(\epsilon+1)^{n-1} + d_n^{(\lambda,\mu)}(\epsilon) + d_n^{(\mu,\lambda)}(\epsilon)\right]. \tag{D.31}$$

D.3.4. Other transforms

One can also find the inverse Laplace transform of the square of the functions Fc, relevant for the QCE(2). Defining

$$\mathrm{Fc}_{n,2}(s) \equiv s^{-n}\,\mathrm{Fc}_0^2(s), \tag{D.32}$$

one obtains with the same methods as above for its inverse Laplace transform

$$\mathrm{fc}_{n,2}(\epsilon) = \frac{1}{\Gamma(n)} \left\{ \Gamma(\gamma)(\epsilon+2)^{n-\gamma}\, \mathrm{fc}_{\gamma,2}(\epsilon) - \frac{2}{\sqrt{\pi}} \sum_{k=1}^{n-\gamma} \Gamma(n-k)(\epsilon+2)^{k-1}\, \mathrm{fc}_{n-k+\frac{1}{2}}(\epsilon) \right\}, \tag{D.33}$$

with the starting functions for half integer and integer n being

$$\mathrm{fc}_{\gamma,2}(\epsilon) = \begin{cases} \left[1 - \frac{4}{\pi} \arctan\left(\sqrt{\epsilon+1}\right)\right] \Theta(\epsilon) & \gamma = 1, \\ \frac{\Theta(\epsilon)}{\sqrt{\pi}\sqrt{\epsilon+2}} \times \frac{2}{\pi} \arctan\left(\sqrt{\epsilon(\epsilon+2)}\right) & \gamma = \frac{1}{2}. \end{cases} \tag{D.34}$$

These starting functions can be found by convolution of the functions fc_γ with each other. The same can be done for arbitrary k for the functions $\mathrm{Fc}_n^{(k)}$ defined analogously, relating the powers k to lower powers $k-1$ recursively, with the only complication being in the starting functions, that might not be closed form expressions but have to be calculated numerically.

D.4. Application to the cluster expansion

D.4.1. QCE(1)

As the inter- and intra-cycle diagrams have the same value, they do not have to be calculated separately. The coefficient functions $g_{l,\pm}^{(N,d)}$, Eq. (1.236), involve functions

$$b_\nu^{(k)}(\epsilon) = \mathcal{L}_s^{-1}\left[s^{-k-1} a_\nu(s)\right](\epsilon), \qquad k = \frac{ld}{2}. \tag{D.35}$$

By using the relations derived above one directly obtains

$$\begin{aligned} b_\nu^{(k)}(\epsilon) = {} & \left[-\frac{1}{\pi} \frac{\nu}{1+\nu^2} \frac{\epsilon^k}{\Gamma(k+1)} \pm \frac{\eta}{\sqrt{\pi}} \frac{\nu^2}{\sqrt{1+\nu^2}} \frac{\epsilon^{k-\frac{1}{2}}}{\Gamma\left(k+\frac{1}{2}\right)} \right] \Theta(\epsilon) + \frac{\eta\nu}{\sqrt{\pi}}\, \mathrm{fc}_{k+\frac{1}{2}}^{(\eta)}(\epsilon) \\ & - \frac{1}{2}\left(1+\nu^2\right)^k \left[\mathrm{g}_{k+1}^{(\eta,\nu)}\left(\frac{\epsilon}{1+\nu^2}\right) \pm \mathrm{fc}_{k+1}^{(\eta)}\left(\frac{\epsilon}{1+\nu^2}\right) \right] \\ & - \nu^2\left(1+\nu^2\right)^{k-1} \left[\mathrm{g}_{k}^{(\eta,\nu)}\left(\frac{\epsilon}{1+\nu^2}\right) \pm \mathrm{fc}_{k}^{(\eta)}\left(\frac{\epsilon}{1+\nu^2}\right) \right], \end{aligned} \tag{D.36}$$

where the upper sign, together with $\eta = 1$ represents the repulsive case, and the lower sign represents the attractive case above ($\eta = 1$) and below ($\eta = -1$) the resonance. For simplicity, the new function $\mathrm{fc}_n^{(\eta)}$ has been defined as

$$\mathrm{fc}_n^{(\eta)}(\epsilon) = \eta\, \mathrm{fc}_n(\epsilon) + 2\Theta(-\eta) \frac{(\epsilon+1)^{n-1}}{\Gamma(n)} \Theta(\epsilon+1). \tag{D.37}$$

D.4.2. QCE(2) for 4 particles

The QCE(2) parts of the functions $\Delta z_l^{(N,d)}$ in 1.5.4 that are not trivially given by QCE(1) diagrams are

$$\delta z_2^{(4,d)}(s) = 32 \times 4^{-\frac{d}{2}} a_0^2(s), \tag{D.38}$$

$$\delta z_1^{(4,d)}(s) = -32 \times 4^{-\frac{d}{2}} \left[4\, \mathrm{G}_0^{(\eta,\sqrt{2})}(4s) - 4\, \mathrm{H}_0^{(\eta,1,\sqrt{2})}(4s) \right]. \tag{D.39}$$

They contribute to the functions $g_l^{(N,d)}$ as

$$\delta g_2^{(4,d)}(\epsilon) = 8\epsilon^{-d} \left\{ \mathrm{fc}_{d+1,2}(\epsilon) + \Theta(-\eta) \left[\eta\, \mathrm{fc}_{d+1}(\epsilon+1) + \frac{(\epsilon+2)^d}{\Gamma(d+1)} \Theta(\epsilon+2) \right] \right\} \tag{D.40}$$

$$\delta g_1^{(4,d)}(\epsilon) = -128\epsilon^{-\frac{d}{2}} \left[\mathrm{g}_{\frac{d}{2}+1}^{(\eta,\sqrt{2})}\left(\frac{\epsilon}{4}\right) - \mathrm{h}_{\frac{d}{2}+1}^{(\eta,1,\sqrt{2})}\left(\frac{\epsilon}{4}\right) \right], \tag{D.41}$$

in terms of the functions defined in the previous sections.

E. Five-mode approximation

E.1. Classical Hamiltonian function

The classical Hamiltonian function in five mode approximation can be explicitly written in terms of the variables n_k, θ_k as

$$
\begin{aligned}
H_{\mathrm{cl}} = & \sum_{k=-2}^{2} k^2 n_k + \frac{\alpha}{4} \sum_{k=-2}^{2} n_k^2 - \frac{N(N-5)\alpha}{2} - \frac{25\alpha}{8} - 5 \\
& -\alpha \Big[\\
& \quad + n_{-1}\sqrt{n_{-2}n_0}\cos(\theta_{-2} + \theta_0 - 2\theta_{-1}) + n_0\sqrt{n_{-2}n_2}\cos(\theta_{-2} + \theta_2 - 2\theta_0) \\
& \quad + n_0\sqrt{n_{-1}n_1}\cos(\theta_{-1} + \theta_1 - 2\theta_0) + n_1\sqrt{n_0 n_2}\cos(\theta_0 + \theta_2 - 2\theta_1) \\
& \quad + 2\sqrt{n_{-1}n_1 n_0 n_2}\cos(\theta_0 + \theta_1 - \theta_2 - \theta_{-1}) \\
& \quad + 2\sqrt{n_{-1}n_1 n_{-2}n_2}\cos(\theta_1 + \theta_{-1} - \theta_2 - \theta_{-2}) \\
& \quad + 2\sqrt{n_{-1}n_1 n_0 n_{-2}}\cos(\theta_{-1} + \theta_0 - \theta_1 - \theta_{-2}) \\
& \Big]
\end{aligned}
\tag{E.1}
$$

By using the coordinate transformation given in the main text one obtains

$$
\begin{aligned}
\omega = & 1 - z + 6z_2 + \frac{\tilde{\alpha}}{2}\left[\frac{z^2-1}{2} + z_2^2 + l_2^2 + \left(\frac{1-z-2z_2}{2}\right)^2 + \left(\frac{l-4l_2}{2}\right)^2\right] \\
& - \frac{\tilde{\alpha}}{2}\Bigg\{ [1-z-2z_2-(l-4l_2)]\sqrt{z(z_2-l_2)}\cos\left(\varphi + \frac{\varphi_{z_2}-\varphi_{l_2}}{2}\right) \\
& + [1-z-2z_2+(l-4l_2)]\sqrt{z(z_2+l_2)}\cos\left(\varphi + \frac{\varphi_{z_2}+\varphi_{l_2}}{2}\right) \\
& + 2z\sqrt{z_2^2+l_2^2}\cos(2\varphi - \varphi_{z_2}) \\
& + \sqrt{(1-z-2z_2)^2 - (l-4l_2)^2}\times \\
& \quad \Bigg[z\cos(2\varphi) + 2\sqrt{z_2^2+l_2^2}\cos(\varphi_{z_2}) \\
& \quad + 2\sqrt{z(z_2-l2)}\cos\left(\varphi - \frac{\varphi_{z_2}-\varphi_{l_2}}{2}\right) + 2\sqrt{z(z_2+l_2)}\cos\left(\varphi - \frac{\varphi_{z_2}+\varphi_{l_2}}{2}\right)\Bigg]\Bigg\}
\end{aligned}
\tag{E.2}
$$

Setting $l = l_2 = \varphi_{l_2} = 0$ yields

$$\begin{aligned}\omega = 1 - z + 6z_2 - \frac{\tilde{\alpha}}{4}\left[1 - z^2 - 2z_2^2 - \frac{1}{2}(1 - z - 2z_2)^2\right] - \tilde{\alpha} z z_2 \cos(2\varphi - \varphi_{z_2}) \\ - \tilde{\alpha}(1 - z - 2z_2)\Big[\frac{z}{2}\cos(2\varphi) + z_2\cos(\varphi_{z_2}) \\ + \sqrt{z z_2}\left(\cos(\varphi + \varphi_{z_2}/2) + 2\cos(\varphi - \varphi_{z_2}/2)\right)\Big]\end{aligned} \tag{E.3}$$

for the effective Hamiltonian in the high-symmetry surface discussed in the main text.

E.2. Basis characterization for numerical diagonalization

The basis in the five-mode approximation can become extremely large even when the conservation of particle number N and momentum K is taken into account. Therefore it is very useful to have a direct prescription for building the basis that does not produce any additional Fock states, especially when one can apply truncations on the fly. Moreover, when one wants to calculate only a certain block of the Hamiltonian or another operator, this prescription can speed up the calculation enormously. Two such prescriptions have been developed that are equivalent, but lead to different ordering and allow for direct truncation in different ways. It is assumed that $K \geq 0$, as the basis for $K < 0$ can be obtained from this case by changing $n_k \mapsto n_{-k}$ for all $-2 \leq k \leq 2$.

The ordering $n_2 \to n_{-2} \to n_1$

This prescription is very useful for direct hierarchical truncations in the modes $n_{\pm 2}$, followed by n_1. Any allowed state is obtained by successively choosing

$$\max\{0, K - N\} \leq n_2 \leq \left\lfloor \frac{N + \frac{K}{2}}{2} \right\rfloor, \tag{E.4}$$

$$\max\{0, 3n_2 - K - N\} \leq n_{-2} \leq \left\lfloor \frac{N - K + n_2}{3} \right\rfloor, \tag{E.5}$$

$$\max\{0, K - 2(n_2 - n_{-2})\} \leq n_1 \leq \left\lfloor \frac{N + K + n_{-2} - 3n_2}{2} \right\rfloor. \tag{E.6}$$

The ordering $n_0 \to n_2 \to n_1/n_{-2}$

This prescription is useful in the calculation of individual blocks of constant n_0. Define $n = N - n_0$, then, for $K > 0$ one has to successively choose

$$\left\lceil \frac{K}{2} \right\rceil \leq n \leq N, \tag{E.7}$$

$$\max\left\{\delta_{n,L+1}, K-n\right\} \leq n_2 \leq \left\lfloor \frac{n+\frac{K}{2}}{2} \right\rfloor - \delta_{2(n-1),K}, \tag{E.8}$$

$$\max\left\{0, \left\lceil \frac{n+K-3n_2}{2} \right\rceil\right\} \leq n_1 \leq \left\lfloor \frac{2n+K-4n_2}{3} \right\rfloor. \tag{E.9}$$

Here, $\delta_{a,b}$ is the Kronecker delta. These rules are also valid for $K = 0$ if the case $n = 1$ is excluded in the first line. The last line can be replaced by

$$\max\left\{\gamma, 3n_2 - K - n\right\} \leq n_{-2} \leq 2\left\lfloor \frac{n-K+n_2}{6} - \frac{\gamma}{2} \right\rfloor + \gamma, \tag{E.10}$$

where n_{-2} has to increase in steps of two and

$$\gamma = n + K + n_2 \pmod 2 \tag{E.11}$$

takes the values 0 and 1.

As one might expect, the proofs of these relations are tedious, involving many different cases. The proof will be omitted here, but can be performed by writing down the normal-ordered generators of all particle and momentum conserving operators that are not diagonal (they are given by products of four bosonic operators) and then applies them to an allowed state to find all possible states.

Bibliography

[1] R. Feynman, *The Character of Physical Law* (The MIT Press, London, 1965).

[2] M. C. Gutzwiller, *Chaos in Classical and Quantum Mechanics*, Interdisciplinary Applied Mathematics (Springer, New York, 1990).

[3] V. E. Korepin, N. M. Bogoliubov, and A. G. Izergin, *Quantum Inverse Scattering Method and Correlation Functions*, Cambridge Monographs on Mathematical Physics (Cambridge University Press, Cambridge, 1997).

[4] M. Born and R. Oppenheimer, "Zur Quantentheorie der Molekeln", Ann. Phys. **389**, 457 (1927).

[5] J. C. Slater, *Quantum Theory of Molecules and Solids*, *International Series in pure and applied Phyiscs*, volume 1 (McGraw-Hill Book Company, New York, 1963).

[6] W. Nolting, *Fundamentals of Many-body Physics* (Springer-Verlag, Berlin, 2009).

[7] E. Lipparini, *Modern Many-Particle Physics* (World Scientific Publishing, Singapore, 2008), 2nd edition.

[8] J. W. Negele and H. Orland, *Quantum Many-Particle Systems*, Frontiers in Physics (Addison-Wesley, Redwood City, 1988).

[9] D. Cremer, "From configuration interaction to coupled cluster theory: The quadratic configuration interaction approach", WIREs Comput. Mol. Sci. **3**, 482 (2013).

[10] K. Capelle, "A bird's-eye view of density-functional theory", Braz. J. Phys. **36**, 1318 (2006).

[11] P. Hohenberg and W. Kohn, "Inhomogeneous Electron Gas", Phys. Rev. **136**, B864 (1964).

[12] J. Bardeen, L. N. Cooper, and J. R. Schrieffer, "Theory of Superconductivity", Phys. Rev. **108**, 1175 (1957).

[13] F. Dalfovo, S. Giorgini, L. P. Pitaevskii, and S. Stringari, "Theory of Bose-Einstein condensation in trapped gases", Rev. Mod. Phys. **71**, 463 (1999).

[14] N. P. Proukakis and B. Jackson, "Finite-temperature models of Bose–Einstein condensation", J. Phys. B **41**, 203002 (2008).

[15] A. L. Fetter, "Nonuniform states of an imperfect Bose gas", Ann. Phys. (New York) **70**, 67 (1972).

[16] R. Kanamoto, H. Saito, and M. Ueda, "Quantum phase transition in one-dimensional Bose-Einstein condensates with attractive interactions", Phys. Rev. A **67**, 013608 (2003).

[17] B. Hirshberg, V. Rizzi, and M. Parrinello, "Path integral molecular dynamics for bosons", PNAS **116**, 21445 (2019).

[18] F. Bruckmann and J. Wellnhofer, "Diagrammatic representation of scalar QCD and sign problem at nonzero chemical potential", Phys. Rev. D **97**, 014501 (2018).

[19] E. H. Lieb and W. Liniger, "Exact Analysis of an Interacting Bose Gas. I. The General Solution and the Ground State", Phys. Rev. **130**, 1605 (1963).

[20] J. B. McGuire, "Study of exactly soluble one-dimensional N-body problems", J. Math. Phys. **5**, 622 (1964).

[21] L. H. Thomas, "The Interaction Between a Neutron and a Proton and the Structure of H^3", Phys. Rev. **47**, 903 (1935).

[22] I. Bloch, J. Dalibard, and W. Zwerger, "Many-body physics with ultracold gases", Rev. Mod. Phys. **80**, 885 (2008).

[23] T. Langen, R. Geiger, and J. Schmiedmayer, "Ultracold Atoms Out of Equilibrium", Annu. Rev. Cond. Mat. Phys. **6**, 201 (2015).

[24] M. H. Anderson, J. R. Ensher, M. R. Matthews, C. E. Wieman, and E. A. Cornell, "Observation of Bose-Einstein Condensation in a Dilute Atomic Vapor", Science **269**, 198 (1995).

[25] R. G. Dall, A. G. Manning, S. S. Hodgman, W. RuGway, K. V. Kheruntsyan, and A. G. Truscott, "Ideal n-body correlations with massive particles", Nat. Phys. **9**, 341 (2013).

[26] A. N. Wenz, G. Zurn, S. Murmann, I. Brouzos, T. Lompe, and S. Jochim, "From Few to Many: Observing the Formation of a Fermi Sea One Atom at a Time", Science **342**, 457 (2013).

[27] P. M. Preiss, R. Ma, M. E. Tai, A. Lukin, M. Rispoli, P. Zupancic, Y. Lahini, R. Islam, and M. Greiner, "Strongly correlated quantum walks in optical lattices", Science **347**, 1229 (2015).

[28] S. Inouye, M. R. Andrews, J. M. H.-J. Stenger, D. M. Stamper-Kurn, and W. Ketterle, "Observation of Feshbach resonances in a Bose–Einstein condensate", Nature **392**, 151 (1998).

[29] C. Chin, R. Grimm, P. Julienne, and E. Tiesinga, "Feshbach resonances in ultracold gases", Rev. Mod. Phys. **82**, 1225 (2010).

[30] K. Henderson, C. Ryu, C. MacCormick, and M. G. Boshier, "Experimental demonstration of painting arbitrary and dynamic potentials for Bose-Einstein condensates", New J. Phys. **11**, 043030 (2009).

[31] F. Meinert, M. Knap, E. Kirilov, K. Jag-Lauber, M. B. Zvonarev, E. Demler, and H.-C. Nägerl, "Bloch oscillations in the absence of a lattice", Science **356**, 945 (2017).

[32] T. Kraemer, M. Mark, P. Waldburger, J. G. Danzl, C. Chin, B. Engeser, A. D. Lange, K. Pilch, A. Jaakkola, H.-C. Nägerl, and R. Grimm, "Evidence for Efimov quantum states in an ultracold gas of caesium atoms", Nature **440**, 315 (2006).

[33] P. Naidon and S. Endo, "Efimov physics: a review", Rep. Prog. Phys. **80**, 056001 (2017).

[34] C. H. Greene, P. Giannakeas, and J. Pérez-Ríos, "Universal few-body physics and cluster formation", Rev. Mod. Phys. **89** (2017).

[35] H. Moritz, T. Stöferle, M. Köhl, and T. Esslinger, "Exciting Collective Oscillations in a Trapped 1D Gas", Phys. Rev. Lett. **91**, 250402 (2003).

[36] T. Kinoshita, T. Wenger, and D. S. Weiss, "Observation of a One-Dimensional Tonks-Girardeau Gas", Science **305**, 1125 (2004).

[37] B. Paredes, A. Widera, V. Murg, O. Mandel, S. Foelling, I. Cirac, G. V. Shlyapnikov, T. W. Hansch, and I. Bloch, "Tonks-Girardeau gas of ultracold atoms in an optical lattice", Nature **429**, 277 (2004).

[38] T. Kinoshita, T. Wenger, and D. S. Weiss, "Local pair correlations in one-dimensional Bose Gases", Phys. Rev. Lett. **95**, 190406 (2005).

[39] M. Olshanii, "Atomic Scattering in the Presence of an External Confinement and a Gas of Impenetrable Bosons", Phys. Rev. Lett. **81**, 938 (1998).

[40] M. Brack and R. K. Bhaduri, *Semiclassical Physics*, Frontiers in Physics (Westview Press, Boulder, 2003).

[41] F. Haake, *Quantum Signatures of Chaos*, Springer Series in Synergetics (Springer-Verlag, Berlin, 2001), 2nd edition.

[42] A. M. Ozorio de Almeida, *Hamiltonian Systems: Chaos and Quantization*, Cambridge Monographs on Mathematical Physics (Cambridge University Press, Cambridge, 1988).

[43] E.-M. Graefe, M. Graney, and A. Rush, "Semiclassical quantization for a bosonic atom-molecule conversion system", Phys. Rev. A **92**, 012121 (2015).

[44] E. M. Graefe and H. J. Korsch, "Semiclassical quantization of an N-particle Bose-Hubbard model", Phys. Rev. A **76**, 032116 (2007).

[45] D. Wintgen, "Semiclassical path-integral quantization of nonintegrable Hamiltonian systems", Phys. Rev. Lett. **61**, 1803 (1988).

[46] M. Sieber and F. Steiner, "Quantization of chaos", Phys. Rev. Lett. **67**, 1941 (1991).

[47] G. Tanner, P. Scherer, E. B. Bogomolny, B. Eckhardt, and D. Wintgen, "Quantum eigenvalues from classical periodic orbits", Phys. Rev. Lett. **67**, 2410 (1991).

[48] D. Wintgen, K. Richter, and G. Tanner, "The semiclassical helium atom", Chaos **2**, 19 (1992).

[49] H.-J. Stöckmann, *Quantum Chaos* (Cambridge University Press, Cambridge, 1999).

[50] R. Balian and C. Bloch, "Distribution of Eigenfrequencies for the Wave Equation in a Finite Domain. I. Three-dimensional problem with smooth boundary surface", Ann. Phys. (NY) **60**, 401 (1970).

[51] M. Sieber, H. Primack, U. Smilansky, I. Ussishkin, and H. Schanz, "Semiclassical quantization of billiards with mixed boundary conditions", J. Phys. A **28**, 5041 (1995).

[52] Q. Hummel, J.-D. Urbina, and K. Richter, "The Weyl expansion for systems of independent identical particles", J. Phys. A **47**, 015101 (2013).

[53] M. J. Steel, M. K. Olsen, L. I. Plimak, P. D. Drummond, S. M. Tan, M. J. Collett, D. F. Walls, and R. Graham, "Dynamical quantum noise in trapped Bose-Einstein condensates", Phys. Rev. A **58**, 4824 (1998).

[54] A. Sinatra, C. Lobo, and Y. Castin, "The truncated Wigner method for Bose-condensed gases: limits of validity and applications", J. Phys. B: At. Mol. Opt. Phys. **35**, 3599 (2002).

[55] P. G. Silvestrov and C. W. J. Beenakker, "Ehrenfest times for classically chaotic systems", Phys. Rev. E **65**, 035208(R) (2002).

[56] S. Tomsovic, P. Schlagheck, D. Ullmo, J.-D. Urbina, and K. Richter, "Post-Ehrenfest many-body quantum interferences in ultracold atoms far out of equilibrium", Phys. Rev. A **97**, 061606 (2018).

[57] M. Sieber and K. Richter, "Correlations between periodic orbits and their role in spectral statistics", Phys. Scr. **2001**, 128 (2001).

[58] D. Ullmo, "Bohigas-Giannoni-Schmit conjecture", Scholarpedia **11**, 31721 (2016).

[59] F. Haake, S. Gnutzmann, and M. Kuś, *Quantum Signatures of Chaos*, Springer Series in Synergetics (Springer Nature Switzerland, Cham, 2018), 4th edition.

[60] Q. Hummel, J. D. Urbina, and K. Richter, "Partial Fermionization: Spectral Universality in 1D Repulsive Bose Gases", Phys. Rev. Lett. **122**, 240601 (2019).

[61] Q. Hummel, *Semiclassical Theory of Few- and Many-body Quantum Systems with Short-range Interactions*, Ph.D. thesis, Universität Regensburg (2018).

[62] K. Huang, *Statistical mechanics* (John Wiley & Sons, Hoboken, 1987), 2nd edition.

[63] W. T. Grandy, *Foundations of statistical mechanics* (D. Reidel, Dordrecht, 1987).

[64] B. Widom, "The Virial Series of the Ideal Bose-Einstein Gas", Physical Review **96**, 16 (1954).

[65] H. D. Ursell, "The evaluation of Gibbs' phase-integral for imperfect gases", Math. Proc. Cambridge Philos. Soc. **23**, 685 (1927).

[66] G. E. Uhlenbeck and E. Beth, "The Quantum Theory of The Non-Ideal Gas I. Deviations from The Classical Theory", Physica **3**, 729 (1936).

[67] E. Beth and G. E. Uhlenbeck, "The quantum theory of the non-ideal gas. II. Behaviour at low temperatures", Physica **4**, 915 (1937).

[68] T. D. Lee and C. N. Yang, "Many-Body Problem in Quantum Mechanics and Quantum Statistical Mechanics", Phys. Rev. **105**, 1119 (1957).

[69] A. J. F. Siegert and E. Teramoto, "Simplified Derivation of the Binary Collision Expansion and Its Connection with the Scattering Operator Expansion", Phys. Rev. **110**, 1232 (1958).

[70] T. D. Lee and C. N. Yang, "Many-Body Problem in Quantum Statistical Mechanics. I. General Formulation", Phys. Rev. **113**, 1165 (1959).

[71] F. Mohling and W. T. Grandy, "Quantum Statistics of Multicomponent Systems", J. Math. Phys. **6**, 348 (1965).

[72] A. Pais and G. E. Uhlenbeck, "On the Quantum Theory of the Third Virial Coefficient", Phys. Rev. **116**, 250 (1959).

[73] B. J. Baumgartl, "Second and third virial coefficient of a quantum gas from two-particle scattering amplitude", Z. Phys. **198**, 148 (1967).

[74] S. Y. Larsen and P. L. Mascheroni, "Quantum-Mechanical Third Virial Coefficient and Three-Body Phase Shifts", Phys. Rev. A **2**, 1018 (1970).

[75] P. L. Mascheroni, "Low-Temperature Behavior for the Quantum Virial Coefficients", Phys. Rev. Lett. **25**, 726 (1970).

[76] S. K. Adhikari and R. D. Amado, "Low-Temperature Behavior of the Quantum Cluster Coefficients", Phys. Rev. Lett. **27**, 485 (1971).

[77] P. Grüter and F. Laloë, "Ursell operators in statistical physics I: Generalizing the Beth Uhlenbeck formula", J. Phys. I **5**, 181 (1995).

[78] P. Grüter and F. Laloë, "Ursell Operators in Statistical Physics II: Microscopic Properties of a Dilute Quantum Gas", J. Phys. I **5**, 1255 (1995).

[79] P. Grüter, F. Laloë, A. E. Meyerovich, and W. Mullin, "Ursell Operators in Statistical Physics III: Thermodynamic Properties of Degenerate Gases", J. Phys. I **7**, 485 (1997).

[80] M. Holzmann, P. Grüter, and F. Laloë, "Bose-Einstein condensation in interacting gases", Eur. Phys. J. B **10**, 739 (1999).

[81] G. Baym, J.-P. Blaizot, M. Holzmann, F. Laloë, and D. Vautherin, "Bose-Einstein transition in a dilute interacting gas", Eur. Phys. J. B **24**, 107 (2001).

[82] J. N. Fuchs, M. Holzmann, and F. Laloë, "Ursell operators in statistical physics of dense systems: the role of high order operators and of exchange cycles", Eur. Phys. J. B **25**, 463 (2002).

[83] P. Borrmann and G. Franke, "Recursion formulas for quantum statistical partition functions", J. Chem. Phys. **98**, 2484 (1993).

[84] K. Wodkiewicz, "Fermi pseudopotential in arbitrary dimensions", Phys. Rev. A **43**, 68 (1991).

[85] Q. Hummel, J. D. Urbina, and K. Richter, "Canonical description of 1D few-body systems with short range interaction", (2016), `arXiv:1603.02775`.

[86] H. A. Bethe, "An attempt to calculate the number of energy levels of a heavy nucleus", Phys. Rev. **50**, 332 (1936).

[87] X.-J. Liu, H. Hu, and P. D. Drummond, "Virial Expansion for a Strongly Correlated Fermi Gas", Phys. Rev. Lett. **102**, 160401 (2009).

[88] H. Hu, X.-J. Liu, and P. D. Drummond, "Universal contact of strongly interacting fermions at finite temperatures", New J. Phys. **13**, 035007 (2011).

[89] Q. Hummel, J. D. Urbina, and K. Richter, "The Weyl expansion for systems of independent identical particles", J. Phys. A: Math. Theor. **47**, 015101 (2014).

[90] S. Y. Larsen, M. Lassaut, and A. Amaya-Tapia, "A generalized Uhlenbeck and Beth formula for the third cluster coefficient", Ann. Phys. **374**, 291 (2016).

[91] I. S. Gradshteyn and I. M. Ryzhik, *Table of Integrals, Series, and Products* (Elsevier, Burlington, 2007), 7th edition.

[92] E. H. Lieb, "Exact Analysis of an Interacting Bose Gas. II. The Excitation Spectrum", Phys. Rev. **130**, 1616 (1963).

[93] B. Geiger, Q. Hummel, J. D. Urbina, and K. Richter, "Nonlocal pair correlations in Lieb-Liniger gases: A unified nonperturbative approach from weak degeneracy to high temperatures", Phys. Rev. A **97**, 063612 (2018).

[94] M. Yasuda and F. Shimizu, "Observation of two-atom correlation of an ultracold neon atomic beam", Phys. Rev. Lett. **77**, 3090 (1996).

[95] A. Öttl, S. Ritter, M. Köhl, and T. Esslinger, "Correlations and counting statistics of an atom laser", Phys. Rev. Lett. **95**, 090404 (2005).

[96] M. Schellekens, R. Hoppeler, A. Perrin, J. Viana Gomez, D. Boiron, A. Aspect, and C. I. Westbrook, "Hanbury Brown Twiss Effect for Ultracold Quantum Gases", Science **310**, 648 (2005).

[97] T. Jeltes, J. M. McNamara, W. Hogervorst, W. Vassen, V. Krachmalnicoff, M. Schellekens, A. Perrin, H. Chang, D. Boiron, A. Aspect, and C. I. Westbrook, "Comparison of the Hanbury Brown–Twiss effect for bosons and fermions", Nature **445**, 402 (2007).

[98] S. Manz, R. Bücker, T. Betz, C. Koller, S. Hofferberth, I. E. Mazets, A. Imambekov, E. Demler, A. Perrin, J. Schmiedmayer, and T. Schumm, "Two-point density correlations of quasicondensates in free expansion", Phys. Rev. A **81**, 031610(R) (2010).

[99] A. G. Manning, S. S. Hodgman, R. G. Dall, M. T. Johnsson, and A. G. Truscott, "The Hanbury Brown-Twiss effect in a pulsed atom laser", Opt. Express **18**, 18712 (2010).

[100] S. S. Hodgman, R. G. Dall, A. G. Manning, K. G. H. Baldwin, and A. G. Truscott, "Direct Measurement of Long-Range Third-Order Coherence in Bose-Einstein Condensates", Science **331**, 1043 (2011).

[101] W. RuGway, A. G. Manning, S. S. Hodgman, R. G. Dall, A. G. Truscott, T. Lamberton, and K. V. Kheruntsyan, "Observation of transverse Bose-Einstein condensation via hanbury brown-twiss correlations", Phys. Rev. Lett. **111**, 093601 (2013).

[102] T. Schweigler, V. Kasper, S. Erne, I. Mazets, B. Rauer, F. Cataldini, T. Langen, T. Gasenzer, J. Berges, and J. Schmiedmayer, "Experimental characterization of a quantum many-body system via higher-order correlations", Nature **545**, 323 (2017).

[103] A. Vogler, R. Labouvie, F. Stubenrauch, G. Barontini, V. Guarrera, and H. Ott, "Thermodynamics of strongly correlated one-dimensional Bose gases", Phys. Rev. A **88**, 031603(R) (2013).

[104] E. Haller, M. Rabie, M. J. Mark, J. G. Danzl, R. Hart, K. Lauber, G. Pupillo, and H. C. Nägerl, "Three-body correlation functions and recombination rates for bosons in three dimensions and one dimension", Phys. Rev. Lett. **107**, 230404 (2011).

[105] T. J. Elliott and T. H. Johnson, "Nondestructive probing of means, variances, and correlations of ultracold-atomic-system densities via qubit impurities", Phys. Rev. A **93**, 043612 (2016).

[106] M. Streif, A. Buchleitner, D. Jaksch, and J. Mur-Petit, "Measuring correlations of cold-atom systems using multiple quantum probes", Phys. Rev. A **94**, 053634 (2016).

[107] H. Bernien, S. Schwartz, A. Keesling, H. Levine, A. Omran, H. Pichler, S. Choi, A. S. Zibrov, M. Endres, M. Greiner, V. Vuletić, and M. D. Lukin, "Probing many-body dynamics on a 51-atom quantum simulator", Nature **551**, 579 (2017).

[108] M. Gaudin, *The Bethe Wavefunction* (Cambridge University Press, Cambridge, 2014).

[109] J. C. Zill, T. M. Wright, K. V. Kheruntsyan, T. Gasenzer, and M. J. Davis, "A coordinate Bethe ansatz approach to the calculation of equilibrium and nonequilibrium correlations of the one-dimensional Bose gas", New J. Phys. **18**, 17 (2016).

[110] C.-N. Yang and C. Yang, "Thermodynamics of a One-Dimensional System of Bosons with Repulsive Delta-Function Interaction", J. Math. Phys. **10**, 1115 (1969).

[111] E. J. K. P. Nandani, R. A. Roemer, S. Tan, and X.-W. Guan, "Higher-order local and non-local correlations for 1D strongly interacting Bose gas", New J. Phys. **18**, 055014 (2016).

[112] P. Deuar, A. G. Sykes, D. M. Gangardt, M. J. Davis, P. D. Drummond, and K. V. Kheruntsyan, "Nonlocal pair correlations in the one-dimensional Bose gas at finite temperature", Phys. Rev. A **79**, 043619 (2009).

[113] C. A. Tracy and H. Widom, "The dynamics of the one-dimensional delta-function Bose gas", J. Phys. A: Math. Theor. **41**, 485204 (2008).

[114] V. Dotsenko, "Replica Bethe ansatz derivation of the Tracy–Widom distribution of the free energy fluctuations in one-dimensional directed polymers", J. Stat. Mech. **2010**, P07010 (2010).

[115] S. Prolhac and H. Spohn, "The propagator of the attractive delta-Bose gas in one dimension", J. Math. Phys. **52**, 122106 (2011).

[116] M. D. Hoffman, P. D. Javernick, A. C. Loheac, W. J. Porter, E. R. Anderson, and J. E. Drut, "Universality in one-dimensional fermions at finite temperature: Density, pressure, compressibility, and contact", Phys. Rev. A **91**, 033618 (2015).

[117] A. Y. Cherny and J. Brand, "Polarizability and dynamic structure factor of the one-dimensional Bose gas near the Tonks-Girardeau limit at finite temperatures", Phys. Rev. A **73**, 023612 (2006).

[118] K. V. Kheruntsyan, D. M. Gangardt, P. D. Drummond, and G. V. Shlyapnikov, "Pair Correlations in a Finite-Temperature 1D Bose Gas", Phys. Rev. Lett. **91**, 040403 (2003).

[119] M. Kormos, Y. Z. Chou, and A. Imambekov, "Exact three-body local correlations for excited states of the 1D Bose gas", Phys. Rev. Lett. **107**, 230405 (2011).

[120] B. Fang, A. Johnson, T. Roscilde, and I. Bouchoule, "Momentum-Space Correlations of a One-Dimensional Bose Gas", Phys. Rev. Lett. **116**, 050402 (2016).

[121] G. E. Astrakharchik, J. Boronat, J. Casulleras, and S. Giorgini, "Beyond the Tonks-Girardeau Gas: Strongly Correlated Regime in Quasi-One-Dimensional Bose Gases", Phys. Rev. Lett. **95**, 190407 (2005).

[122] E. Haller, M. Gustavsson, M. J. Mark, J. G. Danzl, R. Hart, G. Pupillo, and H.-C. Nägerl, "Realization of an Excited, Strongly Correlated Quantum Gas Phase", Science **325**, 1224 (2009).

[123] M. Girardeau, "Relationship between Systems of Impenetrable Bosons and Fermions in One Dimension", J. Math. Phys. **1**, 516 (1960).

[124] R. E. Crandall, "Exact propagator for reflectionless potentials", J. Phys. A: Math. Gen. **16**, 3005 (1983).

[125] B. A. Lippmann and J. Schwinger, "Variational Principles for Scattering Processes. I", Phys. Rev. **79**, 469 (1950).

[126] H. P. Baltes and E. R. Hilf, *Spectra of Finite Systems* (B-I Wissenschaftsverlag, Mannheim, 1976).

[127] E. Fermi, "Motion of neutrons in hydrogenous substances", Ricerca Scientifica **7**, 13 (1936).

[128] G. Breit, "The Scattering of Slow Neutrons by Bound Protons. I. Methods of Calculation", Phys. Rev. **71**, 215 (1947).

[129] K. Huang and C. N. Yang, "Quantum-mechanical many-body problem with hard-sphere interaction", Phys. Rev. **105**, 767 (1957).

[130] M. Randeria, J. M. Duan, and L. Y. Shieh, "Superconductivity in a two-dimensional Fermi gas: Evolution from Cooper pairing to Bose condensation", Phys. Rev. B **41**, 327 (1990).

[131] C. A. Sá De Melo, M. Randeria, and J. R. Engelbrecht, "Crossover from BCS to Bose superconductivity: Transition temperature and time-dependent Ginzburg-Landau theory", Phys. Rev. Lett. **71**, 3202 (1993).

[132] C. Grosche, "Path integrals for two- and three-dimensional δ-function perturbations", Ann. Phys. (NY) **506**, 283 (1994).

[133] M. Abramowitz and I. A. Stegun (eds.), *Handbook of mathematical functions* (Dover Publications, New York, 1965), 9th edition.

[134] S. Albeverio, F. Gesztesy, R. Hoegh-Krohn, and H. Holden, *Solvable models in quantum mechanics* (Springer Science & Business Media, New York, 1988).

[135] S. Scarlatti and A. Tea, "Derivation of the time-dependent propagator for the three-dimensional Schrödinger equation with one point interaction", J. Phys. A: Math. Gen. **23**, L1033 (1990).

[136] S. Y. Larsen, "Quantum-mechanical pair-correlation function of hard spheres", J. Chem. Phys. **48**, 1701 (1968).

[137] M. Holzmann and Y. Castin, "Pair correlation function of an inhomogeneous interacting Bose-Einstein condensate", Eur. Phys. J. D **7**, 425 (1999).

[138] M. Randeria and E. Taylor, "Crossover from Bardeen-Cooper-Schrieffer to Bose-Einstein Condensation and the Unitary Fermi Gas", Annu. Rev. Condens. Matter Phys. **5**, 209 (2014).

[139] S. Tan, "Energetics of a strongly correlated Fermi gas", Ann. Phys. **323**, 2952 (2008).

[140] S. Tan, "Large momentum part of a strongly correlated Fermi gas", Ann. Phys. **323**, 2971 (2008).

[141] S. Tan, "Generalized virial theorem and pressure relation for a strongly correlated Fermi gas", Ann. Phys. **323**, 2987 (2008).

[142] J. T. Stewart, J. P. Gaebler, T. E. Drake, and D. S. Jin, "Rification of universal relations in a strongly interacting fermi gas", Phys. Rev. Lett. **104** (2010).

[143] F. Werner and Y. Castin, "General relations for quantum gases in two and three dimensions: Two-component fermions", Phys. Rev. A **86**, 13626 (2012).

[144] S. Jensen, C. N. Gilbreth, and Y. Alhassid, "The contact in the unitary Fermi gas across the superfluid phase transition", (2019), `arXiv:1906.10117`.

[145] J. Levinsen and D. S. Petrov, "Atom-dimer and dimer-dimer scattering in fermionic mixtures near a narrow Feshbach resonance", Eur. Phys. J. D **65**, 67 (2011).

[146] G. Jaeger, "The Ehrenfest Classification of Phase Transitions: Introduction and Evolution", Arch. Hist. Exact Sci. **53**, 51 (1998).

[147] L. D. Landau and E. M. Lifschitz, *Lehrbuch der theoretischen Physik* (Akademie-Verlag, Berlin, 1970), 2nd edition.

[148] K. G. Wilson and J. Kogut, "The renormalization group and the ϵ expansion", Phys. Rep. **12**, 75 (1974).

[149] S.-k. Ma, *Modern Theory of Critical Phenomena*, Frontiers in Physics (W. A. Benjamin, Massachusetts, 1976).

[150] P. M. Chaikin and T. C. Lubensky, *Principles of condensed matter physics* (Cambridge University Press, Cambridge, 1995).

[151] T. Vojta, "Quantum phase transitions in electronic systems", Ann. Phys. **9**, 403 (2000).

[152] S. Sachdev, *Quantum Phase Transitions* (Cambridge University Press, Cambridge, 2011), 2nd edition.

[153] G. Dvali, D. Flassig, C. Gomez, A. Pritzel, and N. Wintergerst, "Scrambling in the black hole portrait", Phys. Rev. D **88**, 124041 (2013).

[154] H. J. Groenewold, "On the Principles of Elementary Quantum Mechanics", Physica **12**, 405 (1946).

[155] F. Bruckmann and J.-D. Urbina, "Rigorous construction of coherent state path integrals through dualization", (2018), `arXiv:1807.10462`.

[156] C. Gardiner and P. Zoller, *Quantum Noise: A Handbook of Markovian and Non-Markovian Quantum Stochastic Methods with Applications to Quantum Optics*, Springer Series in Synergetics (Springer, Berlin, 2004), 3rd edition.

[157] H.-W. Lee, "Theory and application of the quantum phase-space distribution functions", Phys. Rep. **259**, 147 (1995).

[158] M. Błaszak and Z. Domański, "Phase space quantum mechanics", Ann. Phys. **327**, 167 (2012).

[159] T. Curtright and C. Zachos, "Wigner trajectory characteristics in phase space and field theory", J. Phys. A: Math. Gen. **32**, 771 (1999).

[160] M. Tabor, *Chaos and Integrability in Nonlinear Dynamics: An Introduction* (John Wiley & Sons, Hoboken, 1989).

[161] T. Pudlik, H. Hennig, D. Witthaut, and D. K. Campbell, "Tunneling in the self-trapped regime of a two-well Bose-Einstein condensate", Phys. Rev. A **90**, 053610 (2014).

[162] M. V. Berry, "Regular and irregular semiclassical wavefunctions", J. Phys. A: Math. Gen. **10**, 2083 (1977).

[163] J. Gómez, K. Kar, V. Kota, R. Molina, A. Relaño, and J. Retamosa, "Many-body quantum chaos: Recent developments and applications to nuclei", Phys. Rep. **499**, 103 (2011).

[164] J. S. Cotler, G. Gur-Ari, M. Hanada, J. Polchinski, P. Saad, S. H. Shenker, D. Stanford, A. Streicher, and M. Tezuka, "Black holes and random matrices", J. High Energy Phys. **2017**, 118 (2017).

[165] A. I. Larkin and Y. N. Ovchinnikov, "Quasiclassical Method in the Theory of Superconductivity", J. Exp. Theor. Phys. **28**, 1200 (1969).

[166] E. B. Rozenbaum, S. Ganeshan, and V. Galitski, "Lyapunov Exponent and Out-of-Time-Ordered Correlator's Growth Rate in a Chaotic System", Phys. Rev. Lett. **118**, 086801 (2017).

[167] B. Swingle, "Unscrambling the physics of out-of-time-order correlators", Nat. Phys. **14**, 988 (2018).

[168] P. Gaspard, *Chaos, scattering and statistical mechanics* (Cambridge University Press, Cambridge, 1998).

[169] S. Tomsovic, "Complex saddle trajectories for multidimensional quantum wave packet and coherent state propagation: Application to a many-body system", Phys. Rev. E **98**, 023301 (2018).

[170] J. Maldacena, S. H. Shenker, and D. Stanford, "A bound on chaos", J. High Energy Phys. **2016**, 106 (2016).

[171] J. Maldacena and D. Stanford, "Remarks on the Sachdev-Ye-Kitaev model", Phys. Rev. D **94**, 106002 (2016).

[172] A. Bohrdt, C. B. Mendl, M. Endres, and M. Knap, "Scrambling and thermalization in a diffusive quantum many-body system", New J. Phys. **19**, 063001 (2017).

[173] R. Lewis-Swan, A. Safavi-Naini, J. Bollinger, and A. Rey, "Unifying scrambling, thermalization and entanglement through measurement of fidelity out-of-time-order correlators in the Dicke model", Nat. Commun. **10**, 1581 (2019).

[174] B. Kobrin, Z. Yang, G. D. Kahanamoku-Meyer, C. T. Olund, J. E. Moore, D. Stanford, and N. Y. Yao, "Many-Body Chaos in the Sachdev-Ye-Kitaev Model", (2020), `arXiv:2002.05725`.

[175] W. Cottrell, B. Freivogel, D. M. Hofman, and S. F. Lokhande, "How to build the thermofield double state", J. High Energ. Phys. **2019**, 58 (2019).

[176] G. Berman and G. Zaslavsky, "Condition of stochasticity in quantum nonlinear systems", Physica A **91**, 450 (1978).

[177] J. Rammensee, J. D. Urbina, and K. Richter, "Many-Body Quantum Interference and the Saturation of Out-of-Time-Order Correlators", Phys. Rev. Lett. **121**, 124101 (2018).

[178] J. Chávez-Carlos, B. López-del Carpio, M. A. Bastarrachea-Magnani, P. Stránský, S. Lerma-Hernández, L. F. Santos, and J. G. Hirsch, "Quantum and Classical Lyapunov Exponents in Atom-Field Interaction Systems", Phys. Rev. Lett. **122**, 024101 (2019).

[179] Y. Sekino and L. Susskind, "Fast scramblers", J. High Energ. Phys. **10**, 065 (2008).

[180] B. Swingle, G. Bentsen, M. Schleier-Smith, and P. Hayden, "Measuring the scrambling of quantum information", Phys. Rev. A **94**, 040302 (2016).

[181] B. Swingle and D. Chowdhury, "Slow scrambling in disordered quantum systems", Phys. Rev. B **95**, 060201 (2017).

[182] L. Foini and J. Kurchan, "Eigenstate thermalization hypothesis and out of time order correlators", Phys. Rev. E **99**, 042139 (2019).

[183] A. Kitaev (2015), talks at KITP, `http://online.kitp.ucsb.edu/online/entangled15/kitaev/`, `http://online.kitp.ucsb.edu/online/entangled15/kitaev2/`.

[184] H. Shen, P. Zhang, R. Fan, and H. Zhai, "Out-of-time-order correlation at a quantum phase transition", Phys. Rev. B **96**, 054503 (2017).

[185] Y. Alavirad and A. Lavasani, "Scrambling in the Dicke model", Phys. Rev. A **99**, 043602 (2019).

[186] C. B. Dağ, K. Sun, and L.-M. Duan, "Detection of Quantum Phases via Out-of-Time-Order Correlators", Phys. Rev. Lett. **123**, 140602 (2019).

[187] Q. Wang and F. Pérez-Bernal, "Probing an excited-state quantum phase transition in a quantum many-body system via an out-of-time-order correlator", Phys. Rev. A **100**, 062113 (2019).

[188] Z.-H. Sun, J.-Q. Cai, Q.-C. Tang, Y. Hu, and H. Fan, "Out-of-Time-Order Correlators and Quantum Phase Transitions in the Rabi and Dicke Models", Ann. Phys. **n/a**, 1900270 (2020).

[189] Q. Hummel, B. Geiger, J. D. Urbina, and K. Richter, "Reversible Quantum Information Spreading in Many-Body Systems near Criticality", Phys. Rev. Lett. **123**, 160401 (2019).

[190] M. Rautenberg and M. Gärttner, "Classical and quantum chaos in a three-mode bosonic system", (2019), `arXiv:1907.04094`.

[191] T. Xu, T. Scaffidi, and X. Cao, "Does scrambling equal chaos?", (2019), `arXiv:1912.11063`.

[192] G. Dvali and C. Gomez, "Black holes as critical point of quantum phase transition", Eur. Phys. J. C **74**, 2752 (2014).

[193] R. Kanamoto, H. Saito, and M. Ueda, "Symmetry Breaking and Enhanced Condensate Fraction in a Matter-Wave Bright Soliton", Phys. Rev. Lett. **94**, 090404 (2005).

[194] R. Kanamoto, H. Saito, and M. Ueda, "Critical fluctuations in a soliton formation of attractive Bose-Einstein condensates", Phys. Rev. A **73**, 033611 (2006).

[195] K. Sakmann, A. I. Streltsov, O. E. Alon, and L. S. Cederbaum, "Exact ground state of finite Bose-Einstein condensates on a ring", Phys. Rev. A **72**, 033613 (2005).

[196] A. G. Sykes, P. D. Drummond, and M. J. Davis, "Excitation spectrum of bosons in a finite one-dimensional circular waveguide via the Bethe ansatz", Phys. Rev. A **76**, 063620 (2007).

[197] D. Flassig, A. Franca, and A. Pritzel, "Large-N ground state of the Lieb-Liniger model and Yang-Mills theory on a two-sphere", Phys. Rev. A **93**, 013627 (2016).

[198] L. Piroli and P. Calabrese, "Local correlations in the attractive one-dimensional Bose gas: From Bethe ansatz to the Gross-Pitaevskii equation ", Phys. Rev. A **94**, 053620 (2016).

[199] L. Piroli, P. Calabrese, and F. H. L. Essler, "Multiparticle Bound-State Formation following a Quantum Quench to the One-Dimensional Bose Gas with Attractive Interactions", Phys. Rev. Lett. **116**, 070408 (2016).

[200] L. D. Carr, C. W. Clark, and W. P. Reinhardt, "Stationary solutions of the one-dimensional nonlinear Schrödinger equation. II. Case of attractive nonlinearity", Phys. Rev. A **62**, 063611 (2000).

[201] C. K. Law, H. Pu, and N. P. Bigelow, "Quantum spins mixing in spinor bose-einstein condensates", Phys. Rev. Lett. **81**, 5257 (1998).

[202] H. Pu, C. K. Law, S. Raghavan, J. H. Eberly, and N. P. Bigelow, "Spin-mixing dynamics of a spinor Bose-Einstein condensate", Phys. Rev. A **60**, 1463 (1999).

[203] C. D. Hamley, C. S. Gerving, T. M. Hoang, E. M. Bookjans, and M. S. Chapman, "Spin-nematic squeezed vacuum in a quantum gas", Nat. Phys. **8**, 305 (2012).

[204] C. S. Gerving, T. M. Hoang, B. J. Land, M. Anquez, C. D. Hamley, and M. S. Chapman, "Non-equilibrium dynamics of an unstable quantum pendulum explored in a spin-1 Bose–Einstein condensate", Nat. Commun. **3**, 1169 (2012).

[205] G. S. Agarwal, *Quantum Optics* (Cambridge University Press, New York, 2013).

[206] M. A. Caprio, P. Cejnar, and F. Iachello, "Excited state quantum phase transitions in many-body systems", Ann. Phys. **323**, 1106 (2008).

[207] G. Sierra and J. Rodríguez-Laguna, "$H = xp$ Model Revisited and the Riemann Zeros", Phys. Rev. Lett. **106**, 200201 (2011).

[208] Y. Gu and A. Kitaev, "On the relation between the magnitude and exponent of OTOCs", Journal of High Energy Physics **2019**, 75 (2019).

[209] G. M. Zaslavsky, *The Physics of Chaos in Hamiltonian Systems* (Imperial College Press, London, 2007), 2nd edition.

[210] B. M. Herbst and M. J. Ablowitz, "Numerically induced chaos in the nonlinear Schrödinger equation", Phys. Rev. Lett. **62**, 2065 (1989).

[211] S. Mailoud, F. Borgonovi, and F. M. Izrailev, "Can quantum many-body systems behave as strongly chaotic, being completely integrable ?", (2019), `arXiv:1907.01893`.

[212] L. Diósi, "Wick theorem for all orderings of canonical operators", J. Phys. A: Math. Theor. **51**, 365201 (2018).

[213] S. Teufel, *Adiabatic Perturbation Theory in Quantum Dynamics* (Springer-Verlag, Berlin, 2003).

[214] A. Stottmeister and T. Thiemann, "Coherent states, quantum gravity, and the Born-Oppenheimer approximation. I. General considerations", J. Math. Phys. **57**, 063509 (2016).

[215] E. Schubert, J. Sander, M. Ester, H. P. Kriegel, and X. Xu, "DBSCAN Revisited, Revisited", ACM Trans. Database Syst. **42**, 1 (2017).

[216] "Documentation of DBSCAN in sklearn PYTHON package", `https://scikit-learn.org/stable/modules/generated/sklearn.cluster.DBSCAN.html`.

[217] M. Gaudin, "Boundary Energy of a Bose Gas in One Dimension", Phys. Rev. A **4**, 386 (1971).

[218] M. Nitsch, B. Geiger, K. Richter, and J.-D. Urbina, "Classical and Quantum Signatures of Quantum Phase Transitions in a (Pseudo) Relativistic Many-Body System", Condens. Matter **5**, 26 (2020).

[219] D. Bauch, "The path integral for a particle moving in a δ-function potential", Nuov. Cim. B **85**, 118 (1985).

[220] E. B. Manoukian, "Explicit derivation of the propagator for a Dirac delta potential", J. Phys. A: Math. Gen **22**, 76 (1989).

[221] B. Geiger, J.-D. Urbina, Q. Hummel, and K. Richter, "Semiclassics in a system without classical limit: The few-body spectrum of two interacting bosons in one dimension", Phys. Rev. E **96**, 022204 (2017).

List of publications:

- B. Geiger, J. D. Urbina, Q. Hummel, and K. Richter, "Semiclassics in a system without classical limit: The few-body spectrum of two interacting bosons in one dimension", Phys. Rev. E **96**, 022204 (2017)
- B. Geiger, Q. Hummel, J. D. Urbina, and K. Richter, "Nonlocal pair correlations in Lieb-Liniger gases: A unified nonperturbative approach from weak degeneracy to high temperatures", Phys. Rev. A **97**, 063612 (2018)
- Q. Hummel, B. Geiger, J. D. Urbina, and K. Richter, "Reversible Quantum Information Spreading in Many-Body Systems near Criticality", Phys. Rev. Lett. **123**, 160401 (2019)
- M. Nitsch, B. Geiger, K. Richter, and J.-D. Urbina, "Classical and Quantum Signatures of Quantum Phase Transitions in a (Pseudo) Relativistic Many-Body System", Condens. Matter **5**, 26 (2020).

Acknowledgments

First of all, I want to thank Juli for always being there for me during the last five years and for her tolerance with my excessive working hours, especially in the last four months of the thesis. I am deeply grateful that she gave me the opportunity to work full time on the thesis in the last couple of weeks – I guess cooking is on me for the next two months.

Then, I want to thank my family for always being very supportive during the years of my Ph.D.

As a dear colleague and friend I want to thank Quirin for the very inspiring discussions and also the various occasions of meeting outside the university. As a former supervisor of my "Zulassungsarbeit" and close collaborator afterwards, he has set the theoretical base for a lot of the results presented here and this work would not have been possible without him.

Next I thank JD as a supervisor, colleague, and friend for the support through the years. The ability of JD to spread a passion for physics to all people around him has always fascinated me and it has helped a lot of times when I got fed up with physics. Also, his door has always been open for everyone (even if he was not in the office) and he has modestly helped me out countless times when I got stuck with the physics.

Finally I want to thank Klaus as my "Doktorvater" for the opportunity to work on the fascinating subjects in the field of semiclassical physics under his supervision. As the lecturer of my quantum mechanics and statistics lectures he has contributed to my interest in theoretical physics already on an early stage and conducted me to write my "Zulassungsarbeit" under his supervision – also in the framework of cluster expansions. Apart from his ability to immediately understand complicated problems and providing valuable support, Klaus has given me the freedom and autonomy to work on my thesis at my own pace.

While modern computational methods provide a powerful approach to predict the behavior of physical systems, gaining intuition of emergent phenomena requires almost invariably the use of approximation methods. The ideas and methods of semiclassical physics presented in this thesis provide a systematic road to address non-perturbative regimes, where classical information find its way into the description of quantum properties of systems of few to many interacting particles.

The first part of the thesis provides a semiclassical description of few-particle systems using cluster expansions and novel analytic results for short-range interacting bosons in one and three dimensions are derived. In the second part, complementary approaches for many-particle systems are used to study the non-equilibrium scrambling dynamics in quantum-critical bosonic systems with large particle numbers, revealing an unscrambling mechanism due to criticality that is verified in extensive numerical simulations.

Universitätsverlag Regensburg

ISBN 978-3-86845-164-1

9 783868 451641

gefördert von:

Alumni der physikalischen Fakultät der Universität Regensburg e.V.

Universität Regensburg